The Development of a Locally Based Weather and Climate Model in Southern Africa

Report

to the Water Research Commission

by

TR Maisha[1], PT Mulovhedzi[1], GT Rambuwani[1], LN Makgati[1], M Barnes[1], L Lekoloane[1], FA Engelbrecht[2] , T Ndarana[3] , IL Mbokodo[1], NG Xulu[5] and MM Bopape[1,3,5]

[1]Research Department, South African Weather Service, [2]Global Change Institute, University of Witwatersrand, [3]Department of Geography, Geoinformatics and Meteorology, University of Pretoria, [4]Department of Geography and Environmental Studies, University of Zululand, [5] South African Environmental Observation Network, National Research Foundation

WRC report no. 3181/1/24

ISBN 978-0-6392-0683-7

February 2025

Obtainable from

Water Research Commission
Private Bag X03
Gezina, 0031

hendrickm@wrc.org.za or download from www.wrc.org.za

This is the final report of WRC project no. C2020/2021-00596.

EXECUTIVE SUMMARY

South Africa has been using numerical weather and climate models, developed in the global north, where they are also tested for operational forecasting and informing policy developments for decades. Consequently, these models are generally optimal for the regions where they are developed, leading to potential biases and limitations in other areas. This project addresses the need for South Africa to actively contribute to and engage in model development. The project focuses on enhancing the Conformal Cubic Atmospheric Model (CCAM), developed at the Council for Scientific and Industrial Organisation (CSIRO) of Australia, and has been in use in South Africa for over two decades. The aim of this project is to incorporate local expertise in model improvements, which is crucial for accurate simulations of weather and climate over the Southern Africa Development Community (SADC) region and the surrounding oceans. The project endeavours to improve CCAM's simulation of weather and climate by investigating and understanding the dynamical core of the model, improving cumulus, cloud microphysics, and boundary layer schemes, and conducting further research of the model’s capability in simulating selected high-impact weather events that have affected the SADC region. The goal is to build local capacity in model development, making South Africa an independent contributor to the development and use of numerical weather and climate models. The project's outcomes include coordinated efforts among universities and the South African Weather Service (SAWS), concentrating on a single model, the CCAM, to efficiently address regional needs. Through this initiative, South Africa aims to overcome historical challenges, enhance operational models, and contribute to the global trend of model development, incorporating local domain expertise. Moreover, the project extends modelling training to other SADC countries equipped with High-Performance Computing (HPC) systems, fostering collaboration and knowledge exchange.

The literature study on dynamical cores discusses the significant evolution of global atmospheric models since the 1960s and emphasises the current push towards seamless forecasting systems applicable across various timescales and applications. It introduces the CCAM as a seamless forecasting system proposed for South Africa. The challenges of maintaining multiple numerical frameworks due to differing applications, resolutions, and timescales are underlined, especially for organisations with limited technical and financial resources. Moreover, the importance of numerical approximations in solving the set of primitive equations that govern atmospheric evolution are outlined. The study further highlights the mechanisms of the CCAM, detailing its use of a conformal-cubic grid system and a semi-implicit, semi-Lagrangian scheme. Various horizontal grid systems are explored, with more focus on the advantages of cube-based grids. The reversible staggered grid used by CCAM is discussed for its benefits in computational efficiency. The text also touches on the spatial aspects of CCAM's dynamical core, such as horizontal grid systems and vertical coordinates. Furthermore, the study addresses the applicability of CCAM for a range of timescales, from short-range weather forecasts to climate projections for the far future. It also highlights CCAM's successful use in various applications, including downscaling projects and seasonal predictions. The importance of high-resolution information in contemporary modelling is emphasised, with a consideration of CCAM's ability to resolve convective storms and boundary layer processes. Moreover, the transition to nonhydrostatic equations to enhance the model's

ability to explicitly resolve small-scale motions, necessitating adjustments to parameterization schemes is underlined.

A further investigation of the model found that the CCAM has two boundary layer schemes, the local and non-local schemes, whose mathematical formulations were discussed. The local approach employs the K stability-dependent scheme based on the Monin-Obukhov similarity theory; while the non-local formulation is based on the gradient diffusion approach, which depends on the diffusion coefficient K and gradients of mean variables. The diffusion coefficient K is formulated from the turbulent kinetic energy (TKE) and the eddy dissipation rate and uses the eddy-diffusivity mass-flux (EDMF) approach. Results of the EDMF approach from different models and implementations were analysed and show that coupling the EDMF with TKE improves the simulations of the boundary layer evolution, structure, and properties.

The project further researched on the cloud microphysics schemes within the CCAM. It first outlines the different aspects of these schemes, and then investigates the performance of various cloud microphysics schemes within the CCAM in replicating a severe weather event that led to substantial rainfall and flooding. The analysis involves CCAM simulations of extreme weather events under different experimental conditions, utilising the global forecast system (GFS) analysis and the fifth generation of the European Centre for Medium-Range Weather Forecasts (ECMWF) reanalysis (ERA5) as initial conditions. The current cloud microphysics scheme employed within the CCAM is a single moment scheme which predicts the mixing ratios of various hydrometeors. The microphysical processes that are treated by the cloud scheme include cloud liquid water, water vapour, cloud ice and the changes of various hydrometeors from one phase to another. The subjective comparison conducted shows that all the model simulations consistently exhibit a tendency to inaccurately position intense rainfall, particularly in the central regions of South Africa for the period 21 - 24 April 2019 severe weather event. Furthermore, all simulations consistently underestimate the observed 24-hour accumulated rainfall intensity as recorded by stations, radar, and Integrated Multi-satellite Retrievals for global precipitation measurement (IMERG). The simulations initiated with ERA5 reanalysis shows a slight improvement in the misplacement of heavy rainfall in the central parts of South Africa when compared to the GFS run.

The study of cumulus parameterization within the CCAM comprised three parts, namely, the evaluation of different versions of the CCAM cumulus scheme, hereafter Convjlm, a sensitivity test to identify the optimal settings for the bcon parameter and an investigation into the scale-awareness of the Convjlm cumulus scheme. The first experiment investigated the 2015a, 2015b, 2017, and 2015aM versions of CCAM Convjlm scheme. The study found no significant differences in how the model simulated precipitation across these versions. While diurnal cycles for areal average rainfall showed discrepancies in simulating patterns and amounts of observed precipitation, all versions exhibited a lack of skill in simulating precipitation over the South African domain. Notably, the 2015aM cumulus scheme consistently yielded lower precipitation than other versions, posing a challenge in accurately capturing rainfall spatial distribution.

The second experiment focused on sensitivity tests to identify the optimal setting for the bcon parameter, which is crucial to both the cloud and convection schemes. While the first case demonstrated benefits with bcon=0.1, subsequent cases did not demonstrate significant differences among model runs. The study emphasised that improving forecast accuracy may not solely depend on adjusting the bcon parameter, suggesting the need to consider additional parameters for enhanced forecasting.

The third experiment focused on the scale-awareness of the Convjlm cumulus scheme. The experiment tested the CCAM applied at five different grid lengths, namely, 25 km, 10 km, 6 km, 3 km and 1 km, to understand the scheme's behaviour at different resolutions. The research was aimed at determining when the convection scheme completely switches off to rely fully on the cloud microphysics scheme, analyse changes in model accuracy and skill with resolution, and explore insights for further model enhancements. Case studies associated with severe rainfall events were analysed, revealing that as resolution increases, the model increases its accuracy in locating intense rainfall events. The report also examines the model's performance in terms of latent and sensible heat release, providing valuable insights for refining the model code for improved accuracy and predictability. Recommendations include a more processed-based analysis, extending scale-awareness tests to sub-kilometre scales, adjusting formulation for scale-awareness, and studying dynamical processes at various grid scales.

The performance of the CCAM in simulating landfalling tropical cyclones was also evaluated with an aim to identify model deficiencies for subsequent model development and improvements. Tropical cyclone Freddy was identified as a case of interest in the study as it is considered the longest-lived storm to date for remaining active for approximately 37 days (WMO, 2023). The outcomes of these experiments are key to inform technical and scientific improvements on the model setup. From the experimental setup, the CCAM was able to reproduce the spatial distribution, intensity and timing of the landfall as well as its track. However, after 72 hours, the CCAM missed the landfalling storm, and simulated a less intense storm. The study recommends further experiments on other tropical cyclone cases to provide detailed analysis on the performance of the model.

A review of the cut-off low (COL) pressure system was also performed since they produce significant amounts of rainfall over South Africa. This has an impact on the amount of water availability over the country. The occurrence of cut-off lows over SA were compared to other parts of the world including South America and Australia. The study focused on the occurrence, development, propagation, dynamical processes and impacts of COLs on society and the environment. The reviews show that at times, COLs may extend to the surface, creating conditions conducive to extreme rainfall and high floods over South Africa, especially when impinged on the coastal escarpment. The slow propagation of COL appears to be largely modulated by a quasi-stationary high-pressure system downstream acting as a blocking system. An analysis shows that during COL occurrences, rainfall is anomalously high and usually complemented by snow, very cold or flooding conditions. In some parts of South Africa, the occurrences of extreme rainfall events (e.g., COLs) reduce the severity of dry conditions when they occur during the austral summer. Although the focus has been on studying specific and individual COL events, which have largely contributed to model development and theories, more studies focusing on climatology and model forecasting of COLs must be conducted using the more recent high-resolution reanalyses and trackers. Moreover, work focusing on its dynamical evolution has been minimal. Therefore, there is a need to investigate the dynamic structure of global COLs.

This research indicates significant progress in modelling in South Africa because the CCAM was not approached as a black box. Through this research four early career scientists got to understand the dynamical core of the CCAM and how it compares with other models, the convection scheme, the cloud microphysics schemes and the boundary layer schemes. Three other students applied the model without considering how it is set up, but through this study, got introduced into modelling. Three PhD students journeyed to Australia to engage with the CCAM developers, returning with enhanced technical skills. Model development is typically a time-consuming endeavour, and the noteworthy contributions of this study will play a crucial role in advancing South Africa towards the independent development and application of models.

Recommendations emanating from this study include:

- Further investigation of the CCAM's dynamical core, including grid setup and non-hydrostatic equations, especially at high resolutions.
- More analysis of the model's boundary layer schemes, including interaction with the ocean and testing alternative options.
- Additional tests with different global datasets and exploring a double moment microphysics scheme to improve rainfall simulation.
- More in-depth analysis of the cumulus convection schemes, including scale-aware behaviour and how it can be further improved at high resolutions.
- Conducting hindcast simulations to systematically evaluate the model's performance over multiple seasons.

ACKNOWLEDGEMENTS

We would like to acknowledge the Water Research Commission for supporting and funding this project. Also, the project team wishes to thank the following people for their contributions to the project.

Reference Group	Affiliation
Dr Brilliant Petja	Water Research Commission
Prof Siva Venkataraman	University of KwaZulu-Natal
Ms Lerato Mpheshea	University of Cape Town
Prof Babatunde Abiodun	University of Cape Town
Dr Gabriel Lekalakala	Department of Water and Sanitation
Other Experts	
Dr Marcus Thatcher	Commonwealth Scientific and Industrial Research Organisation
Prof John MacGregor	Commonwealth Scientific and Industrial Research Organisation
Dr Jack Katzfey	Commonwealth Scientific and Industrial Research Organisation
Dr Sonny Truong	Commonwealth Scientific and Industrial Research Organisation
Project Team Members	
Dr Mary-Jane Bopape (Project Leader)	South African Weather Service (Currently affiliated with National Research Foundation)
Mr Robert Maisha	South African Weather Service (Student: University of Pretoria)
Prof Thando Ndarana	University of Pretoria
Mr Gift Rambuwani	South African Weather Service (Student: University of Pretoria)
Ms Lebogang Makgati	South African Weather Service (Student: University of Cape Town)
Ms Patience Mulovhedzi	South African Weather Service (Student: University of Pretoria)
Mr Lesetja Lekoloane	South African Weather Service (Currently affiliated with African Bank)
Dr Michael Barnes	South African Weather Service

	(Currently affiliated with Monash University)
Mr Nkosinathi Xulu	University of Zululand (Student: University of Zululand)
Mr Innocent Mbokodo	South African Weather Service (Student: Northwest University)
Prof Francois Engelbrecht	University of Witwatersrand
Prof Hector Chikoore	University of Limpopo

CONTENTS

LIST OF FIGURES

LIST OF TABLES

ACRONYMS & ABBREVIATIONS

ARS	Automatic Rainfall Stations
AS	Arakawa–Schubert
AWS	Automatic Weather Stations
CABLE	Community Atmosphere–Biosphere Land Exchange model
CAM	Climate and Forecast Australian Model
CAPE	Convective Available Potential Energy
CASIM	Cloud-Aerosol Interacting Microphysics
CCN	Cloud-condensation-nuclei
CCAM	Conformal Cubic Atmospheric Model
CF CCAM	Climate and Forecast Australian Model
CFL	Courant–Friedrichs–Lewy
CHPC	Centre for High Performance Computing
CMC	Canadian Meteorological Centre
COL	Cut-off low pressure system
CSI	Critical Success Index
CSIRO	Commonwealth Scientific and Industrial Organization
EDMF	Eddy-diffusivity mass-flux
ECMWF	European Centre for Medium-Range Weather Forecasts
ERA5	Fifth generation of the ECMWF reanalysis
FBS	Fractions Brier scores
FSS	Fractions Skill Scores
FV3	Finite-Volume Cubed-Sphere
GCM	Global Climate Model
GEM	Global Environmental Multiscale Model
GFS	Global Forecast System
GPM	Global Precipitation Measurement
GMT	Greenwich Mean Time
HPC	High-Performance Computing
IMERG	Integrated Multi-satellite Retrievals for GPM
ICON	Icosahedral Nonhydrostatic
IFS	Integrated Forecasting System

JAXA	Japan Aerospace Exploratory Agency
LDR	Leon Rotstayn cloud microphysics scheme
Mk 3.6	Mark 3.6 version
MSSG	Multi-Scale Simulator for the Geo-environment
NOAA	National Oceanic and Atmospheric Administration
NSSL	National Severe Storms Laboratory
NCEP	National Centers for Environmental Prediction
NWP	Numerical weather prediction
PSD	Particle size distribution
QPE	Quantitative precipitation estimates
RH	Relative humidity
SADC	Southern African Development Community
SAS	Simplified Arakawa-Schubert
SASAS	South African Society for Atmospheric Sciences
SAWS	South African Weather Service
SR	Success ratio
TKE	Turbulent kinetic energy
TS	Threat Score
TRMM	Tropical Rainfall Measuring Mission
UM	Unified Model
UK	United Kingdom
WDM	WRF Double Moment Schemes
WRF	Weather and Research Forecasting
WSM	WRF Single Moment

CHAPTER 1: BACKGROUND

1.1 INTRODUCTION

Weather and climate play pivotal roles in shaping various socio-economic sectors, including agriculture, water resource management, and disaster preparedness (Petzold et al., 2023). The accuracy of weather predictions and climate models is crucial for effective decision-making and risk reduction, particularly in regions with diverse environmental conditions such as Southern Africa (Serdeczny et al., 2017; Schewe et al., 2019; Almazroui et al., 2020). Despite advancements in global weather and climate models, their ability to capture the complexity of the climate dynamics of Southern Africa remains limited (Sebastian et al., 2018). This underscores the necessity for the development of homegrown weather and climate models that address the unique characteristics of the region.

Weather and climate numerical models are necessary tools for operational weather forecasting, climate predictions, and climate projections (Meque et al., 2021). Their outputs play a pivotal role in decision-making processes aimed at mitigating the impacts of weather-related disasters and formulating products tailored to climate-sensitive sectors such as the water and agricultural sectors. Despite the extensive use of these models in South Africa, inherent shortcomings persist within current models, as evidenced by studies highlighting shortcomings in capturing regional phenomena, particularly severe thunderstorms in the north-eastern part of the country (Stein et al., 2019; Keat et al., 2019).

The models used in Southern Africa include the United Kingdom Met Office (UKMO) Unified Model (UM), the Consortium for Small-scale Modelling (COSMO), and the Weather Research and Forecasting (WRF) models (Landman et al., 2012; Mulovhedzi et a., 2021). These models, while instrumental in both research and operational domains, exhibit distinctive behaviours and limitations, as illustrated by studies showcasing variations in simulating locally forced convective activity (e.g., Keat et al., 2019; Mulovhedzi et al., 2021). In addition, these models have been in use in South Africa for many decades both in operational and research mode (Reason et al., 2006).

Model development initiatives around the country have been undertaken between the 1960s and 1980s, mainly by the South African Weather Service (SAWS), and the Council for Scientific and Industrial Research (CSIR; Engelbrecht, 2006; Bopape, 2014). These efforts were put to rest in the mid-1990s due to policy changes in organisations that were leading these initiatives, until the early 2000s when the University of Pretoria developed a non-hydrostatic kernel for a new NWP model with funding from the Water Research Commission (WRC). Even with model development resurrected in the country, South Africa continues to rely on NWP models from developed countries for operational purposes. Some model development initiatives in the country have relied on established modelling systems from developed nations. For instance, Abiodun et al. (2008a and b) enhanced the dynamical core of the Community Atmosphere Model (CAM) to incorporate a stretched grid with higher resolution, focusing on specific areas or processes of interest. This improvement was initiated during his tenure at Iowa State University and continued when he joined the University of Cape Town (UCT). Additionally, at SAWS, Beraki et al. (2014; 2015) coupled the ECHAM4.5 model with the Modular Ocean Model version 3 (MOM3). Further, ongoing developments at the Global Change Institute (GCI) of the University of Witwatersrand, involving ocean model development and coupling with the Conformal Cubic Atmospheric Model (CCAM) and the land surface model CABLE showcase the holistic approach adopted by South African scientists in advancing comprehensive earth system modelling (Bopape et al., 2019).

While researchers globally strive to enhance weather and climate simulations in their respective regions, the African continent has contributed minimally to model development. African scientists, although proficient at identifying model challenges, often lack the capacity to modify these models to suit regional needs. This continues a reliance on model developers primarily situated in the global north, necessitating a radical change towards localized expertise inclusion for development of a comprehensive solution.

In response to these challenges, Bopape et al. (2019) have advocated for a model development framework to empower South Africa in cultivating the capacity for the creation of indigenous models. Acknowledging the extensive timeline required for model development, which can exceed a decade, it becomes imperative to follow a trajectory of building on proven seamless models that align with international standards. The CCAM emerges as a suitable model, having been applied in South Africa for over a decade in weather forecasting, seasonal forecasting, and climate projections.

The CCAM, with its dynamic evolution from an initially hydrostatic to a non-hydrostatic model core, has demonstrated adaptability in simulating small-scale processes, including thunderstorms. The adoption of a cubic gnomonic grid on a sphere, as instituted by McGregor (1996), enhances accuracy in comparison to traditional latitude-longitude grids. Furthermore, recent developments in global modelling trends, such as the UK Met Office's decision to shift from a latitude-longitude Unified Model to a cube-based system (Walters et al., 2017), affirm the suitability of CCAM's grid structure for contemporary and future computational resources, facilitating ultra-high-resolution models.

The advent of High-Performance Computing (HPC) systems in Southern Africa, facilitated through the Southern Africa Development Community (SADC) Cyber-Infrastructure Framework, marks a pivotal moment for advancing numerical weather and climate modelling. Countries within the SADC region, including Mozambique, Botswana, Namibia, Tanzania, Zambia, Madagascar, Mauritius, and Lesotho, have received HPC systems. This development empowers scientists to run sophisticated numerical models, catalysing skills development, and collaborative endeavours within the region.

This research aims to bridge the existing gap by focusing on the development of a region-specific weather and climate model for Southern Africa. Motivated by the challenges faced by current global models, especially in accurately predicting phenomena like droughts, floods, and heatwaves in the region, the proposed model seeks to enhance forecasting accuracy. By leveraging local data, incorporating regional topographical features, and accounting for localised climate processes, the model aims to provide valuable insights into Southern Africa's climate variability and change. The primary objective is to develop a locally based weather and climate model specifically designed to simulate Southern Africa's weather and climate patterns accurately. The research also aims to evaluate the performance of the developed model against existing global models and assess its potential applications in key sectors such as agriculture, water resource management, and disaster risk reduction.

The report is structured as follows: chapter 2 provides a comprehensive review of the CCAM model dynamical core. The set of primitive equations used in weather modelling are introduced. Various model coordinate systems are also introduced and explained as well as the CCAM cubic grid. Chapter 3 describes the boundary layer parameterization used within the CCAM system. At least two boundary layer schemes for turbulent mixing are used in the model and discussed. Chapter 4 describes an overview of the CCAM cloud microphysics scheme tested and subjective verification results are presented. In Chapter 5, we describe in detail the CCAM cumulus parameterization scheme, and subjective and quantitative verification results from experiments conducted are included. In Chapter 6, the performance of the CCAM model was evaluated at various grid resolutions in simulating extreme weather events (i.e., cut-off lows, tornado, hail and heatwave) over South Africa. Chapter 7 provides the study of simulation of tropical cyclones by the CCAM model over the Indian Ocean domain. In Chapter 8 we present a review of cut-off low pressure systems that made landfall over South Africa in detail. This work has been peer-reviewed and published in an international research Journal. In Chapter 9 we provide information on the capacity building initiatives, stakeholder engagement and information dissemination. Lastly, we provide a list of references for all chapters.

1.2 PROJECT AIMS

The following were the aims of the project:

1. Investigate the performance of CCAM using different resolutions from inertial subrange (i.e., large eddy simulations) to coarse resolutions where most of the reliance is placed on parameterisation schemes.
2. Investigate the performance of CCAM when simulating different weather patterns over Southern Africa with midlatitude, subtropical and tropical systems included.
3. Test and improve the cumulus, microphysics, and boundary layer schemes and introduction of other schemes in the CCAM to improve simulations of weather over Southern Africa.
4. Understand the dynamical core of the CCAM system, its advantages, and disadvantages and if there are any improvements necessary.

1.3 SCOPE AND LIMITATIONS

This study focused on the use of the CCAM as well as understanding its parametrization schemes. A wide range of the literature review on different components of numerical weather and climate models including dynamical core, and physical parameterization of convection, cloud microphysics and boundary layer processes of the weather and climate models was conducted. These were compared with the CCAM code, and also informed the experiments conducted in the study. The knowledge gained from the literature review provides a baseline for understanding the CCAM, which is the model chosen in this study.

In order to run the model, scientists working on the project had to download the CCAM suite from the Commonwealth Scientific and Industrial Research Organisation (CSIRO) of Australia, together with various scripts that are used to setup and run the model. A number of input datasets including bathymetry, topography, land cover, sea surface temperature climatology, sea ice, as well as aerosol also had to be downloaded. Once the suite was acquired, the suite needed to be configured and compiled on the Centre for High Performance Computing (CHPC). For this to be achieved, relevant libraries including NetCDF, HDF5, Fortran, etc and as well other utilities needed to be installed on the CHPC. After installation, the model domain was set up together with the required nests (for dynamical downscaling). This includes setting up the correct microphysics, cumulus parametrization, boundary layer and radiation schemes. Once the setup was complete, input data was sourced from different meteorological centres, i.e. global forecast system (GFS) and the ERA5 reanalysis. These datasets are required to initialise the model. When the project started, a number of the scientists working on the project had either not run a model before, and had not run CCAM and therefore this project provided them with the experience of setting up, compiling, and running a model on an HPC system.

In the study, a number of high impact weather events were simulated and analysed. These include cut-off low systems, upper air troughs, tropical cyclones, thunderstorms, and the analysis of both the CCAM simulations, ground observations and remote sensing data resulted in these systems being better understood by the researchers. In addition to skills built in setting up and running the models, skills were also built on the use of statistical and visualisation tools such as Python and GrADS.

From this work, some limitations were experienced - All four of the aims of the project were addressed, however, there were limitations with a part of aim 3. For aim three the project team had to test and improve the cumulus, cloud microphysics and boundary layer schemes in the CCAM. The team conducted an extensive literature review, including papers that the CCAM schemes are based on and also studied the CCAM code to understand the different parametrization schemes. Identifying the effect of experiments conducted is easier in idealised simplified models, however with the real earth systems, it is not straightforward to determine the cause of the error. For example as experiments were conducted, it became clear that some of the shortcomings in the model simulations may be due to external factors such as the forcing model, which means even with a perfect CCAM, there would still be short comings in the model output. The sparsity of ground stations observations in some areas across the country makes it challenging to validate the model simulations. A number of international studies on model development are based on experimental observation campaigns that are very expensive to conduct and so far, we have not had one in South Africa and therefore observations available to inform local model development continue to be less than ideal.

CHAPTER 2: THE CCAM DYNAMICAL CORE

2.1 INTRODUCTION

Since their inception in the 1960s, global atmospheric models have undergone significant evolution, finding application in various contexts across different timescales, from numerical weather prediction and seasonal forecasting to climate studies. Generally, various numerical frameworks have been developed to cater for distinct applications, resolutions, and timescales, posing challenges for entities with limited technical and financial resources. A current global trend advocates for unified systems that seamlessly cater for various timescales and applications, such as operational centres like the UK Met Office and the European Centre for Medium-Range Weather Forecasts (ECMWF). The proposed CCAM atmospheric framework aims to serve as such a seamless forecasting system tailored for South Africa.

The fundamental principle of global atmospheric models involves solving a set of primitive equations to calculate the atmosphere's evolution. However, these models face limitations due to resolution constraints, leaving some processes unresolved. Typically, atmospheric models consist of two components: the dynamical core, where resolved processes are determined by the primitive equations, and the model physics, addressing unresolved processes through parameterization, including convection, boundary layer dynamics, and cloud microphysics (Gross et al., 2018).

The set of primitive equations effectively describes atmospheric motions across various spatial scales, ranging from sub-kilometer turbulent eddies to synoptic-scale motions like Rossby waves (Klein, 2014). These equations encompass continuity of momentum, mass, and thermodynamics. An illustrative example of these equations, simplified in the x-z plane and neglecting Coriolis, diabatic, and friction terms, can be found in literature (Miller and White, 1984; Engelbrecht, 2006):

$\frac{Du}{Dt}+\frac{1}{\rho}\frac{\partial p}{\partial x}=0$	(2.1)
$\frac{Dw}{Dt}+\frac{1}{\rho}\frac{\partial p}{\partial z}+g=0$	(2.2)
$\frac{D\ ln\ ln\ \rho}{Dt}+\frac{\partial u}{\partial x}+\frac{\partial w}{\partial z}=0$	(2.3)
$\frac{D\ ln\ ln\ T}{Dt}-\kappa\frac{D\ ln\ ln\ \rho}{Dt}=0$	(2.4)

where $D/Dt=\partial/\partial t+u\ \partial/\partial x+w\ \partial/\partial z$, u and w are the wind components in the zonal (x) and vertical (z) directions. The perfect gas law $p=\rho RT$ relates the density (ρ), pressure (p) and the temperature (T) where R is the gas constant and $\kappa=R/c_p$ with c_p the specific heat at constant pressure. Various forms of this equation set exist and can contain various approximations, assumptions and coordinate systems.

The set of primitive equations is both non-linear and highly intricate, making analytical solutions unattainable (Pu and Kalnay, 2018). To address this, numerical approximations become a key method for obtaining a solution. Numerical techniques necessitate discretizing the set of primitive equations, essentially breaking down the earth into a three-dimensional grid, where finite differencing methods are applied to solve for various variables. This process introduces complexities, starting with the need to project the spherical Earth onto a flat grid, like a latitude-longitude grid, potentially leading to inaccuracies, especially near the poles. Global models often use latitude-longitude grids, which may introduce complexities and errors into the numerical framework.

Additionally, there are considerations for representing vertical motion in numerical models. Historically, hydrostatic models, relying on the hydrostatic approximation, were prevalent, but non-hydrostatic models, solving the full continuity equation, have gained prominence. Various vertical coordinate systems, such as pressure and sigma (terrain-following) coordinates, have been explored. Moreover, finite differencing methods in grid-point based models offer options, with more advanced Eulerian methodologies like Arakawa-C grids becoming preferred over centred differencing schemes. Lagrangian schemes, where model grid-points follow the flow of air parcels, provide an alternative, with semi-Lagrangian schemes, redefining grid points at each timestep, being commonly preferred by major NWP centres like National Oceanic and Atmospheric Administration (NOAA) and ECMWF.

In subsequent sections, the dynamical core of CCAM will be comprehensively detailed, covering the set of primitive equations, strategies, and methodologies employed for their solution. Key methodologies, including grid structure, finite differencing, and coordinate systems, will be discussed in comparison with other global modelling centres and general numerical modelling theory. Given the South African Weather Service's goal of deploying a numerical framework for a range of applications, from high-resolution short-range prediction to coarse-resolution climate simulations, the applicability of CCAM across spatial and temporal scales will also be explored.

2.2 DESCRIPTION OF THE DYNAMICAL CORE

2.2.1 The continuous set of primitive equations of the CCAM

The CCAM employs a semi-implicit, semi-Lagrangian form of the set of primitive equations (McGregor 1996) on the conformal-cubic grid. Details of the properties of such a set of equations will be discussed in later sections. The set of primitive equations employed in CCAM as defined by McGregor (2005) are shown in the sections that follow.

2.2.1.1 The horizontal momentum equations

$\frac{d_H u}{dt} + m\frac{\partial \phi_v}{\partial x} + mR_d T_v \frac{\partial\, ln\, ln\, p_s}{\partial x} + \dot{\sigma}\frac{\partial u}{\partial \sigma} = (f + f_m)v + \tilde{N}_u$	(2.5)
$\frac{d_H v}{dt} + m\frac{\partial \phi_v}{\partial y} + mR_d T_v \frac{\partial\, ln\, ln\, p_s}{\partial y} + \dot{\sigma}\frac{\partial v}{\partial \sigma} = (f + f_m)u + \tilde{N}_v$	(2.6)

where m is the mapping factor of the conformal projection, σ are terrain-following vertical coordinates ($\sigma = p/p_s$), ϕ_v is the geopotential (including virtual temperature contributions), $\tilde{N}$ denotes the contributions from parameterizations and R_d is the gas constant for dry air. T_v is the virtual temperature and can be defined by:

$$T_v = T\left[1 + \left(\frac{R_d}{R_v} - 1\right)q\right]$$

where T is the temperature, R_v is the gas constant for water vapour and q is the mixing ratio of water vapour. f is the Coriolis parameter and f_m results from the conformal-cubic mapping projection, where

$$f_m = u\frac{\partial m}{\partial y} - v\frac{\partial m}{\partial x}$$

2.2.1.2 The thermodynamic energy equation

$\frac{d_H T}{dt} + \dot{\sigma}\frac{\partial T}{\partial \sigma} + \frac{R_d T}{c_p \sigma}\frac{\omega}{p_s} = \tilde{N}_T$	(2.7)

2.2.1.3 The moisture equation

$\frac{d_H q}{dt} + \dot{\sigma}\frac{\partial q}{\partial \sigma} = \tilde{N}_q$	(2.8)

2.2.1.4 The continuity equation

$\frac{d_H\, ln\, ln\, p_s}{dt} + D + \frac{\partial \dot{\sigma}}{\partial \sigma} = 0$	(2.9)

where the divergence D is given by

$$D = m^2\left\{\frac{\partial(\frac{u}{m})}{\partial x} + \frac{\partial(\frac{v}{m})}{\partial y}\right\}$$

2.2.2 Spatial aspects of the CCAM dynamical core

2.2.2.1 The horizontal grid systems

a) Latitude-longitude grids

Historically, global modelling centres have employed the widely used regular latitude-longitude grid. However, a notable challenge with this grid type is the presence of polar singularities, where longitude grid lines converge towards the poles, potentially leading to violations of conservation laws, commonly referred to as the "pole problem" (Collins et al., 2013). Addressing this problem often involves increasing the length of the timestep, incurring significant computational expenses (Randall et al., 2002). The elevated zonal resolution near the poles results in inefficient utilisation of computational resources across the rest of the domain. While some solutions involve employing special filters for small scales or utilising separate coordinate systems around the poles, these approaches may introduce errors that propagate throughout the domain and might not scale efficiently on parallel computers (Heikes et al., 2013; Rančić et al., 1996).

Several strategies have been explored to mitigate the pole problem while maintaining the regularity of the latitude-longitude grid. For instance, a previous version of the Global Forecast System (GFS) deployed a regular grid with a triangular grid specifically around the poles (Collins et al., 2013). Presently, the Met Office's UM used across various timescales, still relies on a regular latitude-longitude grid and offers an alternative of using a rotated pole to minimise errors in specific global regions by shifting the singularity away from the pole towards the equator (Bush et al., 2020). More sophisticated attempts have introduced innovations like the Yin-Yang grid, which utilises two overlapping sections of the latitude-longitude grid that avoid the singularity at the pole (Kageyama and Sato, 2004).

b) Icosahedral grids

To address the pole problem, one grid approach that has been developed involves the use of icosahedral-type grids. These grids are constructed by applying triangular meshes onto the 20 faces of an icosahedron and projecting the mesh vertices onto a sphere (Wang and Lee, 2011). This results in a grid comprising either triangles or hexagons, both of which exhibit quasi-uniform size distribution across the Earth. The concept of icosahedral grids was initially introduced by Sadourny et al. (1968) and has since been widely adopted in various forms. Notably, the operational NWP model of the German Weather Service (“Deutscher Wetterdienst” - DWD), known as the Icosahedral Nonhydrostatic model (ICON; Bonaventura, 2004), employs an icosahedral-triangular grid. Beyond addressing the pole problem, icosahedral grids provide quasi-uniform grid resolution throughout the entire domain, contributing to enhanced computational efficiency. A global icosahedral system can be conceptualised as a network of interconnected regional models, where each of the 20 faces functions as an individual regional model, showcasing remarkable versatility. Additionally, the choice of grid cell shape plays a crucial role; for instance, hexagonal grids lack support for nesting since it is not feasible to construct a larger hexagon using smaller hexagons. This limitation, however, does not apply to triangular and square grid cell shapes.

c) Cubic grids

Cube-based grids share fundamental similarities with icosahedral grids, operating on the principle of projecting geometric shapes onto a sphere. In this case, the six (6) faces of a cube are projected onto the sphere, with each face comprising rectangles or gridlines where the vertices of each rectangle represent grid points (Ullrich, 2011). Analogous to their icosahedral counterparts, cubic grids offer quasi-uniform resolution, circumvent polar singularities, and exhibit remarkable versatility. Noteworthy is the apparent advantage of cubic grids over icosahedral grids, as cubed grids possess fewer (8) vertices resulting in singular points. However, this reduction in singular vertices may also imply that these singularities could be more pronounced when compared to those in icosahedral grids. The rectangular structure of each face in the cube facilitates seamless integration with latitude-longitude discretization schemes, presenting square grid cells as opposed to hexagonal or triangular ones.

Currently, there is an apparent trend among global NWP modelling centres favouring cube-based grids. Indeed, two prominent NWP modelling centres, namely ECMWF and National Oceanic and Atmospheric Administration (NOAA), have recently transitioned to cube-based grids. In 2016, ECMWF upgraded the dynamical core of its Integrated Forecasting System (IFS) by adopting a cubic-octahedral grid (Malardel et al., 2015). More recently, in 2020, NOAA followed suit by upgrading its GFS suite to the Finite-Volume Cubed-Sphere (FV3) dynamical core (GFS v16), employing a cubed-spherical grid (Harris et al., 2020).

d) Vertical coordinates

Various vertical coordinates have been used in numerical modelling frameworks. Pressure coordinates are one of the most “natural” to meteorologists. Their advantages are however more extensive than this. Pressure coordinate systems are well suited to observations which are taken with respect to pressure levels. From a model development perspective, pressure vertical coordinates also simplify the sets of primitive equations by eliminating density from the equation set (Engelbrecht, 2006). This is a crucial factor for a choice of numerical framework where model development skill sets are fledgling. However, pure pressure vertical coordinate systems are not well suited in numerical models as they intersect the earth surface. This led to the development of terrain-following pressure coordinate systems or sigma (σ) levels (Phillips, 1957) where $\sigma = p/p_{surface}$. The σ-levels have been developed further. For example, the eta (η) vertical coordinate system makes use of the mean sea level pressure as lower bound reference pressure (Mesinger et al., 2012). The CCAM makes use of the traditional σ coordinate system.

Global atmospheric models have traditionally functioned below the hydrostatic limit. Nevertheless, advancements are rapidly facilitating the operation of these systems beyond this limit. It is noteworthy that full pressure coordinate systems encounter challenges in non-hydrostatic frameworks, potentially becoming singular under conditions of substantial vertical acceleration (Laprise, 1998). The conventional belief was that σ coordinates, utilising hydrostatic pressure as the reference pressure, represents the exclusive approach to address this issue. However, Engelbrecht (2006) has innovatively formulated fully-elastic equation sets within a σ-coordinate framework, grounded in the entire pressure field. This methodology has been successfully implemented and tested within the CCAM framework, showcasing its efficacy in overcoming the limitations associated with non-hydrostatic conditions.

e) The conformal-cubic grid system

Global atmospheric models have traditionally functioned below the hydrostatic limit. Nevertheless, advancements are rapidly facilitating the operation of these systems beyond this limit. It is noteworthy that full pressure coordinate systems encounter challenges in non-hydrostatic frameworks, potentially becoming singular under conditions of substantial vertical acceleration (Laprise, 1998). The conventional belief was that σ coordinates, utilising hydrostatic pressure as the reference pressure, represented the exclusive approach to address this issue. However, Engelbrecht (2006) has innovatively formulated fully-elastic equation sets within a σ-coordinate framework, grounded in the entire pressure field. This methodology has been successfully implemented and tested within the CCAM framework, showcasing its efficacy in overcoming the limitations associated with non-hydrostatic conditions. An example of the conformal-cubic grid applied within the CCAM is shown in Figure 2.1.

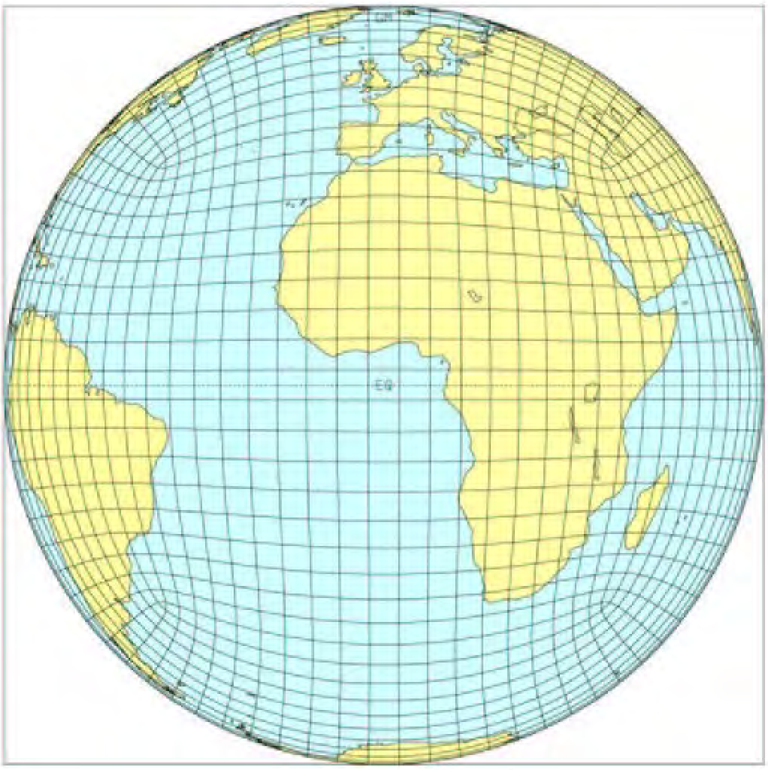

Figure 2.1: The Conformal-cubic C20 grid centered over Africa – taken directly from McGregor (2005).

In the deployment of the C-C grid within the CCAM, a critical consideration pertains to the vertices of the cube. It is imperative to recognize that the C-C grid exhibits heightened resolution in proximity to the cube's vertices. This heightened resolution, particularly near steep orography, can engender stationary resonances when the Courant–Friedrichs–Lewy (CFL) condition surpasses unity, as evident in a semi-Lagrangian primitive equation set like that employed in the CCAM (McGregor, 1996). To maintain a relatively large timestep for computational efficiency, meticulous attention must be directed towards siting vertices over regions devoid of orography.

McGregor (1996) exemplifies this approach by siting vertices primarily over the ocean, except for one vertex situated above the relatively flat West Siberian plain.

McGregor (1996) conducted advection tests on the C-C grid, employing a semi-Lagrangian advection scheme, and juxtaposed the results with those obtained using the latitude-longitude grid. The findings illuminated significantly smaller advection errors with the C-C grid compared to the longitude-latitude grid. The enhanced resolution and strategic vertex placement advocated by McGregor (1996) remarkably mitigated advection errors over the C-C vertices, surpassing the challenges associated with the pole problem on the latitude-longitude grid. Furthermore, advection tests on a stretched C-C grid revealed negligible errors, comparable to those observed in the unstretched configuration.

2.2.2.2 The Spatio-temporal discretization of the CCAM dynamical core

a) The semi-implicit, semi-Lagrangian scheme

The CCAM employs a semi-implicit, semi-Lagrangian formulation of the primitive equations (McGregor 1996), a methodology increasingly prevalent in global NWP models (Williamson, 2007). Notably, other widely used models such as the UM (Bush et al., 2020), ECMWF IFS (Malardel et al., 2015), the Canadian Meteorological Centre's (CMC) Global Environmental Multiscale Model (GEM; Côté *et al*., 1998), and NOAA's GFS utilise variations of semi-implicit semi-Lagrangian or finite volume semi-implicit Lagrangian schemes.

Lagrangian schemes, characterised by grid-points dynamically following air parcels, present an alternative to traditional Eulerian schemes. Despite their benefits, such as stable longer timesteps, Lagrangian schemes tend to concentrate air parcel arrival points in zones of convergence or divergence, resulting in voids in specific regions (Smith, 2000). Semi-Lagrangian schemes, a refinement of Lagrangian approaches, redefine air parcels at each timestep, allowing for the calculation of transport in a Lagrangian manner with constant quantities along trajectories. These schemes, commonly employing backward trajectories, enhance computational efficiency through the use of a bi-cubic interpolator (McGregor, 2005) for trajectory-based interpolation. Eulerian grid-point methods address the remaining terms in the primitive equation set.

The advantages of semi-Lagrangian advection schemes include stability for longer timesteps, combining the strengths of Eulerian and Lagrangian approaches while avoiding clustering issues seen in pure Lagrangian schemes (Smith, 2000). The computational efficiency of implicit schemes, particularly semi-implicit ones, is crucial in atmospheric modelling, as they implicitly solve fast-moving sound and gravity waves while explicitly addressing other processes (Mesinger and Arakawa, 1976).

However, challenges exist with semi-Lagrangian schemes, notably Doppler shifting of stationary forcing, as observed near mountainous regions. This can lead to significant truncation errors associated with time-averaging in semi-implicit schemes (Williamson and Laprise, 2000). To mitigate this, the CCAM employs a methodology involving off-centering the time-averaged term along the Lagrangian trajectory, as suggested by McGregor (2005). While this approach has demonstrated some success in reducing noise in solutions associated with stationary waves (Williamson and Laprise, 2000), it does not entirely eliminate the issue (Héreil and Laprise, 1996).

b) Horizontal staggered grid point arrangement in CCAM

Atmospheric models have evolved from employing simple unstaggered grids, such as the Arakawa-A grid, for distributing wind components across the grid. Research indicates that unstaggered grids exhibit suboptimal dispersion properties. Despite their simplicity, as they allow wind components to be defined at the same grid points, unstaggered grids simplify parameterization schemes and semi-Lagrangian advection. In contrast, staggered grids, exemplified by the Arakawa C-grid, have gained popularity in NWP models due to their enhanced dispersion behaviour over unstaggered grids, particularly in the presence of large Rossby radius of deformation (McGregor, 2005). Alternatives like the staggered Z-grid proposed by Randall (1994), which stores vorticity and divergence rather than wind components, have demonstrated improved dispersion properties across various Rossby radius of deformation.

The CCAM utilises the reversible staggered, or R-grid, as described by McGregor (2005). The R-grid represents a hybrid approach, combining the simplicity of the unstaggered A-grid with the dispersion benefits of the staggered C-grid. In this scheme, primary variables are stored on an unstaggered A-grid, providing the dynamical core with the simplicity of the A-grid. To address potential erroneous dispersion behaviour, gravity wave terms are transformed to the staggered C-grid before calculation and then reversed back to the unstaggered A-grid post-calculation. The R-grid has demonstrated comparable dispersion behaviour to Z-grid by Randall (1994), proving effective across both small and large scales. This characteristic is particularly significant for a model intended to resolve small-scale processes at high resolutions. Detailed formulas for the unstaggered-staggered interpolator and a concise numerical evaluation of the R-grid scheme employed in the CCAM can be found in McGregor (2005).

c) Vertical motion in the CCAM

The CF-CCAM employs a solution methodology based on a hydrostatic set of primitive equations, as detailed by McGregor (2005). Hydrostatic models hinge on the hydrostatic approximation, a fundamental assumption within the set of primitive equations. This approximation posits that vertical acceleration can be effectively approximated by hydrostatic balance for processes larger than the meso-scale (tens of kilometres). Consequently, fine-scale vertical motions, characteristic of phenomena like the updrafts and downdrafts in thunderstorms, remain beyond the scope of the primitive equation set used in the CCAM. Instead, these finer-scale processes are simulated through the utilisation of parameterization schemes incorporated into the CCAM.

Advancements in global computational capabilities have enabled the realisation of ambitions for kilometre-scale and sub-kilometre scale simulations. NWP systems, seeking to explicitly resolve smaller-scale processes like convective-scale phenomena, are increasingly adopting non-hydrostatic formulations of the primitive equations. Examples include the UM (Bush et al., 2020) and the GFS (Harris et al., 2020), both of which have transitioned to non-hydrostatic primitive equation sets. Notably, the operational ECMWF IFS currently employs a hydrostatic solver (ECMWF, 2020), though a code incorporating a nonhydrostatic solver is undergoing research-mode testing at ECMWF (Kuhnlein et al., 2019).

A specific nonhydrostatic set of primitive equations has been developed for a C-C grid by Engelbrecht (2006), with the explicit aim of supplanting the hydrostatic set within the CCAM. An advantageous aspect for the SAWS and local CCAM users is that this non-hydrostatic equation set was locally developed by Engelbrecht (2006). Furthermore, successful testing within the CCAM environment has demonstrated the relative ease with which the nonhydrostatic equation set can be implemented (Engelbrecht, 2006). This presents a potential pathway for the CCAM to transition to the non-hydrostatic set proposed by Engelbrecht (2006), enabling a seamlessly adaptable model across all time-ranges and resolutions.

2.2.3 Applicability of the CCAM for high resolution and short-range applications

The CF CCAM originated as a climate-scale model, extensively applied in climate-scale simulations as evidenced by studies conducted by Nguyen et al. (2012), McGregor et al. (2016), and Engelbrecht (2019). While the SAWS is mandated to conduct climate-scale simulations, it concurrently holds the responsibility of providing atmospheric forecasts across varying timescales to both SA and SADC region. This encompasses immediate nowcasts with lead-times measured in hours, small- to medium-range forecasts spanning days, and seasonal forecasts extending up to month-long lead times. Consequently, the modelling system employed by the organisation must exhibit flexibility across these temporal scales.

Engelbrecht et al. (2011) and Landman et al. (2015) have delved into the efficacy of the CCAM at the seasonal timescale, demonstrating success through rainfall verification in these simulations. Seasonal predictions in Java, Indonesia, have further supported these findings (Satyawardhana and Gammamerdianti, 2019). Notably, certain inaccuracies in relatively coarse-resolution simulations have been acknowledged, prompting considerations of potential resolution-related implications, as posited by Engelbrecht et al. (2011). Mitigation strategies, including statistical postprocessing (Barnston and Tippett, 2017) and leveraging ensemble forecasting (Landman et al., 2014), have been proposed as effective interventions.

The CCAM's proficiency in capturing sub-daily variability is fundamental to short to medium-range time-scale forecasting. Engelbrecht et al. (2011) and Landman et al. (2015) have reported on the model's aptitude at these timescales with initial conditions from the GFS at 15 km and 60 km horizontal resolutions, yielding satisfactory outcomes. Positioned as a potentially seamless forecasting system, the CCAM has demonstrated comparative performance to the operational system of the SAWS, the UM (Landman et al., 2012). However, it is significant to note that this comparison does not extend to the updated UM version or the short-term forecasts at the higher 1.5 km and 4.4 km resolutions currently employed at the SAWS.

Given the contemporary surge in computational capacity enabling high-resolution modelling, a novel operational modelling system within the SAWS necessitates applicability at high- to ultra-high resolutions. The CCAM has exhibited successful application in high-resolution downscaling endeavours at climate time scales, achieving horizontal resolutions down from 8 to 15 km for the sub-Saharan region (Engelbrecht, 2019) and globally (Thatcher and McGregor, 2008). Additionally, experiments have ventured into ultra-high resolutions of around 1 km over South Africa (Engelbrecht et al., 2011). Nevertheless, a critical consideration when contemplating the CCAM at high resolution pertains to its ability to explicitly resolve convective storms and boundary layer processes. The inherent hydrostatic nature of the CCAM may impede the explicit resolution of small-scale motions, particularly at quasi-kilometre and sub-kilometre resolutions. Consequently, an exploration of introducing a non-hydrostatic equation set for the SAWS CCAM version is warranted. The introduction of such a set could potentially explicitly resolve certain convection and boundary layer processes, necessitating the adaptation of distinct parameterization schemes.

2.3 DISCUSSIONS

In this report, the dynamical core of the CCAM has been outlined and compared to other existing NWP systems. The literature suggests that the CCAM could be a good starting point for model development in South Africa. The CCAM makes use of a cubic-type grid, more specifically the conformal-cubic grid, which many centres have tended towards over the recent past. The semi-implicit, semi-Lagrangian scheme used is generally used globally and possesses many advantages. The R-grid staggering of the CCAM gives the modelling framework the superior accuracy of staggered grids with the simplicity of the unstaggered grid. This provides an easier platform for new model developers to continue development on the framework. Furthermore, grid stretching techniques allow for enhanced regional resolution at low computational cost.

The CCAM does have its drawbacks and considerations to contend with. The placement of cube vertices is a crucial consideration to eliminate potential topographically related noise from the solutions and retain optimal computational efficiency. A potential downfall of the CCAM is the hydrostatic primitive equation set on which it is built. This could prevent small-scale motions such as convection and large boundary layer eddies to be explicitly resolved. A potential solution may be provided by the nonhydrostatic framework of Engelbrecht (2006), which can be implemented within the CCAM framework. If implemented, the new non-hydrostatic CCAM would need to be thoroughly tested amongst the hydrostatic CCAM and other modelling frameworks at a range of timescales and horizontal resolutions.

Although most applications of the CCAM have been related to the climate time scale, it has been shown that the CCAM can be readily used at a variety of different time scales as was identified by Engelbrecht et al. (2011) and Landman et al. (2015). Although some testing of the system at shorter timescales has been done, testing of the system at these timescales will need to be done far more rigorously, with verification on multiple parameters including rainfall, temperature, wind and its ability to simulate extreme weather phenomena. In addition, its ability at ultra-high and sub-kilometre resolution needs to be thoroughly tested for the CCAM to fill the SAWS needs as a seamless forecasting system.

CHAPTER 3: THE CCAM PLANETARY BOUNDARY LAYER SCHEME

3.1 INTRODUCTION

An atmospheric boundary layer (ABL) modelling seeks to represent the evolution and dissipation of turbulence in the atmosphere. This is done through parameterisation of various processes which occur within the ABL since the dynamical core of the model does not fully resolve them. ABL parameterisation also seeks to approximate nature and therefore involves human interpretation and creativity (Stull 1988). This has resulted in many different parameterisation schemes being developed, tested and implemented. However, to formulate a correct parameterisation scheme, there is a need for a recognition of the closure problem resulting from the turbulent nature of the mixing within the ABL (Holt and Raman 1988). This is known as the turbulence closure problem, since deriving a set of closed equations for the evolution of a grid-box mean is not possible due to a number of unknowns being larger than the number of equations.

There are two main philosophies to address the closure problem. The first advocates that unknown quantities at any point be parameterised by the mean atmospheric values or gradients of known quantities at the same point (Lock et al. 2000). This is known as local closure and is equivalent to molecular diffusion. The second approach is described by Lock et al. (2000), and is known as the non-local closure, which says that unknown quantities at one point can be parameterised by atmospheric values or gradients of known quantities at various points in space. This is equivalent to advection processes.

One of the disadvantages of local closure is its inability to represent the effects of larger eddies. These include a limitation to simulate turbulent mixing within adjacent layers symmetrically (Xie et al. 2012). The non-local approach accounts for the effects of larger eddies and therefore better represents the evolution of a well-mixed convective ABL (Bèlair et al. 1999). Schemes of a non-local nature are computationally expensive. To counter for the expenses, some studies have shown that including non-local effects in turbulence schemes based on eddy diffusivity coefficients, help better represent the convective ABLs (e.g., Mailhot and Benoit 1982; Troen and Mahrt 1986). In theory, there is an indefinite number of orders from which lower or higher orders of parameterisation schemes can be formulated.

The CCAM approach to parameterising the ABL is in terms of the turbulent vertical mixing based on both local /and non-local formulations. The local approach employs the first-order stability-dependent scheme based on the Monin-Obukhov similarity theory (McGregor et al. 1993). This was developed utilising the methods of the theory of similitudes by Monin and Obukhov (1954), which concluded that the vertical changes of mean flow, turbulence, characteristics in the surface layer is only dependent on the surface momentum flux measured by friction velocity, buoyancy flux, and height. However, the CCAM stability functions which relate the surface fluxes to their mean gradients, differs from the original suggestion by Monin and Obukhov (1954) in that it uses the gradient Richardson number instead of the height.

On the other hand, the non-local formulation of the ABL is based on the gradient diffusion approach, which depends on the diffusion coefficient K and gradients of mean variables (McGregor et al. 1993). The scheme that is employed to calculate K is formulated from the turbulence kinetic energy (TKE) and the eddy dissipation rate and uses the eddy-diffusivity/mass-flux (EDMF) approach described by Hurley (2007). This approach uses mass-flux scheme following Soares et al. (2004) which parameterises the counter-gradient term in the vertical heat flux equation.

3.2 LITERATURE REVIEW AND ANALYSIS

3.2.1 The local parameterization scheme of the CCAM

A first-order local diffusion approach in which the sub-grid scale turbulence and vertical kinematic flux of tracer C is taken proportional to the local gradient of the transported quantity, is formulated as

$$\underline{w'C} = -K_C \frac{\partial C}{\partial z} \tag{3.1}$$

Where the local scheme of the CCAM is depicted in equation (3.1), but the diffusion coefficients K_C are expressed as follows (equation 3.2):

$$K_C = l^2 \left|\frac{\partial v}{\partial z}\right| F_m(Ri_b), \tag{3.2}$$

The Blackadar (1962) expression for the mixing length (l) is as follows (equation 3.3):

$$l = \frac{kz}{1+\frac{kz}{\lambda}} \tag{3.3}$$

Where k is the asymptomatic mixing length and is an adjustable constant. The variable z represents height, and for both the stable and unstable cases, the function F_C is respectively represented by equation 3.4 as follows:

$$F_m = (1 + b'_m Ri_b)^{-2} \tag{3.4}$$

and

$$F_m = 1 - \frac{b_m Ri_b}{1+c_m|Ri_b|^{1/2}} \tag{3.5}$$

where

$$c_m = 5C_{DN} b_m \left(\frac{z}{z_0}\right)^{1/2} \tag{3.6}$$

and

$$C_{DN} = \frac{k^2}{\left\{ln\left(\frac{z}{z_0}\right)\right\}^2} \tag{3.7}$$

z_0 represents the roughness length for momentum, and *k* is the von Kármán constant. The Ri_b is the bulk Richardson number (equation 3.8)

$$Ri_b = \frac{g\frac{\partial\theta}{\partial z}}{\theta\left|\frac{\partial V}{\partial z}\right|^2} \tag{3.8}$$

where *g* is gravitational acceleration and θ is a column-wise potential temperature.

3.2.2 The non-local parameterization scheme of the CCAM

The non-local formulation of tracer C, unlike in equation (3.1), considers the non-local transport and is written as follows (equation 3.9):

$$\underline{w'C} = -K_C\left(\frac{\partial C}{\partial z} - \gamma_C\right) \tag{3.9}$$

Expanding from equation (3.9), the turbulence scheme used to calculate K is the standard $E - \varepsilon$ model. The model solves the prognostic equations for the turbulence kinetic energy (E) and the eddy dissipation rate (ε)

$$\frac{dE}{dt} = \frac{\partial}{\partial z}\left(K\frac{\partial E}{\partial z}\right) + P_S + P_b - \varepsilon \tag{3.10}$$

$$\frac{d\varepsilon}{dt} = \frac{\partial}{\partial z}\left(c_{\varepsilon 0}K\frac{\partial \varepsilon}{\partial \sigma}\right) + \frac{\varepsilon}{E}\left(c_{\varepsilon 1}\left(P_S + max(0, P_b) + max(0, P_T)\right) - c_{\varepsilon 2}\varepsilon\right) \tag{3.11}$$

where

$$P_S = K\left(\left(\frac{\partial u}{\partial z}\right)^2 + \left(\frac{\partial v}{\partial z}\right)^2\right) \tag{3.12}$$

$$P_b = -\frac{g}{\theta_v}K\left(\frac{\partial\theta_v}{\partial z} - \gamma_{\theta_v}\right) \tag{3.13}$$

$$P_T = -\frac{\partial}{\partial z}\left(K\frac{\partial E}{\partial z}\right) \tag{3.14}$$

$$K = c_m\frac{E^2}{\varepsilon} \tag{3.15}$$

and $c_m = 0.09$, $c_{\varepsilon 0} = 0.69$, $c_{\varepsilon 1} = 1.46$, and $c_{\varepsilon 2} = 1.83$.

3.2.3 Analysis of the parameterization schemes used by the CCAM

The scheme employed by the CCAM non-local closure scheme is based on the gradient diffusion, with diffusion coefficient K formulated from the TKE and the eddy dissipation rate and uses the EDMF approach described by Hurley (2007). This approach uses a mass-flux scheme following Soares et al. (2004) which parameterises the counter-gradient term in the vertical heat flux equation. This also assumes that in the CBL, the sub-grid-scale fluxes result from two different mixing scales: small eddies, which are parameterised by an eddy-diffusivity approach, and thermals, which are represented by a mass-flux contribution. Figure 3.1 below shows a schematic view of a shallow cumulus convective boundary layer and mass-flux formulation of the EDMF scheme from Soares et al. (2004). The EDMF scheme has been tested on various models. For example, Soares et al. (2008) used the EDMF scheme on a one-dimensional version of the MesoNH model and tested it for a dry convective boundary layer case. Their results indicated that the EDMF-TKE closure can realistically reproduce the counter gradient fluxes and the fluxes and the top-entrainment.

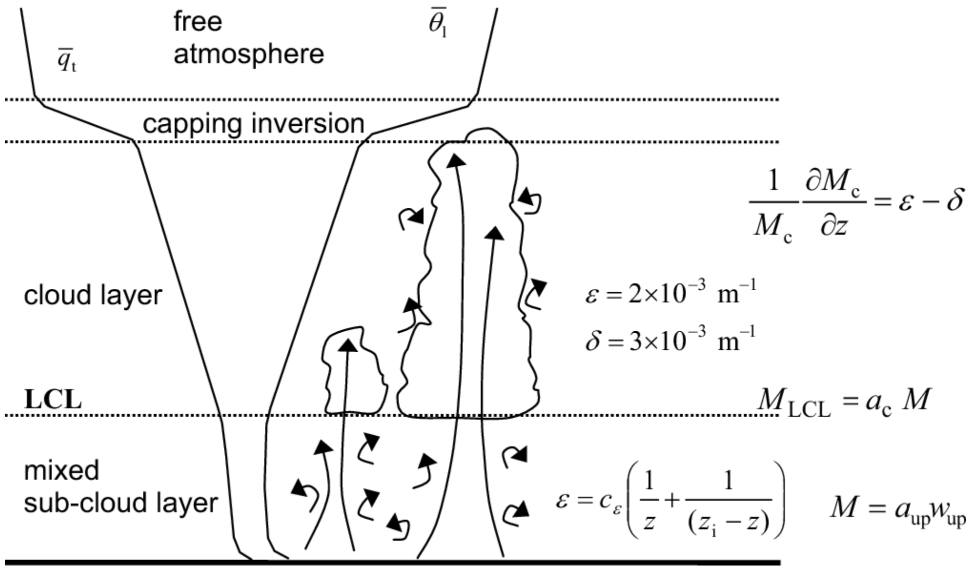

Figure 3. 1: Schematic view of a shallow cumulus convective boundary layer and mass-flux formulation of the EDMF scheme.

Figure 3.2 below is an example of how their scheme reproduces the potential temperature compared to a large eddy model (LES) simulation. One important advantage of the EDMF approach, as in their study, is that it allows for the unified parameterisations to represent shallow moist convection, and the cloud-topped boundary layer in general, by allowing for condensation in the updraft.

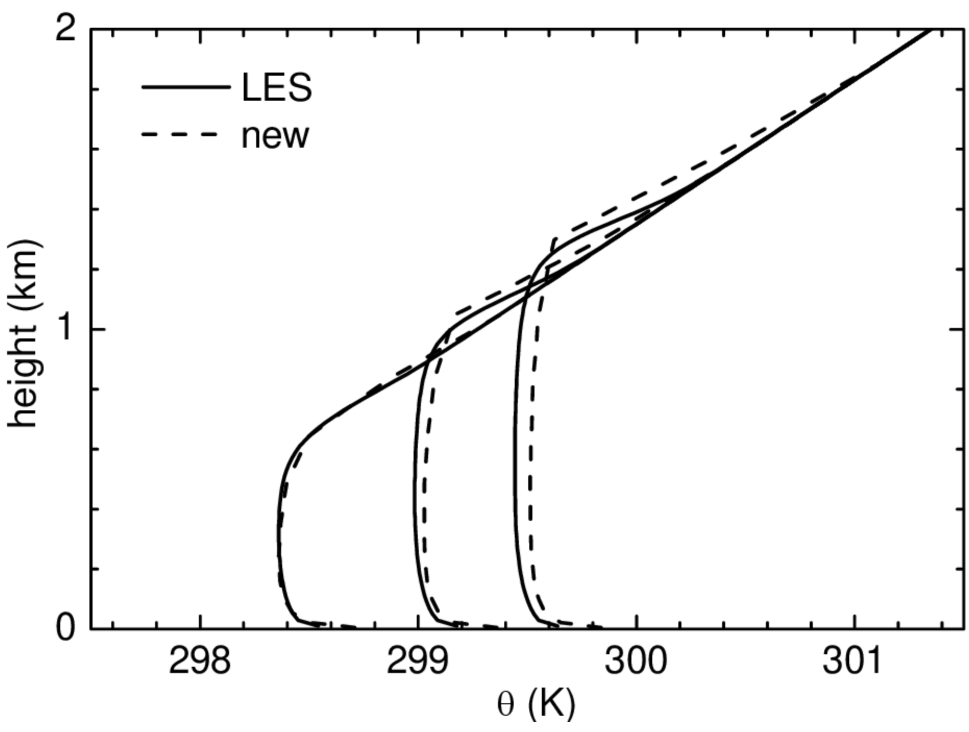

Figure 3. 2: Hourly averaged potential temperature profiles at hours 2, 4 and 6. Results from the KNMI LES, and from the new EDMF scheme (new) with a vertical resolution corresponding to the ECMWF model 40-level grid.

Furthermore, Witek et al. (2011) has shown that the EDMF scheme can be coupled to the TKE prognostic equation. In their study, they embedded the EDMF framework in a one-dimensional model and evaluate it against the LES simulations. Their results indicate that the scheme represents the structure and evolution of the mean model variables very accurately and can properly capture the CBL height dynamics and the well-mixed neutral profile in the middle of the CBL. Moreover, the new one-dimensional model is quite robust in respect to its sensitivity to vertical and temporal resolution changes.

3.3 CONCLUSIONS

This chapter outlines two parameterisations of the ABL by the CCAM. The first uses the local approach to close the dynamical primitive equations, while the second uses the non-local approach. The local approach employs the K stability-dependent scheme based on the Monin-Obukhov similarity theory; while the non-local formulation is based on the gradient diffusion approach, which depends on the diffusion coefficient K and gradients of mean variables. The diffusion coefficient K is formulated from the TKE and the eddy dissipation rate and uses the EDMF approach. Results of the EDMF approach from different models and implementations were analysed and show that coupling the EDMF with TKE improves the simulations of the boundary layer evolution, structure, and properties.

CHAPTER 4: THE CCAM MICROPHYSICS SCHEME

4.1 INTRODUCTION

The cloud microphysics scheme comprises a set of physical processes that govern the formation of cloud droplets and ice particles, their growth, decay, and eventual transformation into precipitation on a grid-scale (Houze, 1993). This scheme primarily focuses on parameterizing key water substances, including cloud droplets, rain droplets, water vapor, snow, graupel, and hail. Various microphysical parameterization models, such as Bin parameterization models, Bulk parameterization models, Lagrangian trajectory parameterization models, and Hybrid bin parameterization models, can be employed to capture the microphysical processes associated with these water substances (Straka, 2009; Stensrud, 2007; Iguchi et al., 2012; Li et al., 2010).

Cloud microphysics can be categorised into two main types: the microphysics of warm clouds, which occurs when temperatures are above 0°C, and the microphysics of cold clouds, which occurs when temperatures drop below 0°C, allowing for the coexistence of both ice and liquid water (Houze, 1993; 2014). Figure 4 .1 illustrates the key precipitation types and microphysical processes that are parameterized within atmospheric models.

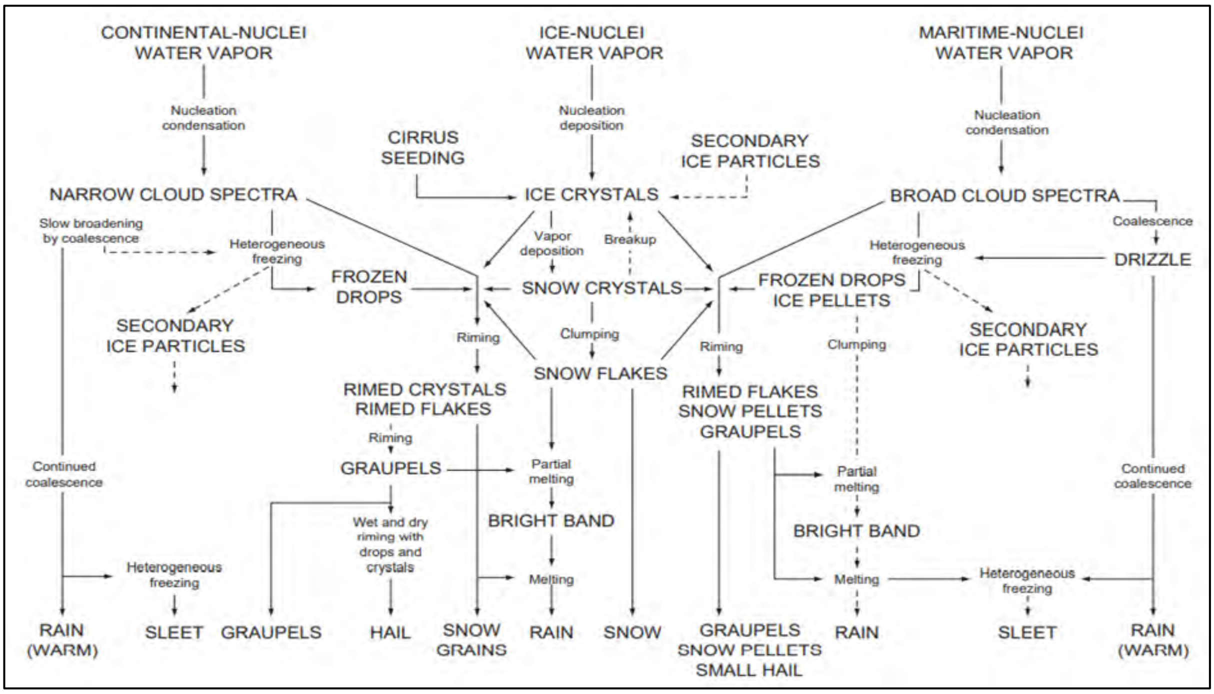

Figure 4.1: The types of precipitation and microphysics processes that are parametrized within the atmospheric models (Adopted from Braham and Squires, 1974).

4.1.1 Types of microphysical parameterization models

There are various types of cloud microphysics models which include bin, bulk and hybrid parameterization schemes.

a) Bin parameterization models

In Bin parameterization models, which are also known as spectral bin, explicit microphysics, bin-resolving, or size-resolving microphysics, microphysical particles of a specific water category are grouped into size bins, representing various divisions along the spectrum of drop sizes (Li et al., 2009; Li et al., 2010). The evolution of each bin is individually computed using predictive equations (Li et al., 2009; Li et al., 2010). This spectrum of drops ranges from minute cloud droplet sizes (almost 4 micrometres) to larger raindrops (4 to 8 mm) for modelling rain formation (Straka, 2009). Each bin is assumed to be exponentially larger than the preceding bin by a certain order, with the form of the particle-size distribution function (e.g., the gamma function) for hydrometeor types considered known (Houze, 1993). The predictive equations used to calculate the evolution of each bin are derived from the water continuity equation (equation 4.1):

$$\frac{Dqi}{Dt} = Si,\ \ i = 1, \ldots, n \qquad (4.1)$$

where, *qi* represents the mixing ratio of a specific type of water substance (the mass of water per unit mass of air), and *Si* is the cumulative effect of sources and sinks for that particular category of water. The bin microphysics approach differs from earlier-generation models in terms of the complexity of representing microphysical processes (Khain *et al*., 2015). However, it comes with a significant computational cost for operational use due to the numerous bins and predictive equations (each particle size's mixing ratio must be predicted as a separate variable; Lee and Baik 2018; Ogura and Takahashi, 1973; Soon, 1974). The bin microphysics process can be further divided to model either warm or cold clouds, depending on the location of the cloud in question, specifically in the lower troposphere where the temperature exceeds 0°C.

b) Bulk parameterization models

Bulk microphysics calculates the particle size distribution (PSD) using a functional form (Zhang et al., 2008), and is more computational cost-effective for operational purposes. This approach employs a comprehensive description of cloud microphysical properties through a semi-empirical representation of PSDs. In many cases, these parameterizations predict mixing ratios and number concentrations (Straka, 2009). With recent advances in computing power, it has also become possible to predict the third moment, such as radar reflectivity. The bulk microphysics scheme primarily diverges from other methods in its assumptions about the shape of particle size distributions, relationships between particle diameter and terminal fall speed, and associations between particle mass and diameter, among other factors (Molthan and Colle, 2012). The bulk microphysics method includes various classes, such as single-, double-, and triple-moment schemes. For PSDs represented by f(m), the k-th moment can be expressed by equation 4.2, where m denotes the mass of a particle and k is an integer value:

$M^{(k)} = \int_0^{\infty} m^k f(m) dm$ ………………………………………………………………………………………..(4.2)

- for one or single-moment schemes, k = 1 (uses mass content of hydrometeors)
- for double moment schemes, k = 0, 1 (number concentration and mass content)
- for triple moment schemes, k = 0, 1, 2 (number concentration, mass content and radar reflectivity)

- Single moment bulk microphysics scheme

The PSD is usually represented by exponential distribution, Gamma distribution, and lognormal distribution models (Zhang *et al*., 2008). The models used are most often the exponential and gamma distributions. The gamma distribution equation for precipitating hydrometeor classes (used by many single or double moment microphysics schemes) is given by the following equation:

$N(D) = N_0 D^{\mu} e^{-\lambda D}$ ………………………………………………………………………………………….(4.3)

where, *N(D*) is the total number concentration per unit volume of particles of a given hydrometeor (units: m-3), *D* is particle diameter, N_0 is the intercept parameter that defines the maximum *N* for a diameter of 0, *μ* is a shape parameter, and *λ* is a slope parameter (Seifert and Beheng, 2001). The exponential distribution is a specific form where the shape parameter *μ* = 0. The single moment parameterization scheme predicts the mass mixing ratio only of each parameter (hydrometeor classes).

For example, the United Kingdom (UK) Met Office Unified Model (UM), which is used as an operational numerical weather prediction (NWP) model at the South African Weather Service (SAWS), the microphysics parameterization scheme is based on Wilson and Ballard (1999) with extensive modifications since then. The most recent modifications are documented in Abel and Boutle (2012) where the representation of the raindrop size distribution was improved. Four phases are assumed (liquid, vapour, ice aggregates and rain) and the microphysical processes represented includes fall of ice and rain under gravity; primary nucleation of ice particles by heterogeneous and homogeneous nucleation; deposition and sublimation of ice; aggregation; riming; capture of raindrops by falling ice particles, which increases the ice content; melting of ice particles; evaporation of rain; accretion; and auto-conversion (Wilkinson, 2020).

The Weather and Research Forecasting (WRF) model has multiple single moment microphysics schemes which includes the WRF Single Moment 3 (WSM3; follows Hong et al., 2004), the WSM5 [which is a simple ice scheme that held water vapour, rain, snow, cloud ice and cloud water in five different arrays], WSM6 [extension of WSM5 to include graupel and associated processes], Kessler scheme [a simple warm cloud scheme that includes water vapour, cloud water and rain. The microphysical processes included are rain production, fall of rain, and evaporation of rain (Kessler, 1969)] and NSSL 1 moment (graupel properties are specified), to mention a few, that differ according to complexity. Multiple studies have compared the aforementioned schemes and others to see how they perform over different domains and under different weather regimes (https://www.science.gov/topicpages/s/single-moment+microphysics+scheme.html).

- Double moment microphysics scheme

In contrast with the single moment scheme, double moment schemes predict both the number concentration and mass content of each hydrometeor. For PSDs f(m), the k-th moment is represented by equation (2), where k = 0 (number concentration) and k = 1 (mass content). One example of a double moment scheme is that of Seifert and Beheng (2006), whereby a double moment scheme for mixed phase clouds was developed to improve the explicit representation of clouds and precipitation in mesoscale atmospheric models. Seifert and Beheng's scheme predicts the evolution of both mass and number concentration of the five hydrometeor types (i.e. cloud droplets, raindrops, cloud ice, snow and graupel). The scheme parameterized relevant homogeneous and heterogeneous nucleation processes including the activation of cloud condensation nuclei. As a result, the Seifert and Beheng's scheme can distinguish between the continental and maritime environments, and it can also be used to study aerosol effects on precipitation.

The WRF model has several double moment schemes, including the WRF double moment schemes 5 and 6 (WDM5 and WDM6). The development of the two schemes follows Lim and Hong (2010), where the two schemes have the same ice processes and warm rain processes which are double moment calculated. The schemes are also sensitive to cloud-condensation-nuclei (CCN) numbers. The WDM7 scheme is an extension of WDM5 and WDM6, developed to include the hail category separated from graupel (Bae et al., 2018). The Thompson scheme is a bulk scheme that has a double-moment calculation of ice and rain (Thompson *et al.,* 2008). The Morrison 2-moment scheme has six hydrometeors' species including (i.e. water vapour, cloud droplets, cloud ice, rain, snow, and graupel or hail), with a user switch to choose between graupel and hail (Morrison *et al*., 2008). The UM microphysics scheme, the Cloud-Aerosol Interacting Microphysics (CASIM) scheme, has options to be used as either a single-, double- or triple moment scheme. Five microphysical species namely: liquid cloud, rain, ice cloud, snow and graupel are available for CASIM (Miltenberger *et al.,* 2018). For a double moment scheme, properties of PSD are mass mixing ratio and number concentration, with all microphysical species capable of being double moment (Miltenberger *et al*., 2018).

- Triple moment microphysics scheme

Triple moments schemes have been developed to predict number concentration, mass content and radar reflectivity (Milbrandt & Yau, 2005; Shipway & Hill, 2012; Dawson *et a*l., 2014; Loftus *et a*l., 2014; Naumann & Seifert, 2016). Milbrandt and Yau (2005) described a full version of a three-moment scheme for all precipitating hydrometeor types (including both liquid and ice particles). A closure formulation to calculate the source and sink term of the radar reflectivity or third moment of the size distribution was developed. The study then compares idealised hailstorm simulations for one-moment, two-moment and three-moment versions of the scheme and noted the difference in evolution of surface precipitation rate between two-moment and three-moment schemes. Naumann and Seifert (2016) investigated the evolution of the raindrop size distribution for two isolated shallow cumulus clouds cases using large-eddy simulations. Part of their investigation was to use a three-moment microphysics scheme which was able to capture the general development of the relation of the shape parameter to the mean raindrop diameter as compared to the two-moment microphysics scheme for two cases.

c) Hybrid parameterization models

A hybrid scheme represents a blend of both bin and bulk microphysics schemes. Its purpose is to combine the accuracy of bin schemes with the efficiency of bulk schemes. In this parametrization model, the distribution functions for mixing ratios and number concentrations are initially computed using the bin model (after being converted into bins). Subsequently, the outcomes are transferred back to the bulk parameterization for mixing ratio and number concentration distribution (Straka, 2009). It is worth noting that this hybrid scheme tends to be computationally intensive when applied in operational NWP.

One of the examples of a hybrid scheme is Onishi and Takahashi (2011), which was implemented in the Multi-Scale Simulator for the Geo-environment (MSSG), whereby warm microphysical processes are described using the bin parametrization. Processes thereof related to ice formation and evolution are described using bulk approach. The computationally demanding bin scheme handles the physics of the liquid phase, while the efficient bulk scheme addresses the physics of the ice phase. The prognostic variables in the bulk component consist of the mixing ratios of cloud ice, snow, graupel, and the number density of cloud ice particles. On the other hand, the bin component excels in providing precise simulations of liquid droplet growth, that are free from the approximations made in bulk parameterization.

CCAM employs a single moment cloud microphysics scheme (prognostic cloud condensate scheme) from the Mark 3.6 version (Mk 3.6) of the Commonwealth Scientific and Industrial Organization (CSIRO) Global Climate Model (GCM), but with modifications for dynamical downscaling. The scheme is fully described in Rotstayn (1997). The overview of microphysical processes that are treated by the cloud scheme are shown in Figure 4.2 . The prognostic variables are the mixing ratios of cloud liquid water (q_L) and cloud ice (q_I; Rotstayn, 1997). The equations governing the evolution of q_L and q_I prognostic variables are as follows:

$$\frac{\partial q_L}{\partial t} = (q_L)_{C/E} + (q_L)_{F/M} + (q_L)_P + (q_L)_{AV} + (q_L)_{TM} + (q_L)_{CV} \quad \text{(4.4)}$$

$$\frac{\partial q_I}{\partial t} = (q_I)_{C/E} + (q_I)_{F/M} + (q_I)_P + (q_I)_{AV} + (q_I)_{TM} + (q_I)_{CV} \quad \text{(4.5)}$$

where *C/E* represents the formation or dissipation of stratiform cloud due to evaporation or condensation, *F/M* represents freezing or melting, *P* represents formation of precipitation, *AV* represents advection by the large-scale flow, *TM* represents vertical turbulent mixing and *CV* represent convection (Rotstayn, 1997). Processes that are not shown in Figure 4.2Click here to enter text. are the transport by semi-Lagrangian advection and convective and turbulent mixing, and the interactive calculation of cloud properties (Gordon et al., 2002; Rotstayn et al., 2000). In addition, the scheme includes the interactive calculation of cloud radiative properties. The calculations of cloud radiative properties are based on the prognostic variable contents that are generated by the cloud scheme (Rotstayn et al. 2000).

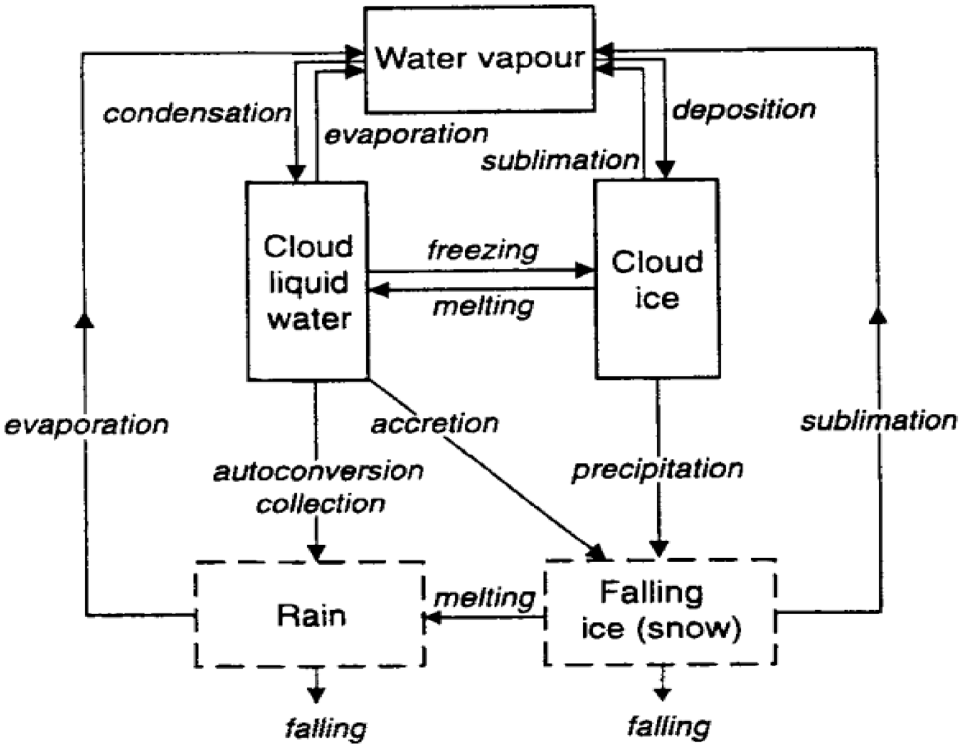

Figure 4.2: An overview of the cloud microphysical processes that are treated within the CCAM cloud microphysics scheme (adopted from Rotstayn, 1997).

The lower section of Figure 4.2 illustrates the process of rain and ice formation, along with the associated subprocesses. Precipitation occurs when the mixing ratios of cloud liquid water and cloud ice are either available or calculated (Rotstayn, 1997; Rotstayn et al., 2000). The calculation involves depleting cloud liquid water and cloud ice through precipitation. Auto-conversion, involving the growth of cloud droplets into precipitating drops through collision and accretion, contributes to the depletion of cloud liquid water. Additionally, rain collects cloud liquid water, and falling ice accretes cloud liquid water. The precipitation of cloud ice leading to falling ice is determined by the flux divergence of an empirically based fall speed from Wu et al. (1999) for ice crystals, as outlined by Gordons et al. (2002). Sublimation of falling snow results in water vapour, and a similar process occurs during the evaporation of falling rain. It is assumed that snow undergoes melting upon entering a temperature layer warmer than 2°C (Rotstayn et al., 2000).

There are a few clouds microphysics options available within the CCAM. Table 4.1 shows these microphysics options, experimental names used for the purpose of reporting in here, and a short description of each item. It must be noted that the work on option ncloud=100 is not included on this report, as the simulations are yet to be conducted.

Table 4. 1: The available options modes of the cloud microphysics scheme available within the CCAM.

Cloud microphysics scheme options	**Experiment name**	**Description**
ncloud=0	***ccam0***	This is an original Rotstayn (1997) Leon Rotstayn cloud microphysics scheme (LDR) cloud microphysics scheme with some modifications applied to the scheme and described in Rotstayn et al. (2000).
ncloud=1	***ccam1***	Same as ncloud=0, but with updated auto conversion scheme
ncloud=2	***ccam2***	This is a Lin et al. (1983) cloud scheme with prognostic snow and graupel.
ncloud=100		This is a double moment of Lin et al. 1983 cloud scheme.

4.2 CASE STUDY DESCRIPTION

The cut-off low pressure system that developed on Sunday 21 April 2019 resulted in heavy rainfall and flooding over the central, eastern and north-eastern parts of South Africa. The KwaZulu-Natal and Eastern Cape provinces were among areas that experienced heavy downpours and flooding. It was reported by/in various media sources that some communities have been displaced in areas like Umlazi and Reservoir Hills, settlements were destroyed (Figure 4.3 A), mudslides (Figure 4.3 B), and loss of over 70 lives due to drowning, collapsing of houses and other structures (SAWS, 2019). In addition, incidents of collapsed walls, flooded roads which led to traffic disruptions, water and electricity supply disruption from the municipality and sinkholes were also reported in affected areas (Floodlist, 2019; SAWS, 2019).

Figure 4.3: Aftermath of the flooding and mudslides (A – destroyed settlements and B – mudslides) (Floodlist News, 2019).

The 24-hour accumulated rainfall recorded from some of the weather stations between 06h00 (Greenwich Mean Time) GMT on 22 April and 06h00 GMT on 23 April 2019 in KwaZulu-Natal exceeded 100 mm (Figure 4.4), with Port Edward recording the most accumulated amount of 176.6 mm. Similarly, the recorded 24-hour accumulated rainfall on the previous day (i.e., 06h00 GMT on 21 April to 06h00 GMT on 22 April 2019) exceeded 200 mm (not shown here) in some of the weather stations near the coastal areas of the Eastern Cape and KwaZulu-Natal provinces.

24 Rainfall (22 April 0600Z to 23 April 0600Z)

	Station Name	24 hr rainfall (mm)
KwaZulu-Natal	Port Edward	176,6
	Paddock	143,2
	Virginia Airport AWS	126,0
	Kwamashu W/W ARS	114,0
	Mount Edgecombe	112,2
	Virginia	110,0

Figure 4.4: The 24-hour accumulated rainfall between 06h00 GMT on 22 April and 06h00 GMT on 23 April 2019 recorded from some of the weather stations in KwaZulu-Natal (SAWS, 2019).

4.3 DATA AND METHODS

The CCAM has been installed and run in research mode on the Centre for High Performance Computing (CHPC) cluster. The model is gradually upgraded over time, and there is a need to update the code and wrapper (associated) scripts to cater for such upgrades on the cluster. The source code of the model was downloaded and installed in August 2022.

Initially, the cloud microphysics scheme featured two options: the original Rotstayn (1997) cloud scheme and the Lin et al. (1983) scheme (Table 4.1). In the updated CCAM version's source code, additional options for cloud microphysics parameterization and other physics, such as the convection cumulus scheme, were introduced. These new options were incorporated into the wrapper script, responsible for submitting and running the model code. Details of these changes are outlined in Appendix 1, where scripts before the code update (Appendix 1a and 1b) are compared with scripts after the update (Appendix 1c and 1d). It is important to emphasise that the revision of the cloud microphysics scheme is interconnected with other physics parameterizations within the model.

4.3.1 Model setup

The CCAM, which is a seamless open-source non-hydrostatic numerical model developed at CSIRO in Australia (McGregor and Dix, 2008; Katzfey et al., 2020) has been utilised to produce simulations for this report. The CCAM simulations were made for three domains namely: 25, 9 and 3 km, respectively, at which the downscaling process/steps were applied. The higher or finer resolution forecast was achieved by running the model in stretch grid mode where Schmidt (1997) transformation was employed. The objective of this study is to evaluate the performance of CCAM at a convection permitting scale, hence only the 3 km simulations are analysed in this report. The topography (in metres) and grid resolution for the 3 km domain are depicted in Figure 4.5 .

- The 25 km horizontal resolution was configured using the C240 cubic grid where each of the six panels has 240 X 240 grid cells, covering longitude from 4˚ West to 56˚ East and latitude from 55˚ South to 5˚ North.
- The 9 km horizontal resolution was configured using the C325 cubic grid where each of the six panels has 325 X 325 grid cells, covering longitude from 11.42˚ to 40.58˚ East and latitude from 39.58˚ to 10.42˚ South.
- The 3 km horizontal resolution was configured using the C738 cubic grid where each of the six panels has 738 X 738 grid cells, covering longitude from 14.93˚ to 37.07˚ East and latitude from 36.07˚ to 13.93˚ South.

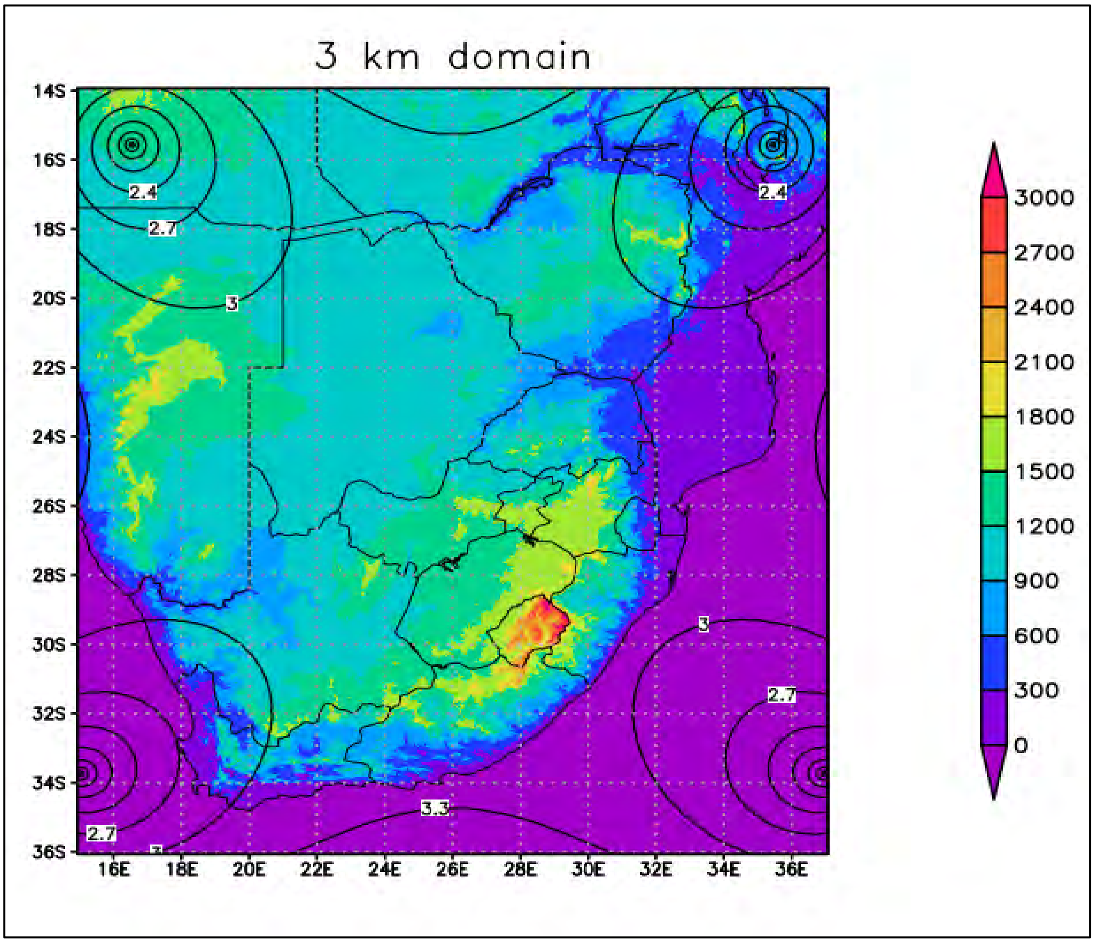

Figure 4.5: The 3 km domain with shaded topography (metres) and contour grid resolution (km). The grid resolution is finer on the inner side of a cubic grid

All simulations were conducted on the CHPC cluster, utilising 36 compute nodes, which is equivalent to 864 processors. Initially, the model was initialised with the National Centers for Environmental Prediction (NCEP) GFS analysis at 00h00 GMT on April 22, 2019, to generate a 48-hour forecast with 35 model vertical levels. Subsequently, a similar model setup was executed, but initialized with fifth generation ECMWF reanalysis (ERA5) datasets, with 27 vertical levels. The CCAM physical parameterizations employed in this report are summarised in Table 4.2.

Table 4.2: A list of physical processes parameterized within a CCAM together with scheme description name and references.

Physical process	**Scheme name**	**Reference**
Radiation parameterization	GFDL-CM3 radiation code	Freidenreich and Ramaswamy, 1999; Schwarzkopf and Ramaswamy, 1999
Cloud microphysics	Single moment prognostic cloud condensate scheme	Rotstayn, 1997; Rotstayn et al., 2000

Turbulent mixing	k-e turbulence closure scheme	Hurley, 2007
Convection parameterization	Mass-flux closure scheme	McGregor, 2003
Land surface	Community Atmosphere–Biosphere Land Exchange model (CABLE)	Kowalczyk et al., 2006

4.3.2 The pre-processing of the initial data (GFS and ERA5)

Figure 4.6 shows the variables, including optional ones, which are necessary to initialise the CCAM. Initial conditions for nudging in the conformal cubic grid were derived from both the GFS analysis (available at https://nomads.ncep.noaa.gov/) and ERA5 (Hersbach et al., 2020) for April 22, 2019, at 00h00 GMT. The data were downloaded and processed using the CDFVIDAR software provided with the CCAM code. Both GFS and ERA5 datasets have a horizontal resolution of 0.25 °x0.25 °. The conversion of these initial conditions from GRIB2 to NetCDF was performed using the G2N component of the model.

Name	Units	Dimension	cdfvidar name in input netcdf file
Geopotential height (optional)	m	3D	hgt, z or geop_ht
Air temperature	K	3D	temp, ta or air_temp
U-component of wind	m/s	3D	u, ua or zonal_wnd
V-component of wind	m/s	3D	v, va or merid_wnd
Relative humidity	% or fraction	3D	rh or relhum
Water vapour mixing ratio (as an alternative to relative humidity)	kg/kg	3D	mix_rto or hus
Surface geopotential height	m	2D	zs, orog, topo or topog
Surface temperature (including sea surface temperature)	K	2D	tss, tos or sfc_temp
Mean sea level pressure (optional)	Pa	2D	mslp, psl or pmsl
Surface pressure	Pa	2D	ps or sfc_pres
Land/sea mask (sea=0, land>0)	index	2D	land, lsm, sftlf, sfc_lsm or land_mask
Sea ice cover fraction (optional)	fraction	2D	fracice, sic or seaice
Snow depth (optional)	m	2D	snod or snow_amt_lnd
Soil temperature (optional)	K	3D	soil_temp
Soil moisture (optional)	m3/m3	3D	soil_moist

Figure 4.6: The list of variables needed as initial conditions to drive the CCAM. Typically, the input files are on pressure levels (hPa) or sigma-pressure levels (Adopted from https://confluence.csiro.au/pages/viewpage.action?pageId=383420556).

4.3.3 Observational data

The Automatic Rainfall Stations (ARS) and Automatic Weather Stations (AWS) gridded data limited to South Africa was used to subjectively validate model simulations. Parameters recorded at these stations include near surface temperature, dew point temperature, mean sea level pressure, wind speed and direction, and rainfall. This data is archived daily at SAWS climate data base. Data archives are available at hourly, six hourly and daily time interval, and hourly data have been requested and used in this report. The data has been quality controlled (Kruger and Shongwe, 2004).

4.3.4 Radar

The SAWS owns about 15 weather radars across South Africa at which 12 of these radars are operational as reported on the SAWS annual report (SAWS, 2022). From the total of these 12 functioning radars, there are eight (8) S-band frequency radars with doppler capabilities (Irene, Polokwane, Ermelo, Ottosdal, Bloemfontein, Durban, Mthatha, and East London), two (2) C-band radars (Cape Town and De Aar), the doppler and one (1) dual-polarised S-band radar (Bethlehem), and lastly Skukuza S-band radar that provide radar reflectivity only. The majority of these radars are installed on the eastern side of the country where major weather activities occur. The horizontal spatial coverage of these radars ranges from 200 (for smaller radius) to 300 km (for bigger radius), with a temporal resolution of six (6) minutes (Becker, 2014). The radar data is used to subjectively evaluate the CCAM simulated precipitation.

4.3.5 IMERG

The National Aeronautics and Space Administration (NASA) and Japan Aerospace Exploratory Agency (JAXA) launched a new generation Global Precipitation Measurement (GPM) mission satellite in 2014 to replace the Tropical Rainfall Measuring Mission (TRMM) (Hou et al., 2014). The GPM data is derived from multiple satellites and provides multi-satellite precipitation products: Integrated Multi-satellite Retrievals for GPM (IMERG). The satellites cover the region between 60°S and 60°N globally at 0.1° x 0.1° horizontal resolution. The half-hourly data is downloaded and used for comparison with CCAM precipitation simulations.

4.4 RESULTS

4.4.1 CCAM initialised using GFS

The accumulated 24-hour rainfall spatial distribution is depicted in Figure 4.7. The top row shows the SAWS stations observations (top left), SAWS radar quantitative precipitation estimates (QPE) (in the middle) and the IMERG satellite product (top right). The bottom row depicts the CCAM simulations with ccam0, ccam1 and ccam2 as defined in Table 4.1. The results show that CCAM is able to simulate the spatial distribution of rainfall across the country, however with some shortcomings, as depicted in Figure 4.7. It should be noted that the model simulations have been interpolated to observation grid at a horizontal resolution of 0.25° using the bilinear interpolation method, for the purpose of rainfall spatial distribution comparison. Furthermore, only the subjective verification of the model simulations has been presented.

Shortcomings in general:

- The model (all setups) seems to mislocate heavy rainfall compared to station observations, radar QPE and IMERG (this is clearly visible in area enclosed within blue oval shape in Figure 4.7)
- The model (all setups) under-estimate rainfall, over the eastern coast by a margin (see area enclosed within parallelogram shape on Figure 4.7). This behaviour is also visible in other areas across the country. The tendency of CCAM to underestimates rainfall is also documented in Bopape et al. (2022).
- The ccam0 and ccam1 have similar spatial distribution of rainfall while the ccam2 tends to isolate heavy rainfall over small areas, as depicted in the coastal areas of KZN and the Eastern Cape (see Figure 4.7).

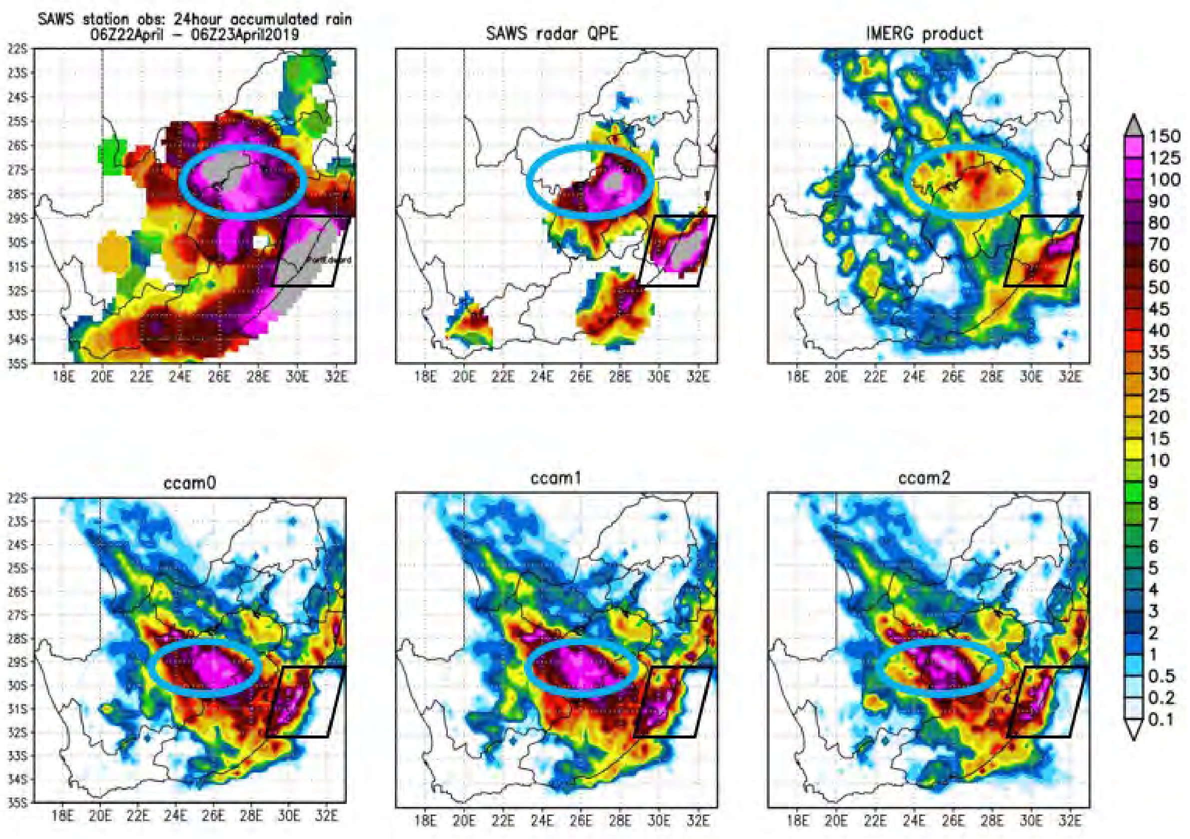

Figure 4.7: The 24-hour accumulated rainfall from 06 GMT 22 April to 06 GMT 23 April 2019. The top row is the SAWS stations observations (top left), SAWS radar quantitative precipitation estimates (QPE) (in the middle) and the IMERG satellite product (top right). The bottom row is CCAM simulations at which ccam0, ccam1, and ccam2 are experimental set-ups.

4.4.2 CCAM initialised using ERA5

From the previous section, it was highlighted that the difference between simulations from ccam0 and ccam1 is too small, hence in this section such comparison is neglected – and only ccam0 and ccam2 forms part of the evaluation process. The 24-hour accumulated rainfall spatial distribution is depicted in Figure 4.8. As in Figure 4.7, the top row shows the SAWS stations observations (top left), SAWS radar QPE (in the middle) and the IMERG satellite product (top right) – and the bottom row depicts CCAM simulations (from ccam0 and ccam2).

The mis-location of simulated heavy rainfall when compared to observation highlighted in section 4.4.1 has at least improved when the model is initialised with ERA5 reanalysis date. However, both ccam0 and ccam2 still underestimates the rainfall intensity when compared to SAWS observation, and radar QPE (see area circled in blue on Figure 4.8). In addition, when looking at the area circled in blue on Figure 4.8, the ccam2 seems to perform better than ccam0 compared with SAWS observation, radar QPE and IMERG. The model seems to have performed worse in terms of getting the intensity compared to observations, especially over the coastal area of KZN and the Eastern Cape (area enclosed by a rectangle in Figure 4.8). In general, the CCAM is able to capture the spatial distribution of rainfall across the country, however with shortcomings as depicted in Figure 4.8.

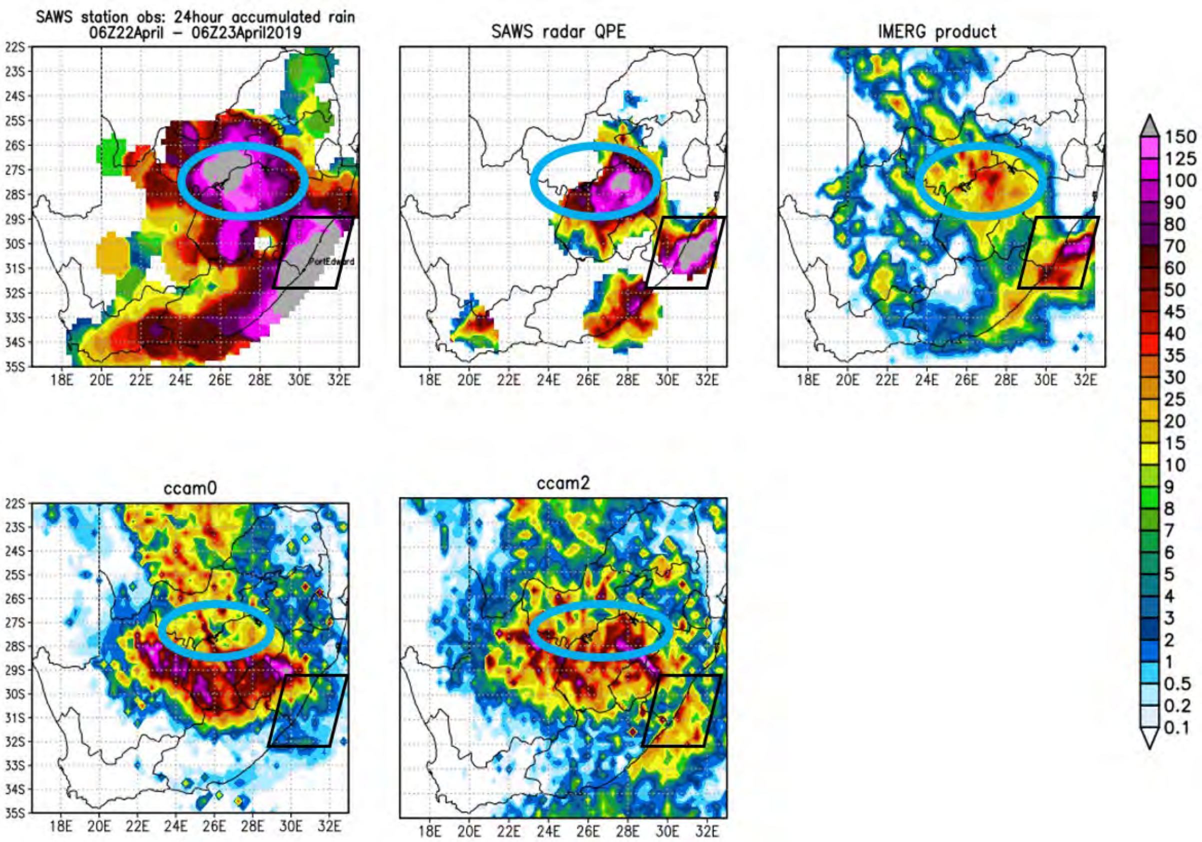

Figure 4.8: The 24-hour accumulated rainfall from the 06 GMT 22 April to 06 GMT 23 April 2019. The top row is the SAWS stations observations (top left), SAWS radar quantitative precipitation estimates (QPE) (in the

middle) and the IMERG satellite product (top right). The bottom row is CCAM simulations at which ccam0 and ccam2 are experimental set-ups and defined in Table 4.1.

Figure 4.9 depicts diurnal cycle illustrating the average rainfall across the South African domain, spanning latitudes from 22.0° to 35.0° South and longitudes from 16.0° to 33.0° East. The cycles represent model simulations, SAWS station observations, radar data, and IMERG. The plotted diurnal cycles cover a 24-hour period from 06 GMT on April 22 to 06 GMT on April 23, 2019. This time frame corresponds to the one used for plotting the cumulative spatial rainfall distribution in Figures 4.7 and 4.8.

Throughout the entire 24-hour period, all simulations consistently underestimated rainfall in comparison to observations from stations, and radar (QPE). The underestimation of rainfall agrees with what has been observed in spatial distribution comparison in the previous sections. Even though the diurnal cycle patterns differ, the simulations seem to agree with IMERG in terms of the amount of rainfall. The diurnal cycle patterns from simulations exhibit similarity and overlap throughout the 24-hour period. All simulations struggle to get at least one of the rainfall peaks observed by stations and radar. The ccam0 initialised with ERA5 reanalysis (ccam0-era5) shows some high values of rainfall towards the end of the diurnal cycle (00 GMT to 06 GMT of 23 April 2019) but the amount is very low.

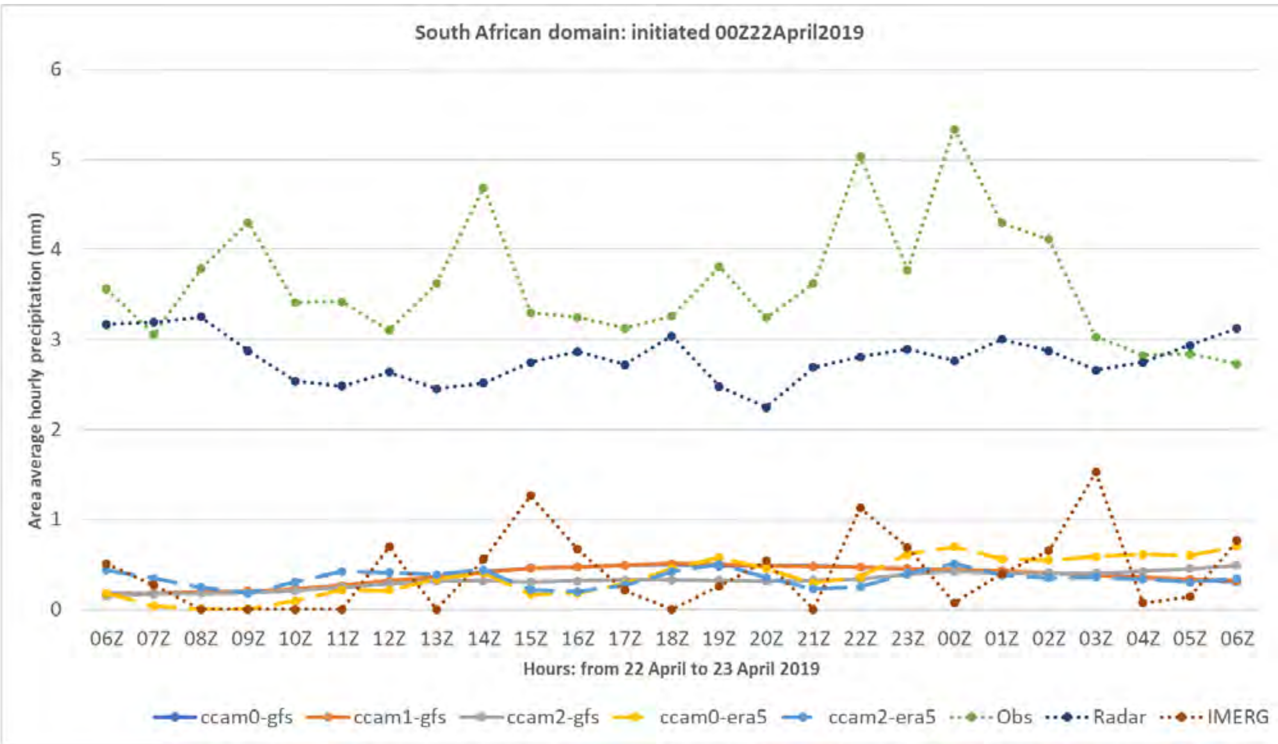

Figure 4.9: The diurnal cycles depicting area averages of rainfall from model simulations, SAWS stations observations (Obs), radar and IMERG over South African domain. The solid lines are model simulations initialised with GFS analysis (ccam0-gfs in blue; ccam1-gfs in dark orange and ccam2-gfs in grey), long dashed lines are model simulations initialised with ERA5 reanalysis (ccam0-era5 in light orange and ccam2-era5 in light blue), and lastly, the round dotted lines are Obs (in green), radar (in dark blue) and IMERG (in dark brown).

The station's observations, radar and IMERG are all behaving differently as shown by diurnal cycles. A notable difference is seen when IMERG seems to have recorded a low amount of rainfall for each hour when compared to observed rain by stations and radar. The rainfall amount observed by stations and radar are high but the diurnal cycle patterns are different as can be seen in Figure 4.9 (the round dotted lines in green and dark blue).

4.5 SUMMARY AND CONCLUSIONS

In this chapter, we explore the performance of various cloud microphysics schemes within the CCAM in replicating a severe weather event that led to substantial rainfall and flooding. The event had widespread detrimental effects across South Africa, particularly impacting parts of KwaZulu-Natal and the Eastern Cape provinces. These impacts included the displacement of people, disruptions to services such as electricity supply, and loss of lives. Our analysis involves CCAM simulations under different experimental configurations (ccam0, ccam1, and ccam2), utilising the GFS analysis and ERA5 reanalysis as initial conditions. The 48-hour simulations spanning from 00 GMT on April 22 to 00 GMT on April 24, 2019, were generated. We subsequently conducted a subjective verification, comparing the model simulations with observed data.

In general, all simulations from various experimental setups successfully capture the spatial distribution of rainfall across South Africa, but with certain limitations.

- When using GFS analysis as input data to the model:

  Simulations across all setups consistently exhibit a tendency to inaccurately position intense rainfall, particularly in the central regions of South Africa. Furthermore, all simulations consistently underestimate the observed 24-hour accumulated rainfall intensity as recorded by stations, radar, and IMERG. Notably, ccam0 and ccam1 showcase a similar spatial distribution of accumulated rainfall, whereas ccam2 tends to concentrate heavy rainfall in more localised areas.
- When using ERA5 reanalysis as input data to the model:
  The simulations continue to exhibit an underestimation of accumulated rainfall when compared to station observations and radar QPE, similar to what is observed when the GFS analysis is used as the initialization. However, there is a slight improvement in the misplacement of heavy rainfall in these simulations. Interestingly, when compared to SAWS observations, radar QPE, and IMERG, ccam2 appears to perform better than ccam0.

The diurnal cycles, illustrating the area-average rainfall from 06 GMT on April 22 to 06 GMT on April 23, further affirm the underestimation of rainfall in all simulations when compared to observations from stations and radar. Interestingly, IMERG appears to be comparable in terms of rainfall amount with all simulations, despite differences in the diurnal cycle patterns.

The technical tasks carried out in this project encompassed installing the CCAM source code on the CHPC Lengau cluster in August 2022. Additionally, there were modifications made to certain scripts (specifically the wrapper script) to integrate other cloud microphysics scheme switches. Furthermore, a namelist file was adopted for the pre-processing of ERA5 into a cubic grid. Some of these modifications and details are presented in Appendix A.

CHAPTER 5: THE CCAM CUMULUS SCHEME

5.1 INTRODUCTION

Cumulus convection parameterization, also referred to as the convection scheme, is crucial for accurately representing precipitation characteristics and processes in NWP models (Huang and Gao, 2017). Further, it serves to overcome the limitations of numerical weather and climate models in depicting physical processes and transports within convective clouds. It predicts the time evolution of the collective influence of individual convective clouds on the large-scale system/environment (Baba, 2020; Arakawa and Schubert, 1974), enhancing the skill and accuracy of NWP models in predicting convective precipitation and the feedback of individual convective clouds to the large-scale weather system. Convection schemes also dictate sub-grid processes within an NWP model, including the vertical distribution of total vertical mass flux, total mass detrainment, and thermodynamic properties of detraining air (Arakawa and Schubert, 1974).

There are primarily two types of convection parameterizations: shallow convection (for fair-weather cumulus and stratocumulus) and deep convection (for congestus and cumulonimbus convection; Pickering, 2015). The cumulus convection scheme consists of a trigger function (describing the activation mechanism for convection), a cloud model (for vertical distribution), and closure assumptions (defining convective intensity/regulation by large-scale/grid-scale variables) (Hong and Pan, 1998; Yano et al., 2013). Additionally, there are different categories of cumulus convection schemes: scale-aware, mass flux, and convective adjustment schemes (Huang et al., 2014; Freitas et al., 2020; Yoshimura et al., 2015; Miller, 1985).

Scale-aware cumulus schemes dynamically adjust to changes in grid size, ensuring a seamless transition from unresolved to resolved cloud scales (Huang et al., 2014; Freitas et al., 2020). Huang et al. (2014) detailed a scale-aware cumulus scheme, integrated into the WRF model, that incorporates a mass flux formulation and addresses microphysical processes within grid-resolved clouds. The scheme adopts the simplified Arakawa-Schubert (SAS) convective parameterization, incorporating the approach by Arakawa and Wu (2013). Microphysical assumptions, derived from Simpson and Wiggert (1969), involve sub-grid convective cloud entrainment via turbulent exchange at cloud edges and organised flow, while detrainment occurs exclusively through turbulent exchange. Processes outlined by Gerard et al. (2009), focusing on cloud ice/water formation, are applied to sub-grid cloud dynamics. Additionally, the scheme considers feedback from subgrid clouds to the large-scale environment, involving thermal and vapour exchange due to entrainment, detrainment of hydrometeors, and compensating subsidence from environmental updrafts within the subgrid cloud (Huang et al., 2014). Notably, the scheme does not incorporate shallow convection parameterization.

Traditional mass flux schemes can be categorised into two primary types: the Tiedtke type and the Arakawa–Schubert (AS) type (Yoshimura et al., 2015). The Tiedtke type follows a bulk cloud model approach, involving the computation of a single updraft with a complex entraining and detraining plume. On the other hand, the AS type is based on the simple spectral cloud model approach, calculating multiple updrafts with varying heights and entrainment rates. Mass flux schemes are widely favoured for their capacity to explicitly compute mass flux for sub-grid scale convective updrafts and downdrafts, as well as their suitability for computing the convective transport of materials (Yoshimura et al., 2015). Meanwhile, the primary goal of adjustment schemes is to achieve a realistic representation of vertical temperature and moisture profiles by concurrently adjusting them to quasi-equilibrium states for both shallow and deep convection (Miller, 1985).

Cumulus parameterization schemes generally consist of three main components: the trigger function, mass flux function/cloud model, and closure assumptions, as discussed by various researchers (Kain, 2004; Yano et al., 2013; Baba, 2020; Arakawa and Schubert, 1974). The trigger function is responsible for identifying horizontal layers where convection initiates or becomes active (referred to as updraft source layers). The cloud model/mass flux function, on the other hand, describes the vertical distribution of convection, while the closure assumptions determine the intensity and regulation of convection by large-scale or grid-scale variables (Hong and Pan, 1998; Yano et al., 2013; Kain, 2004).

The CCAM convection scheme, also known as the Convjlm, is an Arakawa-based mass-flux scheme based on Ooyama (1971) theory. The theory was adopted by Arakawa *et al*. (1969), Arakawa-Gordon scheme of the CSIRO Mk2 GCM (McGregor et al., 1993) and the CSIRO Mk3 Climate System Model (Gordon et al., 2002). The cumulus convection theory of Ooyama (1971) was formulated for large-scale weather systems, such as meso-scale/synoptic scale systems, based on a hypothesis that cumulus clouds can be represented by individual buoyant elements. This hypothesis was based on the fact that a large number of cumulus clouds are commonly associated with large-scale weather systems whose time evolution is determined by the vertical exchange of energy, momentum and water by an ensemble of independent cumulus clouds/buoyant elements. These buoyant elements, also referred to as bubbles, do not interact with each other, and whose behaviour should be calculated using a semi-empirical convection model (Ooyama, 1971). Further, the Convjlm is a modification of Arakawa (1972) and based on McGregor (2003).

5.2 DESCRIPTION OF THE CCAM CUMULUS SCHEME

The Convjlm cumulus scheme is an Arakawa-based mass-flux scheme with a scale awareness (McGregor, 2003; 2005). The scheme assumes that in each convecting grid square, there is an upward mass flux within a saturated aggregated plume along with compensating subsidence of environmental air outside the plume, which may also be in the form of a downdraft (McGregor et al., 1993). The scale-awareness within the Convjlm allows for the scheme to produce mainly resolved precipitation at higher resolutions (Thatcher, 2021). The Convjlm cumulus scheme is also equilibrium-based, assuming that the properties of the large-scale environment are determined by averaging the atmospheric state in the horizontal (over a region large enough to contain many clouds), computing equilibrium statistics for the whole convective ensemble, draw cumulus properties, such as convective mass flux, in each grid box from the large scale environment equilibrium distribution, and use the mass flux and cumulus properties to predict the convective tendencies of the grid box atmospheric variables (Plant and Craig, 2008).

The scheme makes several assumptions (McGregor, 2003), including:

- Two criteria are established concerning cloud base and convection, wherein cloud base is assumed to be the nearly saturated layer located below the saturated plume.
- The scheme presumes an absence of lateral entrainment; hence, saturated air can only infiltrate the plume through the cloud base level, and the level of neutral buoyancy is defined as the cloud top.
- Downdrafts are considered to counteract excessive stabilisation processes and to mitigate the risk of excessive precipitation, particularly in tropical oceanic regions.
- Subsidence of environmental air is observed between the cloud top and cloud base, acting to balance the upward mass flux within the plume.
- The process of detrainment is assumed.
- This approach ensures a straightforward, natural closure method with reduced uncertainty, operating within the framework of convective ensembles.
- Shallow convection is initiated when the cloud top does not exceed 750 hPa, while deep convection is triggered when the cloud-top layer surpasses 800 hPa, and it takes precedence over shallow convection.

The formulation was developed for an unsaturated plume (dry static energy).

$$s_k = c_p T_k + g z_k \quad \text{......5.1}$$

and saturated plume (moist static energy)

$$h_k = s_k + L q_k \quad \text{......5.2}$$

where c_p, g and L are the specific heat of air at constant pressure, the gravitational acceleration, and the specific latent heat of vaporisation, respectively. T, q, z and k are air temperature, moisture mixing ratio, height above the surface and the vertical layer index of the model, respectively.

The trigger function, cloud model and closure assumptions for the Convjlm for moist static energy, as outlined in McGregor et al. (1993), are as follows:

5.2.1 The trigger function

The trigger function defines the conditions for cloud base and criteria for convection. For convection, it assumes that there are distinct layers: a cloud-base layer denoted as kb and a cloud top layer denoted as kt. The cloud base is identified just below the saturated plume, and it is determined by descending to find the lowest, continuously moist-adiabatically unstable layers, while the cloud top is determined at the level of neutral buoyancy. It's also assumed that saturated air enters the buoyant air bubble solely from the cloud-base level without any lateral entrainment.

We define the sub-grid spatial variability factor, α, within the boundary layer and is typically set to 1.1. This factor α is used to enhance the mixing ratio of the air bubble at the potential cloud base, q_{kb}^{p}, which equals the environment value, q_{kb} and is capped by the saturated environment value, q^s_{kb}. The cloud top layer is identified as the uppermost layer in which the bubble is saturated.

For convection to occur, there must be a cloud-base and cloud-top layers, satisfying the following conditions:

- For condition 1 (the moist unstable bubble):

$$h^p_{kb} \geq h^s_k \; for \; kb < k \leq kt$$

- Condition 2 (Near cloud-base, where air plume is at least as moist as the saturated environment):

$$q^p_{kb} \geq q^s_{kb+1}$$

To ensure that the cloud-base and cloud tops meet the above criteria for multiple convective elements, the convection scheme is executed twice during each time step, Δt. Typically, only two passes are performed, as conducting extra passes could introduce additional effects. To prevent the second pass from using the cloud-base and cloud-tops data from the first pass, the mass flux for the first pass is augmented by 2%. Additionally, a convective relaxation time step, τ (usually =1200 s), is employed to account for the cumulative effects of convection during small model time steps. The convective relaxation time is calculated as the effects of convection $\times \frac{\Delta t}{\tau} \; for \; \Delta t < \tau$.

The model initially utilises deep convection when the cloud-top layers are situated above 800 hPa. Shallow convection comes into play when the cloud-top extends to 750 hPa. Shallow convection, characterised by Benard cells or horizontally organised patterns, can be induced through either of the following methods:

- Employing a very short model time step along with a stringent convective adjustment, effectively eliminating convective instabilities instantly.
- For clouds with a depth of less than 200 hPa, detrain and re-evaporate all the resultant precipitation.

The CCAM utilises the enhanced vertical-diffusivity scheme developed by Tidtke (1984). This scheme is applied when low-level relative humidity exceeds 80%, or when the low-level saturated moist static energy of a layer surpasses the saturated values of the layers above it.

5.2.2 The cloud model.

The cloud model describes the formulation applied for compensating subsidence, downdrafts, and entrainment/detrainment. The cloud model operates under the assumption that the positive buoyancy within the air plume is compensated by the subsidence of environmental air between the cloud-top and cloud-base. This compensating subsidence can take the form of a downdraft, which has a cooling effect on the cloud base and helps prevent excessive precipitation forecasts, particularly in tropical oceanic regions. Additionally, further cooling from downward motion can result from the evaporation of precipitation along the downdraft path.

Downdrafts are modelled to begin at a level kd, which is about 75% of the cloud height (in pressure heights) and emerge at the cloud base level kb (mixing ratio=q_D, saturated at emerging downdraft temperature T_D).

Entrainment is proportional to the upward mass flux at each level. However, entrainment of environmental air (mixing ratio=q_{kd}) occurs at the top of the downdraft. The downdraft air at the cloud-base level has these properties:

$T_D = T_{kb} + \frac{s_D - s_{kb}}{c_p} = T_{kb} + \frac{s_{kd} - s_{kb}}{c_p} - (q_D - q_{kd})L/c_p$ …………………………………………………………… (5.3)

and

$q_D = q_{kb}^s - \frac{(T_{kb} - T_D)dq_{kb}^s}{dT}$ ...…………………………………………………………………………………(5.4)

Substituting (5.1) into (5.2) gives:

$$T_D = T_{kb} + \frac{s_D - s_{kb}}{c_p} = T_{kb} + \frac{s_{kd} - s_{kb}}{c_p} - \frac{\left[\left(q_{kb}^s - \frac{(T_{kb} - T_D)dq_{kb}^s}{dT}\right) - q_{kd}\right]L}{c_p}$$

which then result in:

$T_D = T_{kb} + \frac{s_{kd} - s_{kb} - L(q_{kb}^s - q_{kd})}{c_p + Ldq_{kb}^s/dT}$……………………………………………………………………………………..(5.5)

The downdraft mass flux:

$M_D = 0.6M(p_{kb} - p_{kt})/p_0$…………………………………………………………………………………………..(5.6)

where p_{kb}, p_{kt} and p_0 are the pressure at the cloud-base, cloud-top and the surface, respectively. The downdraft mass flux is a function of the upward mass-flux to permit for stronger downdrafts from deep convective cells. It is notable that the downdraft is suppressed whenever net precipitation associated with the evaporating moisture needed to drive the downdraft =0.

The scheme employs a straightforward detrainment methodology, wherein a fraction of the precipitated moisture condensed within the plume, β=0.05, is detrained into the ambient environment as liquid water. This detrained liquid water rapidly undergoes evaporation at the level of detrainment. The distribution of the highest precipitating moisture within the plume follows a linear decrease from its maximum at the cloud-top to zero at the cloud-base. Consequently, the detrainment scheme emulates the basic formation of stratified layers akin to citrus layers.

5.2.3 Closure assumptions

Closure is necessary for resolving the unknowns in applied equations. The scheme has simple, natural closure with reduced uncertainties. The closure works by employing a trigger function whereby when modification for convection in the environment occurs, new cloud-base conditions can be calculated. Moreover, the closure assumes that mass flux should reach its maximum in the updraft to sustain the convective structure between the current cloud base and cloud-top levels. This continues until exhaustion within the 30-minute time step, with durations beyond 30 minutes considered as reaching equilibrium. Contrariwise, anything shorter than 30 minutes is reverted to its original time step. Additionally, this closure implies that heating at mid- and upper-levels surpasses that at the cloud base.

5.3 EXPERIMENTS

Throughout this project, various experiments were conducted to gain insights into the functioning of the CCAM cumulus scheme and to pinpoint any shortcomings it might have. The objective was to identify these gaps and leverage the findings for ongoing CCAM development, ultimately aiming to enhance the model's performance within the Southern African Development Community (SADC) domain. The first experiment involved:

- Evaluation of the different versions of the Convjlm. The aim was to identify the highest performing version and use it for further model development. However, after sharing the results with the model developers, it was advised that we work on the 2017 version, which they are performing their development on.
- Experiments to identify the value of bcon parameter that best augments the model skill in predicting convective rainfall, which also contributes towards predicted total precipitation. The bcon parameter is used by an NCAR scheme in cloudmod.f90 to diagnose cloud cover and includes the convective rainfall rate, calculated in convjlm.f. Noteworthy, after visiting the model developer for training and sharing the results with them, they advised that we rather discontinue studies regarding the bcon parameter as it may lose significance in the near future development of the CCAM.
- After a visit to the model developer, they provided a list of experiments they recommended for us to conduct. This includes testing the scale-awareness of the cumulus scheme, inter-comparison between the old and new detrainment methods, as well as testing the cloud height in relation to the mass-flux correlation for multiple plumes. The former was chosen as a starting point, while the rest were planned for later stages.

5.3.1 Evaluation of the different versions of the Convjlm

At the onset of the project, the model was installed with three different versions of the Convjlm, namely, 2015a, 2015b and 2017 versions. These are specified in the run script. A paper to validate these versions of Convjlm was published at the SASAS 2022 conference proceedings. As this experiment was conducted, the model code was modified to include an additional version: modified 2015a, hereafter 2015aM. Four cases characterised by convective systems and heavy rainfall events were selected: 25 January 2021(tropical cyclone Eloise), 30 December 2017 (Tornado over Soweto, Gauteng), 09 March 2022 (Severe thunderstorm over the Eastern Cape) and 12 November 2019 (Tornado event over Hannover, KwaZulu-Natal). The model setup is outlined in Table 5.1.

Table 5. 1: Model setup for evaluating the different versions of the Convjlm.

Model setup	**Option(s)**
Vertical levels	35
Projection	25 km (C96), 9 km (C192) and 4.4 km (C576)
Number of grid points	25 km (169 * 169), 9 km (673 * 673) and 4.4 km (1537 * 1537)
Forecast hours	48
Boundary layer scheme	Local Ri
Microphysics scheme	Original LDR cloud microphysics with prognostic liquid and ice condensates. Cloud cover is diagnosed. Has updated auto-conversion scheme and prognostic rain.
Radiation scheme	Older/Slower, Freidenreich and Ramaswamy (1999), Schwarzkopf and Ramaswamy (1999), which support direct aerosol effects.
Nudging	Standard
Number of processors	600

Domains for these runs are depicted in figure 5.1. The projections and number of grid points for each domain are listed in Table 5.1. However, for the purpose of this paper, only the 4.4 km configuration runs were discussed. In addition, the different options, or versions, of the cumulus scheme were differentiated in Table 5.2 according to their respective namelist options. Several parameters were introduced to the 2015b and later versions, such as nkuo, ldr, nuvconv, sig_ct,sigcll, sigkscb and sigksct. Moreover, rcrit_l and rcrit_s are only applied on the 2017 version.

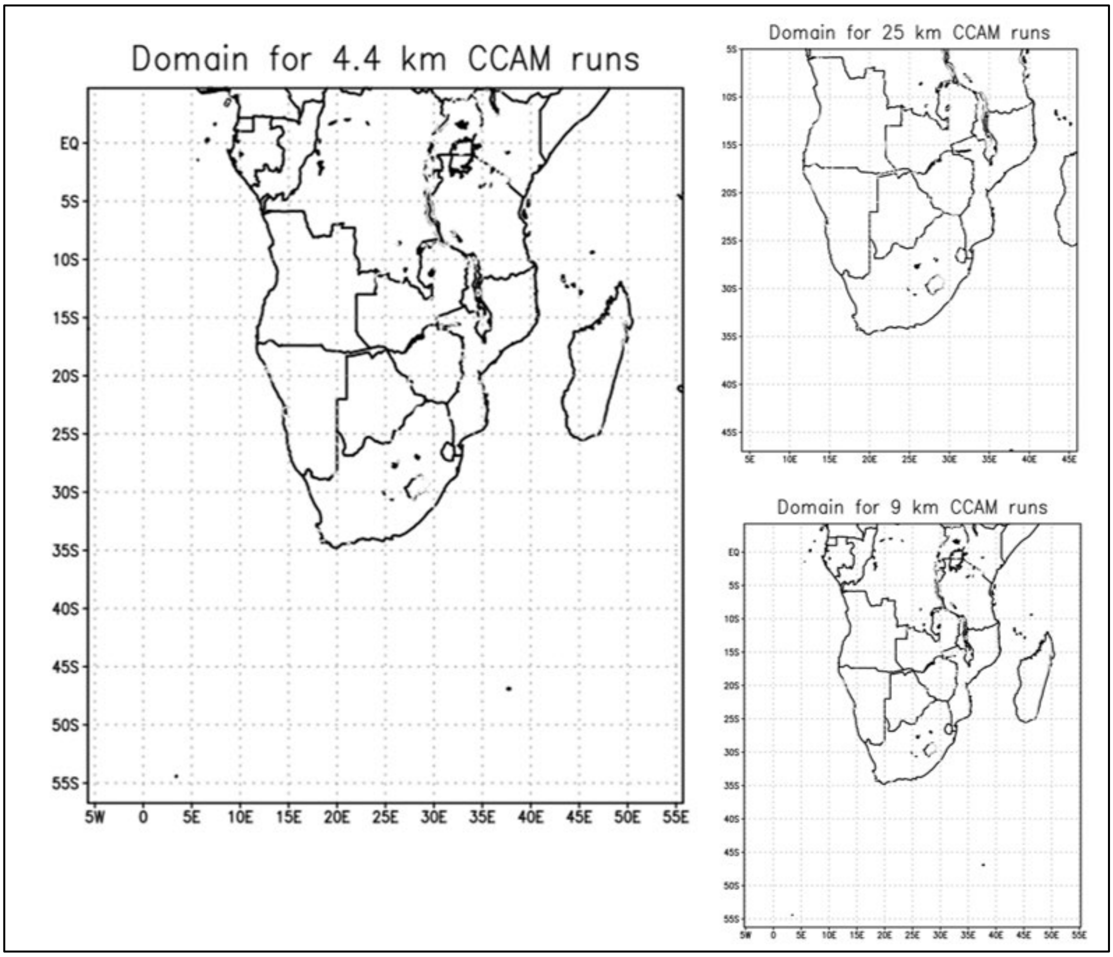

Figure 5.1: Domains for CCAM simulations with the different versions of the CSIRO cumulus scheme.

Table 5. 2: Namelist options for the different versions of the Convjlm cumulus scheme. These are available in the main run-script and kuocom.h. Values used for variable parameters are $acon=0, $bcon=0.04, $ncloud=2 and $nmr=1.

	2015a	***2015b***	***2017***	***2015aM***
Nkuo - convection model		23	21	23
Acon – represents shallow convection; Cloud fraction for non-precipitating convection	$acon	$acon	$acon	$acon
Alflnd - land-weighting ratio for cloud bases	1.20	1.2	1.10	1.1
Alfsea - sea-weighting ratio for cloud bases	1.05	1.10	1.10	1.1
Bcon – represents deep convection: to diagnose cloud cover and includes the convective rainfall rate; Rate at which conv cloud fraction increases with R	$bcon	$bcon	$bcon	$bcon

Convfact - overshooting factor for mass flux	1.05	1.05	1.05	1.05
Convtime - convective time scale; adjustment time (h) of cu scheme	-2030.60	-2030.60	-3030.60	-2525.60
Detrain - fraction of precip into detrainment	0.1	0.1	0.15	0.1
Detrain - fraction into detrainment for shallow clouds		0.	0.	0.
dsig2 - delta-sigma2 for end of shallow clouds	0.1	0.1	0.1	0.1
dsig4 - delta-sigma4 for start of deep clouds		1.	1.	1.
Entrain - entrainment factor; controls fraction mass entrained from environment	-0.5	-0.5	-0.5	-0.5
Fldown - fraction of convective flux into downdraft	-0.3	-0.3	-0.3	-0.3
Iterconv - number of iterations in convjlm	3	3	3	3
Ksc - shallow convection switch (99 for Tiedtke on)	0	0	0	0
Kscmom - shallow convection momentum switch (1 for on)	1		0	
Kscsea - 1 for doing Tiedtke only over sea	0	0	0	0
Ldr - Leon Rotstayn cloud microphysics (ldr) scheme options; 0 for off		1	1	1
Mbase - base test: 1 cfrac; 2 cfrac and omega; for large vertical velocity takes moisture from lowest level, with surface wetness factor included	4	4	1	4
Mdelay - convective delay time in secs	0	0	0	0
Methdetr - meth_shallow_detrainment for convjlm, 2 off ; controls detrainment for shallow vs deep	-2	-1	-1	-1
Methprec - meth_precip (deep_detrainment) for convjlm; controls detrainment profile	5	5	5	5
Nbase - cloud base as being at top of PBL; type of base: 1 simple; 2 linear to sfce	-2	-10	3	-10
Nclddia - conversion of RH to cloudiness, 0, 3	12	12	12	12
Ncloud - specifies the cloud microphysics model	$ncloud	$ncloud	$ncloud	$ncloud

Ncvcloud - convective cloud enhancement in radrive	0	0	0	0
Nevapcc - option to controls auto entrain fraction depending on cloud depth 0; evap scheme of convective rain	0	0	0	0
Nevapls - evap scheme of large-scale rain	0	0	0	0
Nmr -bulk cloud properties	$nmr	$nmr	$nmr	$nmr
Nrhcrit - Hal's original 0; for jlm 7, 8	-3	10	10	10
nstab_cld - 0 off, 3 for stability-enhanced cll		0	0	0
Nuvconv - controls convective mixing of momentum (-3: 30% of possible full value; -2 also OK). 0 off, 1 to turn on momentum mixing		-3	-3	-3
rcrit_l - critical humidities over land for ldr newcloud			$rcrit_l	
rcrit_s - critical humidities over sea for ldr newcloud			$rcrit_s	
Rhcv - RH trigger for convective scheme	0.1	0.1	0.	0.1
Rhmois - used by conjob, convjlm for nevapcc=5	0.	0.	0.	0.
sig_ct - min sig value of cloud tops (for convjlm)		1.	1.	1.
Sigcll - sig value of low cloud base (for cll)		0.95	0.95	0.95
Sigkscb - for tiedtke shallow convection		0.95	0.95	0.95
Sigksct - for tiedtke shallow convection		0.8	0.8	0.8
tied_con - trigger using upward vertical vels to enhance available PBL moisture (10 for 200 km, increasing for smaller ds); tiedtke diffusion constant	0.	0.	0.	0.
tied_over - tiedtke overshooting constant	2626.	2626.	2626.	2626.
tied_rh - tiedtke RH trigger			0.	
ngwd - Coefficient to limit launching height	**-5**	**-20**	**20**	**-20**
helim - Maximum launching height	800	1600	1600	1600
fc2 - Coefficient for calculating Froude number	1	0.5	0.5	0.5

sigbot_gwd - Lowest sigma level for gravity wave drag	0	1	1	1
alphaj - Coefficient for Chouinard et al model	1E-06	0.025	0.025	0.025

The 0.25° GFS data was used to initialise the CCAM. Throughout the model runs, only the choice of convection scheme was changed, while the rest of the model setup was kept constant. Model output from the 4.4 km runs were used to identify the version of the Convjlm that has the performance in predicting selected severe rainfall events over South Africa. Ground observations, also known as synops, were used to validate the model. The number of stations with valid data varied hourly. These synops were available in text format and were converted to a 0.25° x 0.25° resolution.

The total rainfall in the model consists of both large-scale and convective-scale components. To assess model accuracy, the diurnal cycles of total hourly rainfall and parameterized rainfall were compared with ground observations from approximately 370 stations across the entire country. Noteworthy, total rainfall is made up of large-scale rainfall, which is produced by the microphysics scheme, plus parameterized rainfall, which is simulated by the cumulus scheme. The diurnal cycle variation served as an indicator of the model's accuracy in simulating precipitation (Han et al., 2019). Averaging was performed over areas affected by the specific weather event under investigation to eliminate potential interference from precipitation in other regions of the country on the study day. Additionally, an analysis of the spatial distribution of rainfall in the area impacted by the weather system was conducted to evaluate the model's ability to simulate the location and intensity of precipitation in relation to ground observations. This analysis also included an examination of vertical patterns for selected convective parameters, namely, relative humidity (RH), temperature, wind speed, and omega.

Moreover, we calculated skill scores over the area impacted by the rainfall event of interest: the success ratio (SR) and the Threat Score/Critical Success Index (TS/CSI). The respective formulas are shown in equations 5.7 and 5.8. The SR, as defined by Schulz (2011), serves as an accuracy metric, representing the fraction of forecasts that align with observations. The CSI, also defined by Schulz (2011), is a measure of correspondence between correctly forecasted events and observed events.

$$SR = \frac{hits}{hits + false\ alarms} \quad \text{.......(5.7)}$$

$$CSI = \frac{hits}{hits + misses + false\ alarms} \quad \text{.......(5.8)}$$

5.3.1.1 Description of case studies

- Tropical cyclone Eloise: 25 January 2021

On 25 January 2021, tropical cyclone Eloise moved over the eastern regions of Botswana, leading to increased cloud cover and substantial rainfall in the Limpopo, KwaZulu-Natal, and North-West provinces of South Africa

(SAWS, 2021). Tropical cyclone Eloise was the second tropical cyclone to hit the southeast Africa in January 2021, resulting in extensive damage, intense rainfall, and flooding across Madagascar, Mozambique, Zimbabwe, South Africa, Eswatini, and Botswana (Smiljanic et al., 2021). The cyclone originated in the southeast Indian Ocean on 14 January 2021 and it reached Madagascar by the 20th (OCHA, 2022). Following its landfall in Beira, Mozambique, on 23 January 2021, tropical cyclone Eloise weakened into a tropical storm, causing a minimum of 6 fatalities, 12 injuries, and significant property damage (United Nations, 2022).

❖ Tornado over Soweto: 30 December 2017

On 30 December 2017, the prevailing meteorological pattern featured a broad surface trough stretching from the central interior to the western regions of South Africa, flanked by a high-pressure system situated to the east of the country (SAWS, 2017). On this day, a severe thunderstorm, associated with a tornado, was observed over Soweto in Gauteng, South Africa.

❖ Severe thunderstorm over the Eastern Cape: 09 March 2022

The weather on 9 March 2022 was characterised by a wide surface trough located across the central interior, bordered by high-pressure systems in both the western and eastern regions of the country (SAWS, 2022b). Consequently, thunderstorms were witnessed over a considerable portion of the country, encompassing the Eastern Cape.

❖ Tornado event over Hannover, KwaZulu-Natal: 12 November 2019

The weather of 12 November 2019 was characterised by a broad surface trough over the central interior of the country, flanked by a high-pressure system south of the country, which resulted in a thunderstorm that was associated with a tornado over New Hanover, KwaZulu-Natal (SAWS, 2019b; SAWS, 2019c). An upper-air trough was situated over the south coast along with an upper-air high over Angola, which progressed eastwards as the day continued.

5.3.1.2 Model evaluation

a) Spatial distribution of total rainfall

The spatial representation of rainfall on 25 January 2021, 01 GMT, 06 GMT, 12 GMT, and 18 GMT depicts that the model consistently predicts lower rainfall amounts compared to the observed values (Fig. 5.2). The simulated spatial distribution of the rainfall event closely aligns with the observed data, though the differences in intensity are obvious. While minor differences exist among the model simulations, they are not substantial enough to discern significant improvements, particularly with regard to model simulations with the 2015aM version of Convjlm.

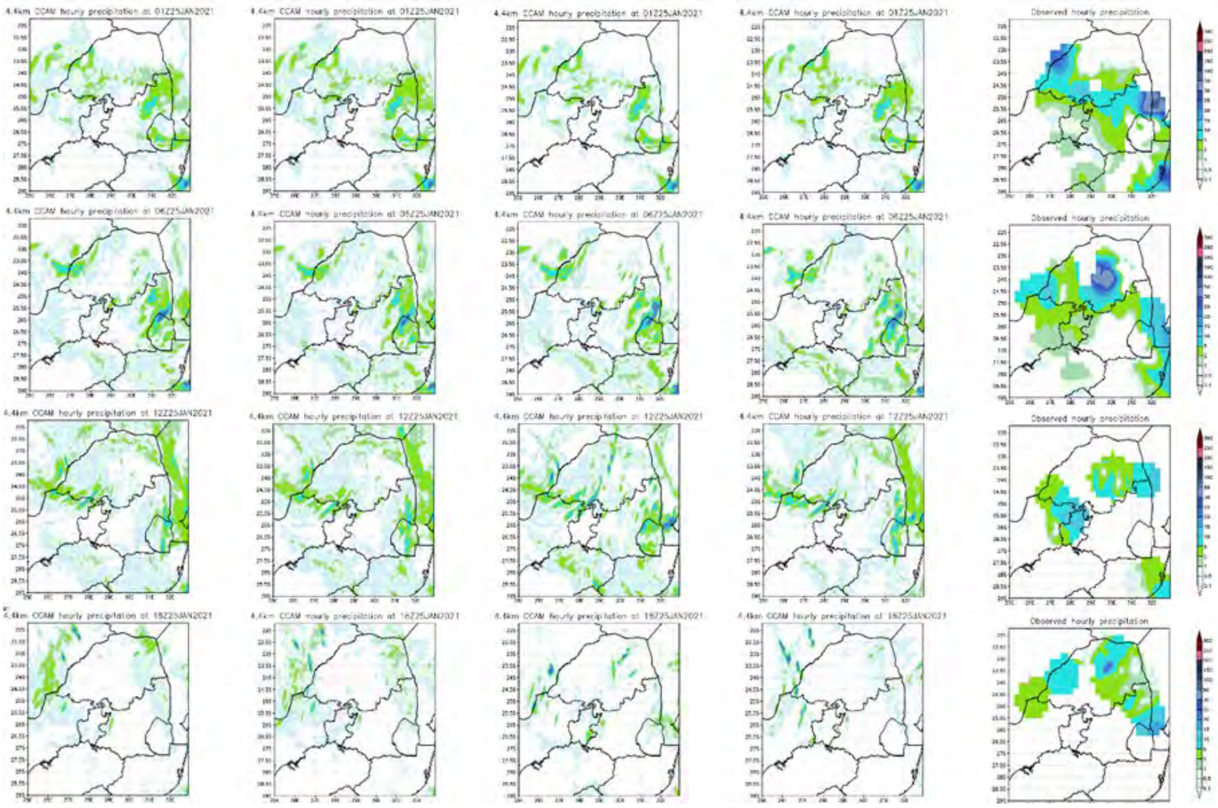

Figure 5.2: Hourly rainfall distribution over the north-eastern parts of the country that were affected by the tropical cyclone during the peak hours of 25 January 2021. These hours (in rows) 01, 06, 12 and 18 GMT. The first four columns represent the model runs with different versions of the Convjlm: first column is the 2015a, second column is the 2015b, third column is the 2017 and the fourth column is the 2015aM. The fifth column is the corresponding ground observations, regridded to 0.25 x 0.25 degrees resolution.

Figure 5.3 depicts the simulations of the spatial distribution of total precipitation over Gauteng and surrounding areas on 30 December 2017, between 13 GMT and 17 GMT, show that the model simulates far less rainfall than the observed. Further, the 2015aM produced much less rainfall as compared to its counterparts, while the model runs with the 2015a and 2015b Convjlm versions simulated relatively more precipitation than their counterparts. However, the model generally located the spatial distribution of precipitation accurately as compared to the course resolution observations.

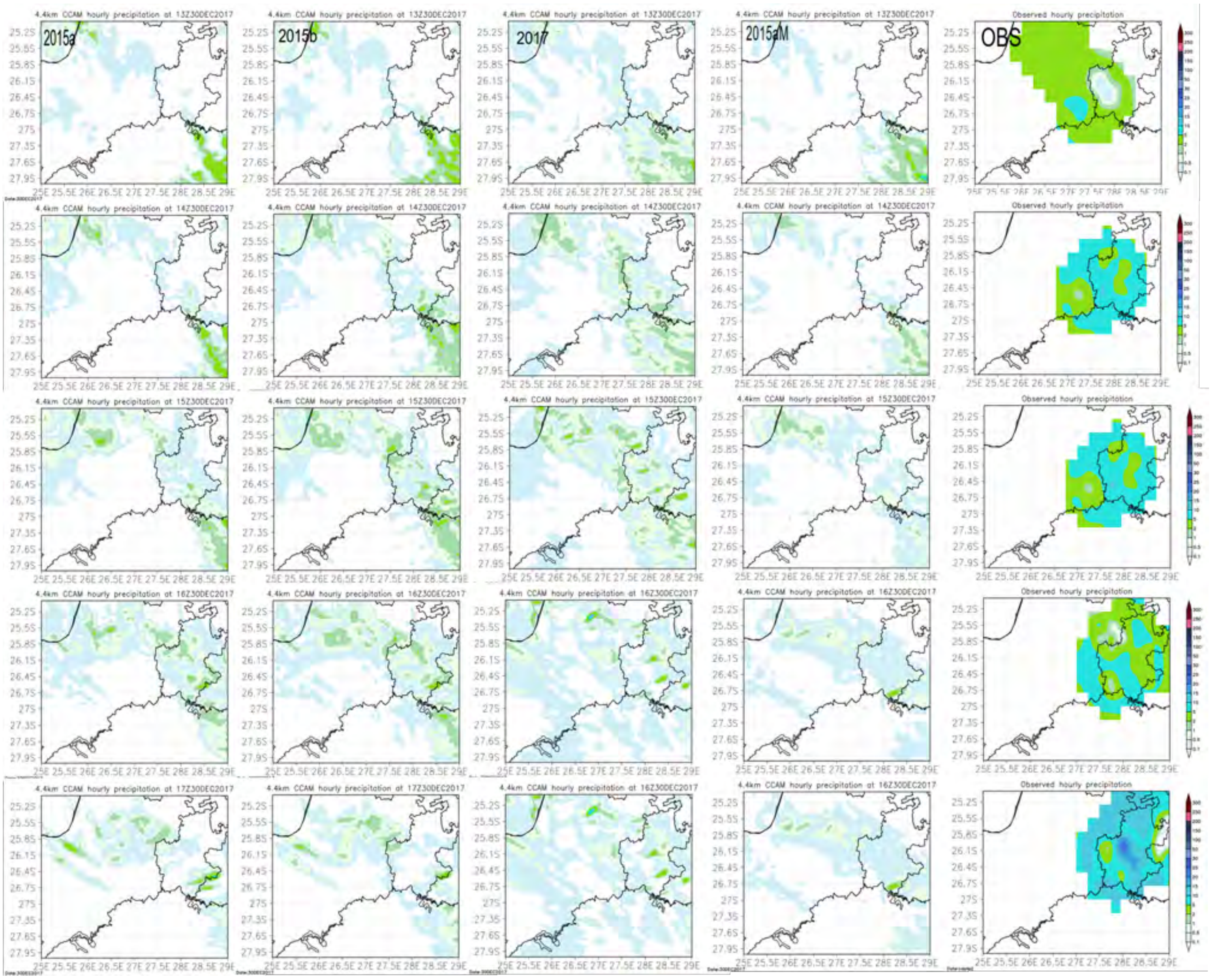

Figure 5.3: Hourly rainfall distribution over Gauteng and surrounding areas during the peak hours of 30 December 2017. These hours (in rows) range from 13 GMT to 17 GMT. The columns represent the model simulations with the different versions of the Convjlm: first column is the 2015a, second column is the 2015b, third column is the 2017 and the fourth column is the 2015aM. The fifth column is the corresponding ground observations, regridded to 0.25 x 0.25 degrees resolution.

The spatial distribution of precipitation on 9 March 2022 was analysed between the heavy rainfall hours (13 GMT – 18 GMT) over parts of the eastern Cape (Fig. 5.4). Once more, the model simulates less rainfall when compared to the surface observations. This is due to the sparse observational network for hourly data in the country. However, the model simulations have a much larger spatial coverage than the observed. This could be the reason behind low biases on the diurnal cycle. The model simulations follow a similar pattern, but the 2015aM usually simulates slightly less rainfall than the rest of the cumulus schemes.

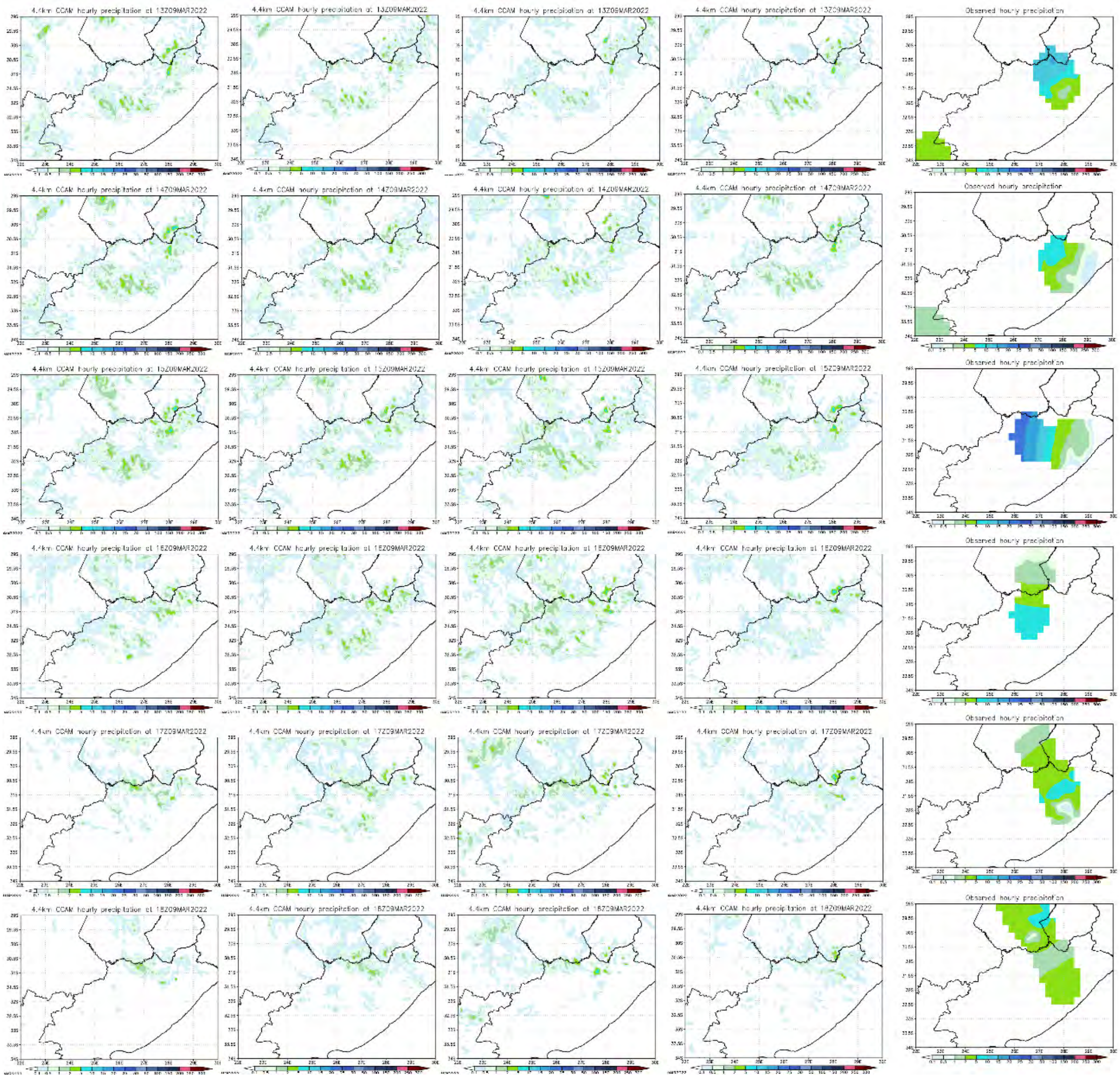

Figure 5.4: Hourly rainfall distribution over parts of the Eastern Cape on 09 March 2022. These are for hours (in rows): 01, 06, 12 and 18 GMT. The first four columns represent the model runs with different versions of the Convjlm cumulus scheme: first column is the 2015a, second column is the 2015b, third column is the 2017 and the fourth column is the 2015aM. The fifth column is the corresponding ground observations, regridded to 0.25 x 0.25 degrees resolution.

The spatial distribution of precipitation over parts of KwaZulu-Natal and surrounding areas on 12 November 2019 between 12 GMT and 17 GMT is depicted in Figure 5.5. As in other cases, the model simulates less rainfall than the observations. The model simulations with the 2015aM version of cumulus scheme produces less rainfall than its counterparts, except between 15 GMT and 17 GMT. The model fails to accurately locate the observed precipitation along the coastline, indicating a lack of accuracy in representing the event.

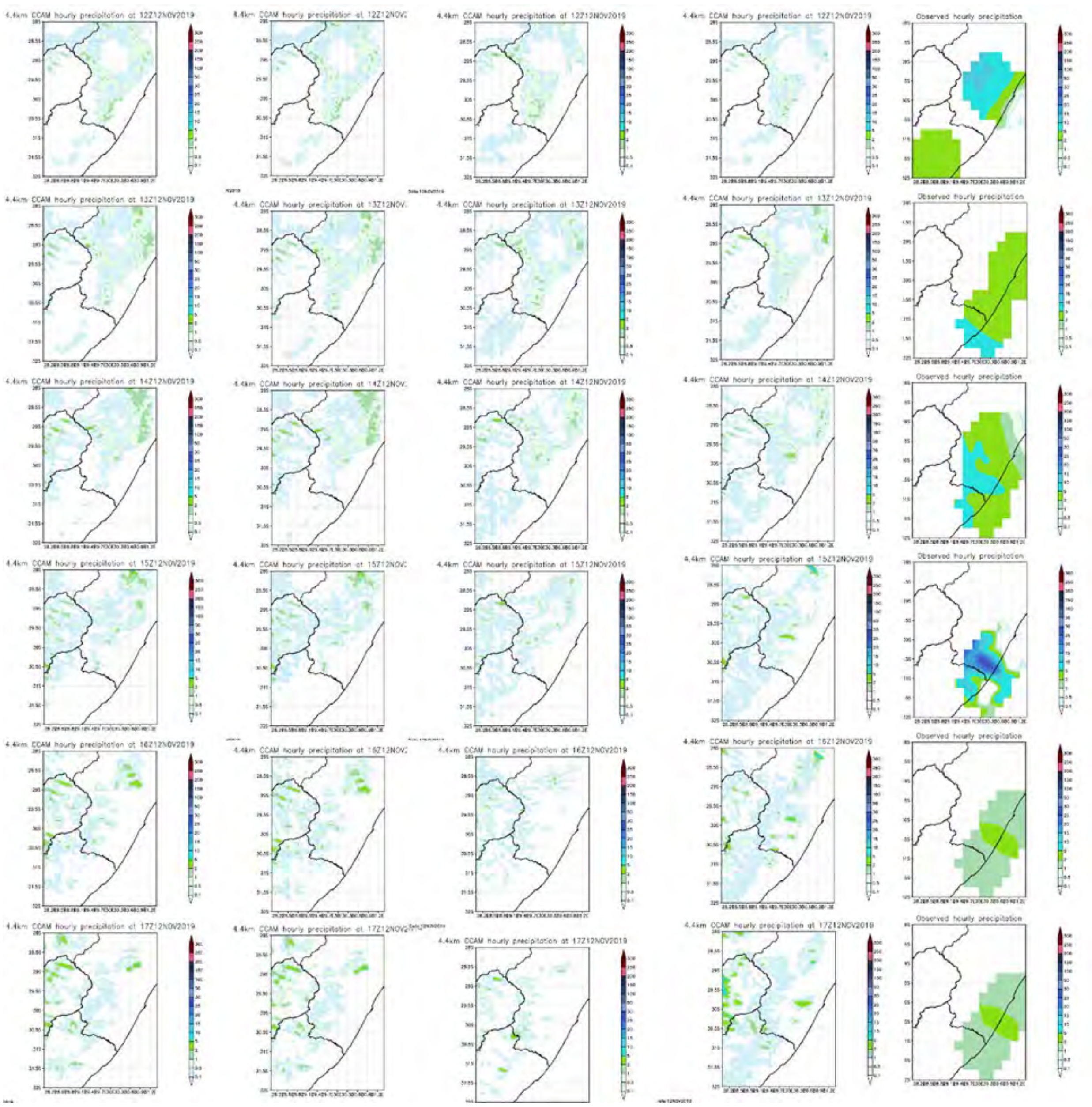

Figure 5.5: Hourly rainfall distribution over parts of KwaZulu-Natal and surrounding areas on 12 November 2019. These are for hours (in rows): 01, 06, 12 and 18 GMT. The columns represent the different versions of the Convjlm: first column is the 2015a, second column is the 2015b, third column is the 2017 and the fourth column is the 2015aM. The fifth column is the corresponding ground observations, regridded to 0.25 x 0.25 degrees resolution.

b) The diurnal cycle of areal averaged precipitation

The storm event of 25 January 2021 commenced several days before the case under analysis, making it challenging to evaluate the model's ability to initialise precipitation accurately. Despite this limitation, the model simulations managed to replicate the overall observed rainfall pattern (Fig. 5.6). This areal average rainfall was calculated over the domain depicted in Figure 5.2. There were several peaks that the model missed, namely, 04 GMT, 12 GMT and 16 GMT peaks. On the other hand, the model captured the peaks at 01 GMT and 09 GMT -10 GMT. Also, it is notable that parameterized rainfall made a limited contribution to the total precipitation.

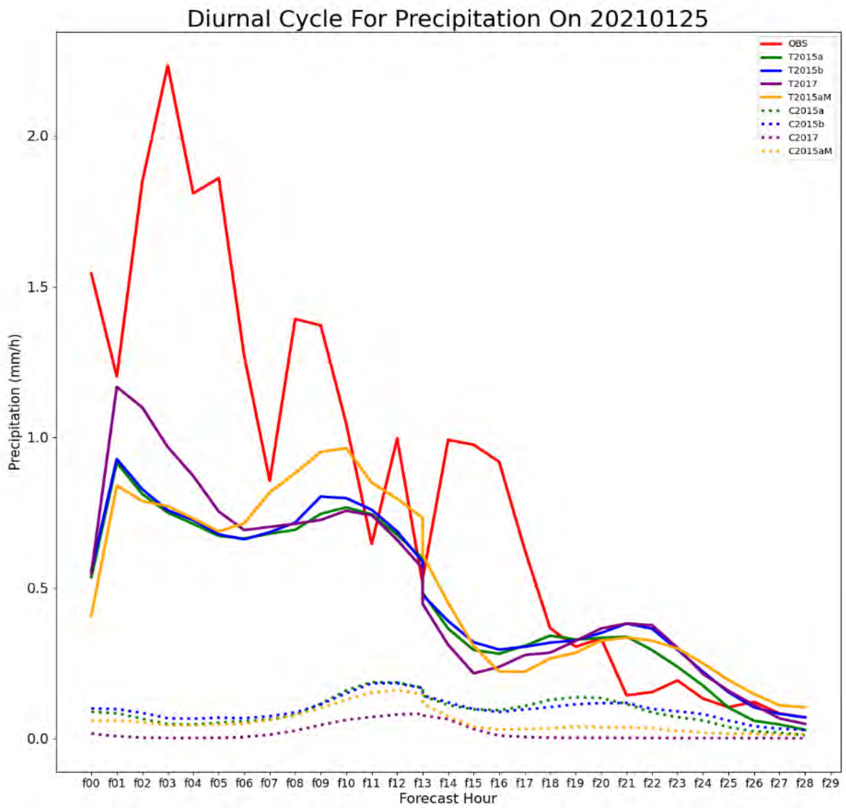

Figure 5.6: Diurnal cycle for areal averaged hourly precipitation for the domain depicted in Figure 5.2 on 25 January 2021. The ground observations (red solid line), the 2015a scheme (green solid line), the 2015b scheme (blue solid line), the 2017 scheme (purple solid line) and the 2015aM scheme (orange solid line). The dotted lines are the respective parameterized rainfall components of the CCAM runs with the different versions of the Convjlm cumulus scheme.

The diurnal cycle for 30 December 2017 over Soweto/Gauteng and surrounding areas depict that heavy rainfall was observed between 13 GMT and 18 GMT (Figure 5.7). The highest peak was observed at 16 GMT. Nevertheless, the model failed to reproduce this peak and initiated rainfall considerably earlier than observed. Model simulations with the 2015a, 2015b, and 2015aM versions of Convjlm cumulus schemes managed to capture the abrupt increase in precipitation intensity at 13 GMT, albeit in a limited amount. The model simulates precipitation amounts generally considerably lower than those observed at the surface, and the parameterized components of the total rainfall had a very limited contribution towards the total model rainfall.

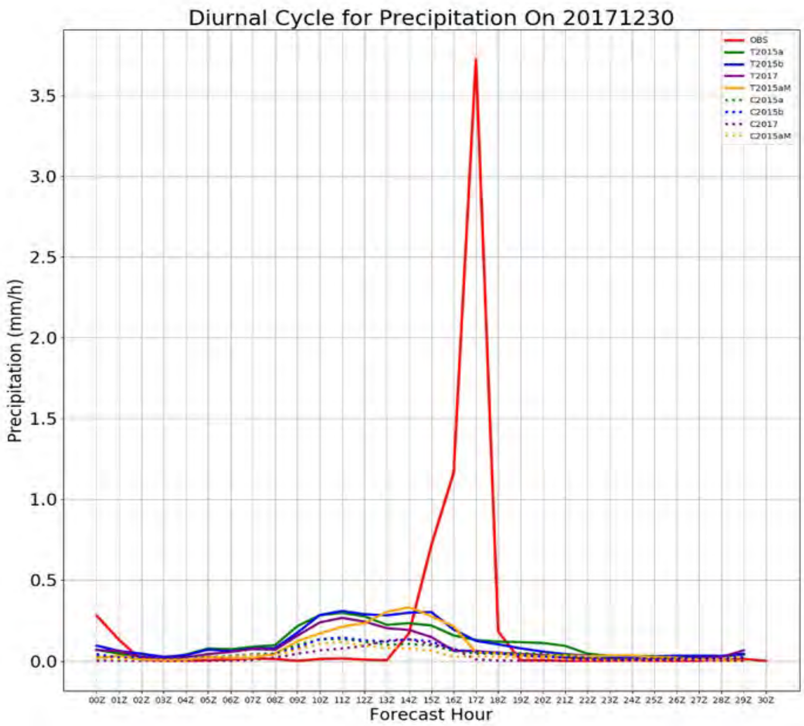

Figure 5.7: Diurnal cycle for areal averaged hourly precipitation for Gauteng and surrounding areas as shown in Figure 5.3 on 30 December 2017. The ground observations (red solid line), the CCAM run with 2015a scheme (green solid line), the CCAM run with 2015b scheme (blue solid line), the CCAM run with 2017 scheme (purple sold line) and the CCAM run with 2015aM scheme (orange solid line). The dotted lines are the respective parameterized rainfall components of the different versions of the Convjlm cumulus scheme.

The areal average precipitation for 9 March 2022 over parts of the Eastern Cape, as depicted in Figure 5.4, shows that the area experienced precipitation for the most parts of the day (Fig. 5.8). The model simulations were able to capture this event quite well, including the peak at 13 GMT. The model run with 2015aM cumulus scheme even captured the peak of rainfall at 14 GMT. The highest peak was observed at 21 GMT and was not captured by the model. Opposite to the former cases, the parameterized rainfall components of precipitation had a significant contribution during the most of the heavy rainfall hours.

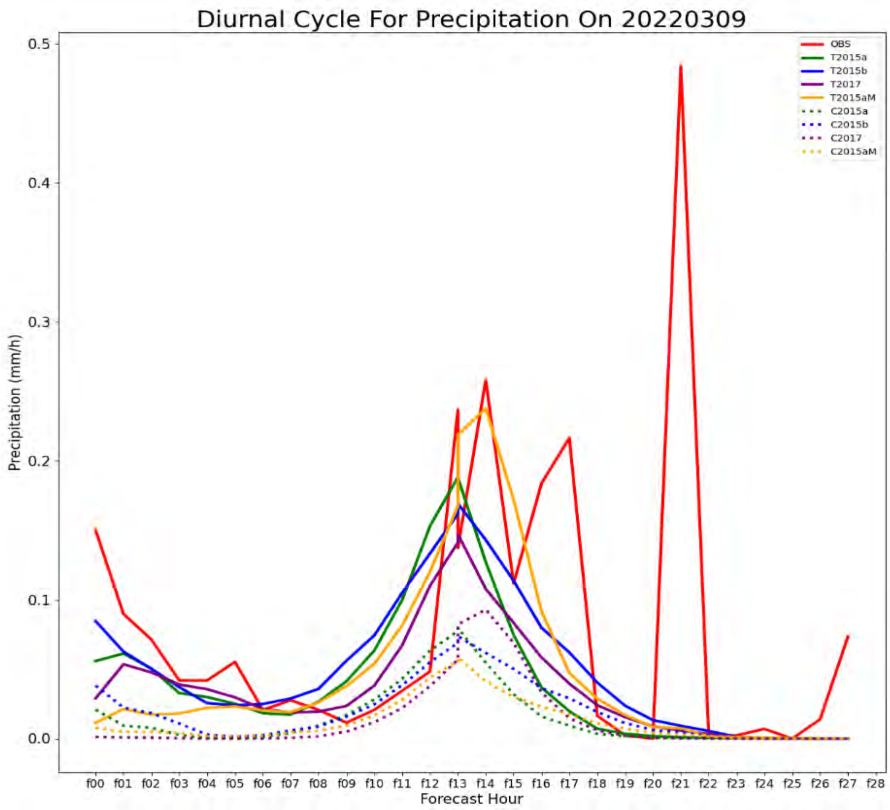

Figure 5.8: Diurnal cycle for areal averaged hourly precipitation for the domain depicted in Figure 5.4 on 09 March 2022. The ground observations (red solid line), the CCAM run with 2015a scheme (green solid line), the CCAM run with 2015b scheme (blue solid line), the CCAM run with 2017 scheme (purple sold line) and the CCAM run with 2015aM scheme (orange solid line). The dotted lines are the respective parameterized rainfall components of the CCAM runs with different versions of the Convjlm cumulus scheme.

The diurnal cycle of precipitation for 12 November 2019 over New Hannover, KwaZulu-Natal and surrounding areas (the area depicted in Figure 5.5) show that some precipitation was observed in the early hours of the day, which was not captured by the model simulations (Fig. 5.9). Heavy precipitation was observed from 12 GMT until 13 GMT, though a small amount was observed at 09 GMT. This event had several observed peaks at 17 GMT, 21 GMT and 23 GMT. The model runs with the 2017 and 2015aM Convjlm cumulus schemes that captured the observed patterns, though simulated rainfall amounts were much lower than the observed. The parameterized rainfall components of the model runs with each cumulus scheme had a trivial contribution towards total simulated precipitation.

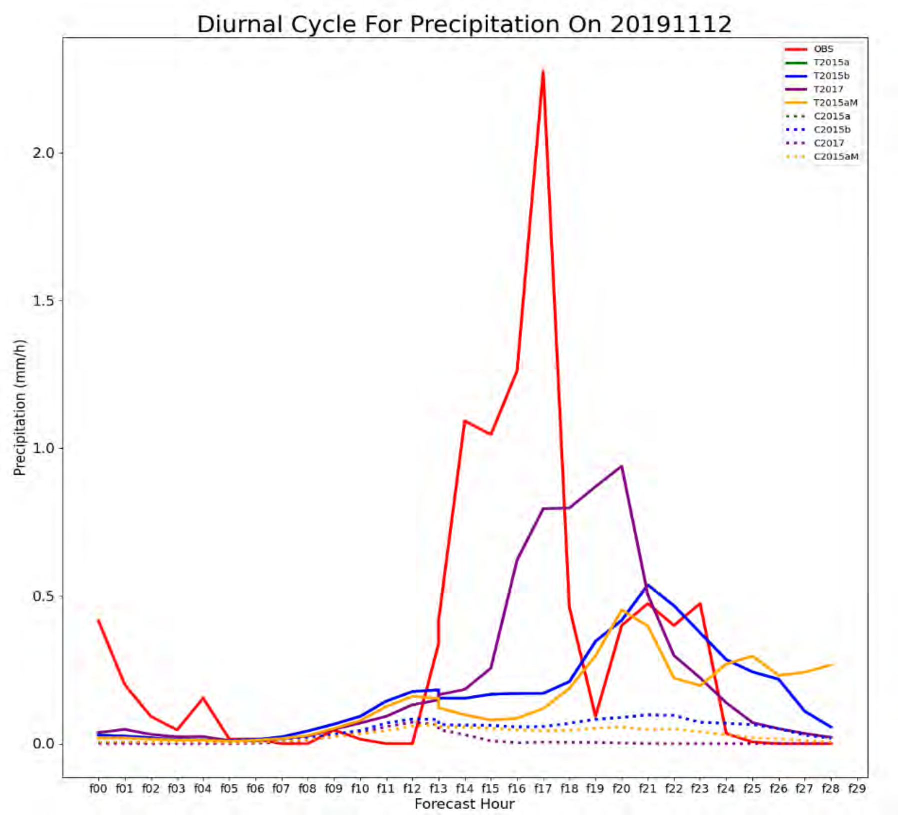

Figure 5.9: Diurnal cycle for areal averaged hourly mm for the area depicted in Figure 5.5 on 12 November 2019. The ground observations (red solid line), CCAM runs with the 2015a scheme (green solid line), CCAM runs with the 2015b scheme (blue solid line), CCAM runs with the 2017 scheme (purple sold line) and CCAM runs with the 2015aM scheme (orange solid line). The dotted lines are the respective parameterized rainfall components of the model runs with different versions of the Convjlm cumulus scheme.

a) Vertical profiles

A point in White River, Mpumalanga (Latitude: -25.33, Longitude: 31.01) was selected for the analysis of vertical pressure patterns as it was within the area affected by Tropical cyclone Eloise on 25 January 2021 (Figure 5.10). The model output at the time was written in 8 vertical levels. These were increased in the subsequent project deliverables. The model simulations show high values of near-surface moisture for all the runs. However, there are some differences in the upper-air moisture content, with the CCAM runs with 2017 Convjlm showing the most dryness from 08 GMT to 18 GMT. The CCAM run with 2015aM shows a very similar pattern to the CCAM run with 2015a Convjlm moisture profile. Temperature and wind profiles from all the runs were similar throughout the day and throughout the atmosphere. Omega profiles differ from one run to another, as the CCAM run with 2015a Convjlm showed negative omega values between 02 GMT to 04 GMT and 06 GMT to 09 GMT, while its counterparts only have this downward movement between 02 GMT and 04 GMT.

The runs then show a neutral atmosphere for the rest of the day except for 21 GMT when the CCAM run with 2017 Convjlm shows negative omega values in the lower atmosphere.

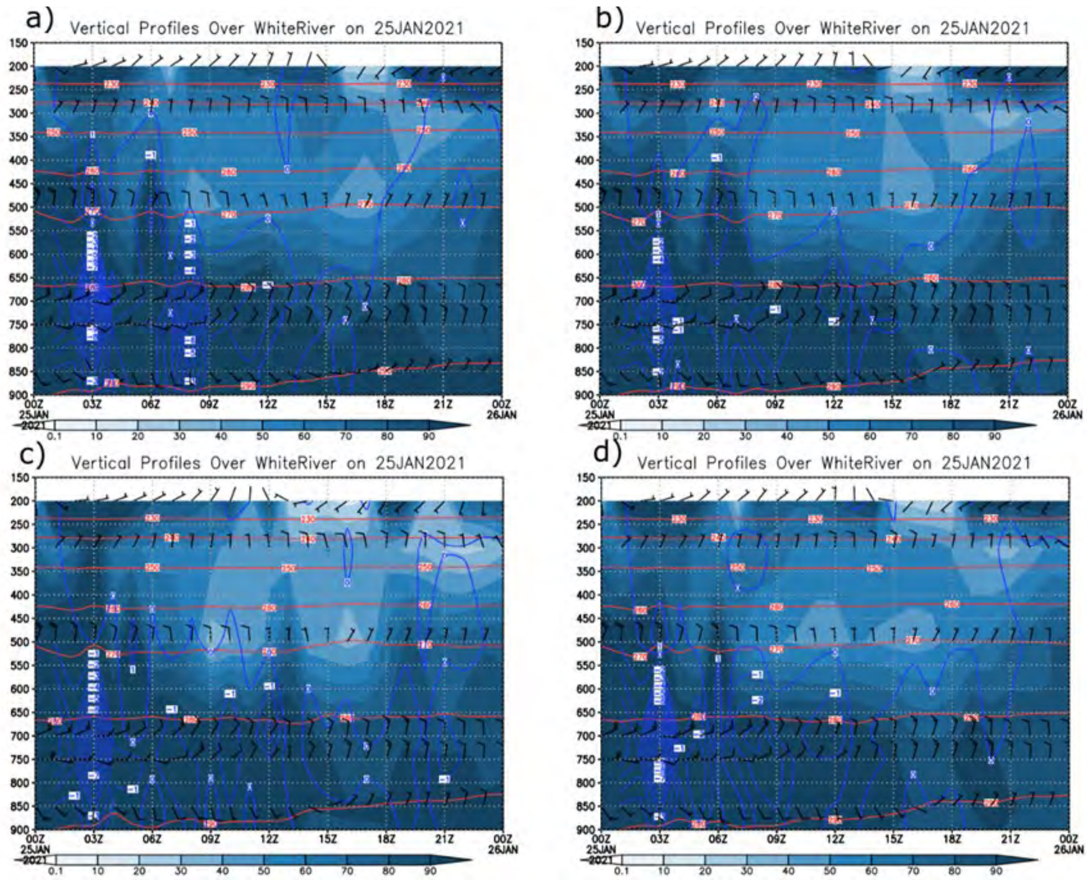

Figure 5.10: Vertical profiles for convective variables over White River, Mpumalanga, South Africa on 25 January 2021: relative humidity (shaded), temperature (red lines), omega (blue lines) and horizontal wind barbs. The variables are available for 8 vertical levels for CCAM runs with Convjlm 2015a version (a), 2015b version (b), 2017 version (c) and 2015aM version (d).

A point over Soweto (Latitude: -26.36, Longitude: 27.77), where a tornado event was observed, was selected for the analysis of vertical profiles for the thunderstorm event of 30 December 2017 for selected convective parameters (Fig. 5.11). There are slight differences in the moisture profiles, where the model run with 2017 Convjlm depicts an extension of high humidity to the upper atmosphere at 14 GMT and 17 GMT, and the CCAM runs with 2015b Convjlm at 19 GMT. The same applied with omega. Simulations with the 2015a and 2015aM Convjlm produced the driest upper air atmosphere over Soweto on 30 December 2017. Temperature and wind profiles followed a similar pattern for all the model runs. Moreover, from 12 GMT onwards, model run with the 2015aM Convjlm shows positive omega values near the surface and upper air subsidence. This was not captured by its counterparts.

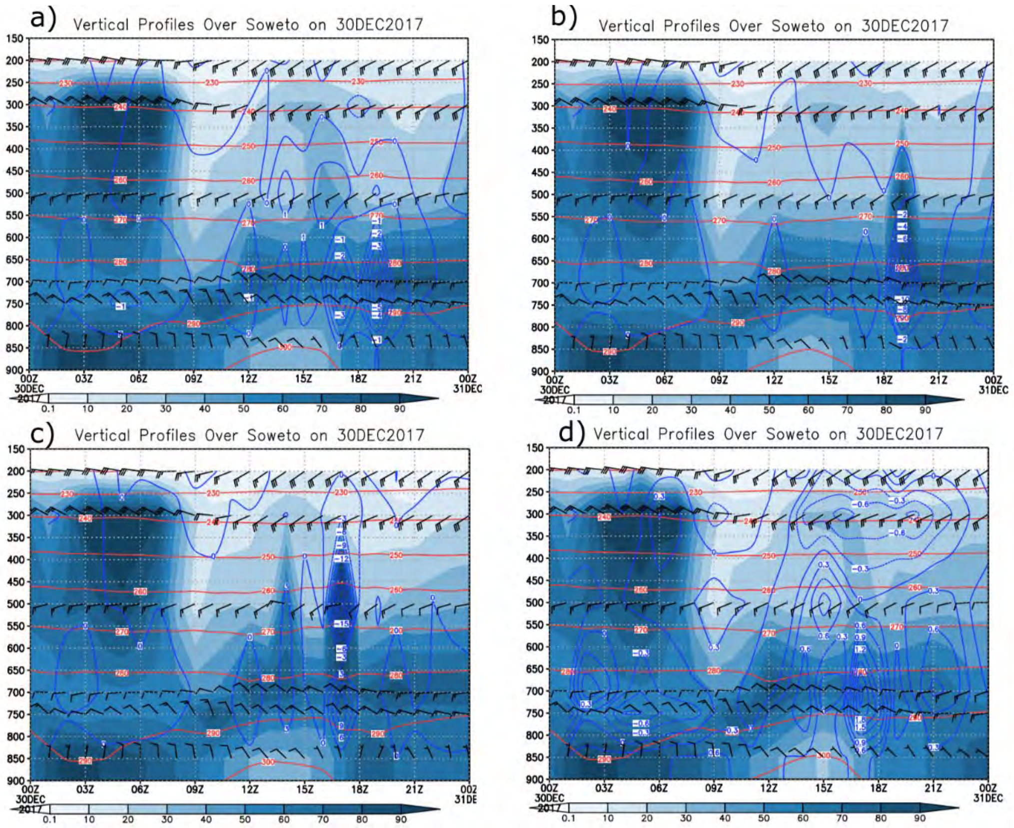

Figure 5.11: Vertical profiles for convective variables for Soweto, Gauteng, South Africa on 30 December 2017: relative humidity (shaded), temperature (red lines), omega (blue lines) and horizontal wind barbs. The variables are available for 8 vertical levels of the CCAM runs with Convjlm 2015a version (a), 2015b version (b), 2017 version (c) and 2015aM version (d).

Queenstown (Latitude: -31.89, Longitude: 26.84), was selected for analysis of the vertical profiles for selected convective parameters (Fig. 5.12). There are minor differences on the relative humidity, temperature and wind profiles amongst the model runs. However, there are obvious differences in the omega profiles from 12 GMT, when the CCAM run with 2015aM has the lowest omega values when compared to its counterparts.

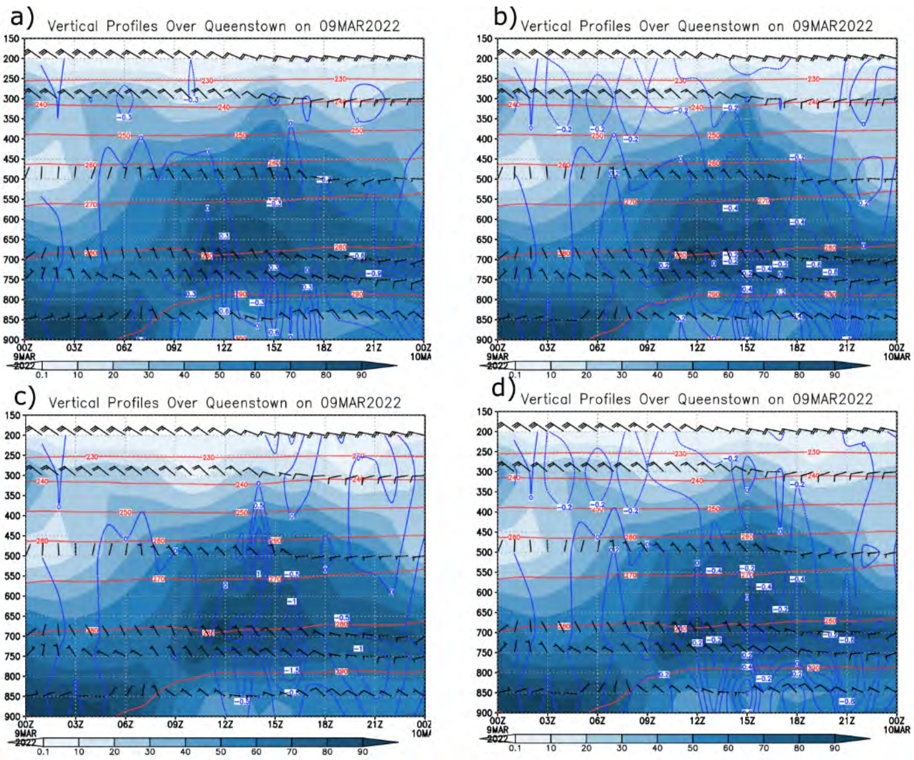

Figure 5.12: Vertical profiles for convective variables over Queenstown, Eastern Cape, South Africa [Latitude: -31.89, Longitude: 26.84] on 9 March 2022: relative humidity (shaded), temperature (red lines), omega (blue lines) and horizontal wind barbs. The variables are available for 8 vertical levels for CCAM runs with Convjlm 2015a (a), 2015b (b), 2017 (c) and 2015aM (d).

Vertical profiles of the selected convective variables over New Hannover, KwaZulu-Natal (Latitude: -29.36, Longitude: 30.52), were analysed for the case of 12 November 2019 to gain further understanding on the model behaviour in relation to the different versions of the Convjlm cumulus scheme (Fig. 5.13). Noticeable differences in the moisture profiles are visible on the CCAM run with 2015aM between 15 GMT and 16 GMT, where there is a column of moist air associated with positive omega values in the upper air and subsidence from 550 hPa downwards. This could be due to the gust front/tornado events, which may have been captured by the CCAM run with 2015aM Convjlm cumulus scheme, or rather only captured at 23 GMT by the rest of the model simulations.

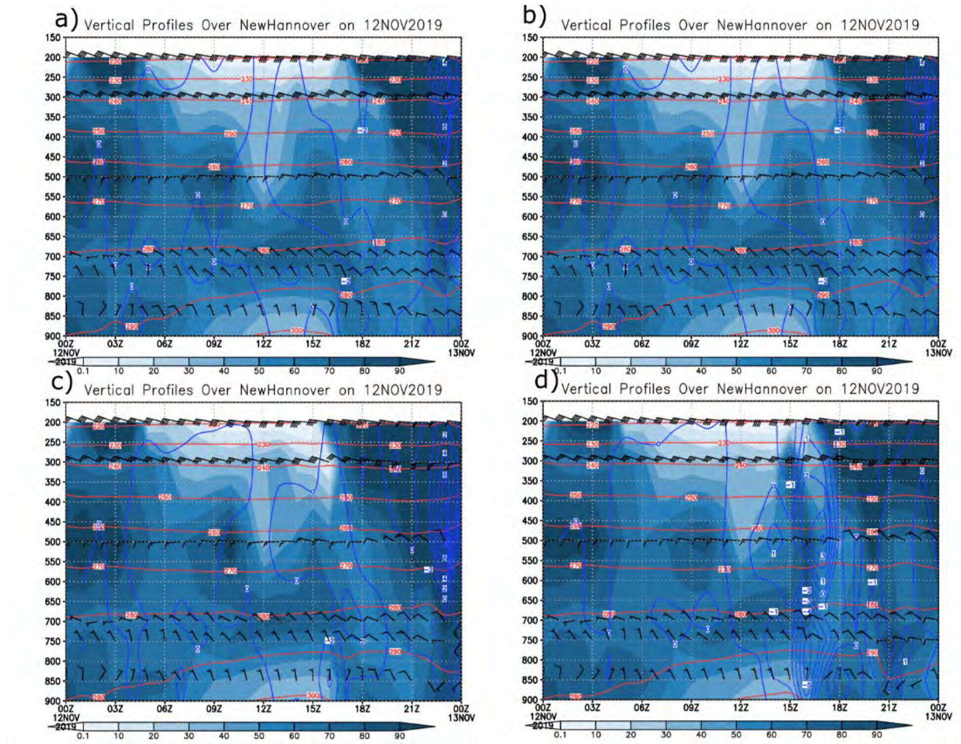

Figure 5.13: Vertical profiles for convective variables over New Hannover, KwaZulu-Natal, South Africa: relative humidity (shaded), temperature (red lines), omega (blue lines) and horizontal wind barbs. The variables are available for 8 vertical levels for CCAM runs with Convjlm 2015a (a), 2015b (b), 2017 (c) and 2015aM (d).

a) Skill scores: Critical success index and Success ratio

Heatmaps for hourly precipitation over 0.1 mm, 5 mm, 10 mm and 20 mm over the South African domain affected by Tropical cyclone Eloise (Fig. 5.14) on 25 January 2021 as depicted in Figure 5.2. They show that when compared to ground observations, the model simulations with the four versions of the Convjlm cumulus scheme have neither accuracy (SR; Fig. 5.14) nor correspondence (CSI; Fig. 5.15).

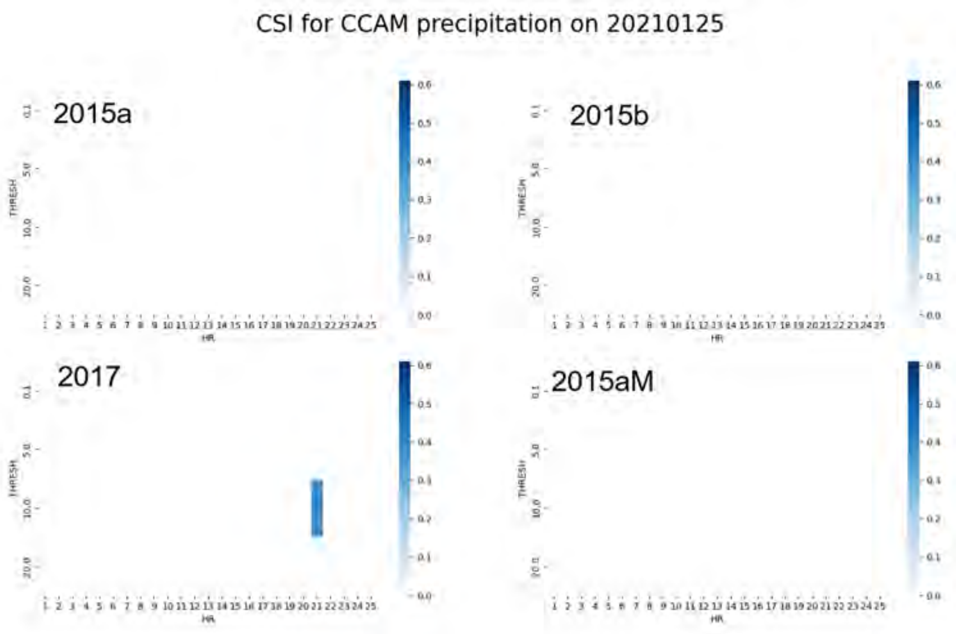

Figure 5.14: Heatmaps for critical success index for hourly precipitation>0.1mm ,5 mm, 10mm and 20 mm over the area depicted in Figure 5.2 on 25 January 2021. CCAM runs with the different versions of Convjlm, namely, the 2015a (top-left), the 2015b (top-right), the 2017 (bottom-left) and the 2015aM (bottom-right) were evaluated against ground observations.

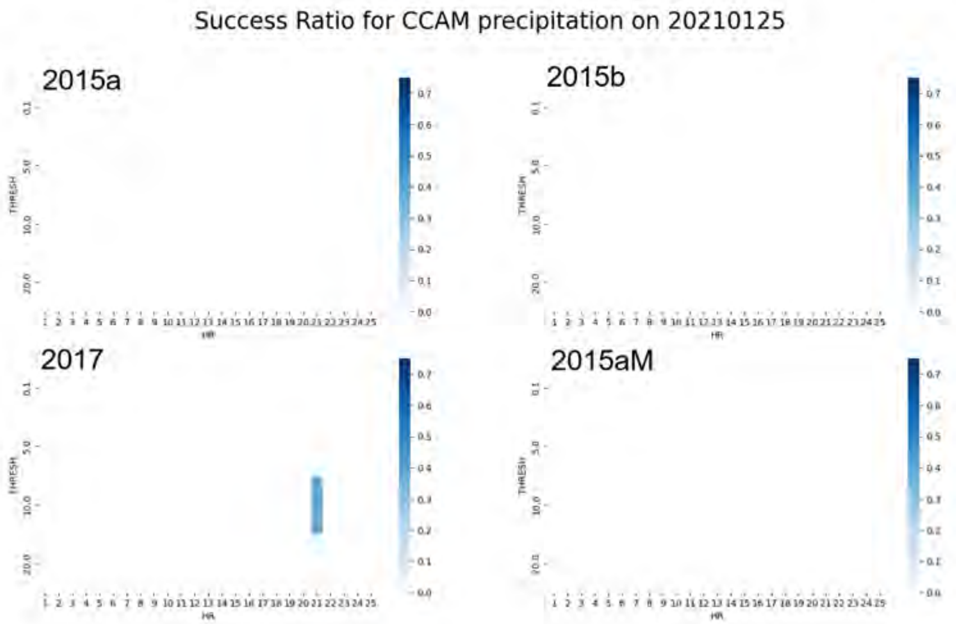

Figure 5.15: Heatmaps for success ratio for hourly precipitation>0.1mm ,5 mm, 10mm and 20 mm over the area depicted in Figure 5.3 on 25 January 2021. The different versions of the Convjlm, namely, the 2015a (top-left), the 2015b (top-right), the 2017 (bottom-left) and the 2015aM (bottom-right) were evaluated against ground observations.

Simulations of the thunderstorm event associated with a tornado event over Soweto on 30 December 2017 shows that the model simulations with 2015a, 2015b and 2017 versions of the Convjlm cumulus scheme had very little accuracy and compared with ground observations (Fig. 5.16 and Fig. 5.17). There were instances of a good measure of accuracy (CSI) for the thresholds under investigation, but those were inconsistent. It is important to note that simulations with the 2015aM Convjlm version showed neither the accuracy nor correspondence.

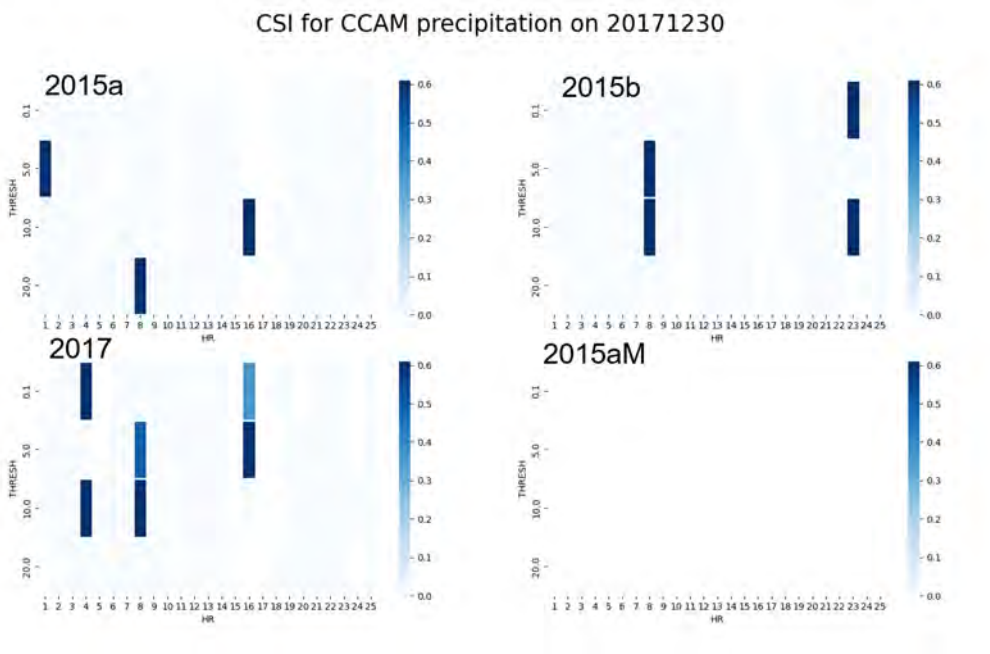

Figure 5.16: Heatmaps for critical success index for hourly precipitation>0.1mm, 5 mm, 10mm and 20 mm over the area depicted in Figure 5.3 on 30 December 2017. The CCAM runs with different versions of the Convjlm, namely, the 2015a (top-left), the 2015b (top-right), the 2017 (bottom-left) and the 2015aM (bottom-right) were evaluated against ground observations.

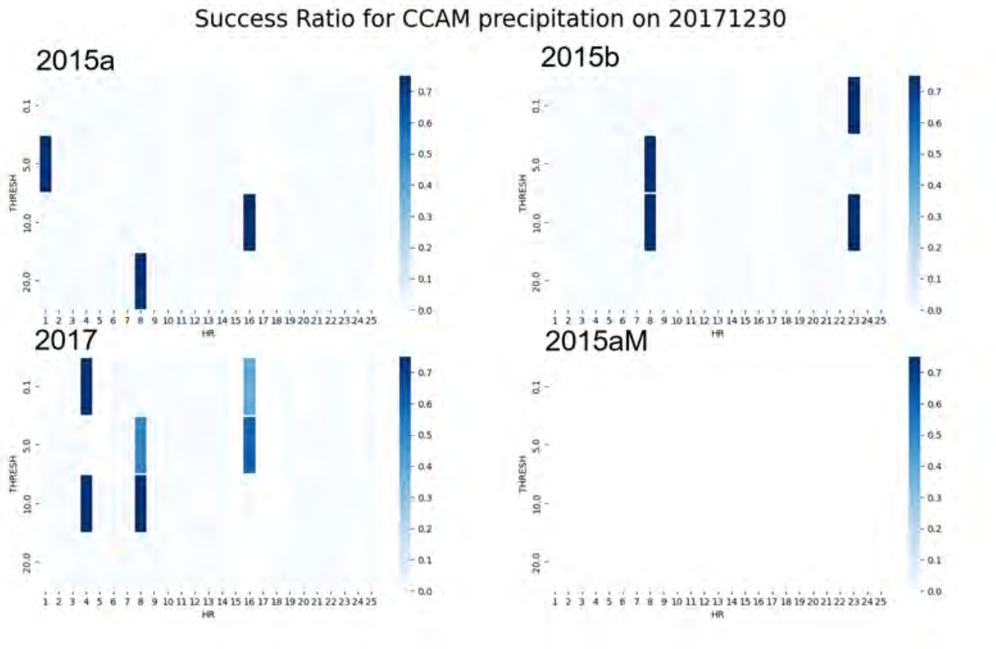

Figure 5.17: Heatmaps for success ratio for hourly precipitation>0.1mm, 5 mm, 10mm and 20 mm over the domain depicted in Figure 5.3 on 30 December 2017. The CCAM runs with different versions of the Convjlm, namely, the 2015a (top-left), the 2015b (top-right), the 2017 (bottom-left) and the 2015aM (bottom-right) were evaluated against ground observations.

Figures 5.19 and 5.20 depict the CSI, a measure of correspondence, and SR, a measure of accuracy, for model runs against ground observations for 0.1 mm, 5 mm, 10 mm and 20 mm hourly thresholds. These are for the rainfall event that occurred over parts of the Eastern Cape on 9 March 2022. There is, unfortunately neither accuracy nor correspondence in predicting rainfall over the area of interest for all the versions of the cumulus scheme.

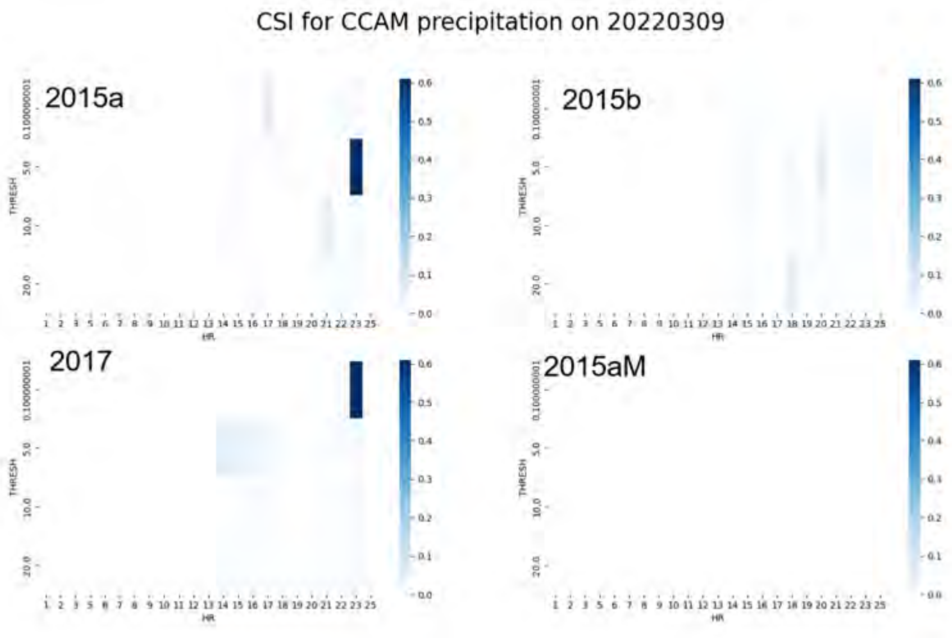

Figure 5.18: Heatmaps for critical success index for hourly precipitation >0.1 mm, 5 mm, 10 mm and 20 mm over the area depicted in Figure 5.4 on 09 March 2022. The CCAM runs with different versions of the Convjlm, namely, the 2015a (top-left), the 2015b (top-right), the 2017 (bottom-left) and the 2015aM (bottom-right) were evaluated against ground observations.

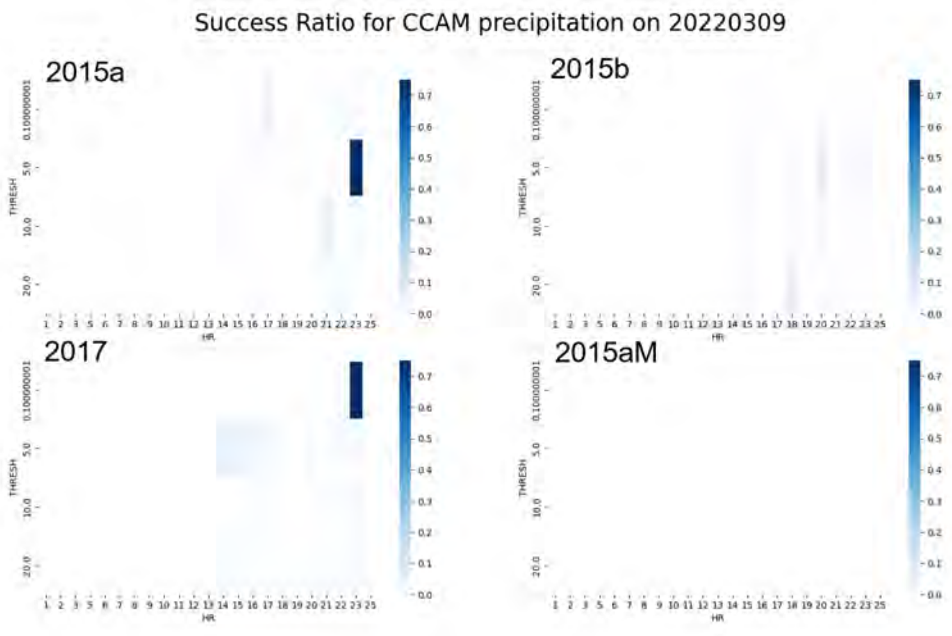

Figure 5.19: Heatmaps for success ratio for hourly precipitation >0.1 mm, 5 mm, 10 mm and 20 mm for area depicted in Figure 5.4 on 9 March 2022. The model runs with different versions of the Convjlm, namely, the 2015a (top-left), the 2015b (top-right), the 2017 (bottom-left) and the 2015aM (bottom-right) were evaluated against ground observations.

There is a good level of correspondence between the model runs with 2015a, 2015b and 2017 Convjlm cumulus scheme in relation to surface observations over the domain shown in Figure 5.4 on 12 November 2019 (Fig. 5.20). However, there is no correspondence for model simulations with the 2015aM Convjlm scheme. Contrary to the former cases, there is a measure of accuracy in predicting precipitation over the area of interest (Fig. 5.21). This accuracy is shown throughout the day, for 0.1 mm, 5 mm, 10 mm and 20 mm thresholds for CCAM runs with 2015a, 2015b and 2017 Convjlm simulations. There is, however, no accuracy in predicting this precipitation with 2015aM Convjlm cumulus scheme throughout the day.

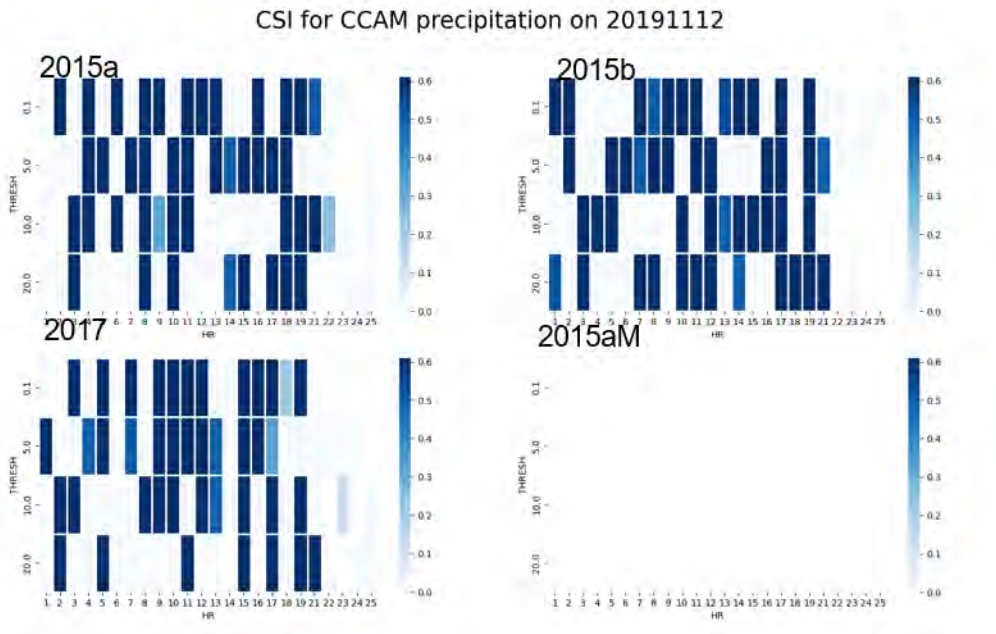

Figure 5. 20: Heatmaps for critical success index for hourly precipitation >0.1mm, 5 mm, 10 mm and 20 mm over parts of KwaZulu-Natal and surrounding areas on 12 November 2019. The different versions of the Convjlm, namely, the 2015a (top-left), the 2015b (top-right), the 2017 (bottom-left) and the 2015aM (bottom-right) were evaluated against ground observations.

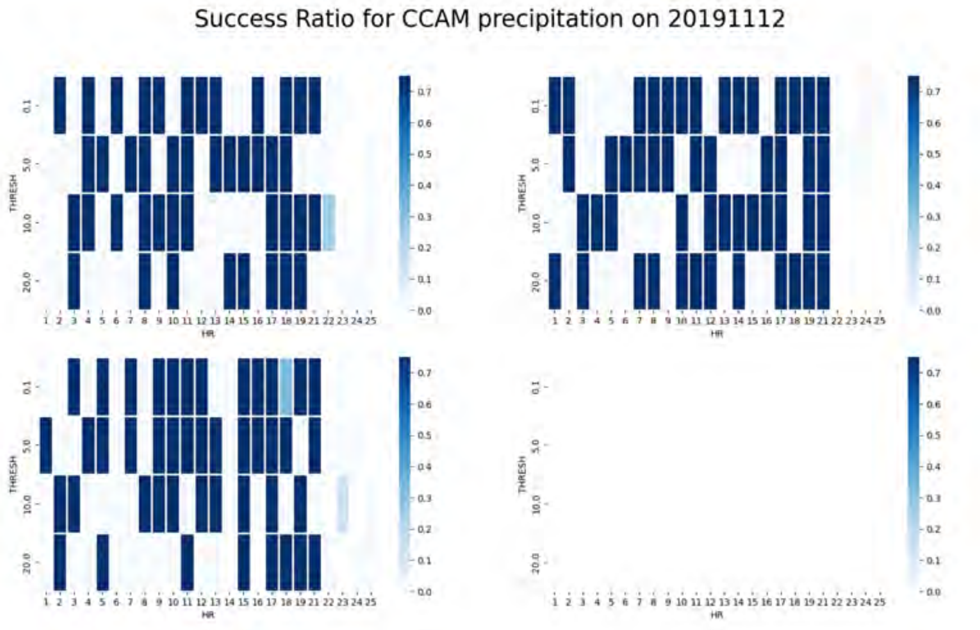

Figure 5.21: Heatmaps for success ratio for hourly precipitation >0.1 mm, 5 mm, 10 mm and 20 mm over parts of KwaZulu-Natal and surrounding areas on 12 November 2019. The different versions of the Convjlm, namely, the 2015a (top-left), the 2015b (top-right), the 2017 (bottom-left) and the 2015aM (bottom-right) were evaluated against ground observations.

5.3.2 Experiments to identify the value of bcon parameter.

The CCAM code was upgraded in August 2022. This is the version agreed upon for further research and development. Also, prior investigations revealed a consistent dry precipitation bias in the model simulations with the different versions and settings of the CCAM cumulus scheme. Moreover, the convective component exhibited minimal contribution towards total precipitation. Consequently, this study conducts experiments to identify the optimal value for the bcon parameter, with an aim to reduce the dry bias and enhance the contribution of the convective rainfall component in the total forecast precipitation. The total precipitation is the sum of convective rainfall (simulated by cumulus convection schemes) and large-scale rainfall (simulated by the cloud microphysics scheme). The bcon parameter, utilised by an NCAR scheme in cloudmod.f90 for diagnosing cloud cover, includes the convective rainfall rate calculated in convjlm.f. Model developers prefer bcon = 0.04 (referred to as CCAMp04) and bcon = 0.1 (referred to as CCAMp1). Model simulations for cases involving Mesoscale Convective Systems (MCSs) were simulated for these bcon values. Additionally, simulations were conducted for bcon = 0.2 (referred to as CCAMp02) and bcon = 0.5 (referred to as CCAMp1) to determine the bcon value that most effectively reduces precipitation bias and increases the contribution of the convective rainfall component to the total precipitation across the South African domain.

Selected case studies for investigating the influence of bcon parameter on the rainfall simulations included cases of high rainfall over parts of the country: 30 December 2017, 12 November 2019 and 09 March 2022 (described in 5.3.1.1). To focus the analysis on the area of interest and filter out the influence of rainfall occurring in other parts of the country, each case focused on investigating precipitation over the area of interest, where the event occurred, and its surrounding areas. Within these domains, the spatial distribution of 24-hour accumulated rainfall for each model run was plotted in comparison to ground observations. Furthermore, the diurnal cycle of areal average rainfall for each simulation over this domain was compared against ground observations. The CCAM simulations were conducted at a horizontal resolution of 6 km, while ground observations across the country were gridded to a horizontal resolution of 0.25°.

Thereafter, Fractions Brier scores (FBS) and Fractions Skill Scores (FSS) were computed for each model simulation against ground observations using equations 5.9 and 5.10. FBS and FSS indicate probabilistic neighbourhood verification schemes that consider observed and forecasted precipitation over a specific grid point of interest and a selected number of its neighbouring cells. Precisely, FBS and FSS assess the fractional coverage of rainfall exceeding a predetermined threshold in a window surrounding forecasts and observations (Zhao and Zhang, 2018). FBS serves as a metric for reliability, resolution, and uncertainty in probability forecasts (Murphy, 1973). On the contrary, FSS serves as a gauge of error in locating rainfall (Roberts, 2008; Skok and Roberts, 2016; Mittermaier, 2021). An FSS = 0 implies a complete mismatch, FSS=1 indicates a perfect forecast, and FSS=0.5 denotes a useful forecast (Zhao and Zhang, 2018).

$$FBS = \frac{1}{n}\sum_{i=1}^{n}(F-O)^2 \ldots \quad (5.9)$$

$$FSS = 1 - \frac{\frac{1}{n}\sum_{i=1}^{n}(F-O)^2}{\frac{1}{n}\sum_{i=1}^{n}F^2 + \frac{1}{n}\sum_{i=1}^{n}O^2} \ldots \quad (5.10)$$

where F is the forecast fractions and O is the observed fractions, both indicated by the number of occurrences of the event of interest over the number of grid points in the window of interest (Duc et al., 2013; Jones, 2014). The model data and observations were regridded to 0.25 x 0.25 ° over the of interest, from which F and O were computed. Table 5.3 depicts the process followed composing up windows for computing F and O.

Table 5.3: Structure for creating neighbourhood windows for computing F and O, which are used to calculate BS and FSS.

(1;1)	(2;1)	(3;1)			
(1;2)	A	(3;2)			
(1;3)	(2;3)	(3;3)			
			B		

These are the steps followed to compute FSS and FBS from the windows depicted in Table 5.3:

a) A neighbourhood window of 3x3 pixels is constructed for forecasts and observations, separately. The neighbourhood window for the pixel marked by A in Table 5.3 would span the eight golden pixels surrounding it. Likewise for the pixel indicated as B.
b) Construct binaries for each pixel: 1 for pixels containing rainfall that exceeds specified threshold and 0 for pixels with rainfall less than the given threshold. In this case, selected rainfall thresholds are 0.1 mm, 0.5 mm, 1 mm, 5 mm, 10 mm and 20 mm.
c) Calculate the total fraction of pixels with the number of occurrences (ones), e.g., for A, compute the number of pixels with 1's and divide by the total number of pixels with valid data in the window, as some pixels may have undefined or missing values/data. If all the pixels within this window have valid data, then the total fraction of pixels with the number of occurrences=total number of pixels with 1's divided by 9 pixels. This process is done for forecasts and observations, separately. The results will then be used to obtain FBS and FSS as shown in equations 5.6 and 5.7. FBS and FSS make a spatial comparison between forecasts and observations, rather than point-to-point comparisons (Faggian et al., 2015).

Furthermore, model output variables that may be associated with convection were examined over grid points of interest. This included the diurnal cycle for cloud base, cloud top, average Convective Available Potential Energy (CAPE), maximum CAPE, latent heat flux, sensible heat flux, and vertical profiles at forecast hours of interest for temperature, relative humidity, omega, total cloud fraction, and mixing ratio. These analyses involved plotting the data to explain any differences or similarities observed in comparison to the verification matrices listed above.

5.3.2.1 Model evaluation

a) Spatial distribution of rainfall

The case of 30 December 2017 shows that CCAM run with a bcon = 0.2 successfully captured the highest 24-hour accumulated precipitation, closest to the area of observed maxima in the southern region of Gauteng (Fig. 5.22). Subsequently, the CCAM run with bcon = 0.1 demonstrated a similar trend. However, the model runs failed to simulate precipitation in the north-eastern parts of Gauteng. Additionally, the model simulations overestimated the light rainfall observed across the rest of the domain.

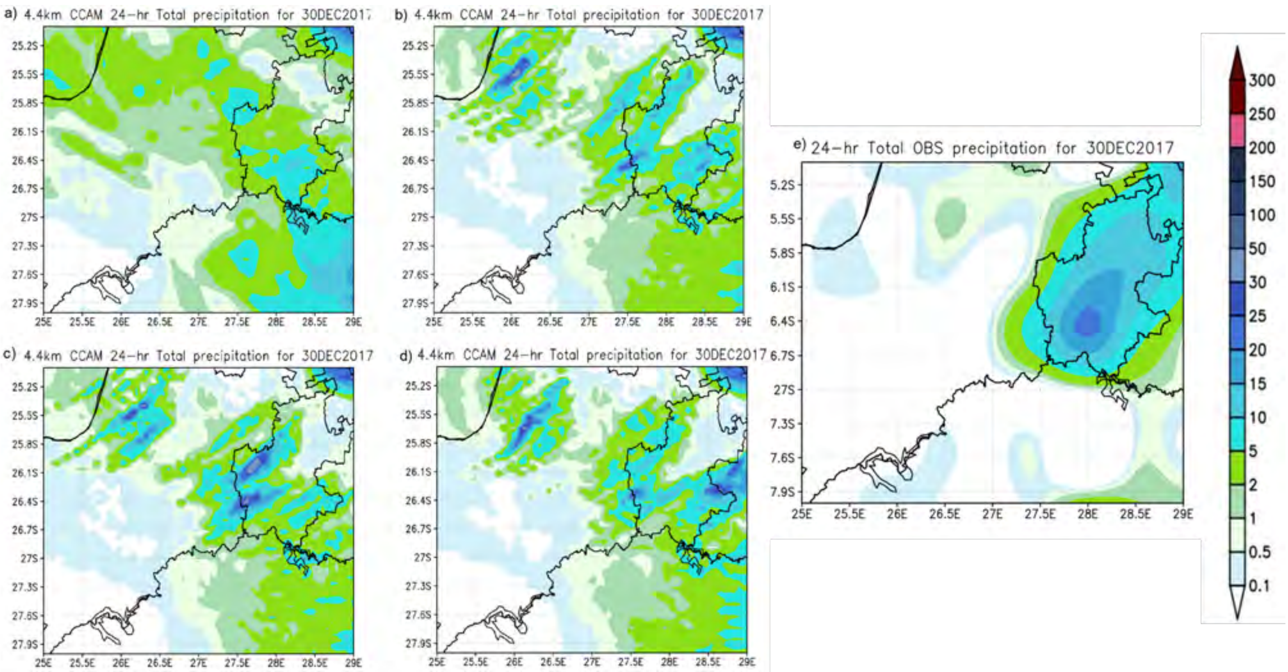

Figure 5.22: 24-hour accumulated rainfall for the tornado event that was witnessed in Soweto, Gauteng in the afternoon of 30 December 2017: a) CCAM simulations with bcon=0.04, b) CCAM simulations with bcon=0.1, c) CCAM simulations with bcon=0.2, d) CCAM simulations with bcon=0.5 and e) ground observations.

The case of 12 November 2019 shows that the southern tip of KwaZulu-Natal province experienced the highest 24-hour total rainfall (Figure 5.23). However, these maxima were not accurately captured by the model simulations, with slight variations observed among them. Additionally, the model simulations exhibited a notable dry bias, a characteristic further evident in the diurnal cycle.

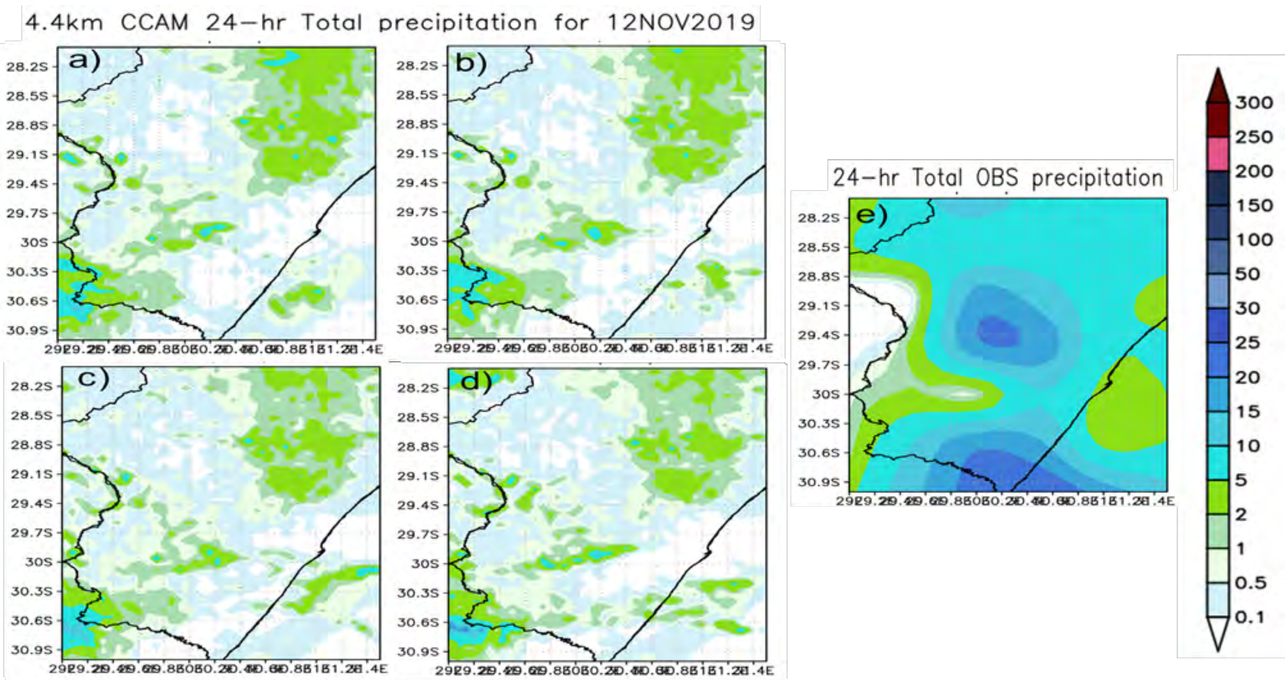

Figure 5.23: 24-hour accumulated rainfall for a severe thunderstorm event that resulted in a tornado over New Hannover, KwaZulu-Natal on 12 November 2019: a) CCAM simulations with bcon=0.04, b) CCAM simulations

with bcon=0.1, c) CCAM simulations with bcon=0.2, d) CCAM simulations with bcon=0.5 and e) ground observations.

In Figure 5.24, it is evident that an exceptionally high level of 24-hour accumulated precipitation occurred over the Eastern Cape on 9 March 2022, yet the model simulations only captured a minimal amount. Similar to the observations, the model simulations indicate that the greatest rainfall occurred in the north-eastern parts of the domain.

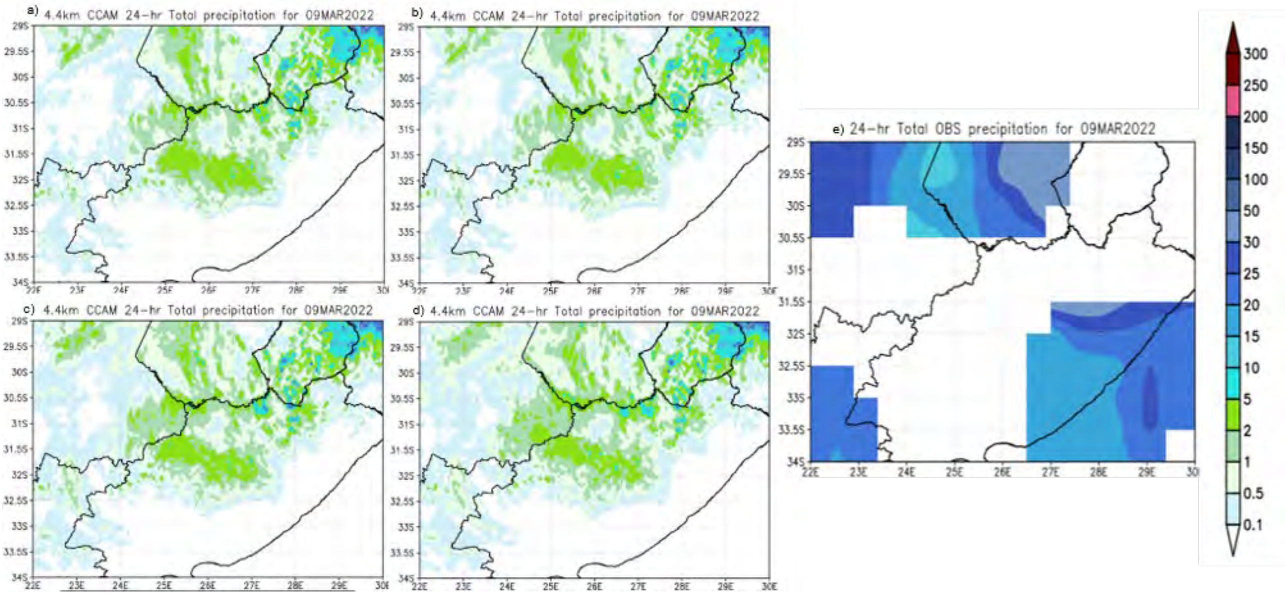

Figure 5.24: 24-hour accumulated rainfall for a severe rainfall event that was observed over the Eastern Cape on 09 March 2022: a) CCAM simulations with bcon=0.04, b) CCAM simulations with bcon=0.1, c) CCAM simulations with bcon=0.2, d) CCAM simulations with bcon=0.5 and e) ground observations.

b) Diurnal cycle of precipitation

In Figure 5.25, the diurnal cycle of areal average rainfall for the domain shown in Figure 5.22 is illustrated. The peak of rainfall was observed between 15 GMT and 18 GMT. The model simulations, however, initiated rainfall earlier than observed, and these simulated rainfall events lasted longer than the observed ones. Across all runs, the parameterized component of total precipitation made a minimal contribution, except for simulations with bcon=0.1. Additionally, during the period of maximum observed rainfall, simulations with bcon=0.1 exhibited the least bias and the highest contribution from parameterized rainfall.

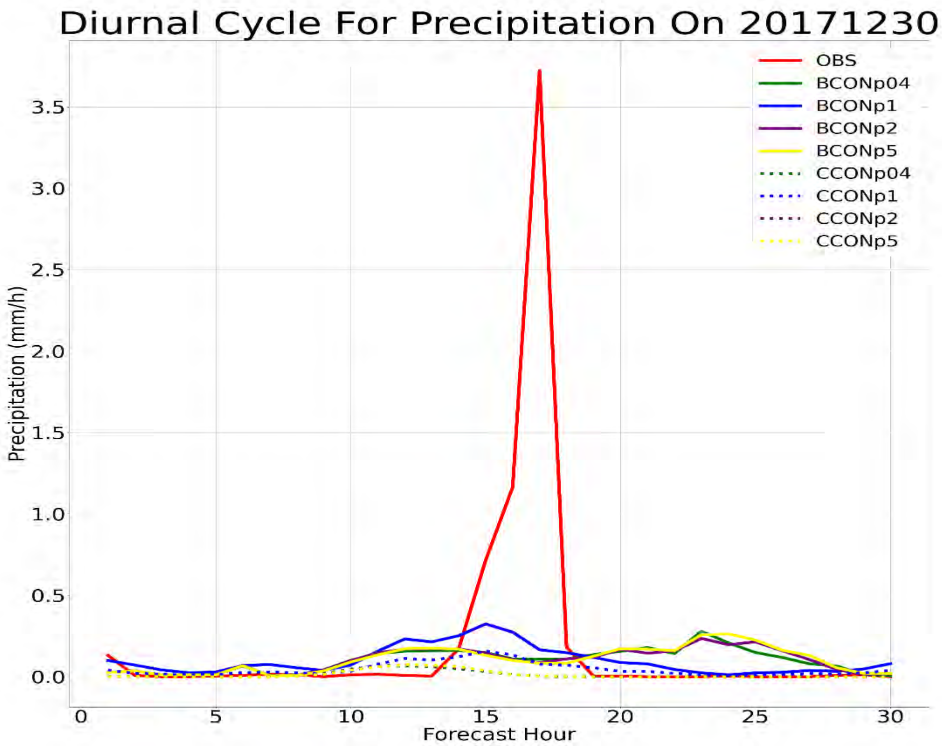

Figure 5.25: Diurnal cycle for precipitation over Gauteng and surrounding areas as shown in Figure 5.22 on 30 December 2017: a) CCAM simulations with bcon=0.04, b) CCAM simulations with bcon=0.1, c) CCAM simulations with bcon=0.2, d) CCAM simulations with bcon=0.5 and ground observations (red). Dotted lines are the respective parameterized rainfall components of each model run.

The case of 12 November 2019 shows evidence that the model simulations generated considerably less precipitation compared to the observed values (Fig. 5.26). Notably, parameterized rainfall components also made minimal contributions, even during periods when the model simulations indicated substantial rainfall.

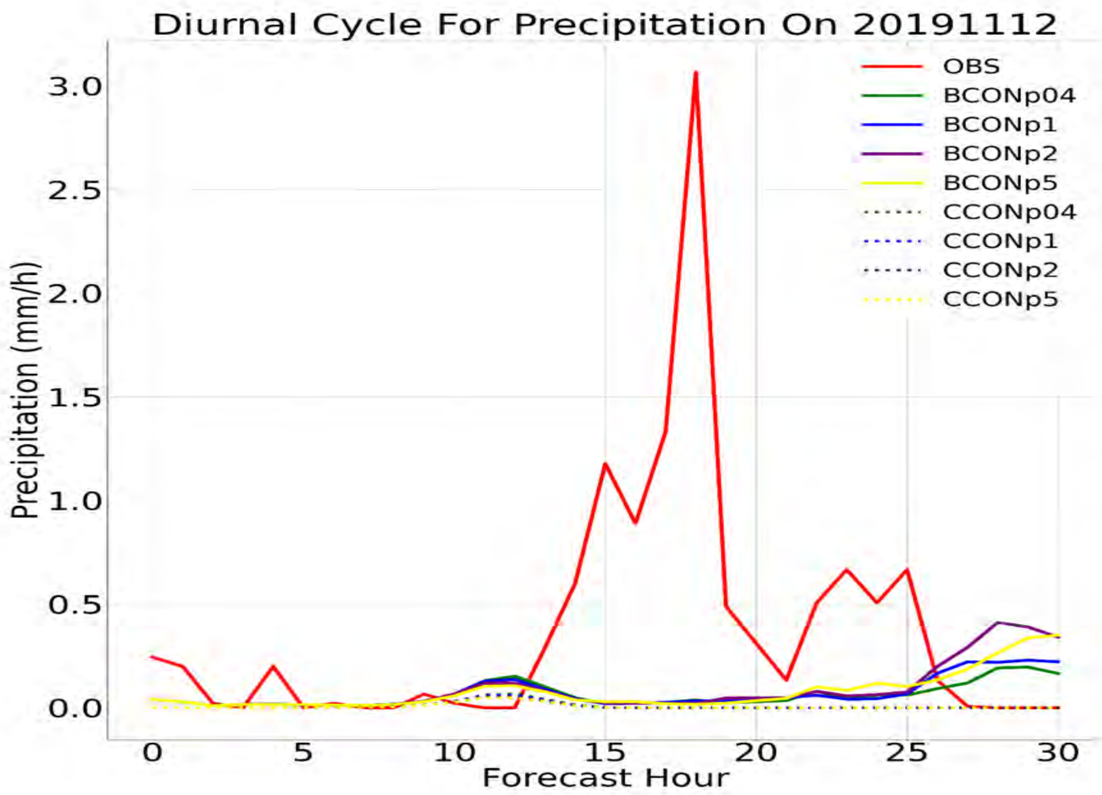

Figure 5.26: Diurnal cycle for precipitation over the domain shown in Figure 5.23 on 12 November 2019: a) CCAM simulations with bcon=0.04, b) CCAM simulations with bcon=0.1, c) CCAM simulations with bcon=0.2, d) CCAM simulations with bcon=0.5 and ground observations (red). Dotted lines are the respective parameterized rainfall components of each model run.

Examining the diurnal cycle for 9 March 2022, it is apparent that a substantial nocturnal rainfall event, which the model failed to capture, commenced after 22 GMT. However, earlier in the period, the models did simulate light rainfall. It is worth noting that the model simulations overlapped, making differences less apparent.

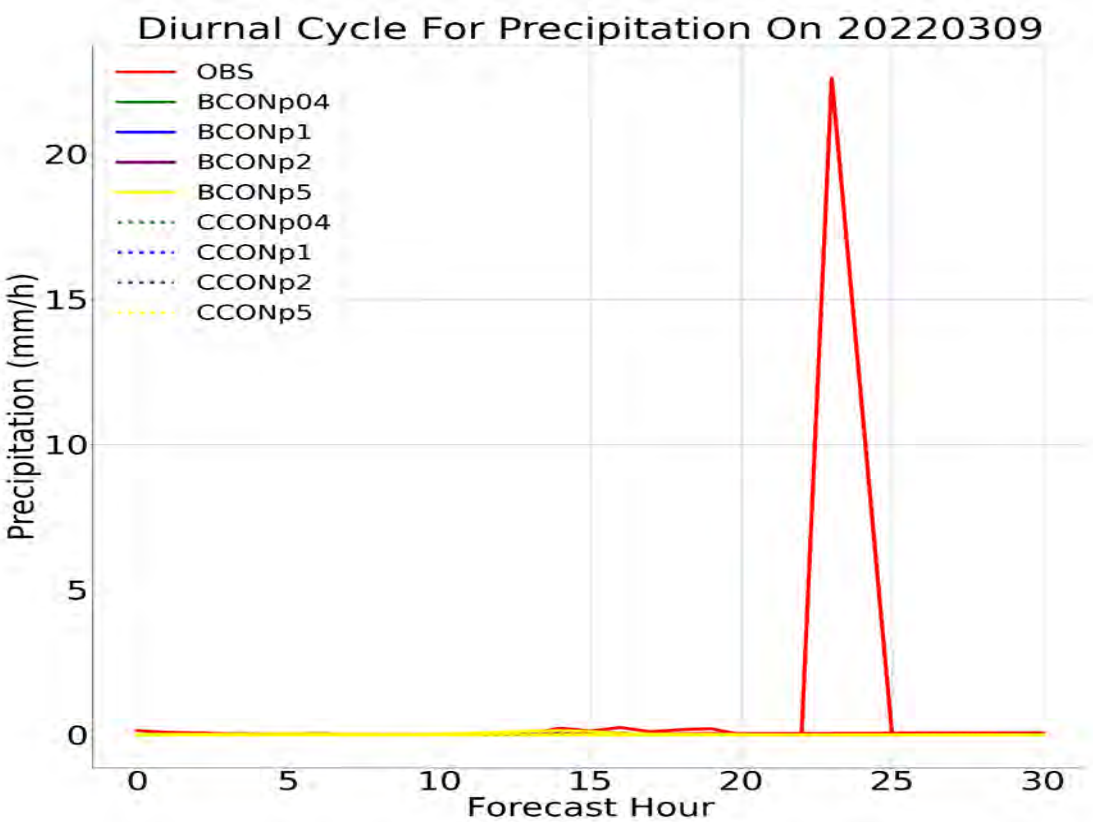

Figure 5.27: Diurnal cycle for precipitation over the Eastern Cape as depicted in Figure 5.24 on 09 March 2022: a) CCAM simulations with bcon=0.04, b) CCAM simulations with bcon=0.1, c) CCAM simulations with bcon=0.2, d) CCAM simulations with bcon=0.5 and ground observations (red). Dotted lines are the respective parameterized rainfall components of each model run.

c) Skill scores: FSS and FBS

Figures 5.28 and 5.29 reveal that the model simulations with varying bcon values generally exhibit similar FBS and FSS. Higher FBS and FSS values are observed for lower rainfall thresholds, specifically 0.1 mm, 0.5 mm, and 1 mm. However, the assessment scores for thresholds of 5 mm, 10 mm, and 20 mm demonstrate low to no skill in accurately locating rainfall events.

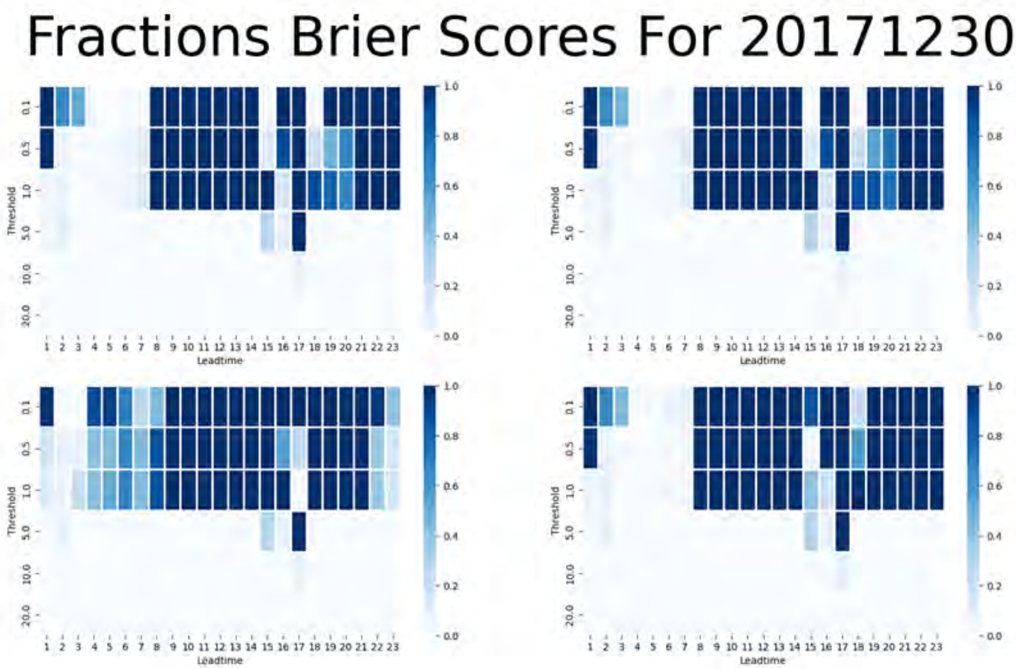

Figure 5.28: Heatmaps for FBS for hourly precipitation>0.1mm, 5 mm, 10mm and 20 mm over the domain shown in Figure 5.22 on 30 December 2017. The different simulations of the CCAM, namely, CCAM simulations with bcon=0.04 (top-left), CCAM simulations with bcon=0.1 (top-right), CCAM simulations with bcon=0.2 (bottom-left), CCAM simulations with bcon=0.5 (bottom-right) were evaluated against ground observations.

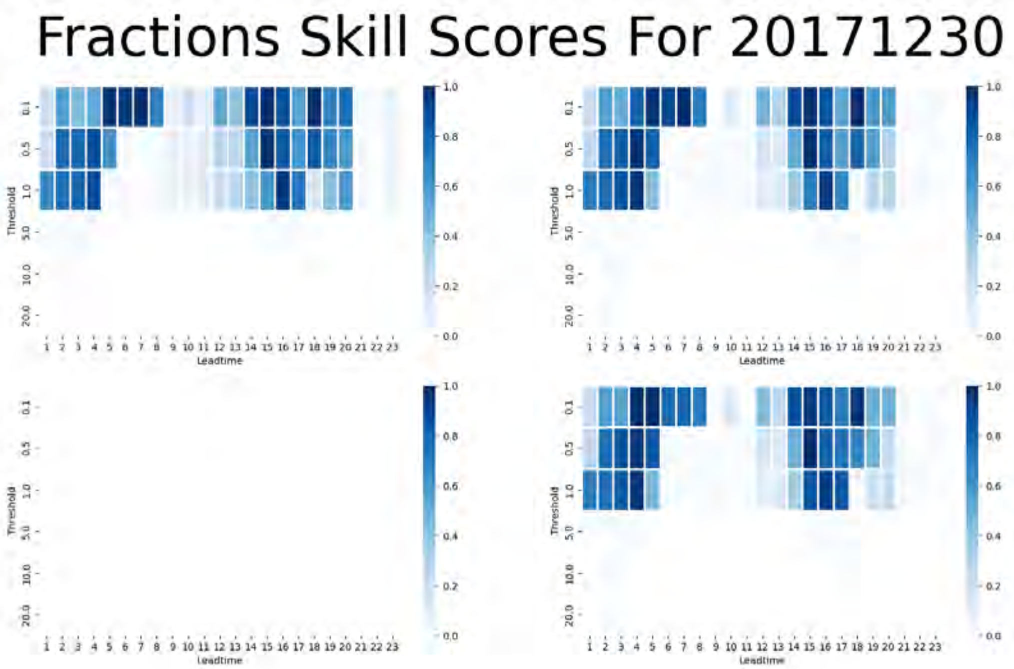

Figure 5.29: Heatmaps for FSS for hourly precipitation>0.1mm, 5 mm, 10mm and 20 mm over the domain shown in Figure 5.22 on 30 December 2017. The different simulations of the CCAM, namely, CCAM simulations with bcon=0.04 (top-left), CCAM simulations with bcon=0.1 (top-right), CCAM simulations with

bcon=0.2 (bottom-left), CCAM simulations with bcon=0.5 (bottom-right) were evaluated against ground observations.

FBS exhibits remarkable similarity across all model runs for the case of 12 November 2022, demonstrating higher values for lower thresholds and lower values for higher thresholds (Fig. 5.30). Heatmaps representing FSS indicate a lack of skill for CCAM simulations with bcon=0.2, as depicted in Figure 5.31. However, the remaining simulations display minimal skill and occasional usefulness.

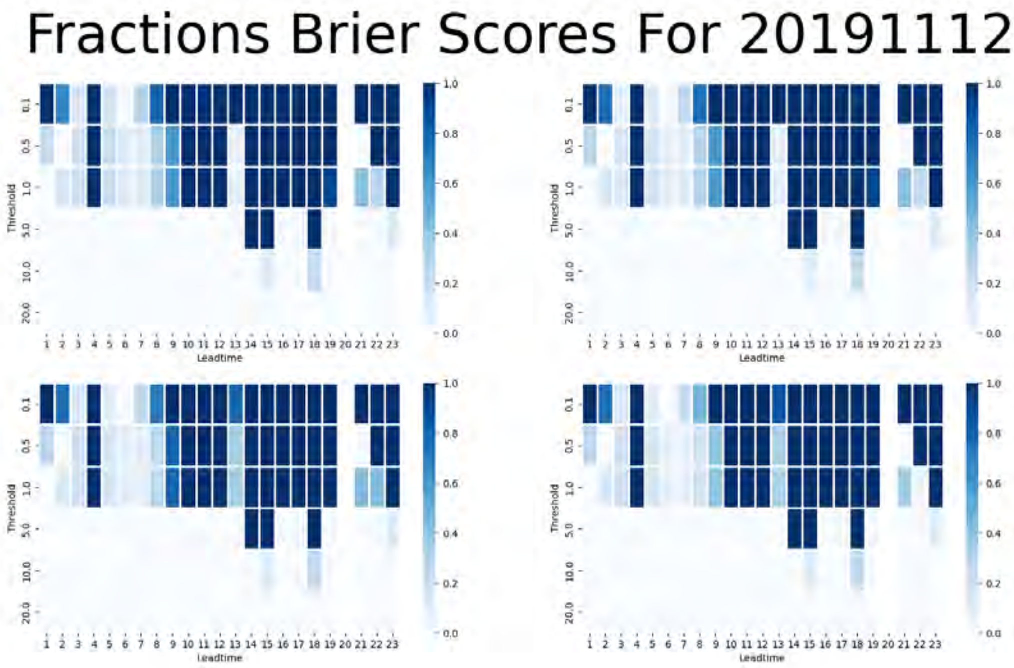

Figure 5.30: Heatmaps for BFS for hourly precipitation >0.1 mm, 5 mm, 10 mm and 20 mm over the area depicted in Figure 5.23 on 12 November 2019. The different simulations of the CCAM, namely, CCAM simulations with bcon=0.04 (top-left), CCAM simulations with bcon=0.1 (top-right), CCAM simulations with bcon=0.2 (bottom-left), CCAM simulations with bcon=0.5 (bottom-right) were evaluated against ground observations.

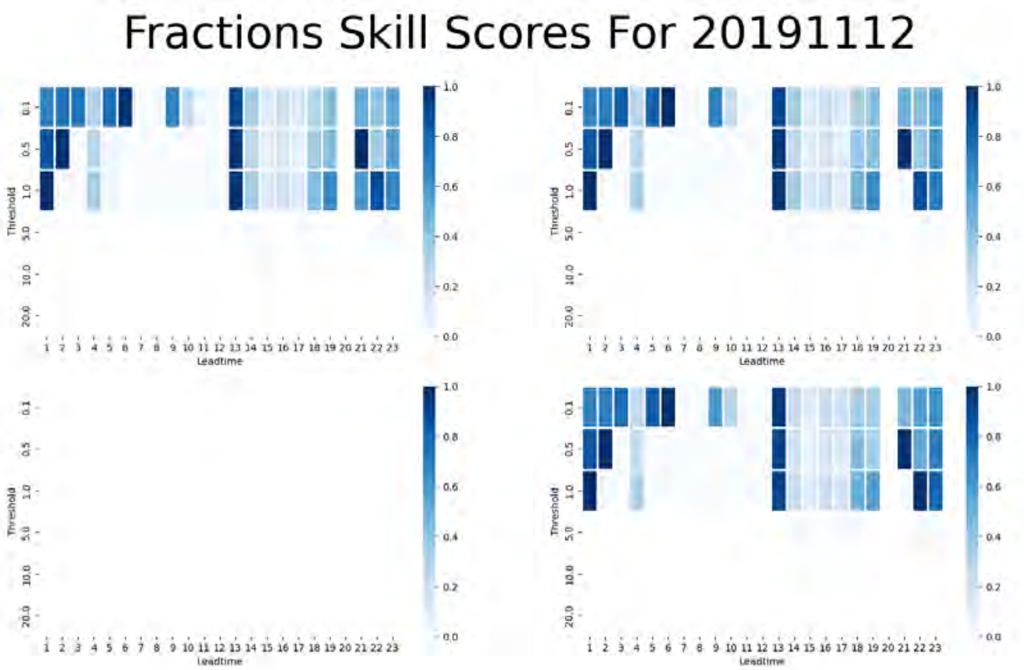

Figure 5.31: Heatmaps for FSS for hourly precipitation >0.1mm, 5 mm, 10 mm and 20 mm over the area depicted in Figure 5.23 on 12 November 2019. The different simulations of the CCAM, namely, CCAM simulations with bcon=0.04 (top-left), CCAM simulations with bcon=0.1 (top-right), CCAM simulations with bcon=0.2 (bottom-left), CCAM simulations with bcon=0.5 (bottom-right) were evaluated against ground observations.

Clear distinctions among the FBS of various simulations for parts of the Eastern Cape on March 9, 2022, are not obvious (Figure 5.32). In general, the values are notably high for lower thresholds and lower for higher threshold values, except for 23 GMT, when all thresholds exhibited an FBS of 1, indicating low resolution, reliability, and high uncertainty. Similar to the case of 12 November 2019, simulations with bcon=0.2 demonstrated no skill across all thresholds throughout the day (Figure 5.33). However, the remaining simulations displayed comparable skill scores with slight variations. At 22 GMT, only simulations with bcon=0.04 exhibited some usefulness for lower threshold values, while all simulations showed no skill at 23 GMT for all thresholds.

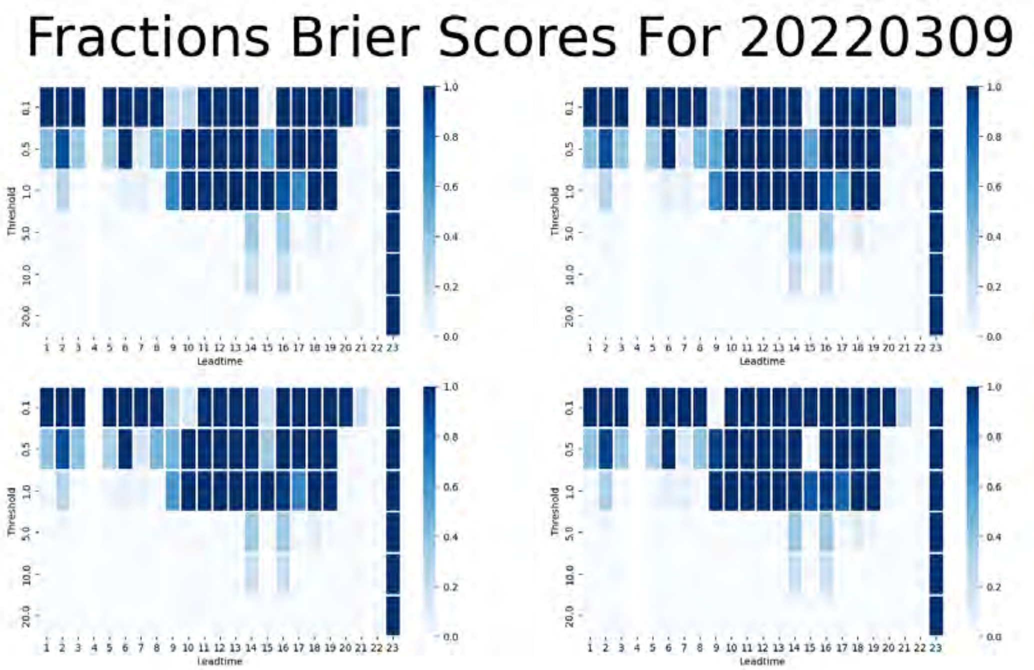

Figure 5.32: Heatmaps for FBS for hourly precipitation>0.1mm, 5 mm, 10mm and 20 mm for the domain depicted in Figure 5.24 on 09 March 2022. The different simulations of the CCAM, namely, CCAM simulations with bcon=0.04 (top-left), CCAM simulations with bcon=0.1 (top-right), CCAM simulations with bcon=0.2 (bottom-left), CCAM simulations with bcon=0.5 (bottom-right) were evaluated against ground observations.

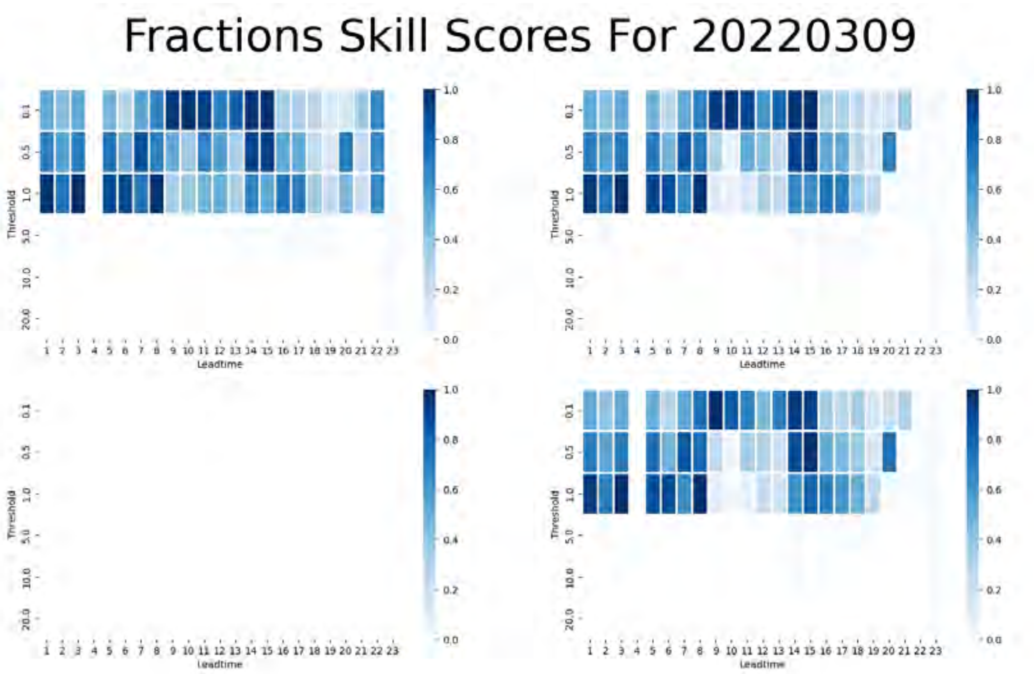

Figure 5.33: Heatmaps for FSS for hourly precipitation>0.1mm, 5 mm, 10mm and 20 mm for the domain depicted in Figure 5.24 on 09 March 2022. The different simulations of the CCAM, namely, CCAM simulations

with bcon=0.04 (top-left), CCAM simulations with bcon=0.1 (top-right), CCAM simulations with bcon=0.2 (bottom-left), CCAM simulations with bcon=0.5 (bottom-right) were evaluated against ground observations.

d) Profiles for related parameters

Profiles depicting convective or related parameters for 30 December 2017 over a specific point of interest, i.e. Lenasia, Soweto [Latitude: -26.36, Longitude: 27.77], are presented in Figures 5.34 to 5.36. While all simulations simulated similar cloud bases and cloud tops, CCAM simulations with bcon=0.1 exhibited the most long-lived clouds (Figure 5.34). These simulations also showed lower maximum CAPE during the initial stages of the event compared to the other runs. However, both the maximum CAPE and the duration of the event increased at later stages, even when the other runs did not simulate such conditions. Notably, during the period when rainfall maxima were observed (between 15 GMT and 18 GMT), simulations with bcon=0.1 displayed the highest latent heat flux and the lowest sensible heat flux. Fluxes for all runs were relatively consistent for the remainder of the period.

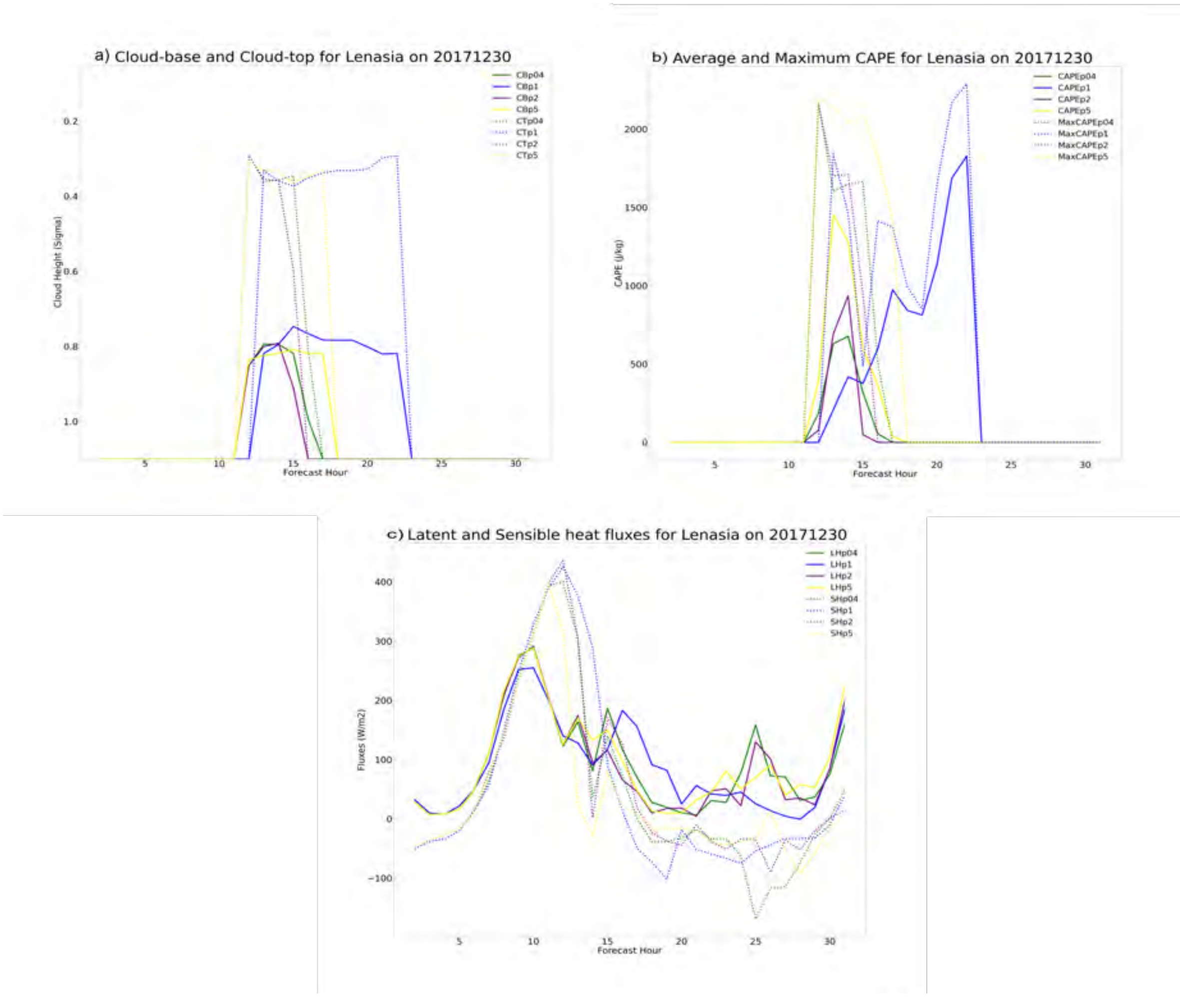

Figure 5.34: Time series for Lenasia, Soweto [Latitude: -26.36, Longitude: 27.77] on 30 December 2017: a) cloud-base (CB) and cloud-top (CT), Average (CAPE) and maximum CAPE (MaxCAPE), and c) latent (LH) and sensible heat fluxes (SH). CCAM simulations with bcon=0.04 (green), CCAM simulations with bcon=0.1 (blue), CCAM simulations with bcon=0.2 (purple) and CCAM simulations with bcon=0.5 (yellow).

Vertical profiles for temperature were the same for all the runs and selected hours over Soweto (Fig. 5.35 – 5.36). Likewise, relative humidity profiles followed a similar pattern, though simulations with bcon=0.1 occasionally showed higher humidity than the rest of the runs. Omega profiles in Figures 5.35 -5.36 depict that each simulation retains its own pattern with no correlation to the other runs. Simulations with bcon=0.1 had cloud fraction amounts, while the counterparts simulated none. Moreover, the mixing ratios for all the simulations and selected hours had the same pattern with slight differences in amounts.

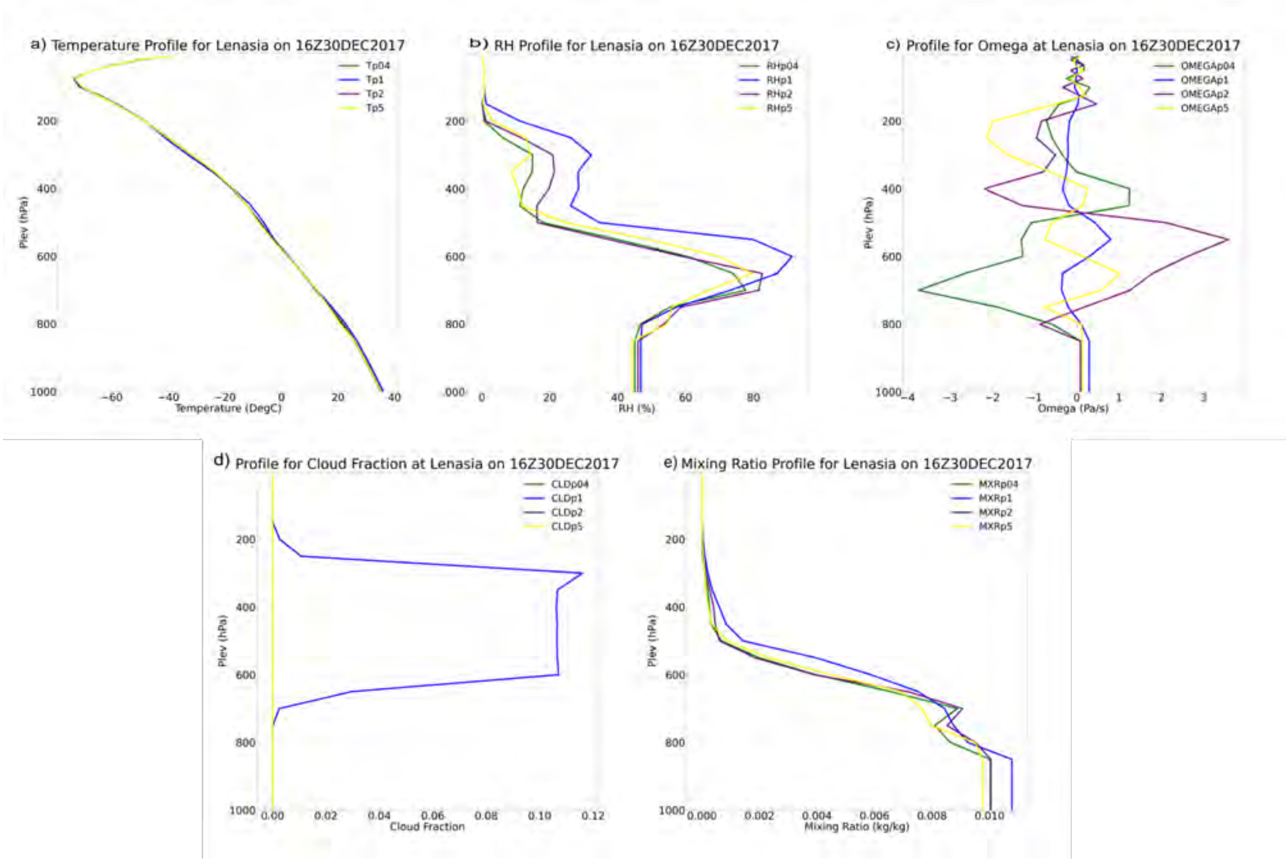

Figure 5.35: Vertical profiles for Lenasia, Soweto [Latitude: -26.36, Longitude: 27.77] at 16 GMT on 30 December 2017: (a) temperature, (b) Relative humidity (RH), (c) omega, (d) total cloud fraction and (e) mixing ratio. CCAM simulations with bcon=0.04 (green), CCAM simulations with bcon=0.1 (blue), CCAM simulations with bcon=0.2 (purple) and CCAM simulations with bcon=0.5 (yellow).

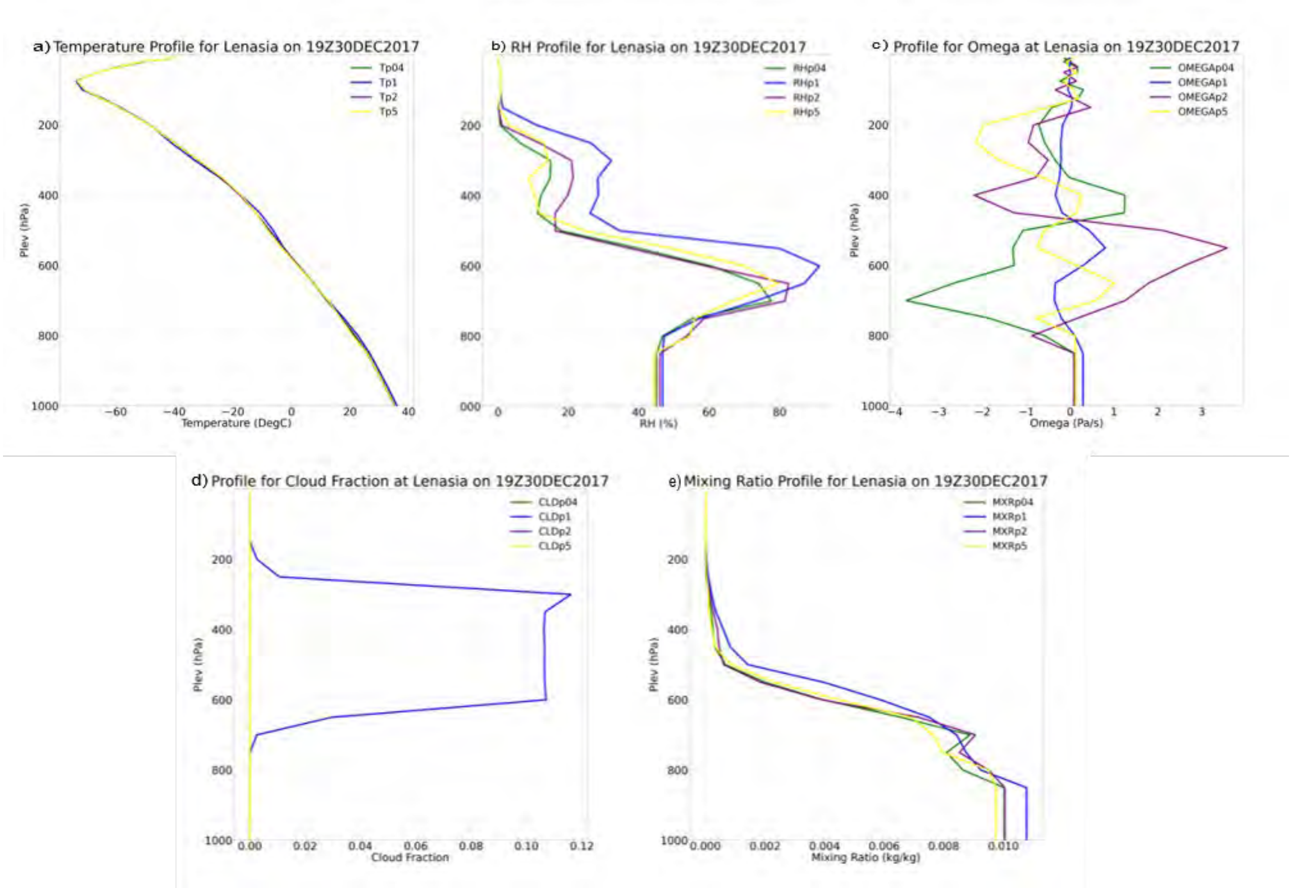

Figure 5.36: Vertical profiles for Lenasia, Soweto [Latitude: -26.36, Longitude: 27.77] at 19 GMT on 30 December 2017: (a) temperature, (b) Relative humidity (RH), (c) omega, (d) total cloud fraction and (e) mixing ratio. CCAM simulations with bcon=0.04 (green), CCAM simulations with bcon=0.1 (blue), CCAM simulations with bcon=0.2 (purple) and CCAM simulations with bcon=0.5 (yellow).

Figures 5.37 to 5.39 show profiles of convective or related parameters over a specific grid point, i.e., over New Hannover, KwaZulu-Natal [Latitude: -29.36, Longitude: 30.52]. The model runs depict similar (with slight variations) cloud bases, cloud tops, CAPE, average CAPE, latent heat flux, and sensible heat flux throughout the day (Fig. 5.37). The vertical profiles for temperature were consistent for all runs and selected hours (Fig. 5.38–5.39). Similarly, the relative humidity profiles followed a uniform pattern across all runs. The omega profile displayed close similarities among simulations for the selected hours. Furthermore, the model simulations yielded similar cloud cover fractions for all runs, and the mixing ratios exhibited a consistent pattern across all simulations and selected hours.

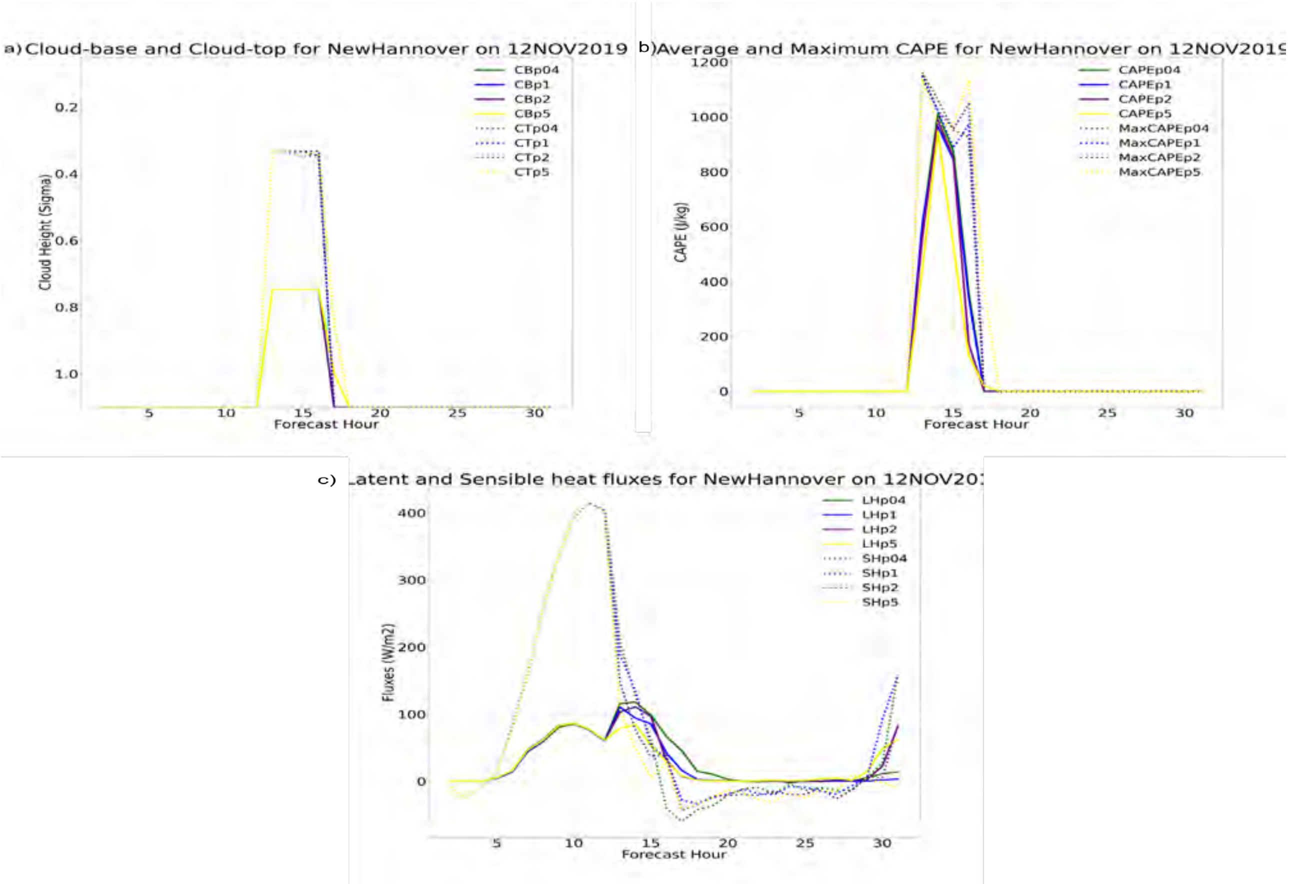

Figure 5.37: Time series for New Hannover, KwaZulu-Natal [Latitude: -29.36, Longitude: 30.52] on 12 November 2019: a) cloud-base (CB) and cloud-top (CT), Average (CAPE) and maximum CAPE (MaxCAPE), and c) latent (LH) and sensible heat fluxes (SH). CCAM simulations with bcon=0.04 (green), CCAM simulations with bcon=0.1 (blue), CCAM simulations with bcon=0.2 (purple) and CCAM simulations with bcon=0.5 (yellow).

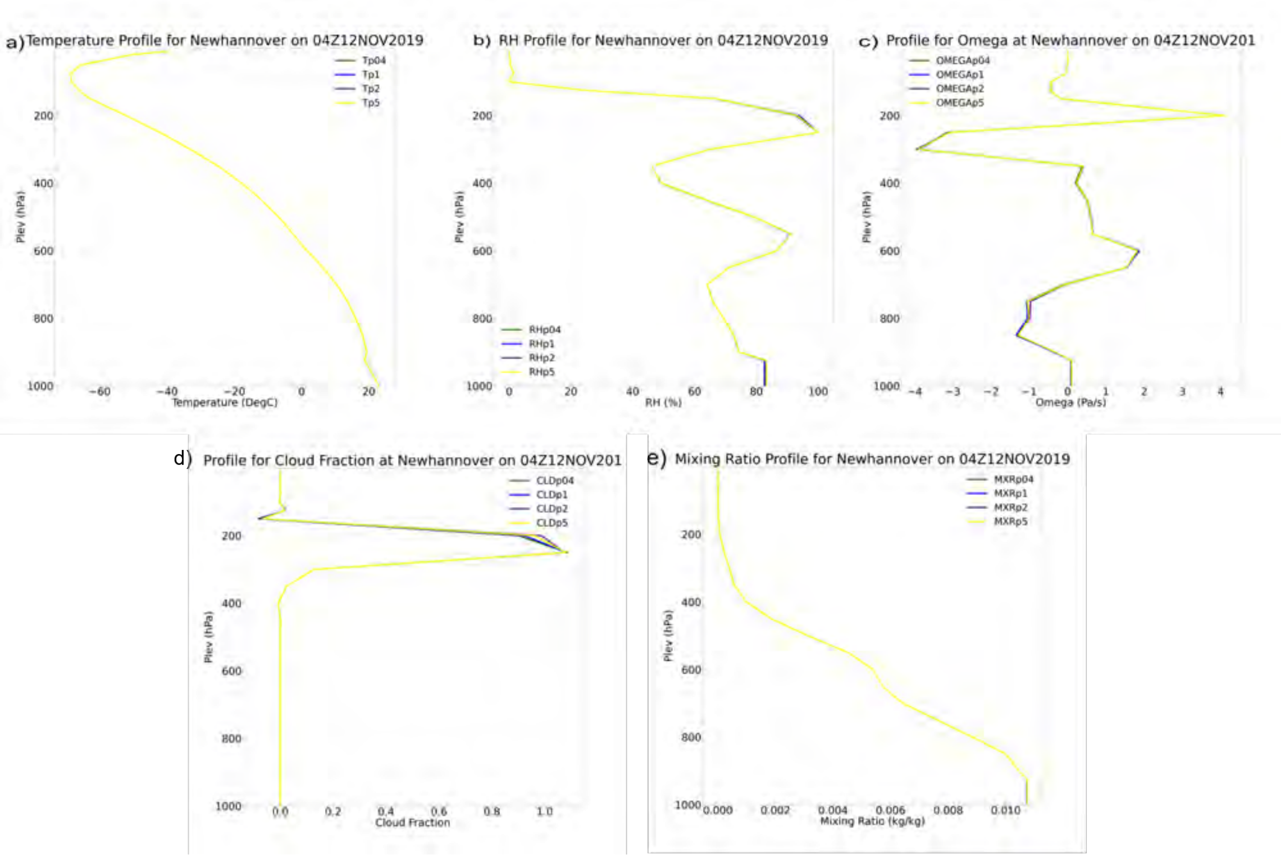

Figure 5.38: Vertical profiles for New Hannover, KwaZulu-Natal [Latitude: -29.36, Longitude: 30.52] at 04 GMT on 12 November 2019: (a) temperature, (b) Relative humidity (RH), (c) omega, (d) total cloud fraction and (e) mixing ratio. CCAM simulations with bcon=0.04 (green), CCAM simulations with bcon=0.1 (blue), CCAM simulations with bcon=0.2 (purple) and CCAM simulations with bcon=0.5 (yellow).

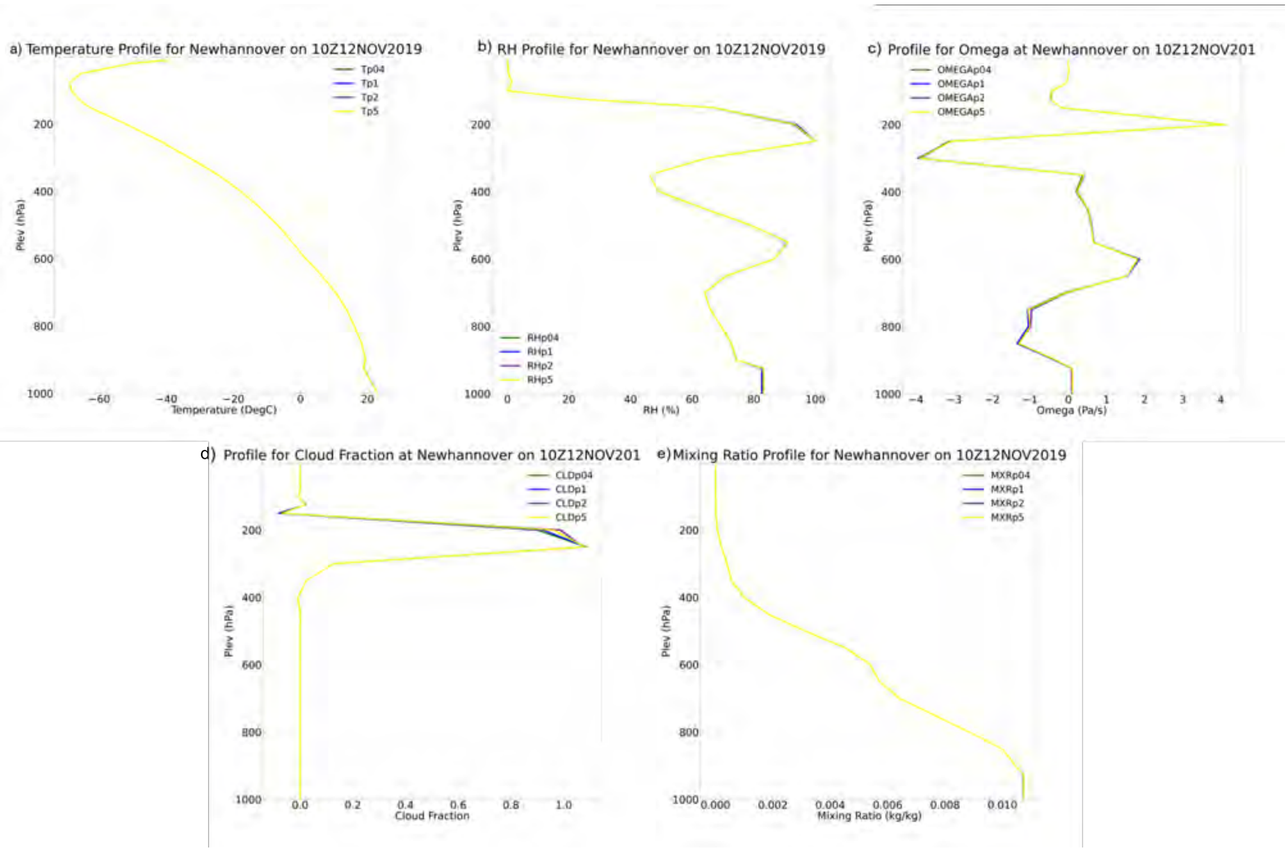

Figure 5.39: Vertical profiles for New Hannover, KwaZulu-Natal [Latitude: -29.36, Longitude: 30.52] at 10 GMT on 12 November 2019: (a) temperature, (b) Relative humidity (RH), (c) omega, (d) total cloud fraction and (e) mixing ratio. CCAM simulations with bcon=0.04 (green), CCAM simulations with bcon=0.1 (blue), CCAM simulations with bcon=0.2 (purple) and CCAM simulations with bcon=0.5 (yellow).

Figures 5.40 to 5.42 present profiles of convective or related parameters over a specific grid point, i.e. Queenstown [Latitude: -31.89, Longitude: 26.84] on 9 March 2022. The model runs show an absence of clouds: cloud bases and cloud tops were absent, with similar maximum CAPE, very little average CAPE, and comparable latent heat flux and sensible heat flux throughout the day (Fig. 5.40). Vertical profiles for selected hours over Queenstown, are illustrated in Fig. 5.41 to 5.42. Both temperature and relative humidity profiles followed a consistent pattern across all runs. The omega profile demonstrated close similarities among the simulations for the selected hours. Furthermore, the model simulations simulated equivalent amounts of cloud cover fractions for all runs, and the mixing ratios show similar patterns across all simulations and selected hours.

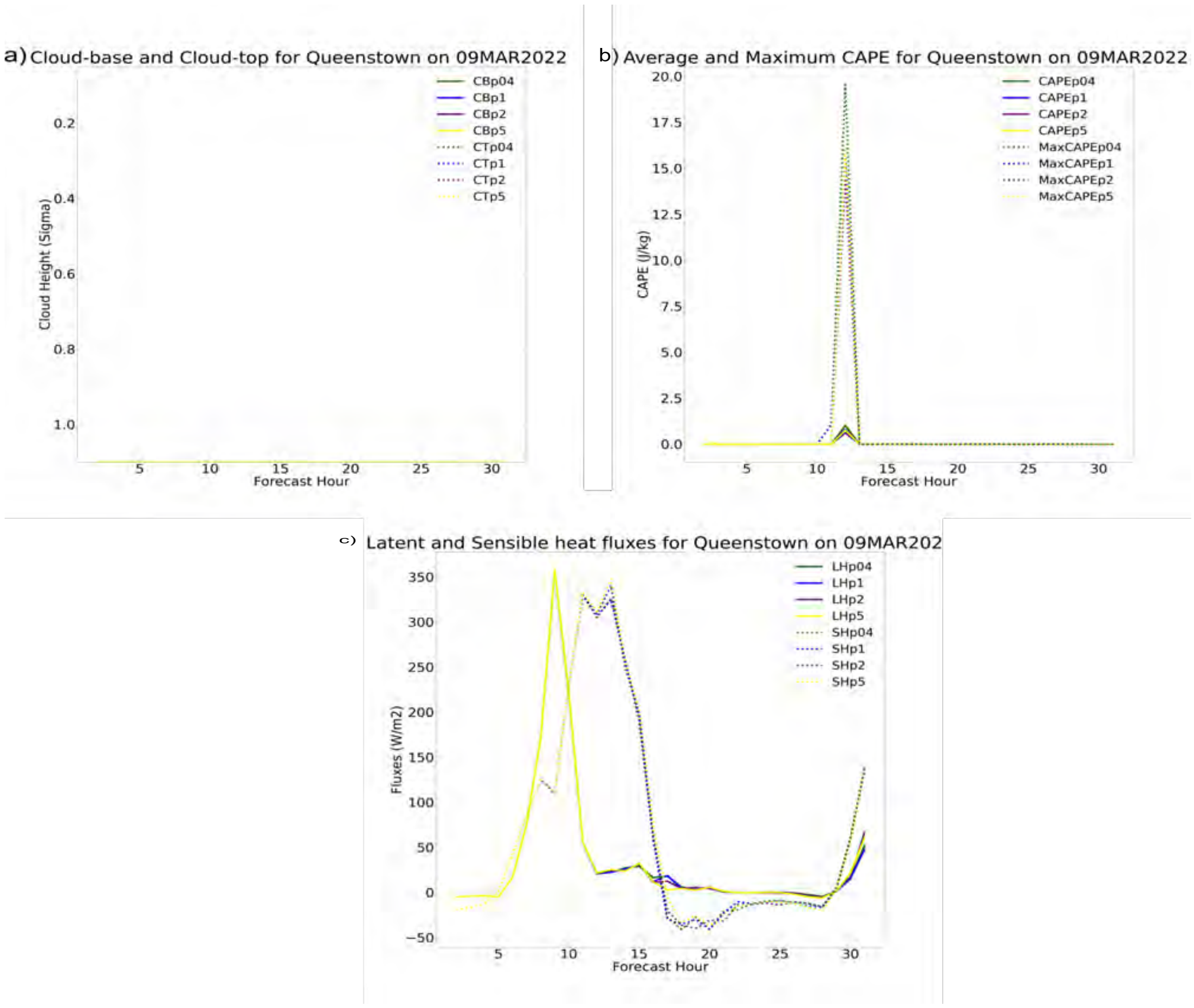

Figure 5.40: Time series for Queenstown, Eastern Cape [Latitude: -31.89, Longitude: 26.84] on 09 March 2022: a) cloud-base (CB) and cloud-top (CT), Average (CAPE) and maximum CAPE (MaxCAPE), and c) latent (LH) and sensible heat fluxes (SH). CCAM simulations with bcon=0.04 (green), CCAM simulations with bcon=0.1 (blue), CCAM simulations with bcon=0.2 (purple) and CCAM simulations with bcon=0.5 (yellow).

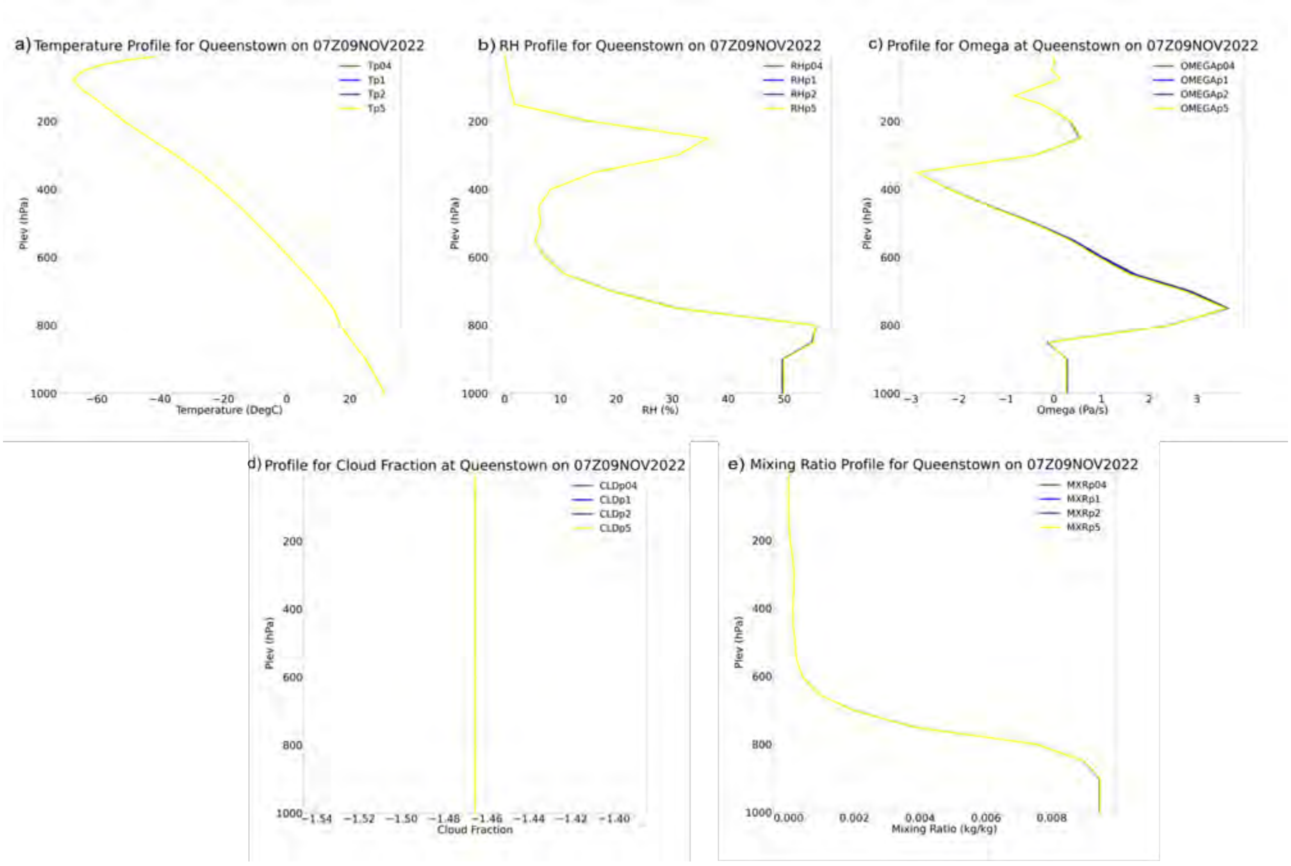

Figure 5.41: Vertical profiles for Queenstown, Eastern Cape [Latitude: -31.89, Longitude: 26.84] at 07 GMT, 09 March 2022: (a) temperature, (b) Relative humidity (RH), (c) omega, (d) total cloud fraction and (e) mixing ratio. CCAM simulations with bcon=0.04 (green), CCAM simulations with bcon=0.1 (blue), CCAM simulations with bcon=0.2 (purple) and CCAM simulations with bcon=0.5 (yellow).

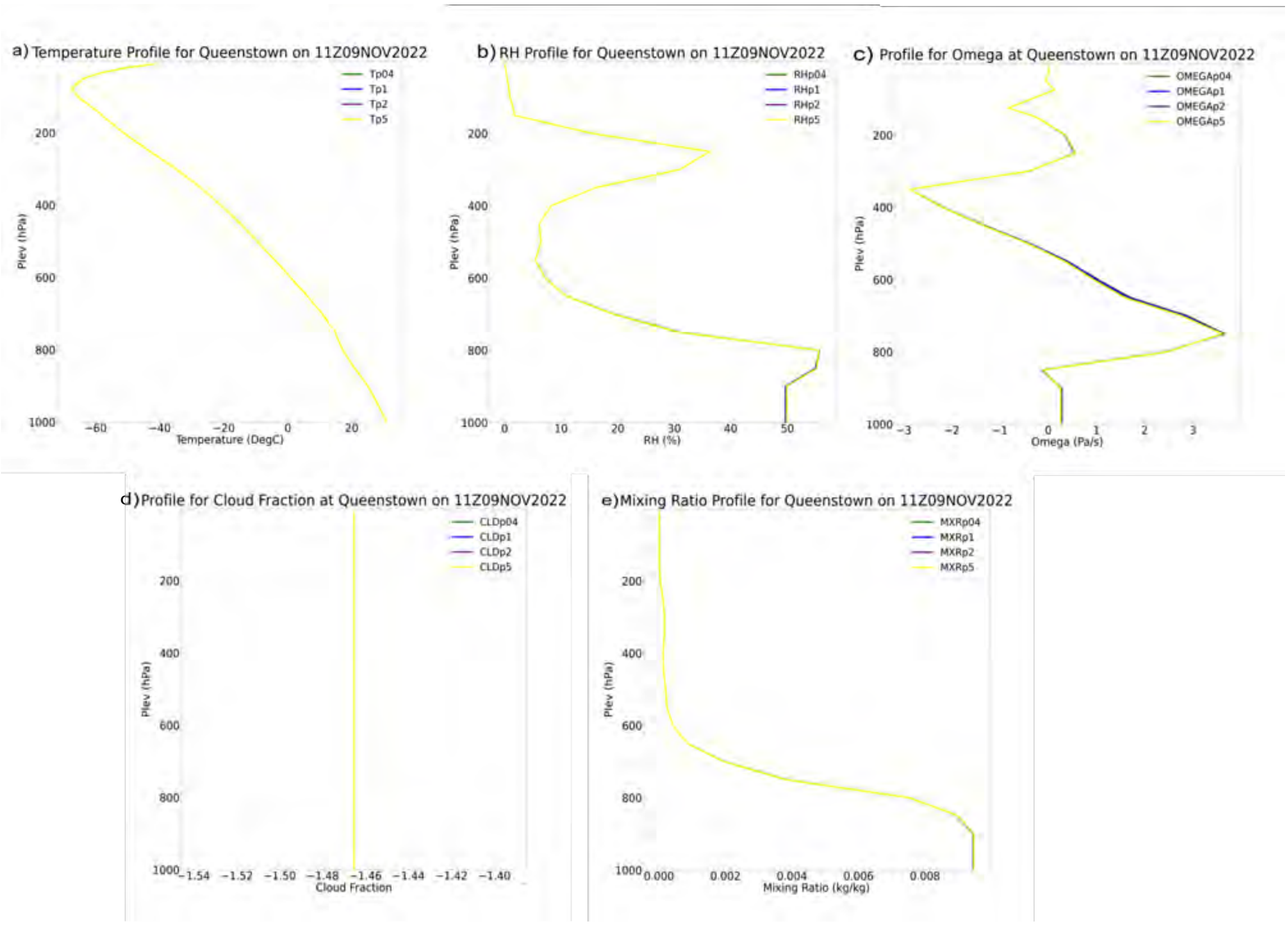

Figure 5.42: Vertical profiles for Queenstown, Eastern Cape [Latitude: -31.89, Longitude: 26.84] at 11 GMT, 09 March 2022: (a) temperature, (b) Relative humidity (RH), (c) omega, (d) total cloud fraction and (e) mixing ratio. CCAM simulations with bcon=0.04 (green), CCAM simulations with bcon=0.1 (blue), CCAM simulations with bcon=0.2 (purple) and CCAM simulations with bcon=0.5 (yellow).

5.3.3 Testing the scale-awareness of the cumulus scheme

At the beginning of July 2023, the project team visited a team of model developers for training, discussions and future planning for the model development project. The visit included presentations where the project team showed their progress in terms of research done on the CCAM. The model developers advised on a new directive, which included research on the model scale-awareness and testing the model spin-up. This section of the report outlines the research done on the scale-awareness of the Convjlm cumulus scheme.

A study by Chow et al., (2019) states that increasing resolution in atmospheric modelling, from 1 km to finer scales, improves the representation of complex topography and allows for the resolution of phenomena such as valley-mountain circulations and moist convection. However, it also highlights challenges, such as the need for new numerical techniques at 10 m resolution and potential issues with convective cell sizes at finer scales, emphasising the importance of studying the transition from coarse to fine scales. Scale-awareness in the model convection schemes were introduced to address the grey zone of convection, aiming to reduce the parameterized component towards zero as the model grid length approaches zero (Mulovhedzi et al., 2023). Further, this design ensures that the convection scheme gradually deactivates at higher resolutions, where convective transport processes are no longer too small compared to the model grid size.

The scale-awareness within the CCAM convjlm is defined by the code depicted in Figure 5.43. Five grid-scales were selected to understand the scale-awareness and how the model simulates convection and related parameters at different scales: 25 km, 10 km, 6 km, 3 km and 1 km. The outcome should outline (1) at what resolution does convection completely switch off, (2) How does the model accuracy and skill change with resolution and (3) how can the these and other results be used to develop the model code.

```
      if(tied_over>0.)then   ! e.g. 2626. gives  tied_b then tied_a  2600 to get old -26
        tied_b=int(tied_over/100.)  !    **** main value ***
        tied_a=tied_over-100.*tied_b
      else  ! for new -ve formula                              JLM 2307
        tied_b=-int(abs(tied_over)/100.)  !    **** main value *** JLM 2307
        tied_a=abs(tied_over)-100.*abs(tied_b) !                JLM 2307
      endif

then further down

      if(tied_b<0.)then  ! newer 2019 scheme    JLM 2307
        do iq=1,ifull
         summ=ds/(em(iq)*10000.)  ! Dec 2019  based on 10km
         factr(iq)=factr(iq)*                              !   JLM 2307 just for itn=1
     &               abs(tied_b)*summ**2/(1.+abs(tied_b)*summ**2)  !   JLM 2307 just for itn=1
        enddo
      elseif (tied_b>0.)then ! previous jlm scheme  JLM 2307
        do iq=1,ifull
         summ=ds/(em(iq)*208498.)
         factr(iq)=factr(iq)*(1.+tied_b)*summ/(1.+tied_b*summ)  ! defined just for itn=1
        enddo
      endif   ! (tied_b<0.) .. else ..
```

Figure 5.43: CCAM convjlm code to describe the scale-awareness of the scheme.

The same cases as in the previous section were used for this investigation, however, only the thunderstorm case associated with a tornado over Lenasia, Soweto on 30 December 2017 is analysed. A peer-review paper related to this was published in the South African Society for Atmospheric Sciences (SASAS) conference proceedings. In addition, a case of severe flooding that was observed over parts of Limpopo, including Thohoyandou, on 2 February 2021 and a thunderstorm that was witnessed over Suncity, North-West province on 15 December 2018 were analysed. Another paper, with a more extensive analysis is due for submission at a reputable international journal. For validation of spatial rainfall distribution, 0.25 x 0.25° resolution ground observations, 30-minute time-interval 0.1x 0.1°. The IMERG (Huffman et al., 2019) and Modern-Era Retrospective analysis for Research and Applications version 2 (MERRA-2), hereafter ERA5-Land rainfall data (GMAO, 2015) were displayed. Time series and vertical profiles for convective and related variables were analysed in addition to that.

5.3.3.1 Case study analysis

a) Spatial analysis of 24-hour accumulated precipitation.

The distribution of 24-hour accumulated rainfall from 06 GMT to 05 GMT on 30 - 31 December 2017, indicates that, at course resolutions, the model predicts rainfall across a broader area, with spatial coverage diminishing as resolution increases (Fig. 5.44 a-e). The coarser resolutions show misplacement and underestimation of the observed intense rainfall in Lenasia, Soweto (Fig. 5.44 c-e), in comparison to ground observations (Fig. 5.44f), IMERG rainfall (Fig 5.44f) and ERA5-Land rainfall (Fig 5.44g). Conversely, the runs at 1 km and 3 km resolutions accurately locate the event, with the 3 km resolution run performing particularly well (Fig. 5.44 a-b).

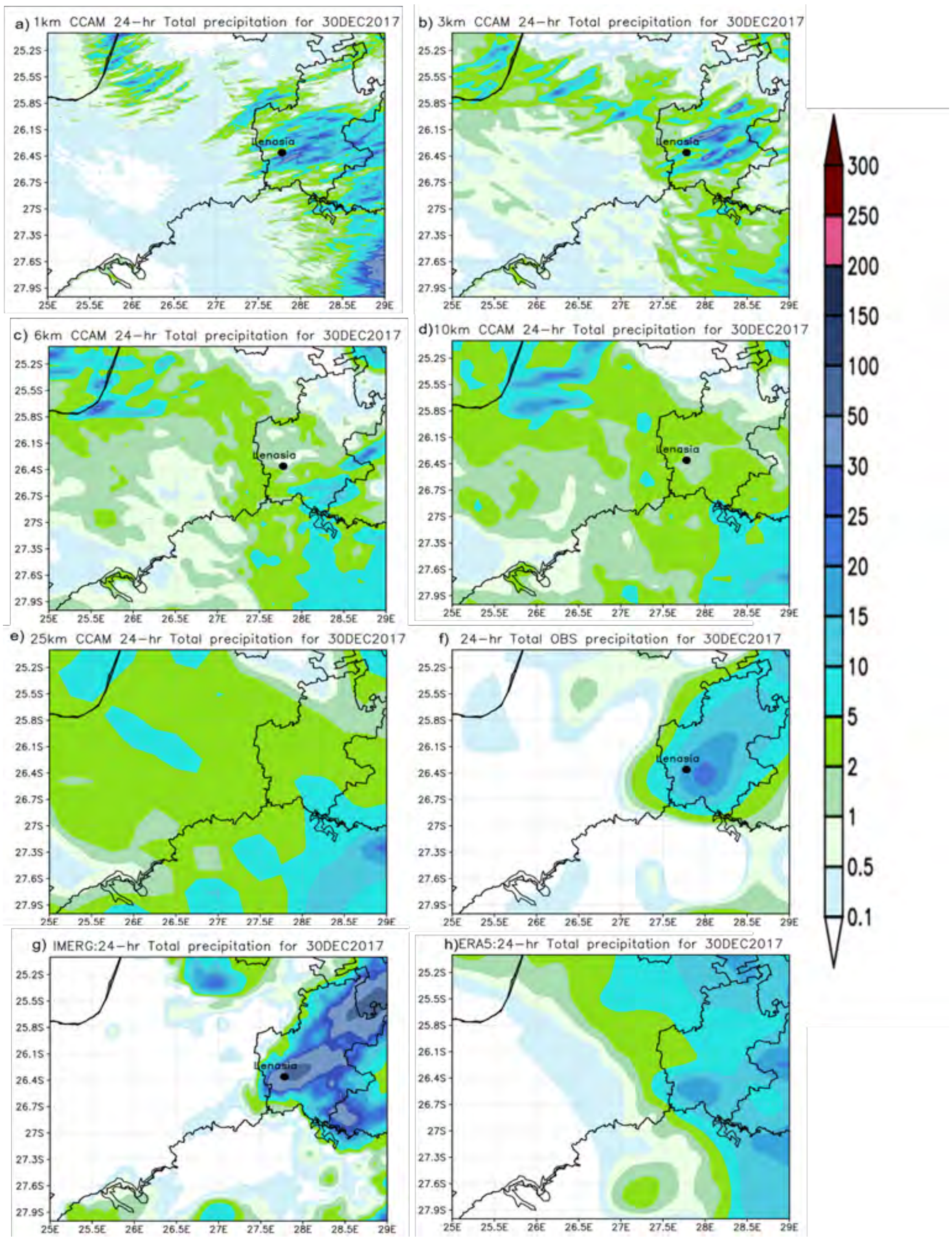

Figure 5.44: 24-hour accumulated rainfall for the thunderstorm event that was witnessed over Gauteng and surrounding areas in the afternoon of 30 December 2017: a) 1 km CCAM simulations, b) 3 km CCAM

simulations, c) 6 km CCAM simulations, d) 10 km CCAM simulations, e) 25 km CCAM simulations, e) ground observations, f) IMERG rainfall and g) ERA5-Land rainfall.

The case of widespread heavy rainfall on 1 February 2021 was severe over most of Limpopo province and Mpumalanga, as shown in Figure 5.45f. Rainfall estimations from IMERG and ERA5 simulated even more intense rainfall (Figure 5.45 g-h). However, the model only captured severe rainfall over the southwestern parts of the domain in Figure 5.45, while the rest of the domain is mainly dominated by light rain (Figure 5.45 a-e). Moreover, the model runs misplace the severe rainfall, with the 3 km run showing the most intense and largest spatial coverage thereof. The 1 km run comes second, while the intensity and spatial coverage diminishes with increasing resolution for the rest of the model runs.

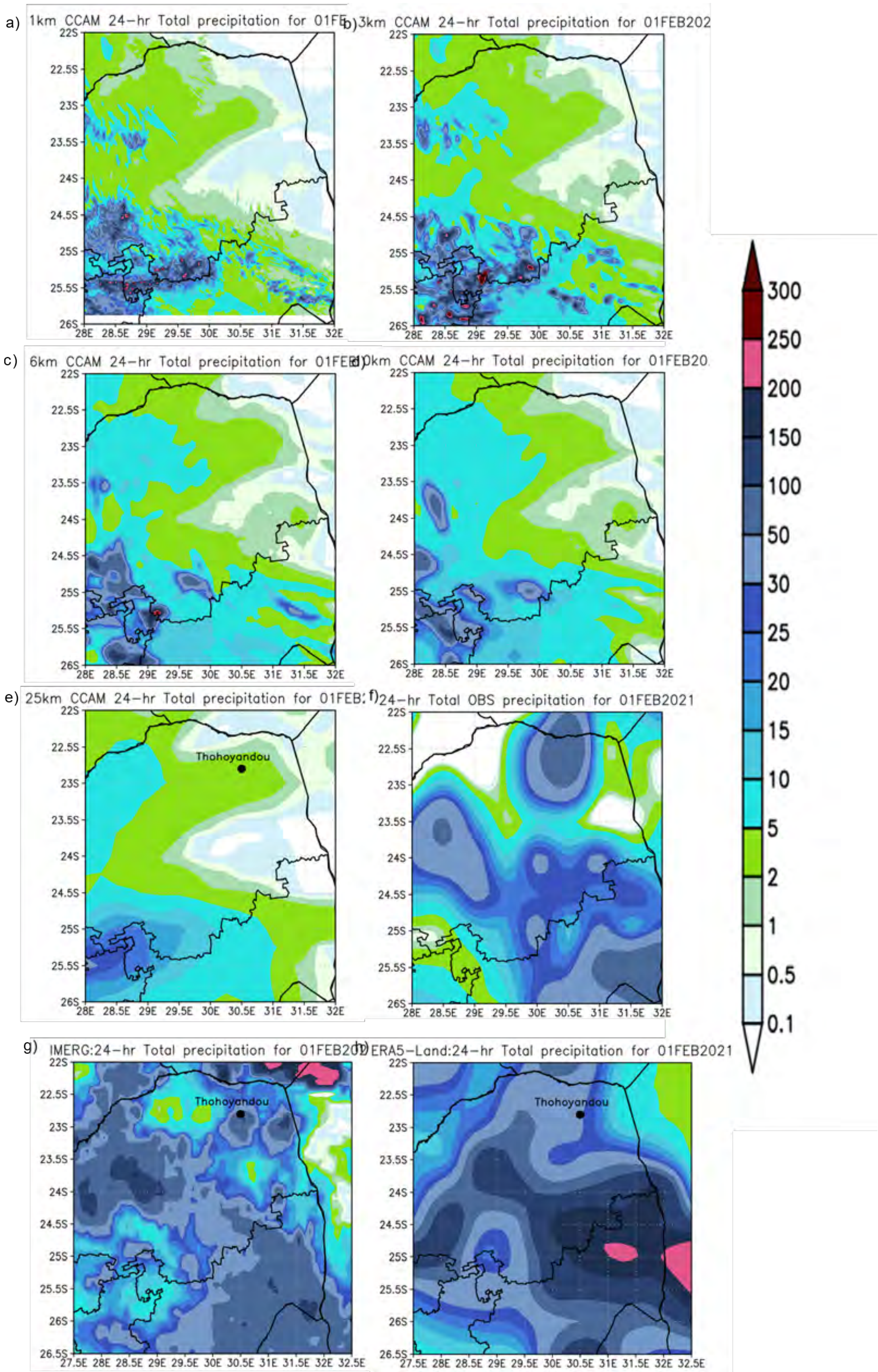

Figure 5.45: 24-hour accumulated rainfall for the thunderstorm event that was witnessed over Limpopo and surrounding areas on 2 February 2021: a) 1 km CCAM simulations, b) 3 km CCAM simulations, c) 6 km CCAM simulations, d) 10 km CCAM simulations, e) 25 km CCAM simulations, e) ground observations, f) IMERG rainfall and g) ERA5-Land rainfall.

The model lagged behind in terms of simulating the rainfall that was observed on 15 December 2018 (Fig. 5.46). The 1 km run (Fig. 5.46a) captured severe rainfall further south-west of the observed (Fig. 5.46f) and IMERG (Fig. 5.46g). The 3 km run simulated the most widespread rainfall, which also reached closest to Sun City, where severe damage due to this event was observed (Fig. 5.46b). The simulations at coarse resolutions exhibited minimal precipitation (Figure 5.46c-e). It is noteworthy that the ERA5 displaced severe rainfall from its actual observed location.

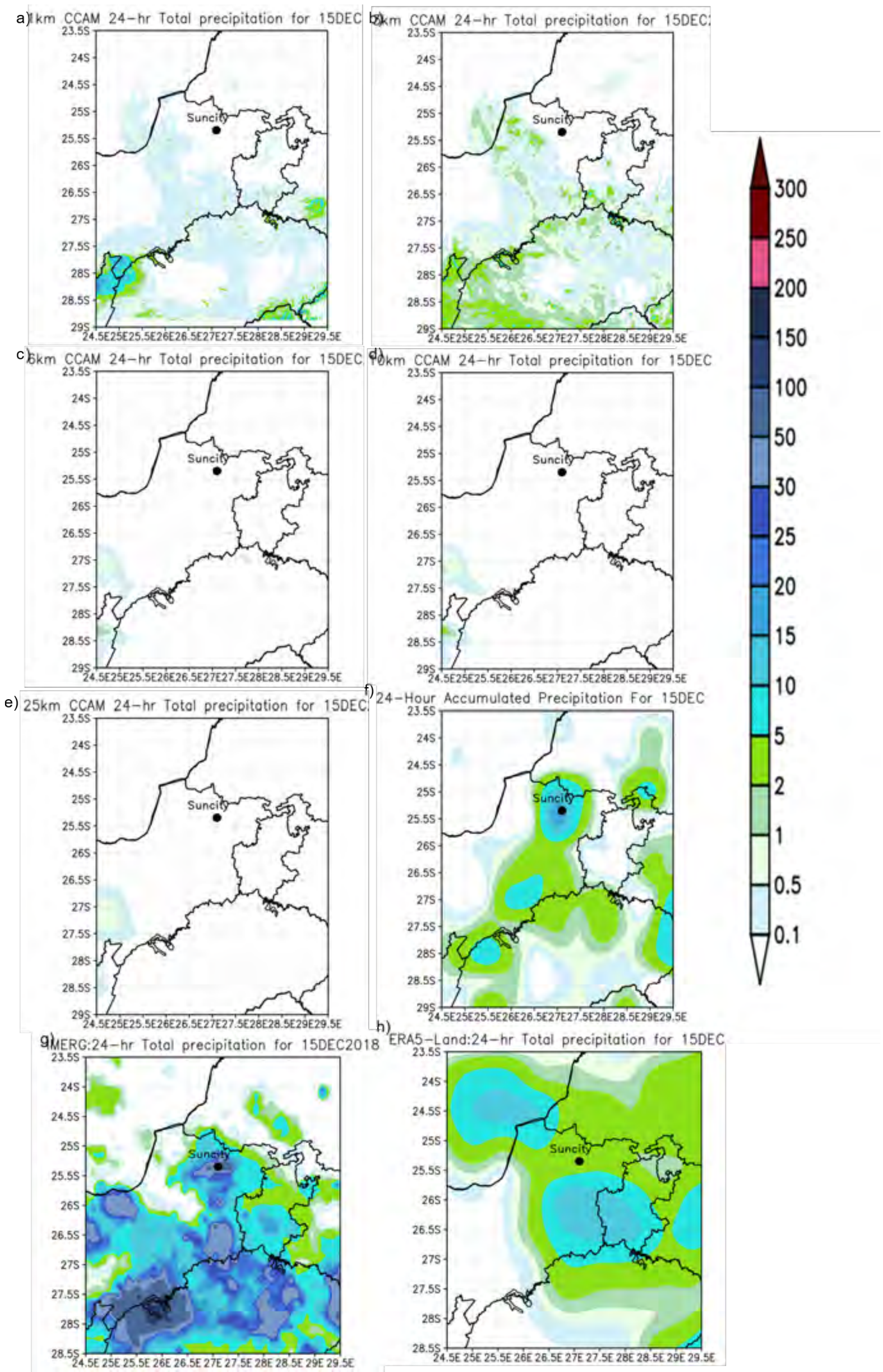

Figure 5.46: 24-hour accumulated rainfall for the thunderstorm event that was witnessed over parts of the North-West province on 15 December 2018: a) 1 km CCAM simulations, b) 3 km CCAM simulations, c) 6 km

CCAM simulations, d) 10 km CCAM simulations, e) 25 km CCAM simulations, e) ground observations, f) IMERG rainfall and g) ERA5-Land rainfall.

b) Time series for areal average rainfall

The diurnal cycle for 30 December 2017 was discussed in Mulovhedzi et al. (2023). The figure revealed that the CCAM initiates rainfall much earlier than the observed, with varying peak simulation times among runs. Additionally, at coarse resolutions, the scale-aware convection scheme, Convjlm, produces large, parameterized rainfall amounts, reducing the areal average bias of total rainfall. However, as resolution increases, the scheme diminishes its parameterized rainfall contribution, leading to an increased bias in total precipitation, particularly evident at 1 km grid length.

The diurnal cycle for 1 February 2021 (for domain shown in Figure 5.45) depicts that the CCAM was able to capture the heavy rainfall onset around 10 GMT for all the runs except the 25 km one (Figure 5.47). This rainfall was mainly simulated by the microphysics scheme as the convective rainfall had trivial contribution. Moreover, the 3 km run showed the highest accuracy: it closely captured the peak at 17 GMT and had a second peak later at forecast hour 25. It was followed closely by the 1 km run.

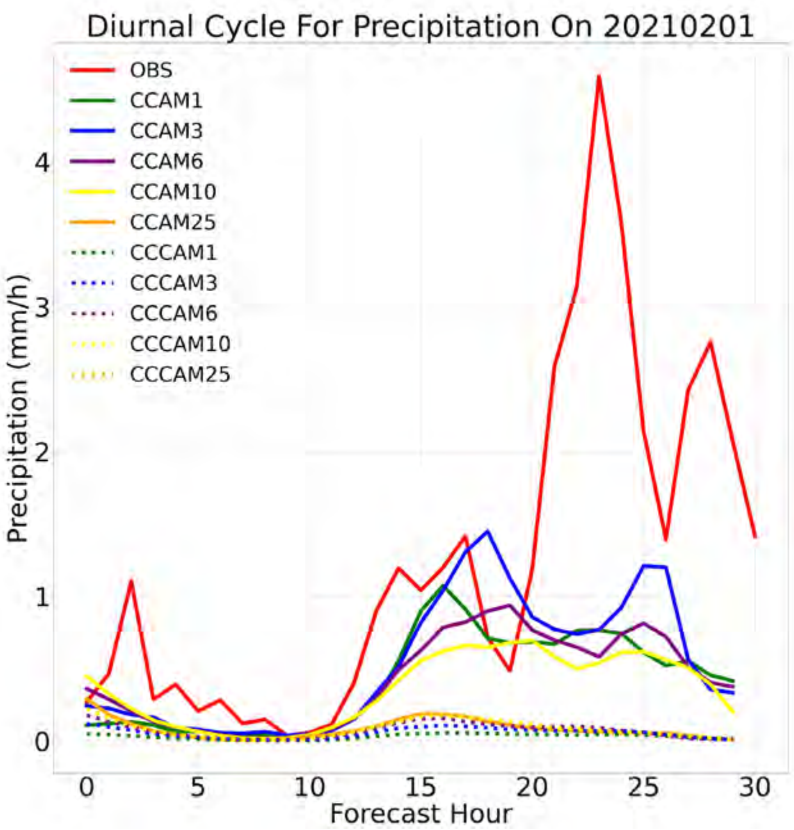

Figure 5.47: Diurnal cycle for areal averaged hourly precipitation for the domain depicted in Figure 5.45 on 2 February 2021. The ground observations (red solid line), the CCAM run at 1 km (green solid line), the CCAM run at 3 km (blue solid line), the CCAM run at 6 km (purple sold line), the CCAM run at 10 km (yellow solid line) and the CCAM run at 25 km (orange solid line). The dotted lines are the respective parameterized rainfall components of the different model runs.

The diurnal cycle for areal average rainfall for the domain depicted in Figure 5.46 for 15 December 2018 agrees with the plot for rainfall distribution (Figure 5.48). Only the 1 km and 3 km runs simulate significant rainfall. The 3 km depicts the most rainfall and captured the peak at 15 GMT. Also, its parameterized rainfall component simulated a high rainfall amount. The 1 km run captured less rainfall, and its parameterized rainfall component was almost switched off. Furthermore, the 1 km run captured a later peak at forecast hour 20.

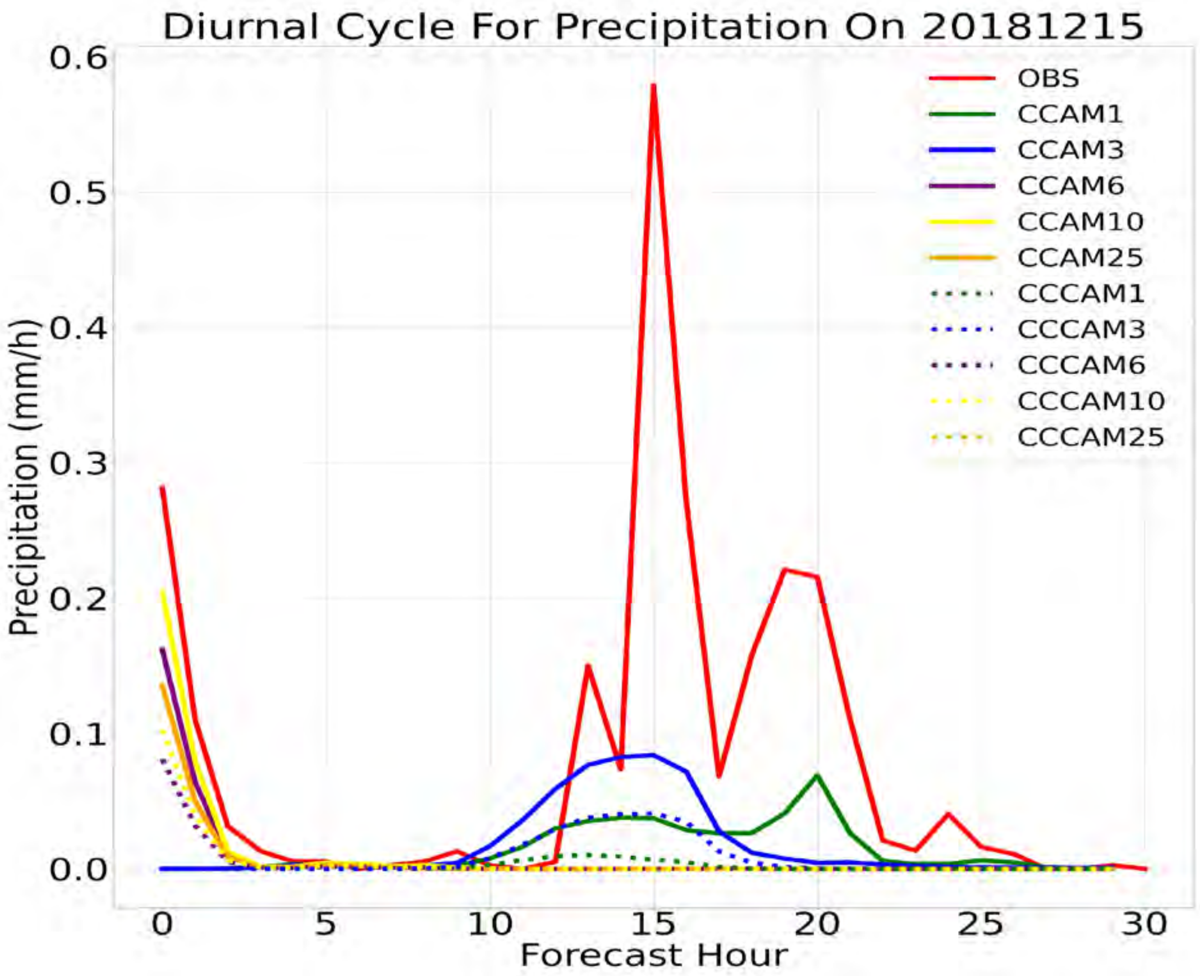

Figure 5.48: Diurnal cycle for areal averaged hourly precipitation for the domain depicted in Figure 5.46 on 15 December 2018. The ground observations (red solid line), the CCAM run at 1 km (green solid line), the CCAM run at 3 km (blue solid line), the CCAM run at 6 km (purple sold line), the CCAM run at 10 km (yellow solid line) and the CCAM run at 25 km (orange solid line). The dotted lines are the respective parameterized rainfall component of the different model runs.

c) Analysis of convective and related processes

Vertical profiles for 30 December 2017 over Lenasia, Soweto, depict relative humidity, temperature, wind speed, and omega for each model run (Figure 5.49) reveal notable distinctions. While the coarser resolution runs exhibit high moisture content near the surface, the 3 km and 1 km resolution runs simulate higher moisture levels at specific periods and levels. Wind patterns also differ: the 1 km and 3 km resolution runs show minimal surface wind throughout the day, while the coarser resolutions display light wind. The 1 km configuration demonstrates wind shear, hinting at tornado formation possibilities, and strong omega fields at 1 km and 3 km resolutions coincide with high humidity, suggesting convective storm activity. Overall, omega profiles vary significantly across runs, emphasising the complexity of their relationship with grid length.

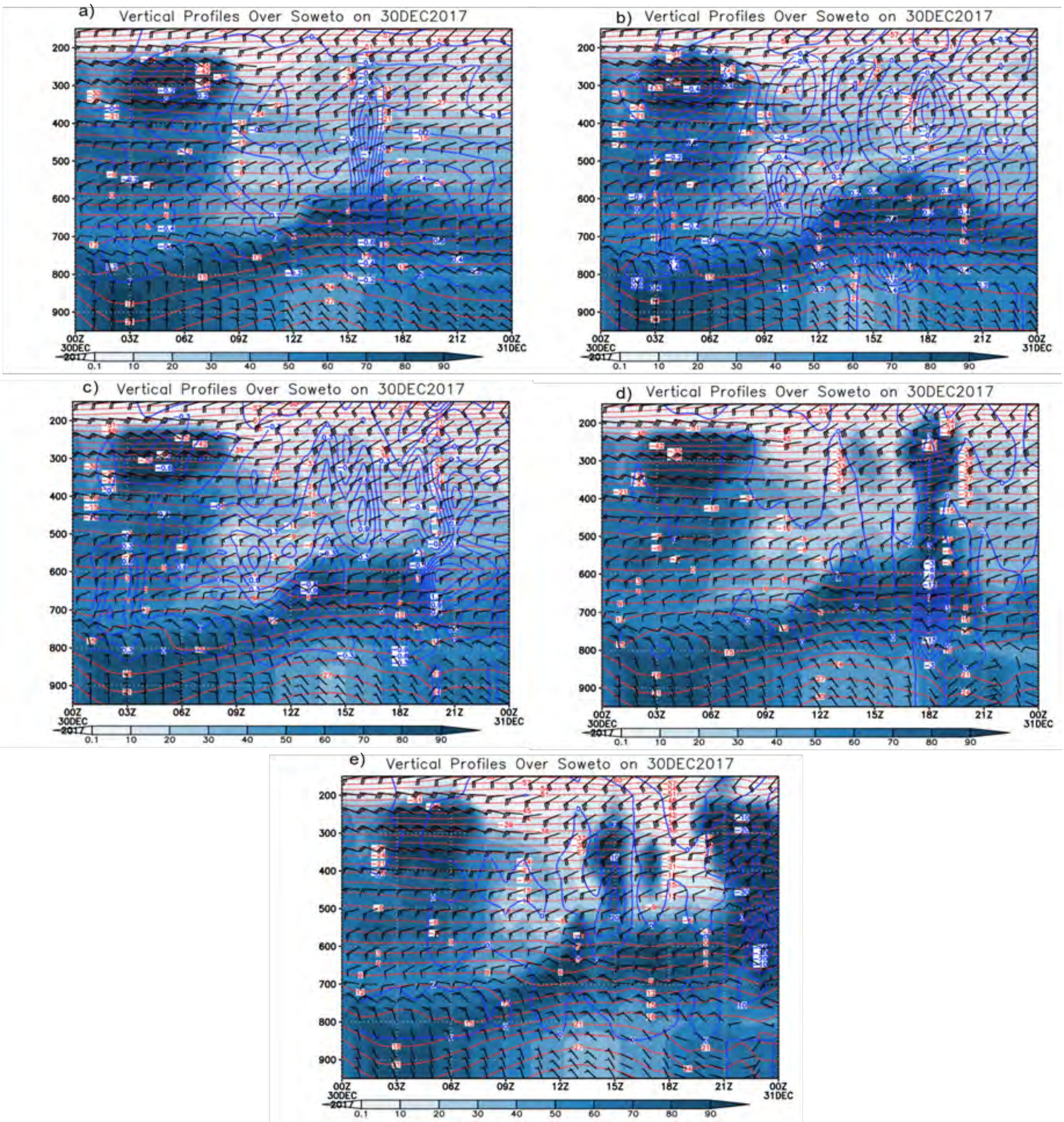

Figure 5.49: Time series for vertical profiles for relative humidity (shaded), temperature (red lines), wind barbs (black) and omega (blue lines). These are for a) 1 km CCAM simulations, b) 3 km CCAM simulations, c) 6 km CCAM simulations, d) 10 km CCAM simulations and e) 25 km CCAM simulations.

Figure 5.50 depicts that for the 3 km CCAM run for Lenasia, Soweto, on 30 December 2017, the model generally released the highest latent heat, followed by the 1 km model run. The coarser resolution runs released the least amount of latent heat. Conversely, a 1 km CCAM run generally releases the most sensible heat. It is followed by the 3 km model run, while the course resolution runs released the least sensible heat.

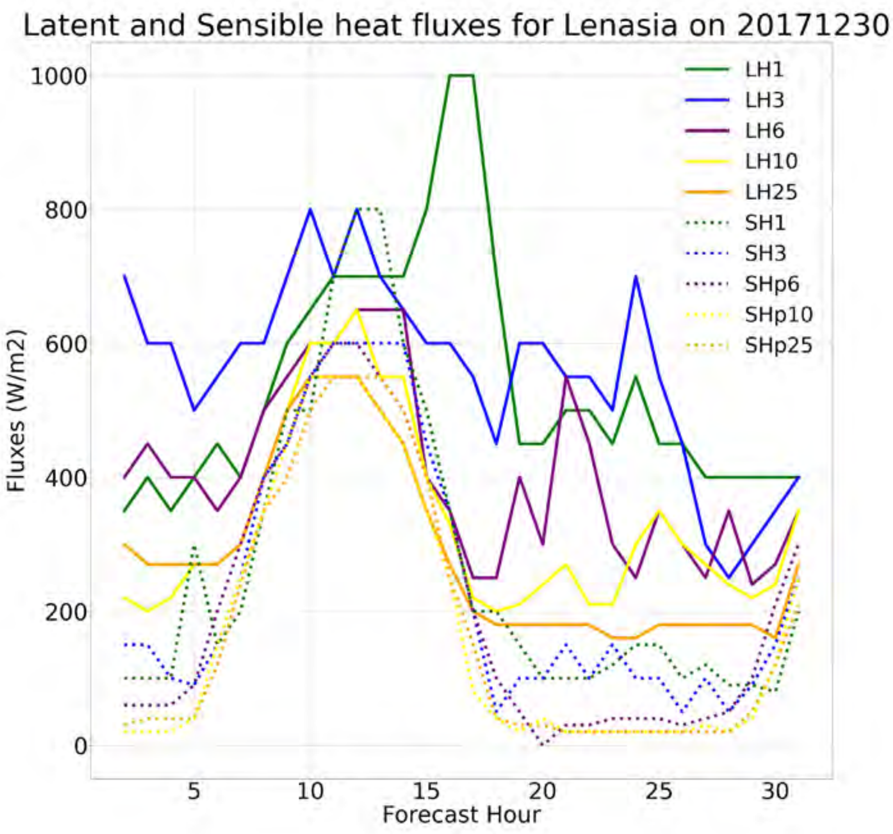

Figure 5.50: Time series for vertical profiles for latent and sensible heat fluxes over Lenasia, Soweto on 30 December 2017. For latent heat flux: the CCAM run at 1 km (green solid line), the CCAM run at 3 km (blue solid line), the CCAM run at 6 km (purple sold line), the CCAM run at 10 km (yellow solid line) and the CCAM run at 25 km (orange solid line). The dotted lines are the respective sensible heat fluxes of the different model runs.

5.4 DISCUSSIONS AND CONCLUSIONS

5.4.1 Evaluation of the different versions of the Convjlm

The CCAM model comprises one cumulus scheme, Convjlm, which initially had three different versions, namely, the 2015a, 2015b and the 2017. However, with help from the CSIRO, we were able to add the 2015aM version. We ran model simulations with the four versions of the cumulus scheme to investigate the benefit in model development and to gain understanding on which version works best for the South African domain. The model runs were compared with observations for precipitation. Furthermore, vertical profiles for selected convective parameters were analysed and only compared amongst the model runs.

There are generally no significant differences in how the model simulates precipitation with different versions of the cumulus scheme. Diurnal cycles for the areal average rainfall over regions affected by the investigated rainfall events revealed that the model simulations were ineffective in simulating both the patterns and amounts of observed precipitation. The model initiated rainfall earlier than observed. However, in certain instances, the model successfully captured spatial patterns and most peaks, albeit with simulated amounts significantly lower than the observed values. Notably, a prominent issue in the simulation of rainfall spatial distribution is observed: the model runs with 2015aM cumulus scheme consistently yields lower precipitation than other versions of the Convjlm cumulus scheme. Although all schemes generate less rainfall than the coarse surface observations, the model generally accurately locates rainfall events. Model statistics indicate a lack of skill in simulating precipitation over the South African domain.

5.4.2 Experiments to identify the value of bcon parameter

A sensitivity test was conducted on three MCS cases, examining various values of the bcon parameter to identify the most suitable setting for the southern African domain. This parameter, vital to both the cloud and convection schemes, was tested with values preferred by model developers, i.e., 0.04 and 0.1, along with additional values, i.e., 0.2 and 0.5. The evaluation measures employed included eye-ball verification, FBS, and FSS.

In the analysis, the first case demonstrated some advantages when using bcon=0.1. However, the subsequent two cases did not exhibit significant differences among the runs. Notably, the first case represented a pure MCS, while the other two cases involved some synoptic (convection) contribution or influence. This variance in case characteristics could potentially account for the differing results observed.

It is crucial to recognize that while the bcon parameter plays a role in forecast skill improvement, enhancing forecast accuracy may not solely depend on adjusting this parameter. Other additional parameters may need consideration, suggesting that there may be a need to adjust (an) additional parameter(s).

5.4.3 Testing the scale-awareness of the cumulus scheme

A scale-awareness of the CCAM Convjlm cumulus scheme was examined. This came as a result of the meeting/workshop held with model developers in July 2023, where the project team engaged in a collaborative effort with model developers. The meetings encompassed training sessions, discussions, and future planning for a model development project. The developers advised that the work on cumulus parameterization development be focused on researching the model's scale-awareness and testing its spin-up, amongst other tasks. This section focused on the investigation of the scale-awareness of the Convjlm cumulus scheme within CCAM, utilising five grid scales, namely, 25 km, 10 km, 6 km, 3 km and 1 km, to understand the scheme's behaviour at different resolutions. The research aims to determine when convection completely switches off, analyse changes in model accuracy and skill with resolution, and explore how these insights can inform further enhancements to the model code.

Several case studies that were associated with severe rainfall were used, such as a thunderstorm associated with a tornado in Soweto on 30 December 2017, severe flooding in Limpopo on 1 February 2021, and a case of thunderstorm in Suncity on 15 December 2018. The cases were analysed to evaluate the spatial distribution of rainfall, vertical profiles and other convective/related parameters. The results demonstrate that as resolution increases, the model accurately locates intense rainfall events, particularly highlighted by the 3 km resolution performing exceptionally well. The report also discusses the diurnal cycle for different events, presenting the model's proficiency in capturing heavy rainfall and parameterized rainfall components. Furthermore, vertical profile analyses reveal notable distinctions in moisture content, wind patterns, and omega fields across different resolutions, emphasising the intricate relationship between these variables and grid length.

In addition to rainfall distribution and vertical profiles, the report assesses the model's performance in terms of latent and sensible heat release. Findings indicate that the 3 km CCAM run generally releases the highest latent heat, followed by the 1 km model run, while coarser resolution runs release the least. Conversely, the 1 km CCAM run typically releases the most sensible heat, followed by the 3 km model run, with coarser resolution runs releasing the least amount. This multi-faceted analysis contributes valuable insights into the behaviour of the Convjlm cumulus scheme at various resolutions and provides a foundation for refining the model code for improved accuracy and predictive capabilities.

CHAPTER 6: PERFORMANCE OF THE CCAM MODEL

6.1 INTRODUCTION

This chapter showcases how the CCAM model, developed at the CSIRO (Commonwealth Scientific and Industrial Organisation) of Australia by (McGregor 1996) and introduced to the South African community by (Engelbrecht et al. 2007) is applied for numerical weather prediction. The system is seamless and is applicable at various time scales from numerical weather prediction (Bopape et al. 2022), climate projection (Maure et al. 2018), urban climate modelling (Thatcher and Hurley 2012; Maisha et al.2023), air quality modelling and seasonal forecasting (personal communications with developers, and this system is currently being developed for South African Weather Service Application and is being used for predicting wind project (https://www.predictwind.com).

The CCAM was run with various configurations through nesting, where the CCAM was initialised with global forecasting system (GFS) data at a horizontal resolution of 25 km over SADC region, nested with a 9 km and 3 km runs or nested with a 4.5 km domain over South Africa. The use of the 4.5 km domain was applied so that such runs could be compared with the SAWS operational Unified Model (UM) runs (either with data assimilation (UMDA) and without data assimilation techniques (UM4 and UM1.5). The CCAM runs were also compared to SAWS observations (rainfall and temperature that were regridded to 25 km, which is also the resolution of the input GFS data). For these case studies, some changes were incorporated, including changes from default land cover to both the 2013 and 2020 land cover data set (see Figure 6.1). Likewise, the cloud microphysics and the cumulus parameterization were upgraded respectively. Both the cloud microphysics and the cumulus parameterization were studied intensively on this project and were reported in the previous chapters (Chapter 4 and 5 respectively). The objective of performing these simulations was to test the performance of the CCAM model in simulating extreme weather events over South Africa.

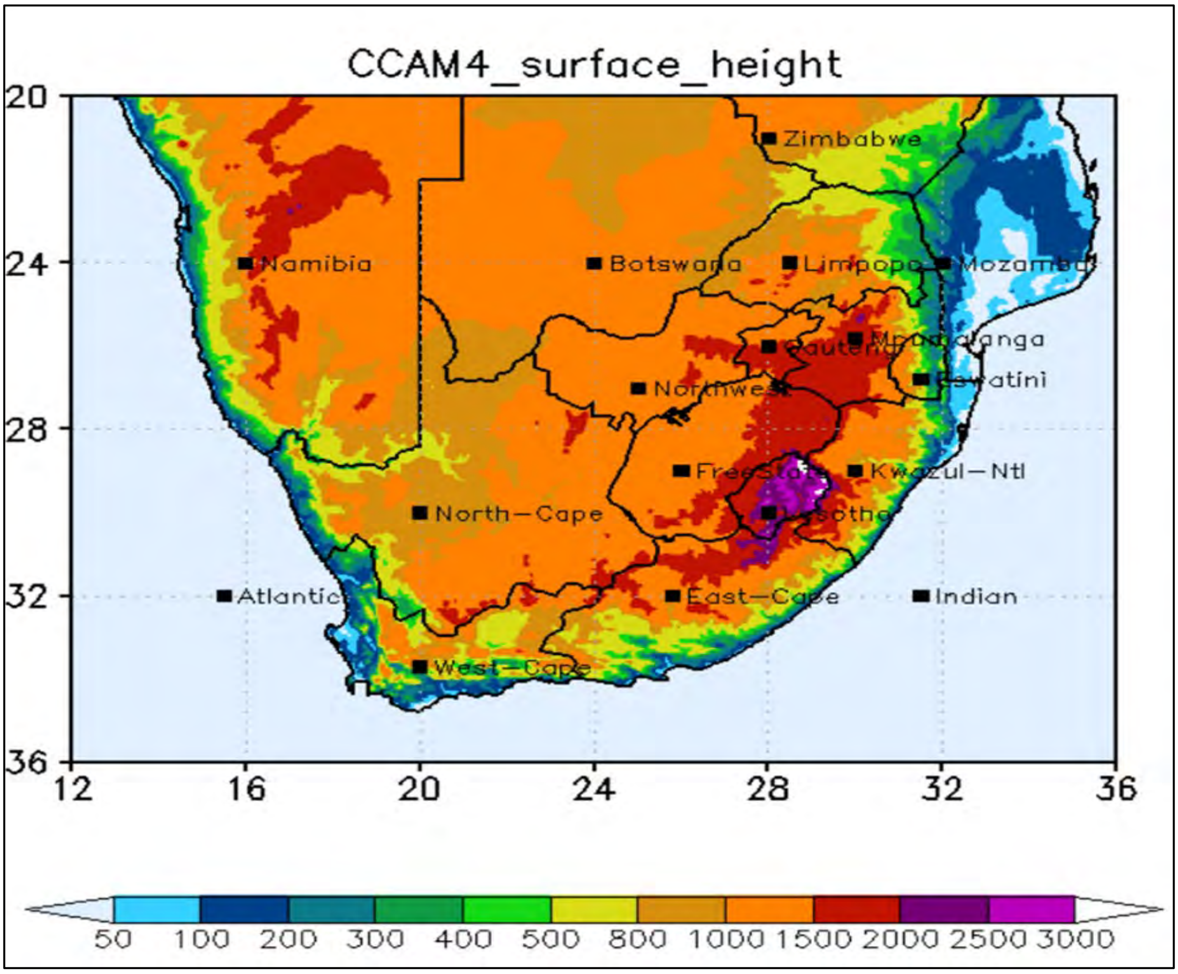

Figure 6.1: The South African surface height from the land cover 2013 showing all the nine (9) provinces, the surrounding oceans and the neighbouring countries

6.2 EXPERIMENTS

Various experiments were conducted using different settings of the CCAM configurations. A list of settings was applied during these experimental designs as well as computing resources are explained for each experiment. The case studies were for selected extreme weather events recorded over South Africa from 2019 until 2023. These case studies include:

(i) A cut-off low over South Africa that resulted in heavy rainfall on 04 April 2019;

(ii) a cut-off low that caused heavy rainfall, structural damages, mudslides and death of more than 300 people over KwaZulu Natal on 11-12 April 2022),

(iii) a heatwave that lasted at least five (5) days over South Africa, (03 - 08 October 2022),

(iv) a severe thunderstorm with tornado over Kwazulu-Natal province (27 June 2023) and

(v) a severe thunderstorm with hail damages over Gauteng (13 November 2023).

6.2.1 Case study: cut-off low over Kwazulu-Natal 22 April 2019

A cut-off low pressure system was observed over South Africa on 22 April 2019. Figure 6.2 shows the synoptic chart of the mean sea level pressure, developed and published by the SAWS, dated 22 April 2019. During this event, there was a surface trough over the central interior of South Africa. A high was located to the south of the country, riding in over the eastern and north-eastern parts transported moisture from the ocean overland. This event was also associated with a cut-off low and was included in severe cut-off low systems studied by Muofhe et al. (2021), when he investigated the performance of the Unified Model when forecasting these events. The event resulted in partly cloudy conditions, then showers and thundershowers, with heavy rainfall observed over North-West, Eastern Cape and Kwazulu-Natal Provinces.

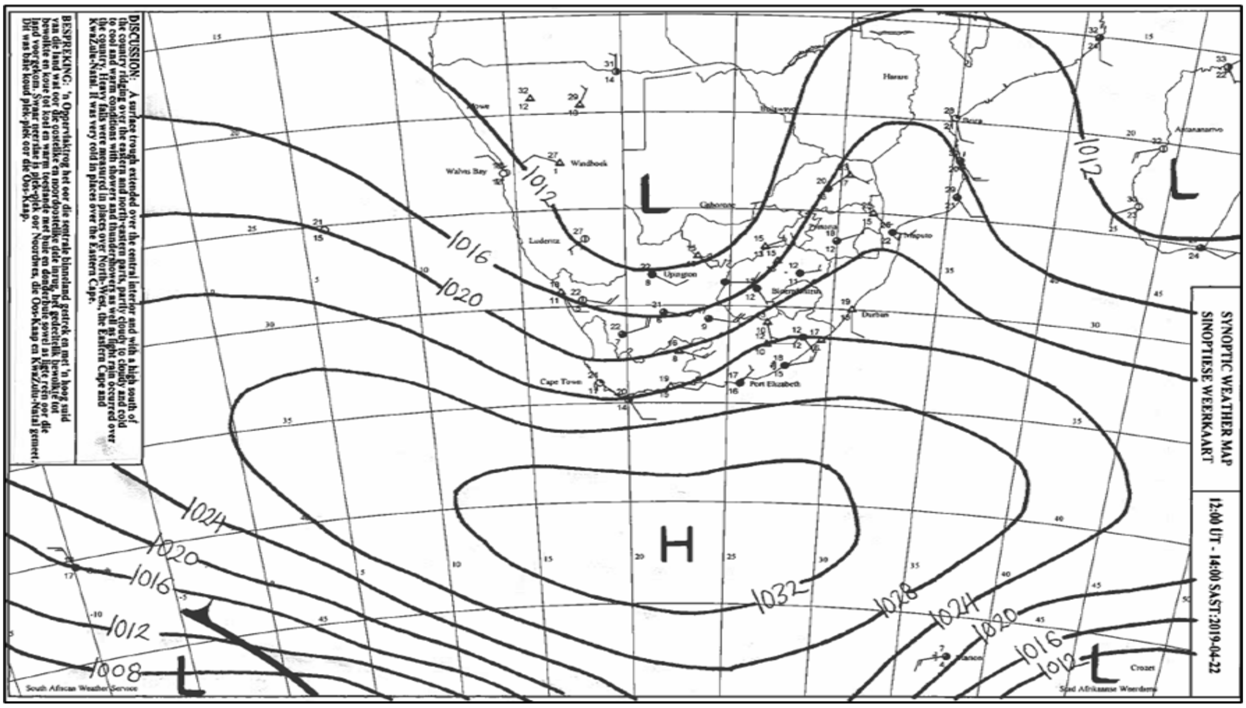

Figure 6.2: the SAWS synoptic scale map of South Africa on the 22 April 2019.

The CCAM was setup as in Table 6.1 below.

Table 6.1: Model setup for evaluating CCAM during the cut-off low on 22 April 2019 with both GFS and ERA5 datasets

Model setup	**Option(s)**
Vertical levels	35 (GFS) and 27(ERA5)
Projection	25 km (C168), and 4.55 km (C696)
dt	dt=20 (for GFS) and dt=12 (for ERA5)
Forecast hours	48
Boundary layer scheme	Local Ri
Microphysics scheme	Original LDR cloud microphysics with prognostic liquid and ice condensates. Cloud cover is diagnosed. Has updated auto-conversion scheme and prognostic rain.
Radiation scheme	Older/Slower, Freidenreich and Ramaswamy (1999), Schwarzkopf and Ramaswamy (1999), which support direct aerosol effects.
Nudging	Standard
Number of processors	600 (25*24)

The 24-hour simulated rainfall forced with both the GFS and ERA5 data at 25 km and 4.5 km are shown in Figure 6.3. The observed SAWS observations were regridded to a horizontal resolution of 0.25 degree and is shown in the last row of Figure 6.3. Large amounts of rainfall were observed across the central parts of the country, aligned in the north-west to south-east alignment. Provinces seen with areas of rainfall in the range between 20 and 50mm are the North-West, Free State, Eastern Cape, Gauteng and the Kwa-Zulu Natal province. The heaviest rainfall was observed along the eastern coastal parts of the country, and particularly the southern parts of Kwa-Zulu Natal province, including the eThekwini municipality, as well as the north-eastern parts of the Eastern Cape province.

The CCAM forced with the ERA5 at both 25 km (Figure 6.3a) and 4.5 km (Figure 6.3c) is found to underestimate rainfall especially in areas where the observed rainfall exceeded 20mm (Figure 6.3e). The higher resolution configuration simulates patches of higher rainfall amounts, however, the simulation underestimates rainfall in general. The heavy rainfall south of KZN and north of the Eastern Cape is not captured by the model simulation, however there is an area of rainfall over 20mm, just east of the coastline. The simulations forced with GFS at both simulations (Figure 6.3b and d) captured the rainfall intensity better. These simulations show rainfall maximum up to 200 mm over KwaZulu-Natal which is similar to observed. This result was not expected because the reanalysis are corrected datasets and are thought to represent the best forcing fields. The shortcoming in the GFS forced simulations, is the slow propagation of the system which results in higher simulated rainfall in the west of the Free State while observations show this rainfall in the east of the same province.

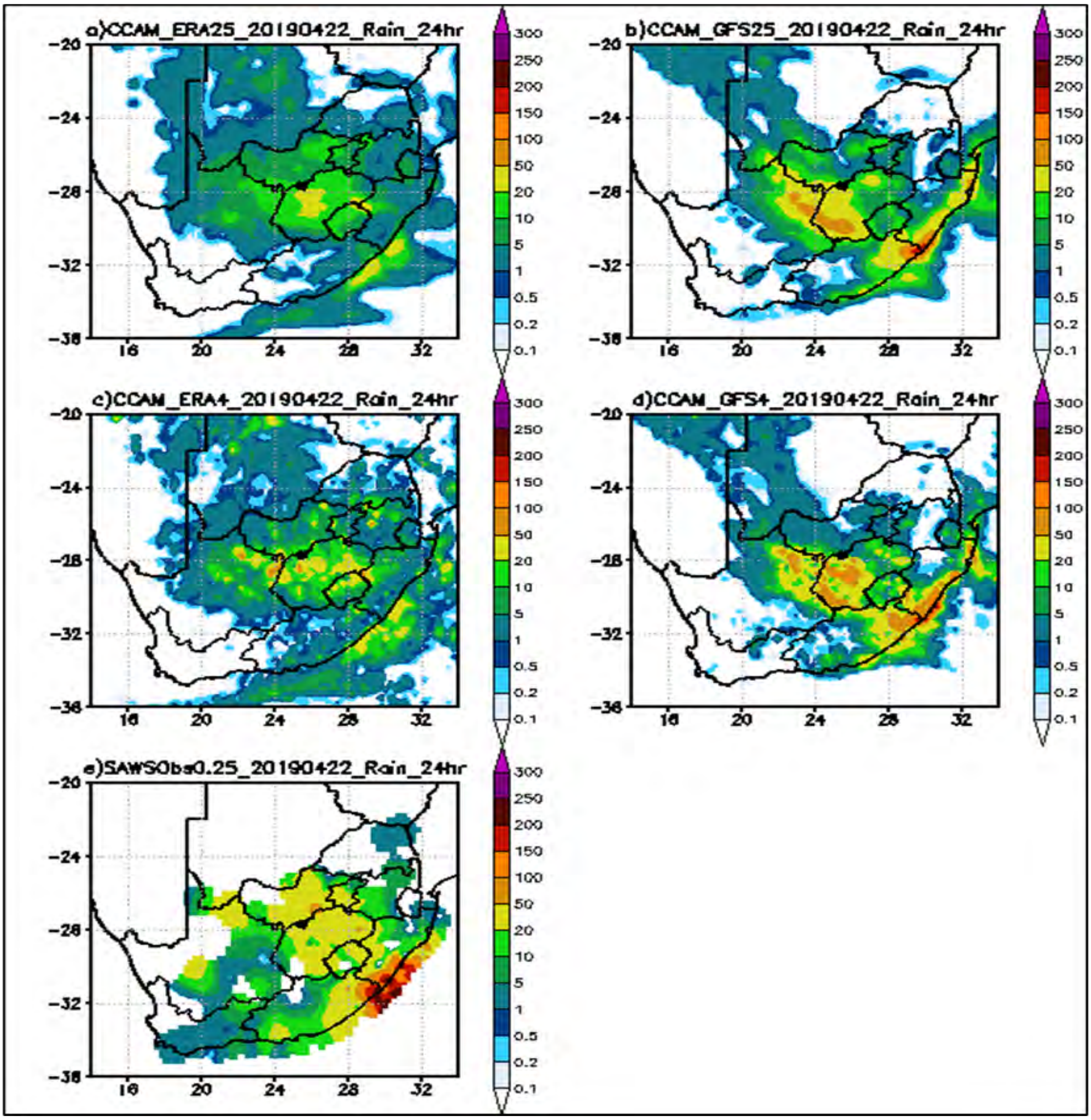

Figure 6.3: The CCAM simulated rainfall with both ERA5 and GFS at 25 km [a) and b)] and 4.5 km [c) and d)] respectively regridded to 25 km and compared to SAWS observations[e)] on 22 April 2019.

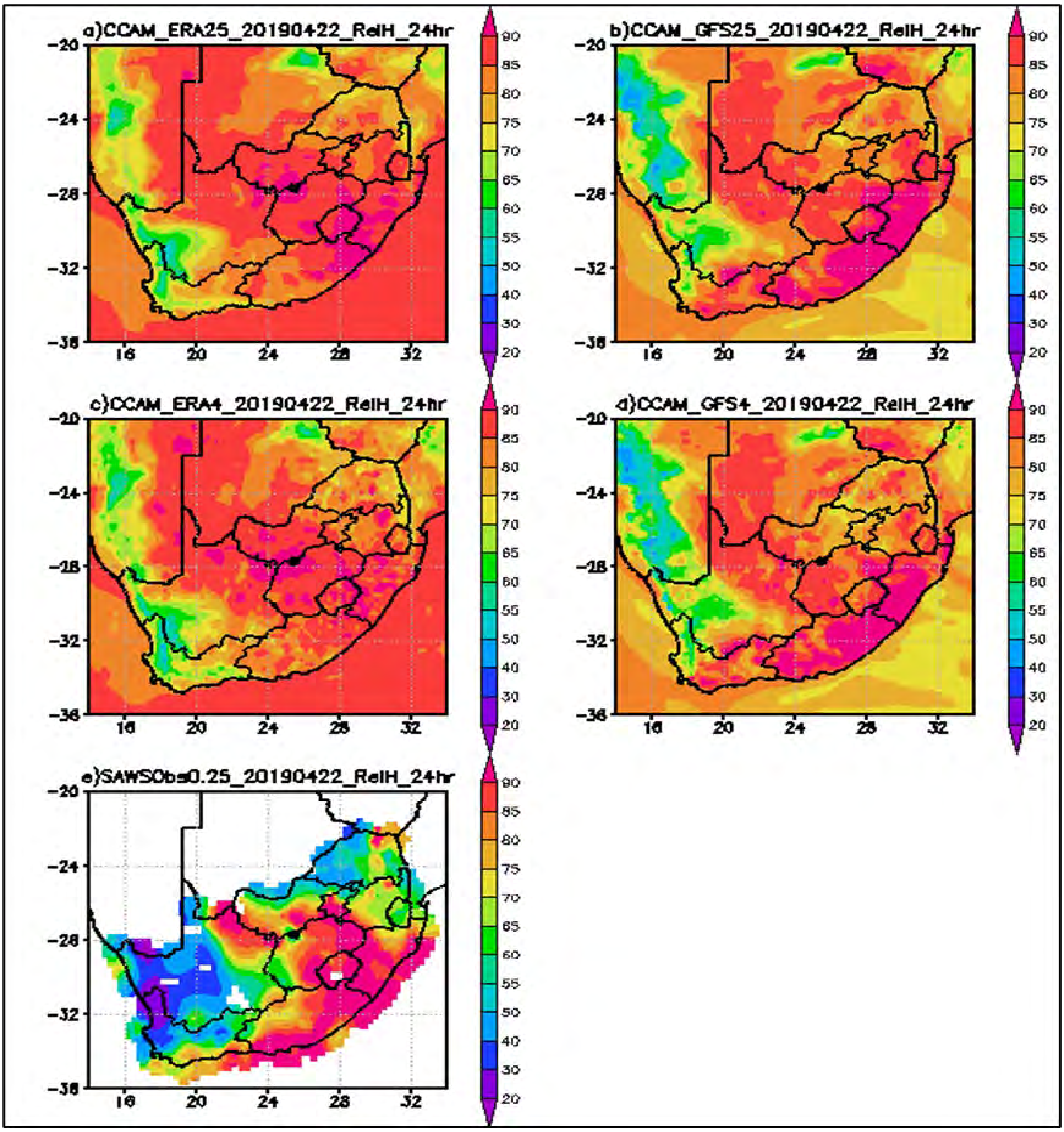

Figure 6.4: The CCAM simulated relative humidity with both ERA5 and GFS at 25 km (a and b) and 4.5 (c and d) km respectively regridded to 25 km and compared to SAWS observations (e) on 22 April 2019.

The relative humidity (Figure 6.4) from the same simulations and observations is in the same order as for rainfall (Figure 6.3). The Northern Cape and Limpopo province have larger areas of lower moisture, while the provinces that received more rainfall have higher moisture levels. The difference in rainfall amounts across the different simulations is not found in the relative humidity simulations. The available moisture in the GFS forced simulation is very high in KZN and Eastern Cape which received very heavy rainfall.

6.2.2 Case study: cut-off low over Kwazulu-Natal 11-12 April 2023

According to the SAWS Media release dated 12 April 2022, a cut-off low pressure system moved over the coastal provinces of South Africa, leading to widespread rainfall over Kwazulu-Natal (KZN) and Eastern Cape Provinces. The impact-based warnings (level 5 to 8) were issued in time by SAWS, but the heavy rainfall was experienced overnight and, in the morning, exceeded the expected rainfall. Parts of KZN province experienced heavy rainfall exceeding 200 mm and others more than 300 mm in 24 hours. Such rainfall is normally experienced during tropical cyclones. Although the cut-off low is associated with widespread instability, which promotes prolonged rainfall, the system that occurred over KZN was enhanced by low-level maritime air from the southern Indian ocean, which led to more rainfall. It should be noted that the original source of moisture was the subtropical warm maritime air, which transported moisture leading to more rainfall (SAWS,2022). The EUMETSAT satellite confirms the occurrence of heavy rainfall over the coastal provinces (Figure 6.5).

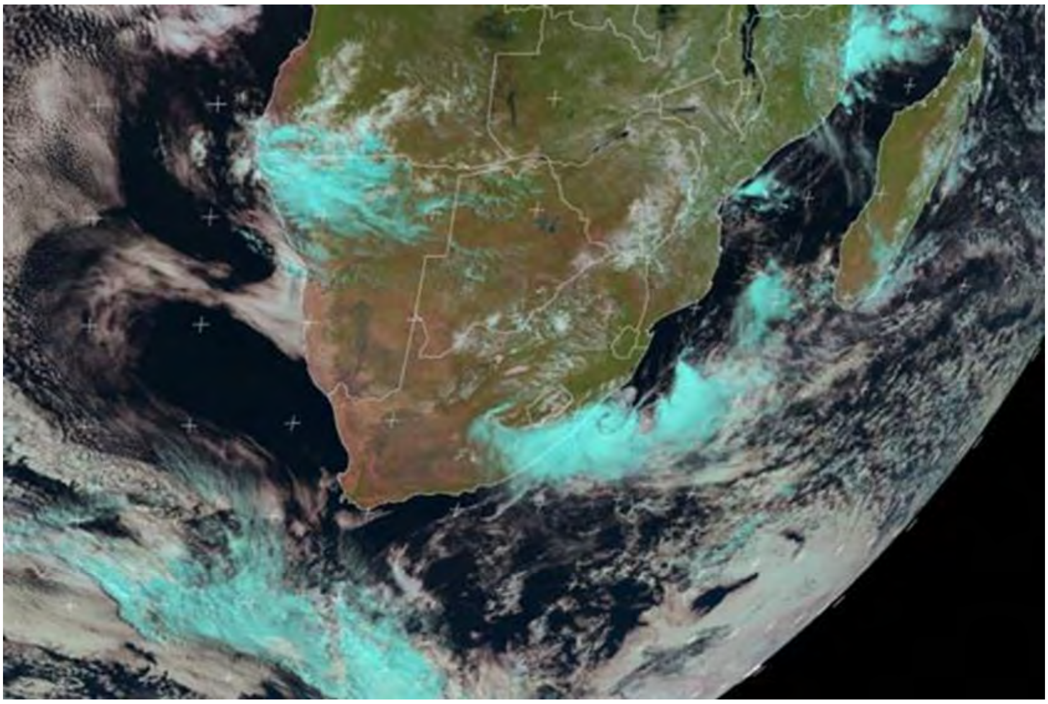

Figure 6.5: Meteosat RGB composite at 09h00 UTC (11h00 SAST) on 12 April 2022, shows deep convective clouds over Kwazulu-Natal and Eastern Cape Provinces, which was associated with heavy rain (Source: Eumetsat, © 2022).

The accumulated rainfall from SAWS observations stations confirms that for the period 08 – 11 April 2022, a large amount of rainfall (200-400mm) fell over Kwazulu-Natal and northern parts of Eastern Cape Provinces (Figure 6.6). Parts of Mpumalanga, Gauteng and Northwest Provinces also received rainfall amounts of range 100 mm to 150 mm over the same period.

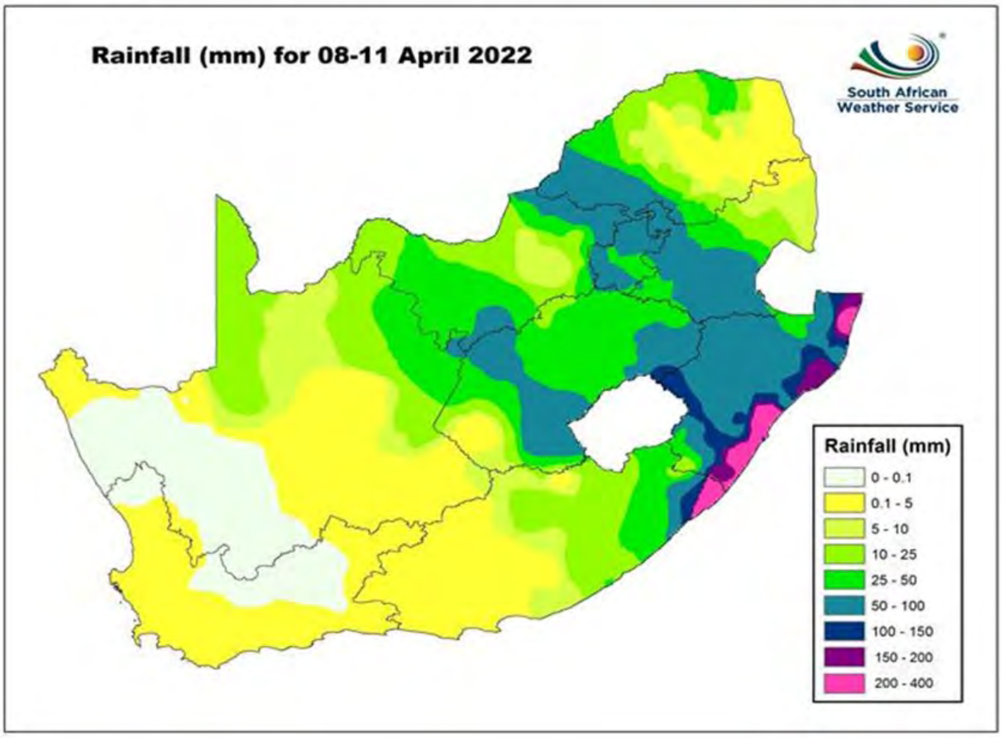

Figure 6.6: The SAWS accumulated rainfall (mm) map for the period 8 to 11 April 2022 (including the first 8 hours of 12 April). Rainfall amount of particular interest and relevance are the values indicated in light pink, indicating 200-400 mm. (Source SAWS). The CCAM was setup as in Table 6.2.

Table 6.2: Model setup for evaluating CCAM during the cut-off low for the period 8 to 11 April 2022 with GFS dataset.

Model setup	Option(s)
Vertical levels	35 (GFS)
Projection	C144 (25km), C192 (9km) and C576 (3km)
dt	dt=20 (for GFS)
Forecast hours	48
Boundary layer scheme	Local Ri
Microphysics scheme	Original LDR cloud microphysics with prognostic liquid and ice condensates. Cloud cover is diagnosed. Has updated auto-conversion scheme and prognostic rain.

Radiation scheme	Older/Slower, Freidenreich and Ramaswamy (1999), Schwarzkopf and Ramaswamy (1999), which support direct aerosol effects.
Nudging	Standard
Number of processors	600 (25*24)

The CCAM 9 km (Figure 6.7b), CCAM 3 km (Figure 6.7d), UM 4 km (Figure 6.7a), UMDA 4 km (Figure 6.7c) and UM 1.5 km (Figure 6.7e) rainfall were regridded to observational data resolution of 25 km for the period 11-12 April 2022. From these model runs, all the UM runs including the UMDA were able to reproduce the observed rainfall maximum on 11 April 2022. The CCAM 9 km, however, did not reproduce the rainfall maximum higher than 300 mm, but the CCAM 3 km was able to reproduce the rainfall maximum over 300 mm depicted over the coastal regions of the KZN (Figure 6.7d).

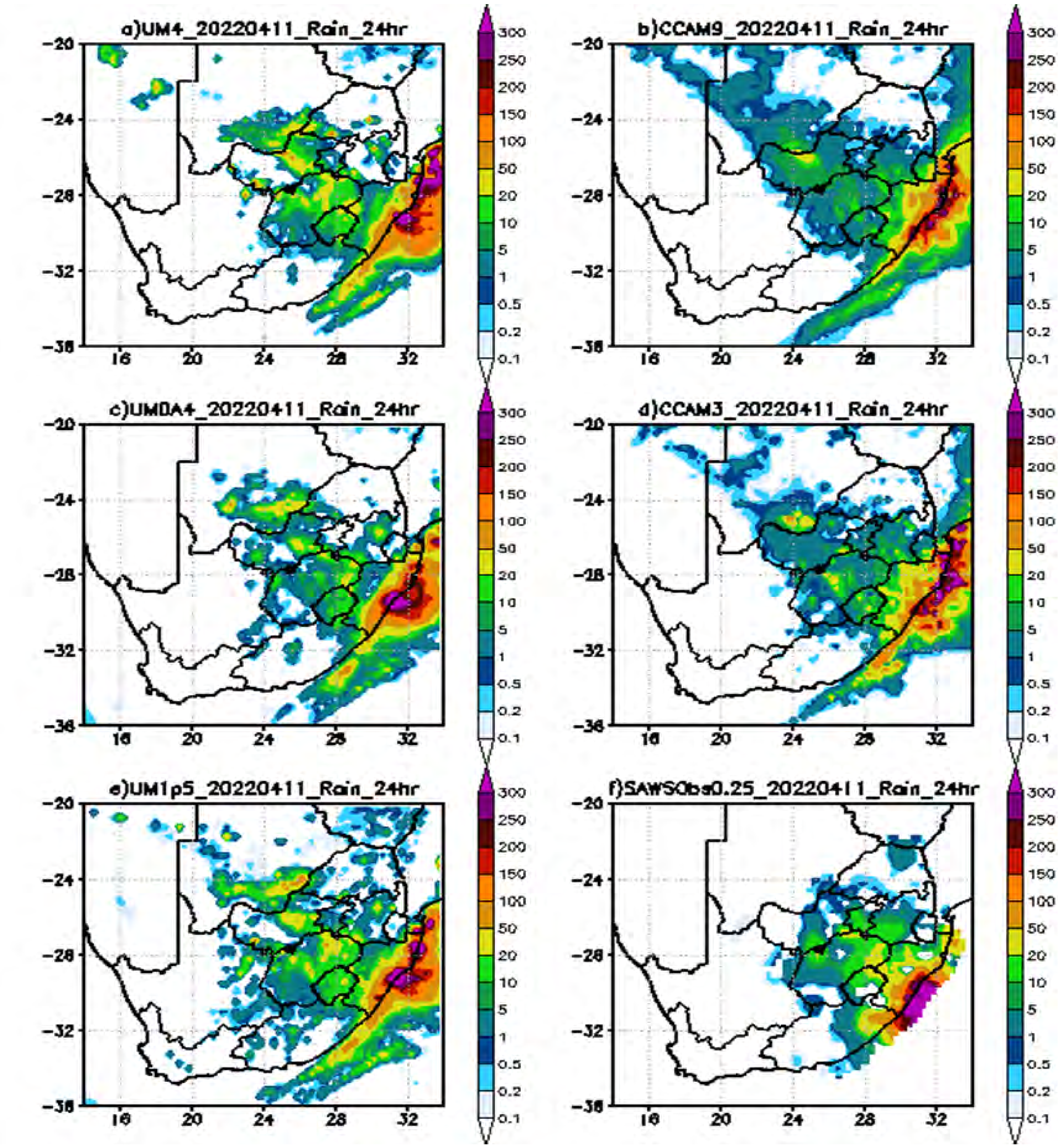

Figure 6.7: The UM 4 km (a), CCAM 9 km (b), UMDA 4 km (c), CCAM 3 km (d), UM 1.5 km (e) rainfall and SAWS stations observations (f). All simulations have been regridded to observational data resolution of 25 km for the period 11 April 2022.

On 12 April 2022, rainfall maximum was slightly reduced to maximum values up to 300 mm (Figure 6.8). All the model runs including CCAM produced the rainfall slightly lower than the observed 300 mm. However, all the models reproduced the observed spatial distribution of the rainfall event.

From this analysis, it is shown that although the models were regridded to the observation grid of 25 km, all the models reproduced the observed spatial rainfall over the country over the two days, showing that both regional models (UM and UMDA) as well as global model (CCAM) can reproduce the spatial distribution and intensity of observed rainfall.

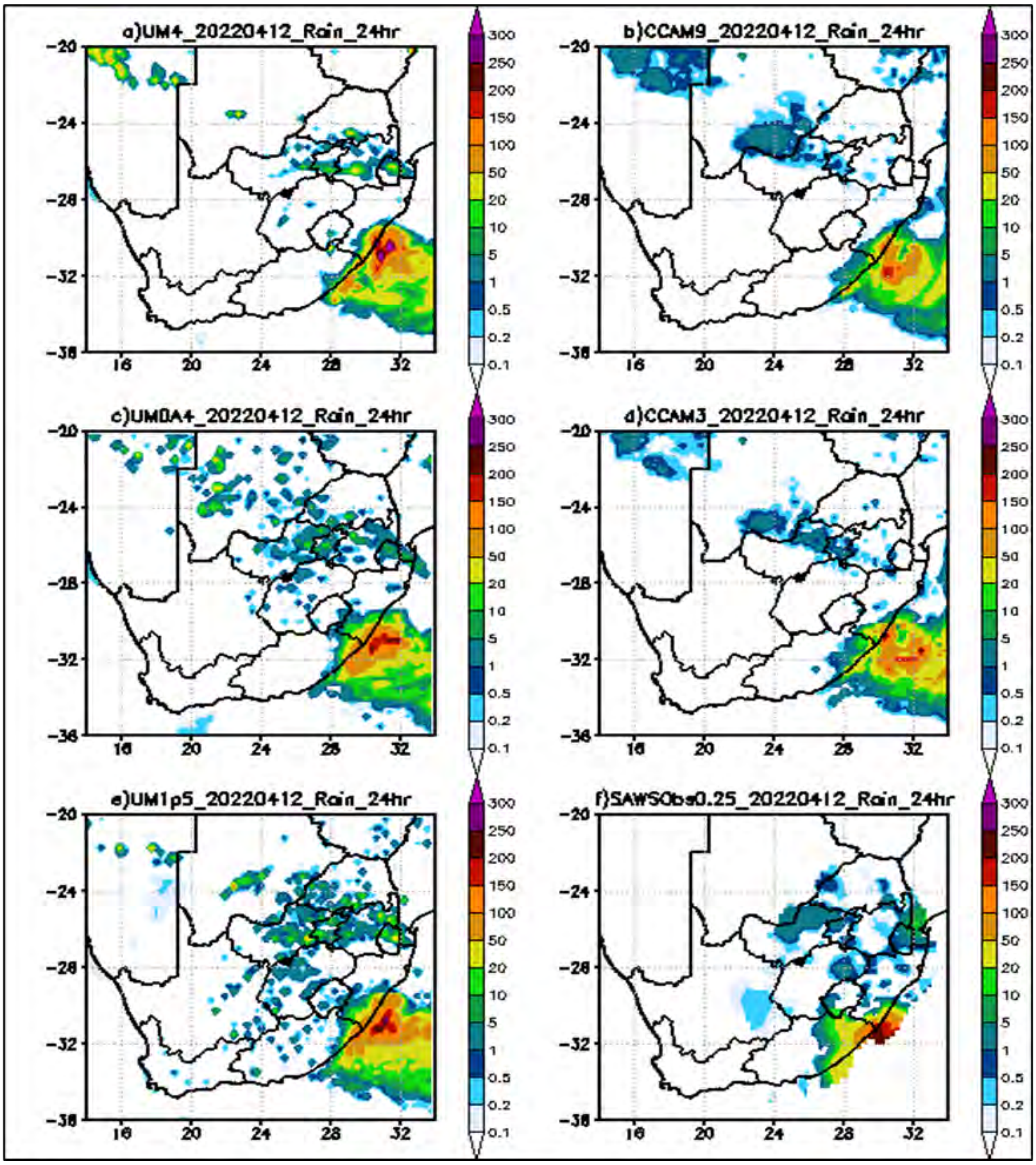

Figure 6.8: The UM 4 km (a), CCAM 9 km (b), UMDA 4 km (c), CCAM 3 km (d), UM 1.5 km (e) rainfall and SAWS stations observations (f). All simulations have been regridded to observational data resolution of 25 km for the period 12 April 2022.

6.2.3 Case study: heat wave over western and northern parts of south Africa, 03-08 October 2022

The SAWS Media release issued a warning for the heatwave over north-western half of South Africa for the period 03 to 08 October 2022, when the country was subjected to very high temperatures (https://www.weathersa.co.za/Documents/Corporate/Medrel4Oct2022_04102022162938.pdf) (see Figure 6.8). Temperatures raised to an average higher than 42°C over parts of Northwest Province and Northern Cape respectively (Figure 6.9).

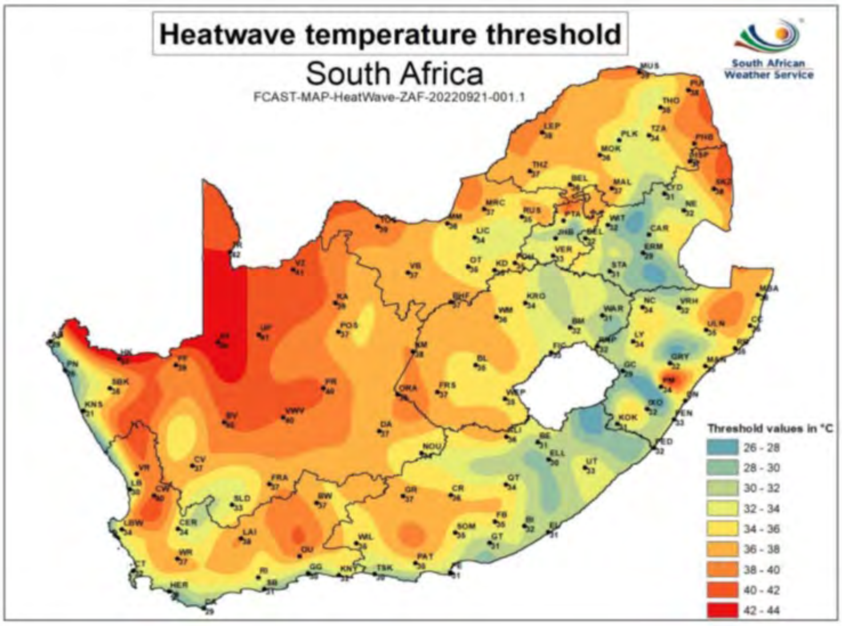

Figure 6.8: The SAWS observed heatwave over SA for the period 03 – 08 October 2022.

The CCAM was setup as in Table 6.2 above. The initial tests use default landcover, but later updated to SA_Landcover_2013. The CCAM runs were compared against the operational UM, UMDA and SAWS observations, respectively (Figure 6.10 and 6.11), but for the first three days, i.e. 03, 04 and 05 October 2022. On 3 October 2022, both the UM4 (Figure 6.10a) and CAM 9 (Figure 6.10b) were able to reproduce the observed high values of maximum temperature over Limpopo, Northwest, Northern Cape, Gauteng, Mpumalanga and Free State Provinces respectively. However, the UMDA4 (Figure 6.10c) and CCAM 3 (Figure 6.10d) reproduced the system especially over Kwazulu-Natal. The UM 1.5 (Figure 6.10e) missed the event over the eastern provinces but captured the event well over the western Provinces.

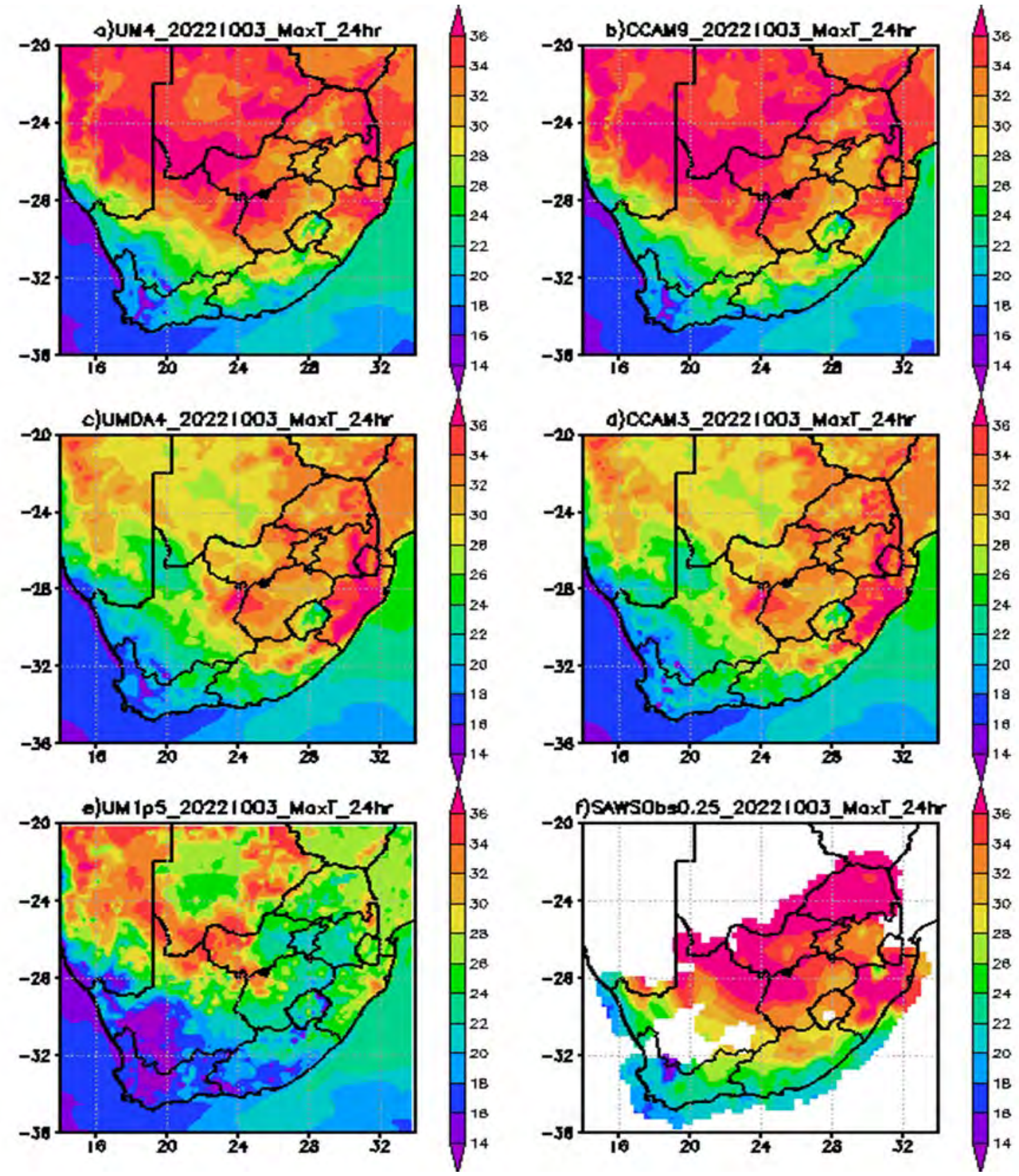

Figure 6.9: The spatial distribution of the UM 4 km (a), CCAM 9 km (b), UMDA 4 km (c), CCAM 3 km (d), UM 1.5 km (e) maximum temperature and SAWS stations observations (f). All simulations have been regridded to observational data resolution of 25 km for the period 03 October 2022.

The Models were also run on the 4th of October, which was the second day of the heatwave (Figure 6.11). The operational UM4 (Figure 6.11a) and the CCAM 9 (Figure 6.11b) and CCAM3 (Figure 6.11d) were able to reproduce the observed system (Figure 6.11f). These models reproduced the observed very high temperatures above 34^0C over the northern provinces of South Africa. However, the CCAM3 heatwave covered less spatial distribution when compared to the UM4 (Figure 6.11a) and the CCAM 9 (Figure 6.11b). The UM1.5 (Figure 6.11e) shows less spatial distribution of the heatwave, which was concentrated on western parts of the northern provinces. The UMDA (Figure 4.11c) did not reproduce the heatwave on the day. Both the UMDA and UM1.5 also show much lower temperatures over the southern parts of the country, which is similar to the UMDA run (Figure 4.11c). From these simulations, it is shown that the UM4 and CCAM 9 which cover large domains (represent synoptic scale systems) were able to reproduce the heatwave event. However, as the resolution increases, the heatwave event is not well represented. The UMDA run could not reproduce the heatwave at all. This could be due to the continuous ingestion of observations, which might have led to changes in the initialisation data.

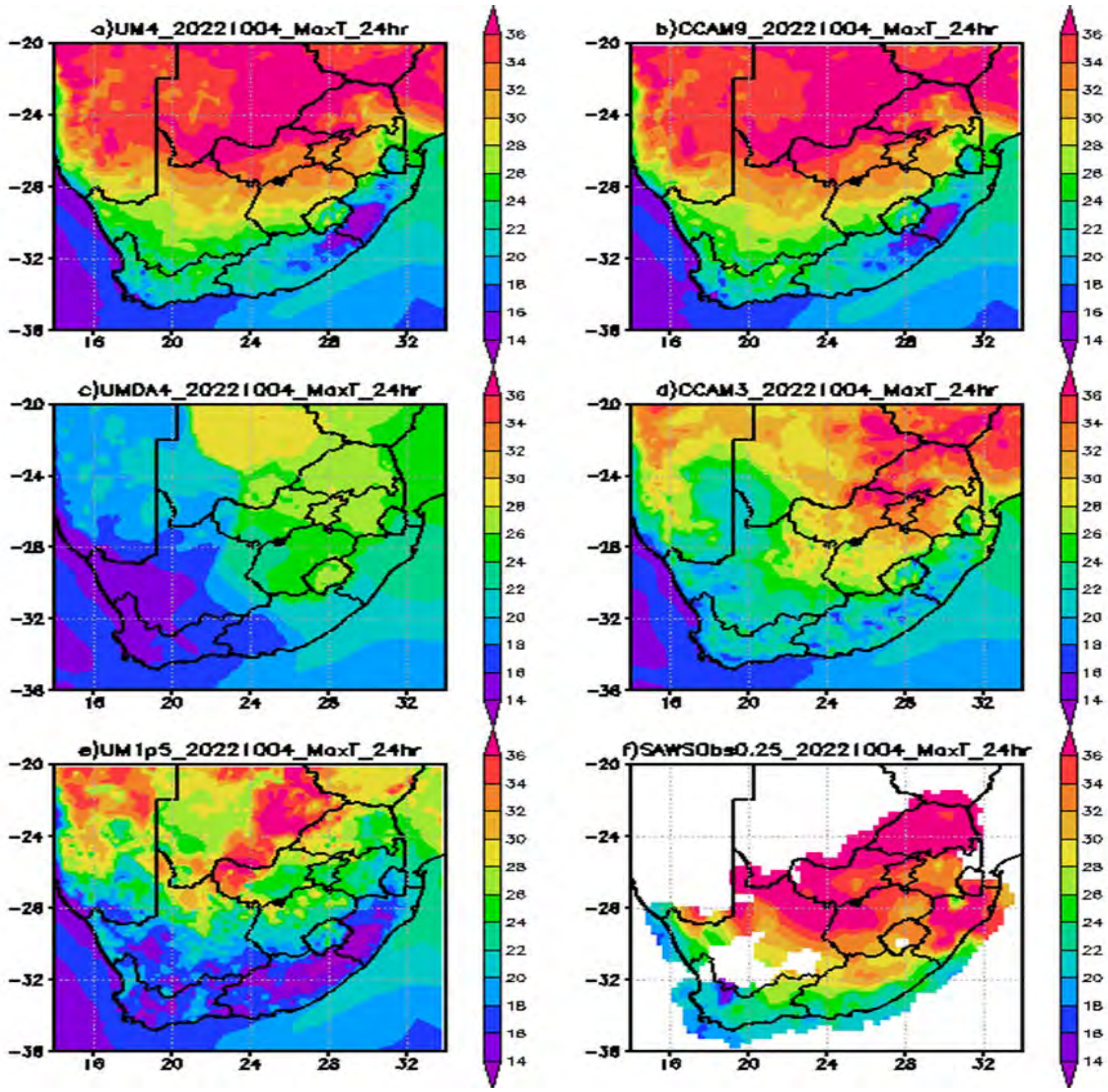

Figure 6.10: The spatial distribution of the UM 4 km (a), CCAM 9 km (b), UMDA 4 km (c), CCAM 3 km (d), UM 1.5 km (e) maximum temperature and SAWS stations observations (f). All simulations have been regridded to observational data resolution of 25 km for the period 4 October 2022.

The CCAM was also run for 5 October 2022 to evaluate if the system is able to capture the continuous heatwave event on the third day. On this day, the SAWS observed temperatures show maximum values higher than 34^{0}C covering the entire northern parts of the country (Figure 6.12f). The observed event was well captured by the UM4 (Figure 6.12a) and UMDA4 (Figure 6.12c). However, the UM1.5 (Figure 6.11e), CCAM 9 (Figure 6.12b) and CCAM3 (Figure 6.12d) underestimated the heatwave event when compared to observed (Figure 6.12f). During all these three days, the UM1.5 was much cooler than the rest of the model simulations.

The results show that the operational UM performed better than the CCAM, and that some more work is required in fine turning the CCAM to capture such an extreme weather event.

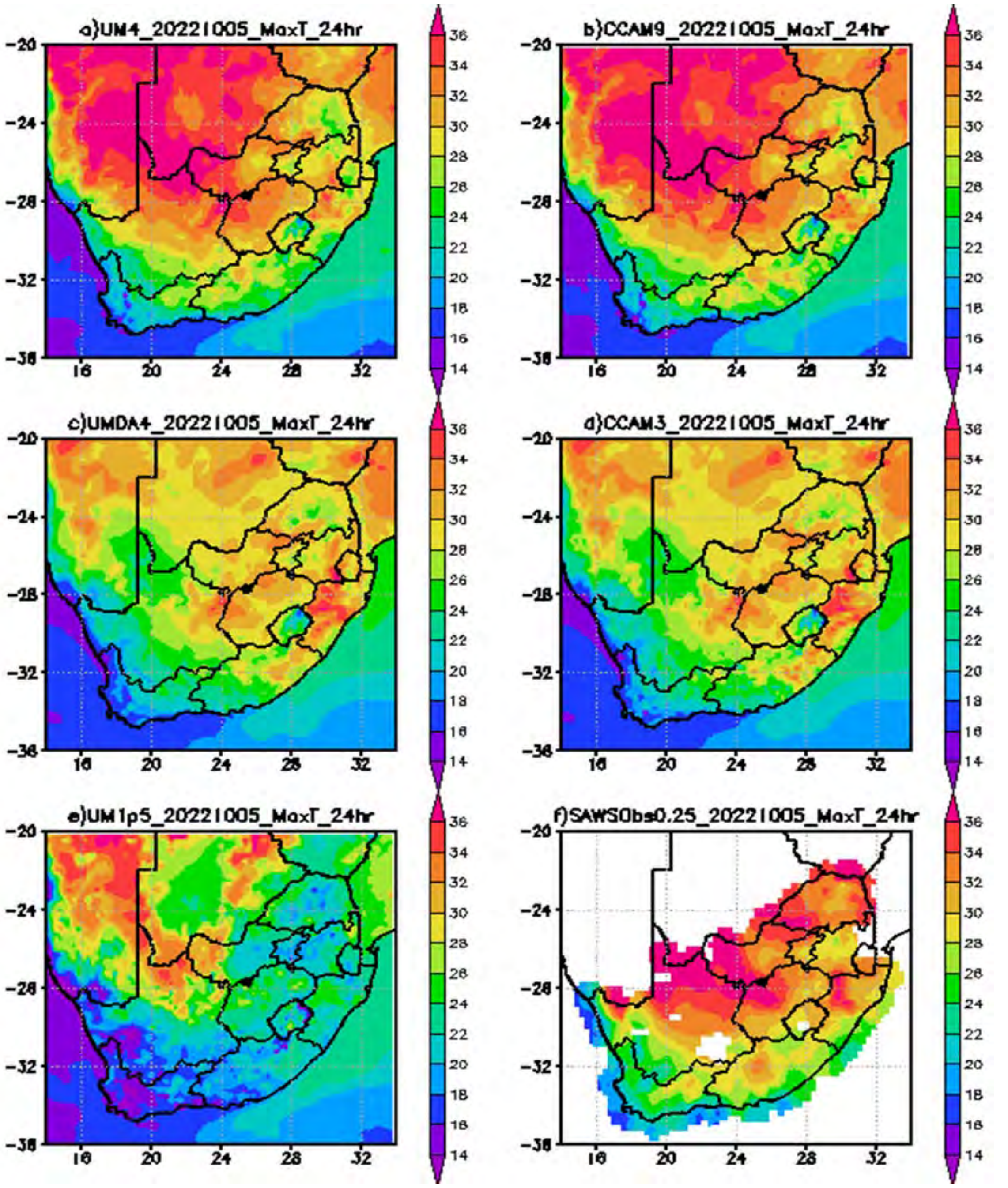

Figure 6.11: The spatial distribution of the UM 4 km (a), CCAM 9 km (b), UMDA 4 km (c), CCAM 3 km (d), UM 1.5 km (e) maximum temperature and SAWS stations observations (f). All simulations have been regridded to observational data resolution of 25 km for the period 5 October 2022.

6.2.4 Case study: Tornado event over Durban, 27 June 2023

According to the Eyewitness News (EWN), dated Tuesday 27 June 2023 (https://ewn.co.za/2023/06/27/watch-two-injured-after-tornado-wreaks-havoc-in-durban), a severe storm occurred over Durban north area including Inanda, which resulted in a tornado event. The tornadic storm resulted in two people injured and infrastructure damages. During this storm, some parts of Kwazulu-Natal received heavy rainfall (Figure 6.13). However, the SAWS Media Release issued on 28 June 2023, mentioned that the weather was dominated by the cut-off low which was located over the west coast of South Africa. This event led to very cold conditions, with storms that produced heavy rainfall, excessive lightning and large amounts of small hail (https://ewn.co.za/2023/06/27/watch-two-injured-after-tornado-wreaks-havoc-in-durban). Figure 6.13 further shows flying debris and uprooted roof materials over the affected areas of Kwazulu-Natal.

Figure 6.12: Image of flying debris (left) and destroyed building (right) because of a tornado over northern parts of Durban, Kwazulu-Natal on Tuesday, 27 June 2023.

The CCAM setup was as in Table 6.3 as follows:

Table 6. 3: Model setup for evaluating CCAM during the cut-off low for the period 13 November 2023 with GFS dataset.

Model setup	Option(s)
Vertical levels	35 (GFS)
Projection	C168 (25km) and C696 (4.5 km)
dt	Dt=20 seconds
Forecast hours	48
Boundary layer scheme	Local Ri
Microphysics scheme	Original LDR cloud microphysics with prognostic liquid and ice condensates. Cloud cover is diagnosed. Has updated auto-conversion scheme and prognostic rain.
Radiation scheme	Older/Slower, Freidenreich and Ramaswamy (1999), Schwarzkopf and Ramaswamy (1999), which support direct aerosol effects.
Nudging	Standard
Number of processors	600 (25*24)

The CCAM Model forecasts (4.5 km) were compared to operational UM (4.4 km) and UMDA (4.5 km) for the two day period: 27-28 June 2023 (Figure 6.14). Although these forecasts do not explicitly show the tornado, they show the spatial and temporal distribution of rainfall over the two day period. All the model simulations show strong agreements over the two day period. On 27 June 2023, all the UM runs show rainfall up to a maximum between 50 and 100 millimetres over the coastal areas of Kwazulu-Natal province (Figure 6.14, below). This UM forecasted rainfall agreed with the CCAM run for the day as well as observed rainfall (Figure 6.14e). It should be noted that in these model runs, the first six hours were taken as model spin-up period. It can also be seen that all the models reproduced rainfall over the Western Cape, Northern Cape and Eastern Cape provinces respectively because of the cut-off low pressure system that covered the entire south coast of the country.

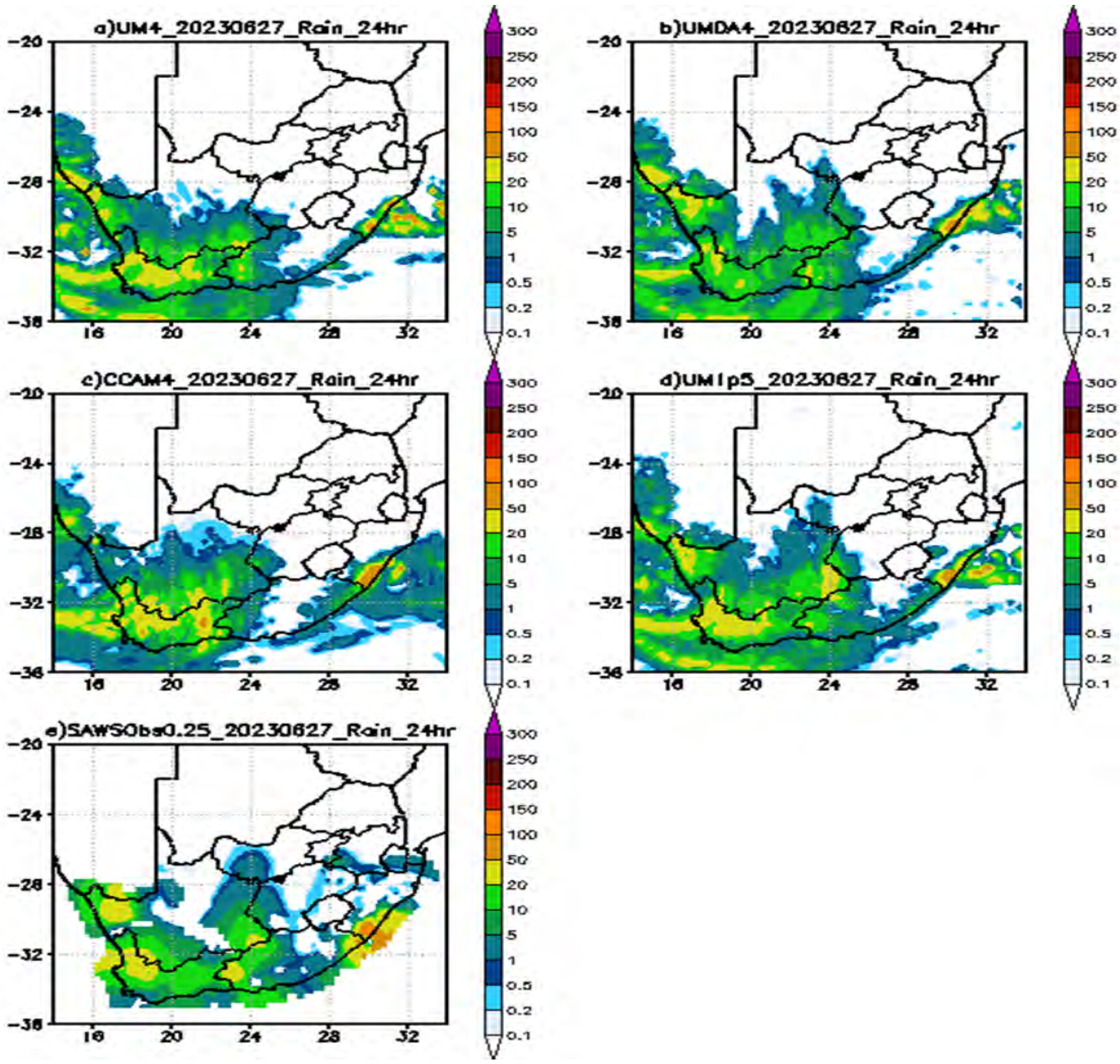

Figure 6.12: The spatial distribution of the UM 4 km (a), UMDA 4 km (b), CCAM 4 km (c), UM 1.5 km (d) rainfall and SAWS stations observations (e). All simulations have been regridded to observational data resolution of 25 km for the period 27 June 2023

On 28 June 2023 (Figure 6.14), the cut-off low pressure system moved further north inland, and covered almost the southern half of the country. As with the previous day, rainfall maximum was also, on average, less than 100 millimetres over Kwazulu-Natal, but with a spread to areas including Eastern Cape Province (Figure 6.14). The CCAM model (Figure 6.14c) run shows very strong agreement with the UM 4 km run (Figure 6.14a), the DA run (Figure 6.14b) also shows some slight agreement with the CCAM, the UM4.5 and UM1.5 runs. It should be noted that the DA run ingests continuous observations into the operational runs to improve the forecasts as compared to all other runs.

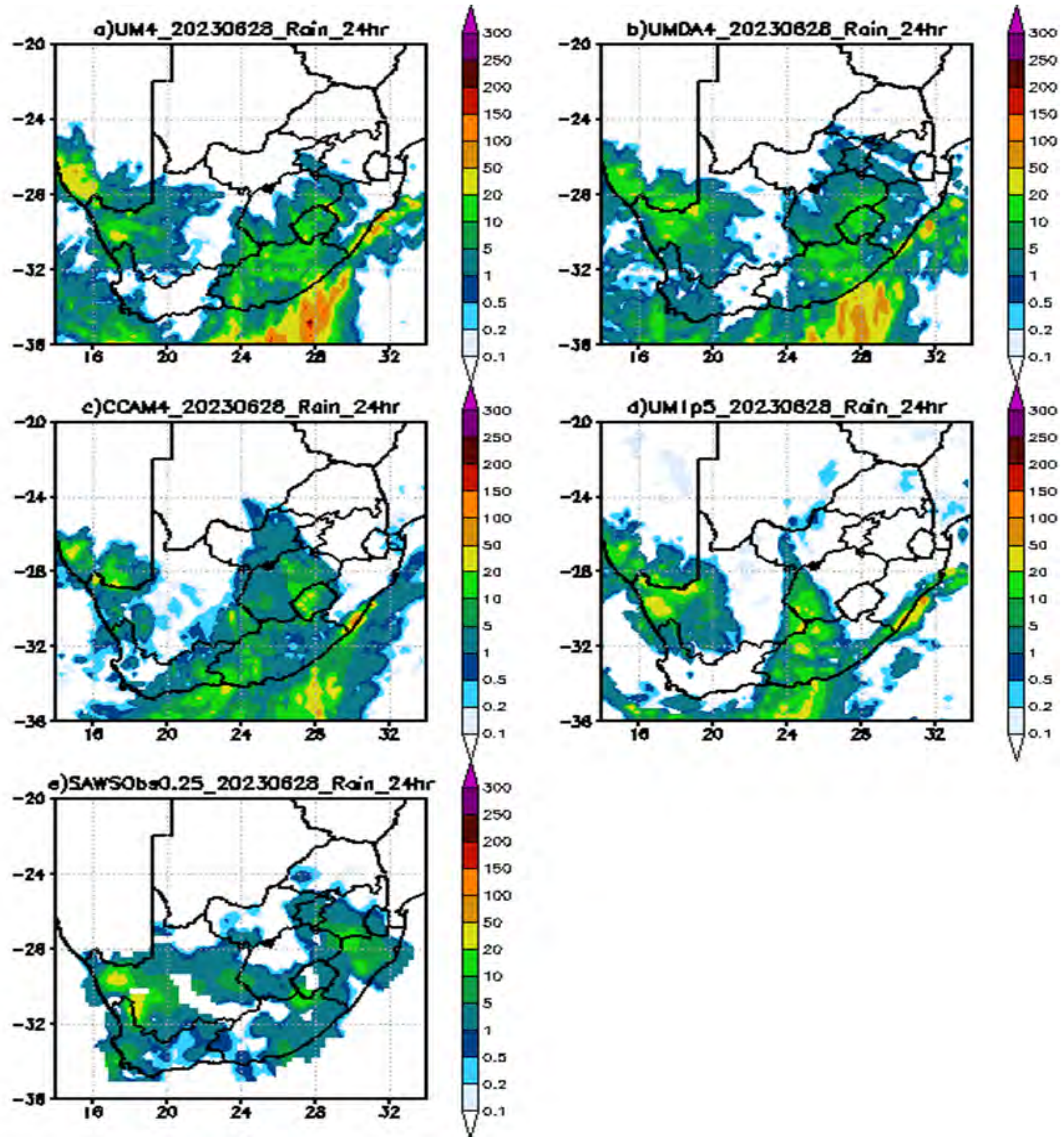

Figure 6:14 The spatial distribution of the UM 4 km (a), UMDA 4 km (b), CCAM 4 km (c), UM 1.5 km (d) rainfall and SAWS stations observations (e). All simulations have been regridded to observational data resolution of 25 km for the period 28 June 2023

6.2.5 Case study: Hailstorm over Gauteng and tornado over Mpumalanga, 13 November 2023

SAWS released a media release warning the community of heavy rainfall, severe hailstones and tornado during the period 13 to 14 November 2023. The SAWS radar and satellite images show that the thunderstorms were severe, resulting in a warning issued for southern parts of Gauteng and Mpumalanga (https://www.weathersa.co.za/Documents/Corporate/Med_rel_14_November_2023__14112023150516.pdf). The Irene radar image (Figure 6.15) shows areas of high reflectivity to the south of Johannesburg that moved east. This is also supported by the Meteologix satellite image (Figure 6.16) on the same day. The Report also mentioned that during such severe thunderstorms, A tornado occurred at Lekwa Local Municipality in Mpumalanga and hailstorms caused severe damage to properties in Midrand, Johannesburg (SAWS Media Release, dated 14 November 2023).

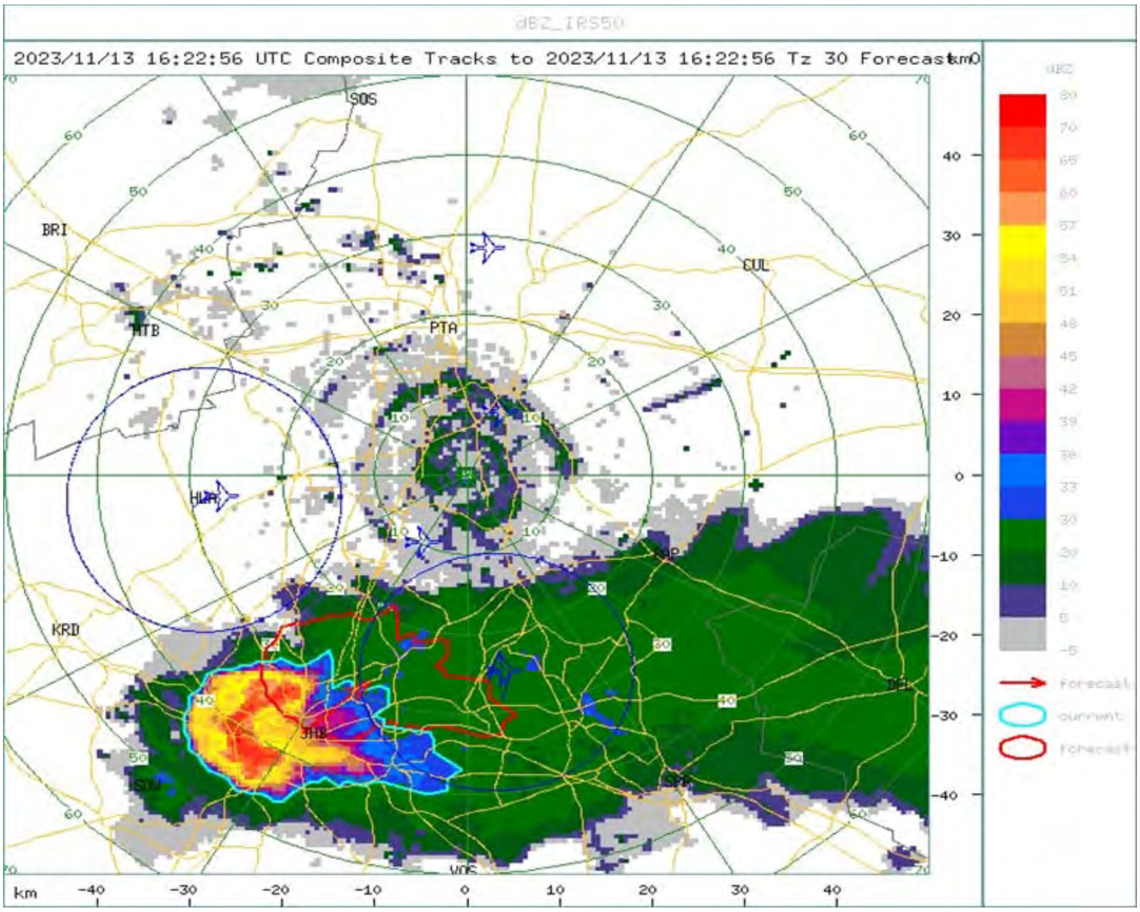

Figure 6.135: The Irene radar image for the period 16h00 UTC on 13 November 2023 showing rainfall over the southern parts of Gauteng Province.

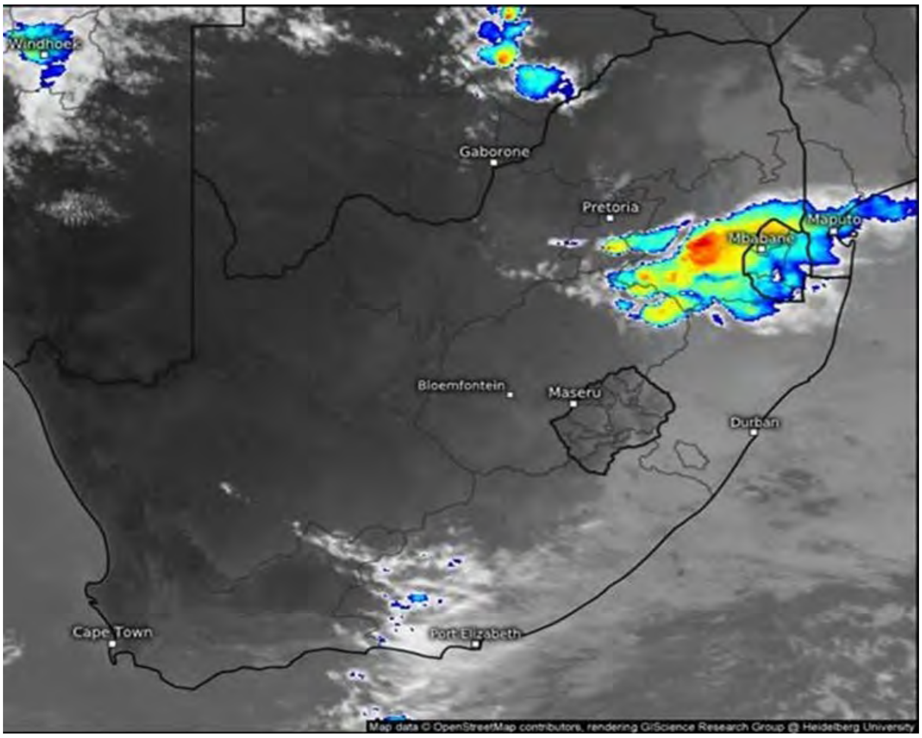

Figure 6.16: The Meteologix satellite image for the period 16h00 UTC on 13 November 2023 showing rainfall over the southern parts of Gauteng Province (SAWS Media Release,13 November 2023).

For this event, the CCAM (Figure 6.17c) was compared to both SAWS operational UM (Figure 6.17a) and UMDA (Figure 6.17b) operational forecasts as well as regridded observations (Figure 6.17e) at a resolution of 0.25 degrees (Figure 6.17 below). All the UM operational runs show similar spatial distribution and intensity of the rainfall over the eastern half of the country including eastern Limpopo, Mpumalanga, and Kwazulu-Natal Provinces (see Figure 6.1 for SA Provinces). These model simulations agree with the observations. However, observations show less spatial distribution over Mpumalanga but Limpopo, Gauteng and Kwazulu-Natal. However, the CCAM simulated rainfall is confined to Gauteng, northern Free State and Mpumalanga, with correct intensity, but with less spatial distribution. Likewise, all the model simulations show similar spatial pattern as the satellite and radar images in the figures above. The less spatial distribution shown in CCAM simulation could be attributed to the convection scheme selected in this study case.

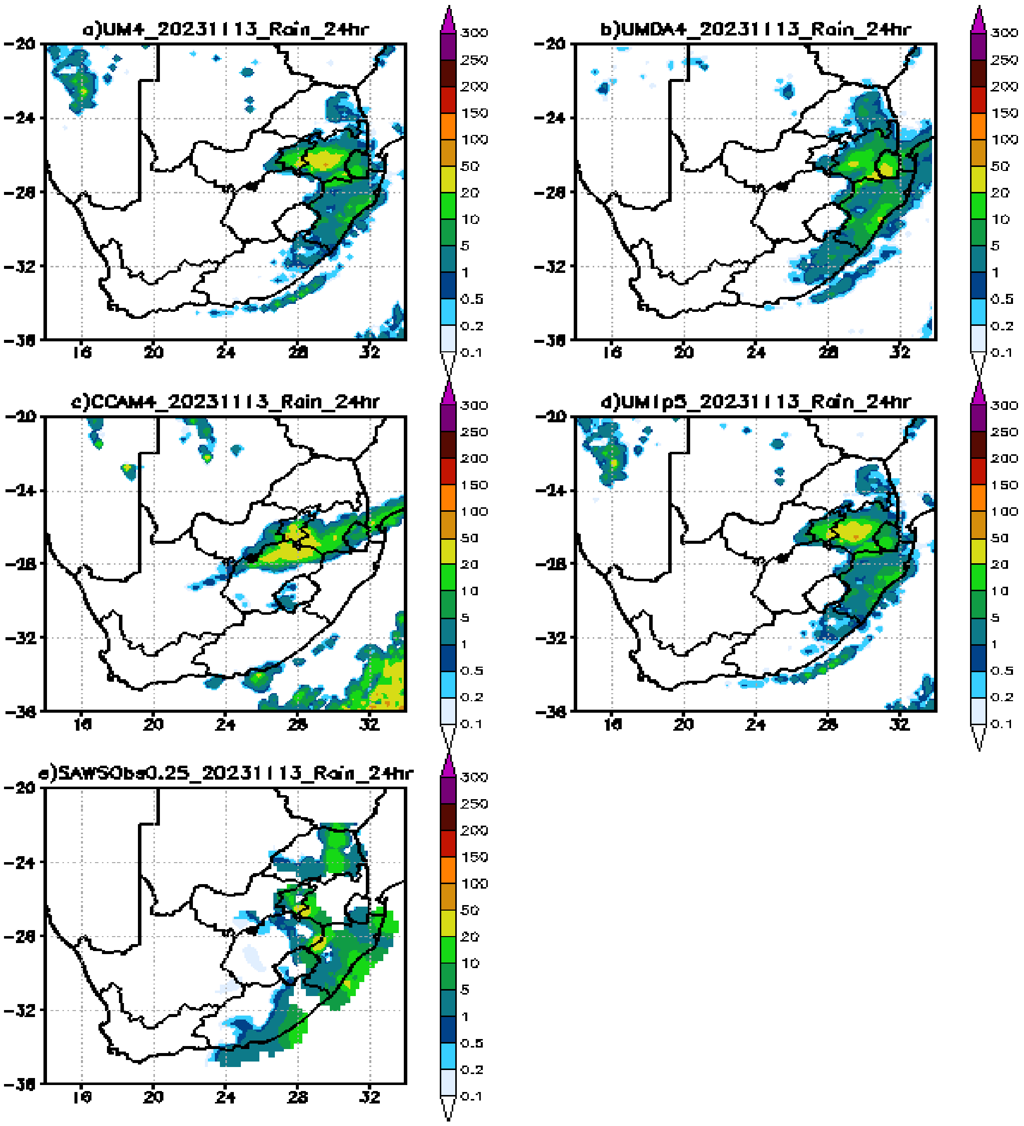

Figure 6.147: The spatial distribution of the UM 4 km (a), UMDA 4 km (b), CCAM 4 km (c), UM 1.5 km (d) rainfall and SAWS stations observations (e). All simulations have been regridded to observational data resolution of 25 km for the period 13 November 2023

From this analysis, it is shown that although the CCAM model results vary per case studies, it seems long term studies of this model could assist in understanding its system dynamics and the way the physical parameterization works. However, there is still some room of improvements on the system as it has been shown that the CCAM system is a very good system for both NWP (Bopape et al. 2022) and climate modelling studies (Muthige et al. 2018; Maisha et al.2023;).

6.3 CONCLUSIONS

In this chapter, various case studies were investigated with the CCAM model runs and compared to three SAWS operational suites, UM4, UM1.5 and UMDA4 as well as observations that have been regridded to a horizontal resolution of 0.25 degree. The models were run for a forecast period of 48 hours (2 days).

The first case study was for a cut-off low over the country during the period 22 April 2019. In this case study, CCAM configurations were initialised with both operational input data, GFS and ERA5 data. For CCAM runs with ERA5, the two model configurations under-predicted the intensity of rainfall over the central interior of South Africa including KwaZulu-Natal. However, when CCAM initialised with GFS data, the model simulated the intensity of the rainfall very well when compared to observations. In this instance, it is suspected that the pressure levels and time steps used could have contributed to ERA5 runs under-predicting the event. However, further investigations are required to correct the errors.

The second case study was for a cut-off low over Kwazulu-Natal in April 2022, which resulted in heavy rainfall over Kwazulu-Natal and parts of the Eastern Cape Province. This extreme weather event led to fatalities over Kwazulu-Natal. In these simulations, the UM4, UM1.5, UMDA4, CCAM9 and CCAM3 correctly simulated the heavy rainfall over the interior of South Africa including KwaZulu-Natal province when compared to observed rainfall. From these runs, one would conclude that the CCAM could be used operationally as a numerical weather prediction model.

The third case study was for a heatwave over most of the northern parts of South Africa, during the period 03 - 08 October 2022. This heatwave was more severe over most of the northern and western interior of South Africa. This heatwave event was analysed during the first three days, and it was shown that during the first day, the UM4 and CCAM 9 km simulated the event very well when compared to the observed maximum temperature. The UMDA4 and CCAM 9 reproduced the observed event very well over Kwazulu-Natal Province. However, the UM1.5 did well over the north-western parts of the domain, but not over the eastern half of the country. During the other two days, the results vary, but the UM4 and CCAM 9 km simulated the event very well when compared to other model configurations and were very comparable to the observed maximum temperature.

The fourth case study was for the tornado event that caused havoc over Durban, South Africa for the period 27 - 28 June 2023. All the model predictions/simulations were able to capture such a severe weather event especially over Kwazulu-Natal Province. The CCAM 4 km was also able to capture this event very well as it was comparable to observations. From these simulations only, it can be concluded that the CCAM could be used as an operational forecasting model.

The fifth case study was for the hailstorm over Gauteng and tornado over Mpumalanga during the period 13 - 14 November 2023. The storm was well tracked by the SAWS radar and Satellite applications. All the UM models used in these runs were able to pick up the spatial distribution and intensity of the storm when compared to observations. However, changes made in the CCAM 4 km run (landcover 2020) resulted in the correct intensity, but less spatial distribution.

From all these experiments, the CCAM was run at a high resolution of either 3 km, 4.5 km and 9 km nested to the CCAM 25 km run that was initialised with both GFS and ERA5 (first experiment) data at a horizontal resolution of 25 km. All the CCAM outputs show that the CCAM model can be run at a numerical weather prediction (NWP) time scale and be used for operational forecasts given that some improvements in land cover, boundary layer schemes, cumulus parameterization and that the best combination of the parametrization be investigated and applied.

In this chapter, various CCAM runs were analysed to evaluate the model performance. These CCAM simulations were performed using various model resolutions through nesting, i.e. 25 km, 9 km and 3 km and 25 km and 4.5 km. Such CCAM simulations were compared against the South African Weather Service observations. Likewise, these simulations were run with different land cover files, i.e. default, 2013 and 2020. In these runs, both the cloud microphysics and cumulus parameterization schemes were updated and they were discussed in the previous chapters. The case studies include the cut-off low (04 April 2019; 11-12 April 2022), heatwave (03 -08 October 2022), thunderstorm with tornado (27 June 2023) and thunderstorm with hail damage (13 November 2023). From these case studies, the results vary with study cases, whereby in all cases, the CCAM correctly capture the spatial and temporal distribution of the extreme weather events. This does also apply to the configurations of the Unified Model (UM).

CHAPTER 7: TROPICAL CYCLONES

7.1 BACKGROUND

Southern Africa has been hit by several high impactful tropical cyclones in recent years, including the record breaking of the deadliest storm (Idai-2019), the strongest tropical cyclone to make landfall (Kenneth-2019) and the longest lasting storm (Freddy-2023), with devastating socio-economic losses. Numerical Weather Prediction (NWP) models are the central hub of a successful early warning system for hazardous/extreme weather and climate related events such as tropical cyclones to enable early action. Although, studies have been undertaken to investigate tropical cyclones over the Southern African region using NWP (Bopape et al., 2021, Mawren et al., 2020; Rapolaki & Reason, 2018; Muthige et al., 2018), there is no NWP model that has been extensively tested on its ability to accurately forecast tropical cyclones affecting the Southern African mainland with intent to be operationalised at the National Meteorological and Hydrological Services (NMHS). The predictive skill of the Conformal-Cubic Atmospheric Model (CCAM) in relation to the intensity, tracks, position and timing of landfall for tropical cyclone Freddy (First landfall) is tested in the study. All simulations are set up at a resolution of 25 km, with 35 vertical eta levels from 12 metres to 44 km suitable for numerical weather prediction. The CCAM simulations are verified against ERA5 reanalysis data. Results show that the CCAM can capture the position and timing of landfall as well as the tracks. Shortcomings are observed at 72-hour lead time where CCAM misses landfall of the storm. The CCAM simulates far less intense storms than observations.

7.2 INTRODUCTION

This chapter evaluates the performance of the CCAM model in simulating landfalling tropical cyclones over Mozambique, that is, determining the centre location of the tropical cyclone and its movement as well as the intensity. Numerical Weather Prediction (NWP) is an important tool in weather forecasting and forms an integral part of early warning systems to enable preparedness measures. Météo France (La Reunion) is the World Meteorological Organisation (WMO) Tropical Cyclone Warning Center (TCWC) for the Southwest Indian Ocean and thus responsible for the monitoring and forecasting of any tropical cyclone related events within the ocean basin. As such, operational NMHS over the Southern African mainland lack NWP capacity for tropical cyclones (Reason & Keibel, 2004). Moses & Ramotonto (2018) reported the frequent use of global models, ECMWF and GFS for tropical cyclone forecasts at Botswana Department of Meteorological Services. The UK Met Office UM is the main operational NWP model at the South African Weather Service (SAWS). Other NWP used at operational centres over the mainland are the Consortium for Small Scale Modeling (COSMO) and the Weather Research and Forecasting (WRF) (Bopape et al., 2019; Meque et al., 2021). The performance of the NWP models in relation to tropical cyclone forecasts is fundamental for forecasters and modellers. Forecasters heavily rely on the model output to issue warnings and advisories ahead of time whereas modellers have interest in the model performance to identify areas of further improvements and development within the model. For SAWS to consider the CCAM for operational purposes, it is necessary that the model be evaluated on its capability to forecast high impact weather events such as tropical cyclones.

7.3 EXPERIMENTS

Experiments in the study were conducted over the study domain, i.e., latitudes 15 ˚S to 35 ˚S, and longitudes 30 ˚ E to 50 ˚ E (Figure 7.1), to eliminate low-pressure systems to the south of 35 ˚ S, especially when producing a time series of maximum wind speeds and minimum sea level pressure. The GFS input data at 00:00Z was used to initialise the CCAM on 22 February 2023 (72 hour forecast lead time), 23 February 2023 (48 hour forecast lead time) and 24 February 2023 (24 hour forecast lead time). Simulations of the recent tropical cyclone Freddy first landfall over Mozambique were produced at a grid length of 25 km and downscaled to 6 km over the study domain at a forecast lead time of 72 hours. CCAM simulations at 6 km are analysed in the study. Simulations of tropical cyclone intensity (maximum wind speed and minimum sea level pressure), tracks, position and timing of landfall are verified against ERA5 reanalysis at a spatial resolution of 25 km.

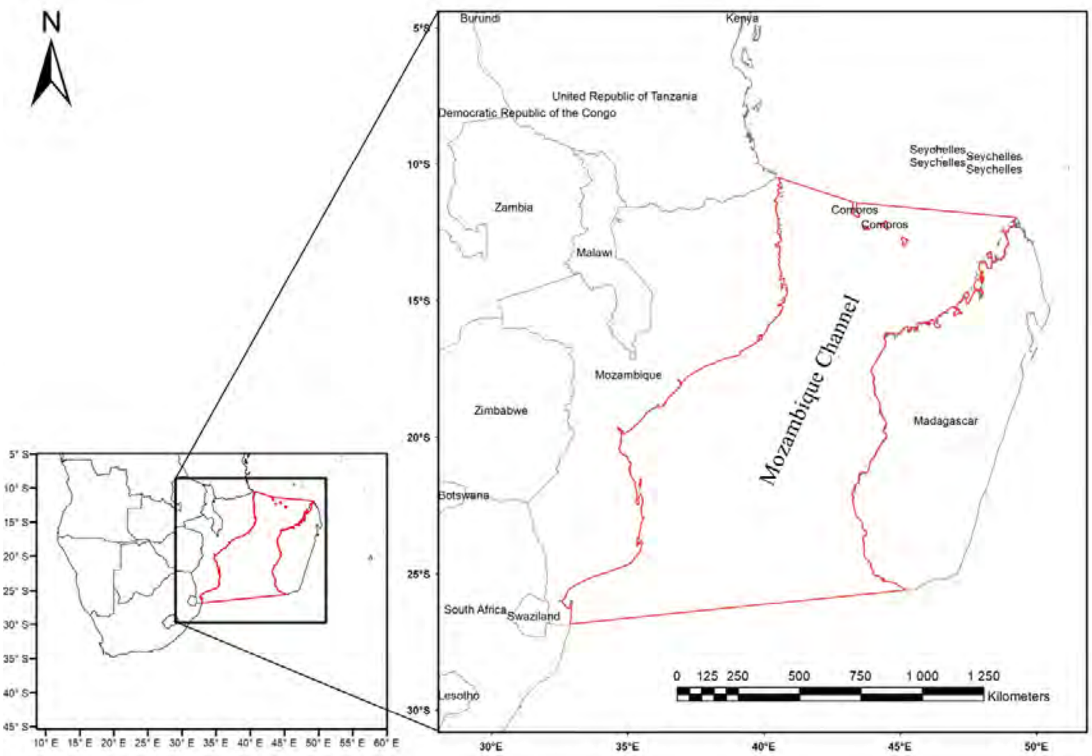

Figure 7.1: Study domain, Mozambique Channel and eastern parts of SADC.

Mozambique Channel covers an area of 700 000 km^2, and located at latitude 19 ° 18 ‘ 14.7 “ S , longitude 40 ° 52 ‘ 38.1 “ E. Tropical cyclone formation in the Mozambique Channel occurs only in January and February, with intense tropical cyclones occurring during the latter part of the season, i.e., February to April (Mavume et al., 2009). Landfall can occur either in Mozambique or Madagascar. Landfall occurs when part of the eyewall passes directly over the coast or adjacent barrier island. Freddy formed over the Australian waters during the 2022-23 tropical cyclone season, travelled approximately over 8851.39 km across the Southern Indian Ocean, making landfall over Madagascar and Mozambique (WMO, 2023). Freddy is reported to have made the first landfall over Mozambique on 24 February 2023.

Figure 7.2 shows the position of Freddy at 72 hour forecast lead time. CCAM positions Freddy to the south of Inhambane at 00Z (a) and 06Z (b) respectively, whilst the ERA5 positions the storm over southern Mozambique, close to the coast, near Inhambane. In addition, ERA5 reanalysis shows an intense storm in (c) and (d) identified from the tight pressure gradients around the centre of the storm.

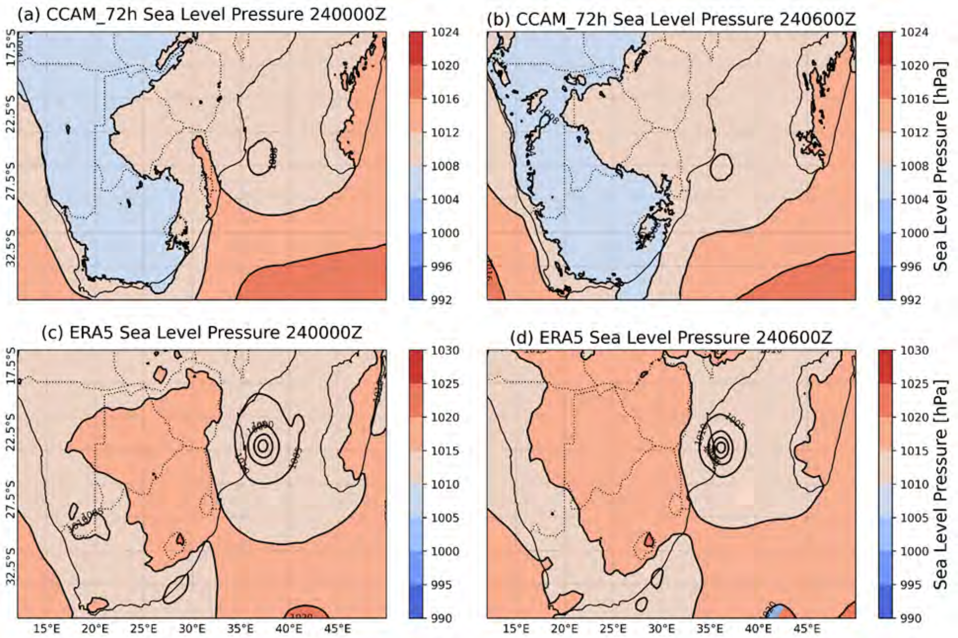

Figure 7.2: (a) and (b) represent CCAM 6 km sea level pressure 72-hour simulations initialised with the GFS 00Z on the 22 February 2023, for the 24 February 2023 during the first landfall of tropical cyclone Freddy at 0000Z and 0600Z respectively, (c) and (d) represent ERA5 reanalysis of sea level pressure circulations on the 24 February 2023 at 0000Z and 0600Z respectively.

In addition, ERA5 reanalysis shows an intense storm in (c) and (d) identified from the tight pressure gradients around the centre of the storm.

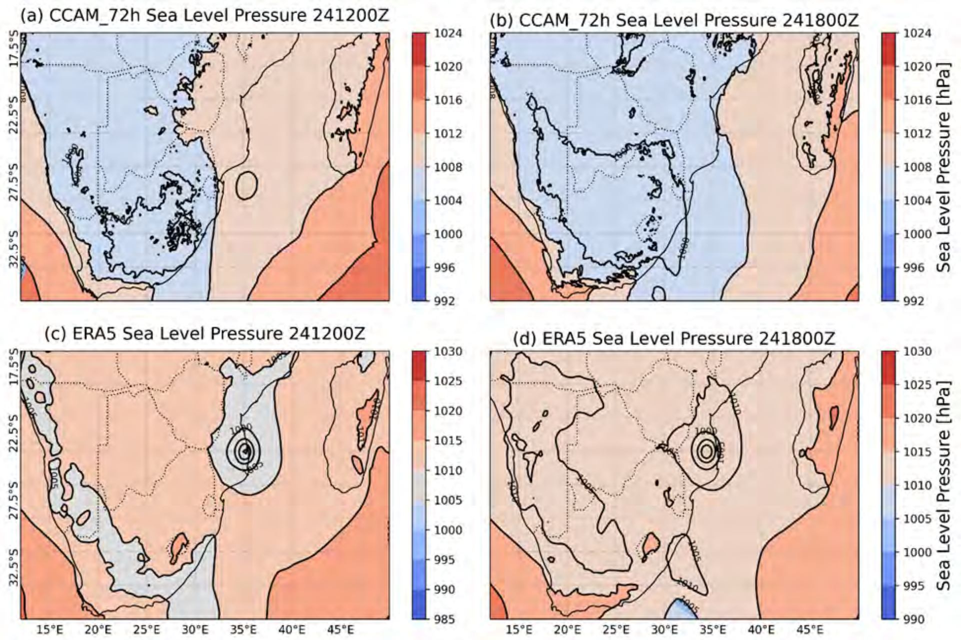

Figure 7.3: (a) and (b) represent CCAM 6 km sea level pressure 72-hour simulations initialised with the GFS 00Z on the 22 February 2023, for the 24 February 2023 during the first landfall of tropical cyclone Freddy at 0000Z and 0600Z respectively. (c) and (d) represent ERA5 reanalysis of sea level pressure circulations on the 24 February 2023 at 1200Z and 1800Z respectively.

CCAM shows that Freddy loops offshore in the afternoon of 24 February 2023 without making landfall, with complete dissipation by the evening (Figure 7.3 (a) and (b)). ERA5 reanalysis shows that Freddy has made landfall near Inhambane around the early afternoon (c) and beginning to penetrate further inland in the evening (d).

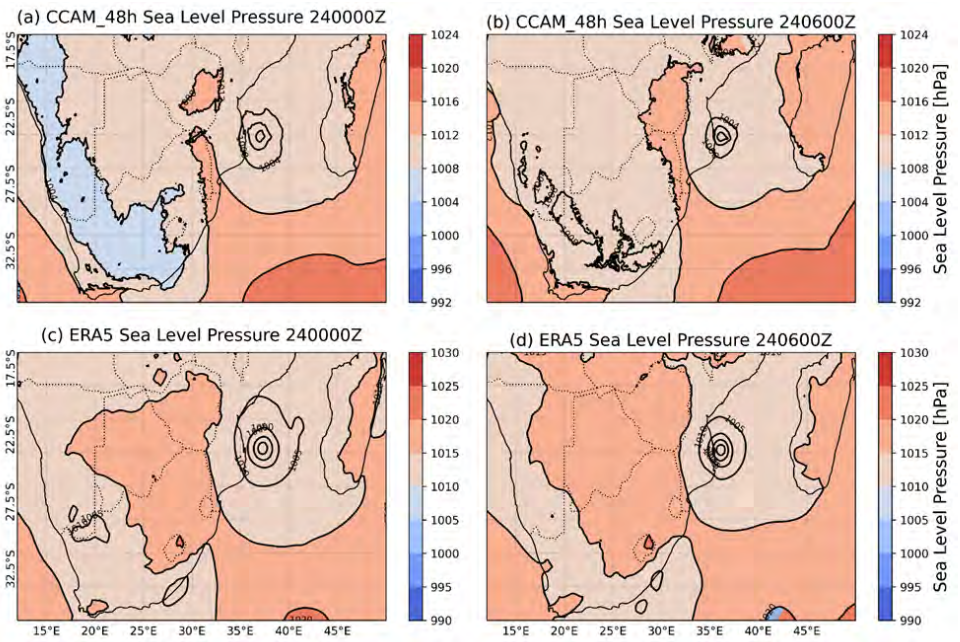

Figure 7.4: (a) and (b) represent CCAM 6 km sea level pressure 48-hour simulations initialised with the GFS 00Z on the 22 February 2023, for the 24 February 2023 during the first landfall of tropical cyclone Freddy at 0000Z and 0600Z respectively. (c) and (d) represent ERA5 reanalysis of sea level pressure circulations on the 24 February 2023 at 0000Z and 0600Z respectively.

In Figure 7.4, simulations are at a forecast lead time of 48 hours, the CCAM positions Freddy much nearer to Inhambane as compared to Figure 7.2 and Figure 7.3. In addition, the positioning of CCAM is similar to observations (c) and (d).

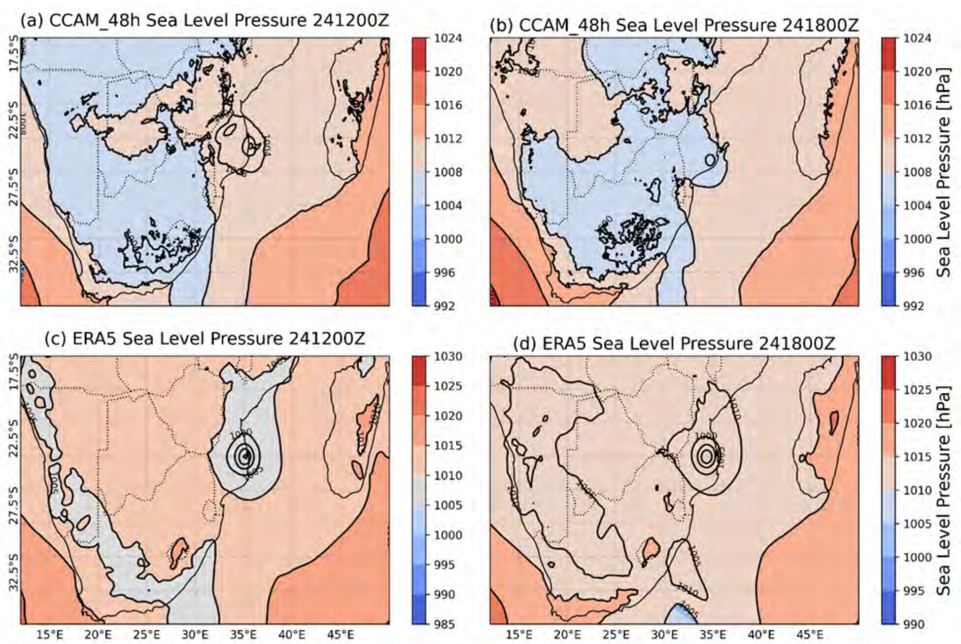

Figure 7.5: (a) and (b) represent CCAM 6 km sea level pressure 48-hour simulations initialised with the GFS 00Z on the 22 February 2023, for the 24 February 2023 during the first landfall of tropical cyclone Freddy at 1200Z and 1800Z respectively. (c) and (d) represent ERA5 reanalysis of sea level pressure circulations on the 24 February 2023 at 1200Z and 1800Z respectively.

CCAM captures the landfall of Freddy near Inhambane during the afternoon on the 24 February 2023 (a), with further inland penetration from the evening (d). Although the CCAM does not capture tight pressure gradients around the centre of the storm, the position and movement of the storm is aligned with observations (c) and (d).

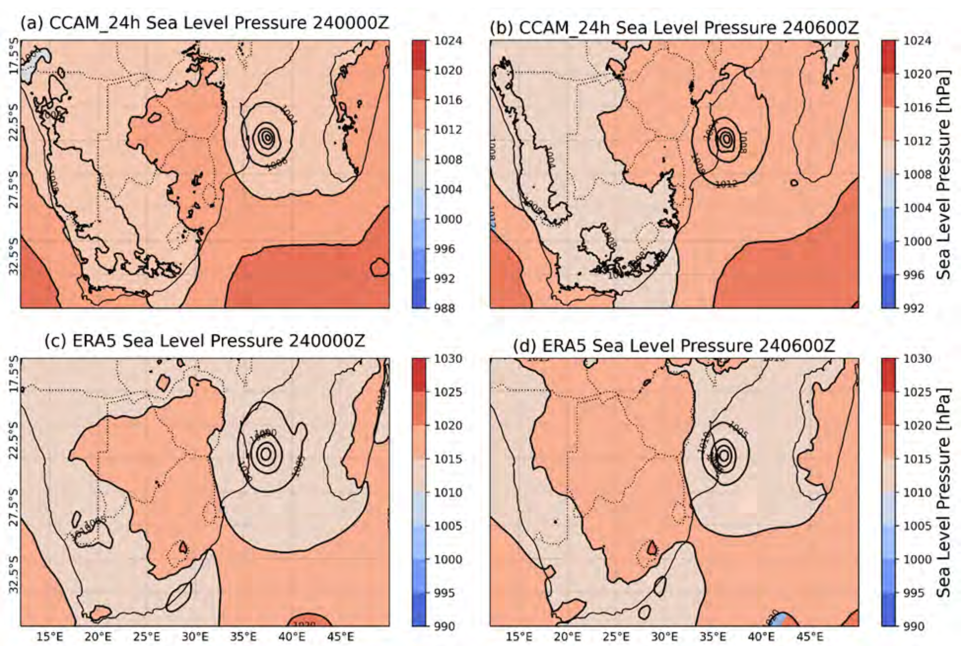

Figure 7.6: (a) and (b) represent CCAM 6 km sea level pressure 24-hour simulations initialised with the GFS 00Z on the 22 February 2023, for the 24 February 2023 during the first landfall of tropical cyclone Freddy at

0000Z and 0600Z respectively. (c) and (d) represent ERA5 reanalysis of sea level pressure circulations on the 24 February 2023 at 0000Z and 0600Z respectively.

Figure 7.6 and Figure 7.7 show CCAM simulations at forecast lead time of 24 hours for all four (4) key forecast time steps (00Z, 06Z, 12Z and 18Z). CCAM captures the tight pressure gradients around the centre of the storm and positions the storm near Inhambane. In (b), the CCAM positions the storm closer to the coast, consistent with observations.

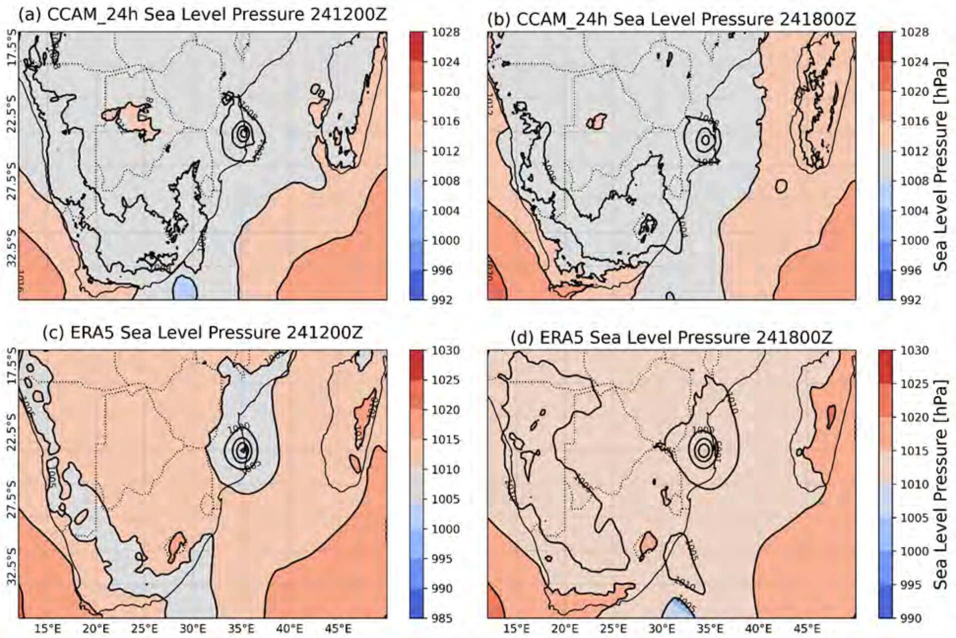

Figure 7.7: (a) and (b) represent CCAM 6 km sea level pressure 24-hour simulations initialised with the GFS 00Z on the 22 February 2023, for the 24 February 2023 during the first landfall of tropical cyclone Freddy at 1200Z and 1800Z respectively. (c) and (d) represent ERA5 reanalysis of sea level pressure circulations on the 24 February 2023 at 1200Z and 1800Z respectively.

The CCAM captures landfall of Freddy at around 1200Z (b) as well as the inland penetration from the evening (b) similar to observations, although pressure gradients are slightly less intact (a) and (b). Generally, the CCAM is able to capture all other circulations, such as the surface trough over the western interior of South Africa, the two high pressure systems (south-west and south-eastern parts) and the weak cold front slipping south/south-east of the country at 24 hour forecast lead time. The SAWS synoptic chart analysis shows the landfall of Freddy around 12:00Z, similar to ERA 5 reanalysis. The chart shows the general circulations over the surrounding oceans and over land (Figure 7.8).

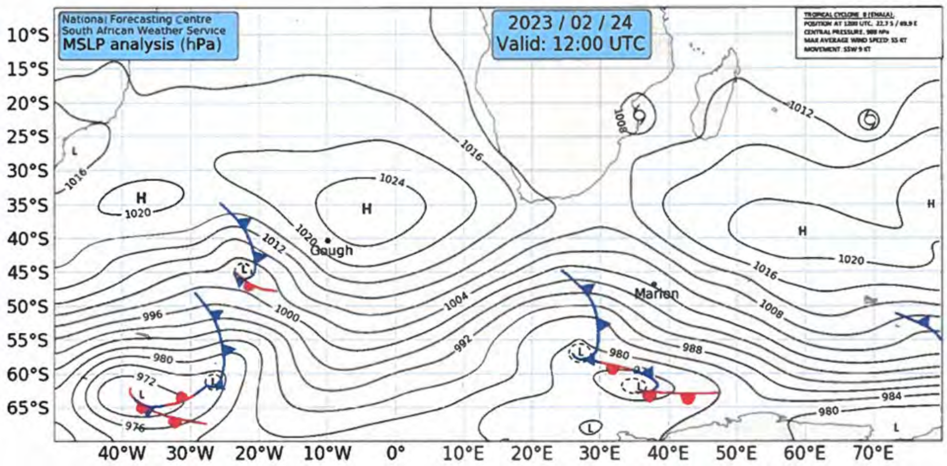

Figure 7.8: South African Weather Service Synoptic chart analysis showing the position of tropical cyclone Freddy during the first landfall on the 24 February 2023 at 1200Z.

The SAWS synoptic chart analysis shows the landfall of Freddy around 12:00Z, similar to ERA 5 reanalysis. The chart shows the general circulations over the surrounding oceans and over land.

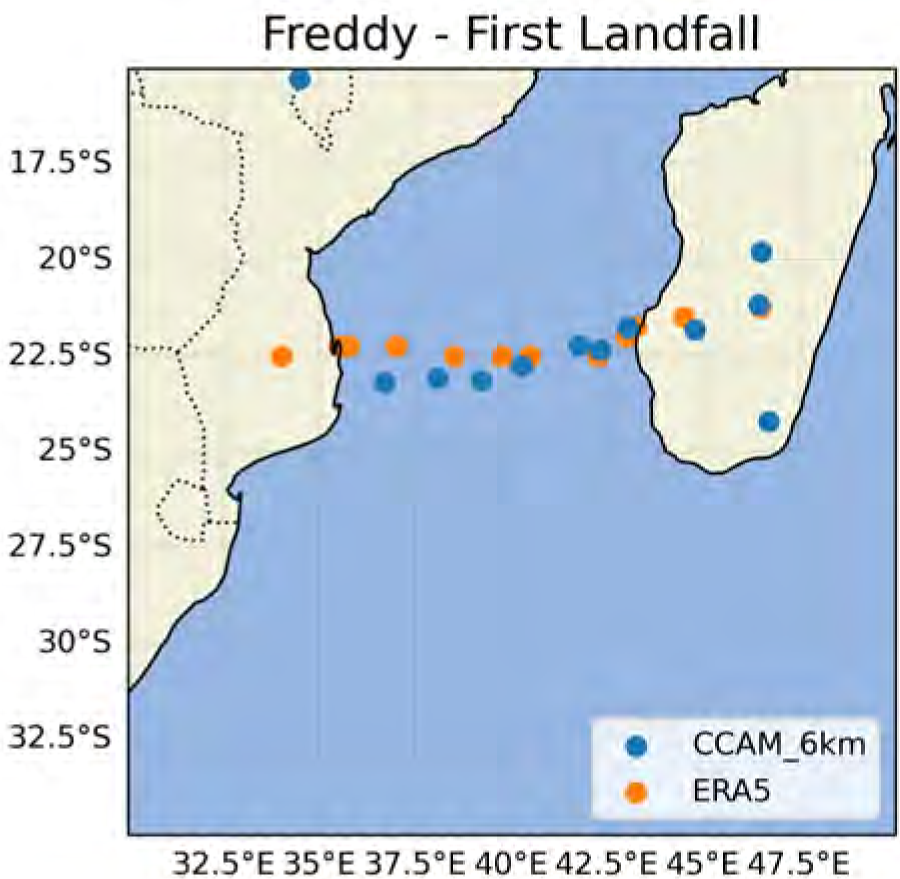

Figure 7.9: Tropical cyclone tracks of Freddy during the first landfall from 22 February 2023 0000Z until 24 February 2023 at 1800Z. Blue represents CCAM simulations, orange represents ERA 5 reanalysis.

Figure 7.9 shows the 6 hourly tracks of Freddy at forecast lead time of 72 hours, i.e., CCAM initialised with the 00Z run on 22 February 2023. The CCAM simulates the tracks mainly over Madagascar during the first 12 to 18 hours. Thereafter, CCAM tracks over the ocean are closer to ERA5, however, CCAM does not capture landfall of Freddy over the coast of Mozambique. Instead, the CCAM positions Freddy far inland of northern Mozambique during the last simulated hour, i.e., 1800Z on the 24 February 2023.

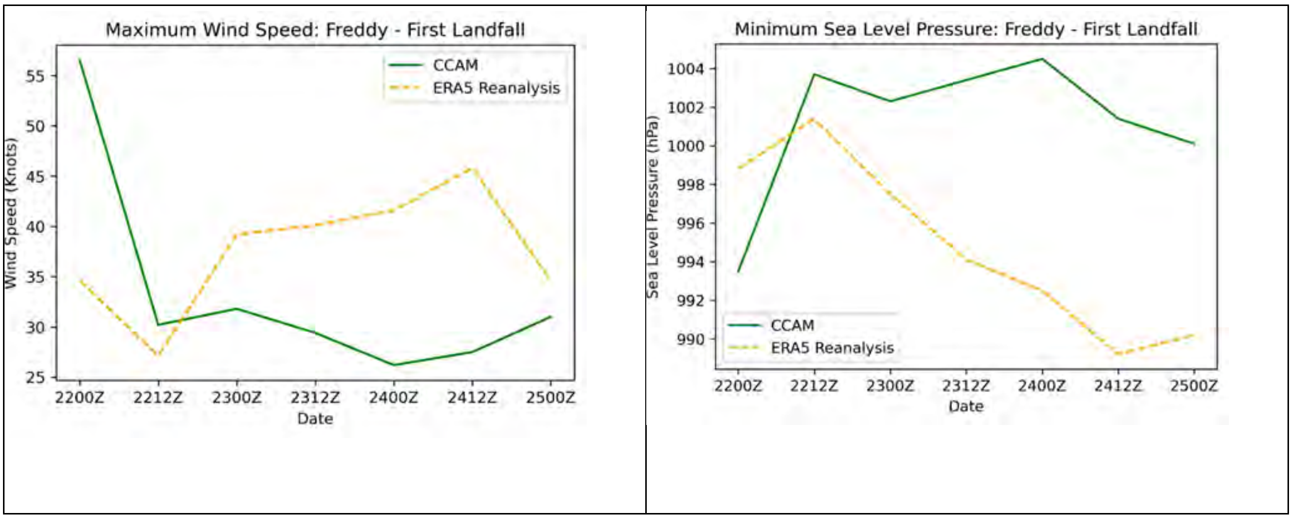

Figure 7.10: Left: Maximum Wind Speed (knots) for Tropical Cyclone Freddy during the first landfall. Right: Minimum Sea Level Pressure (hPa) of Tropical Cyclone Freddy during the first landfall. CCAM 6km simulations are represented by the green colour and thick orange dotted line represents ERA5 reanalysis at 25 km.

Figure 7.10 represents the intensity of Freddy at forecast lead time of 72 hours, i.e., CCAM initialised with GFS 00Z run on the 22 February 2023. The first twelve (12) hours represent the model spin-up period. Generally, the CCAM simulates a less intense storm than observed.

7.4 CONCLUSIONS AND RECCOMENDATIONS

The CCAM was setup at a resolution of 25 km, and downscaled to 6 km, to simulate landfalling tropical cyclones over the Southwest Indian Ocean. The CCAM was initialised with both ERA5 and GFS datasets at a horizontal resolution of 25 km. The model was setup at a lead-time of 24, 48 and 72 hours respectively,

The study concludes that the CCAM fails to capture the landfall of Freddy at least 3 days (72 hours) prior to landfall. The CCAM also positions the storm slightly south of its correct position. Significant improvement in the performance of the model is observed at 48 hours and maintains consistency at 24 hours, where the CCAM correctly positions the storm over southern Mozambique, near Inhambane. The model further captures the correct timing and position of landfall as well as the movement of the storm post landfall. The CCAM is able to capture the general circulation over the country, i.e., the subtropical high-pressure systems over the south-west and south-east of South Africa, however, fails to capture the weak cold front system south of the country at 72 hour and 48 hour forecast lead times. The CCAM captures the latter during the second half period of the 24-hour forecast. In relation to intensity, the CCAM simulates far less intense storms than is observed.

Future experiments to exclude Madagascar to assess the impact of the topography of Madagascar on the intensity of the storm. Furthermore, analysis to include Best Track data which remains not available at the time of writing the report and post grid model simulations to the resolution of observations to ensure that both model and observations are on the same resolution for best verification results. Finally, more tropical cyclone cases to be simulated and compared with the current main operational NWP (UM 4.4km) at SAWS.

CHAPTER 8: CUT-OFF LOWS

The attached chapter is a contribution from the PhD student, who is a member of the project and is sponsored by the WRC project. The attached document is a final version of the article published by the MDPI journal.

8.1 INTRODUCTION

South Africa is located on the southernmost tip of Africa and is predominantly a semi-arid region with high rainfall variability, characterised by frequent extreme weather events. The country is also widely recognised as one of the most vulnerable to climate change due to the low levels of adaptive capacity (particularly among rural communities), combined with a high dependence on rain-fed agriculture [1]. The subcontinent is surrounded by the warm southwest Indian Ocean in the east and the cold South Atlantic Ocean in the west. The disparity in ocean currents is partly responsible for the spatial gradients of rainfall such that arid conditions in the west (cold Benguela current) give way to a subhumid climate in the east (warm Agulhas current). The southwest Indian Ocean plays a vital role in rainfall over South Africa as it is a major source of moisture for the region, transported onshore by trade winds from the Mascarene High pressure system [2]. Furthermore, the spatial vegetation and soil moisture conditions evidently reflect the same west–east gradient over southern Africa.

Most rainfall occurs during the austral summer, but the southwest and coastal regions experience significant rainfall in winter. Several weather systems bring rainfall to the region in summer, including cloud bands from tropical–temperate troughs [3], mesoscale convective systems [4], tropical continental lows [5], and tropical cyclones from the southwest Indian Ocean and Mozambique Channel [6]. During the austral winter, cold fronts, ridging anticyclones [7] and cut-off lows (COLs) are also significant producers of rainfall, especially over the southern districts of South Africa [7–9]. Cut-off lows are unique not only due to their severity and impacts but also because they occur throughout the year [8].

This research focuses on a comprehensive review of the literature on characteristics of COLs from a regional perspective, critically evaluating the existing knowledge whilst establishing possible gaps. The paper is organised into thematic areas and begins by defining COLs and understanding the seasonality and contribution of COLs to annual rainfall over South Africa. The historical impacts of COLs are detailed and the treatment of numerical weather prediction (NWP) models is also evaluated (Figure 8.1).

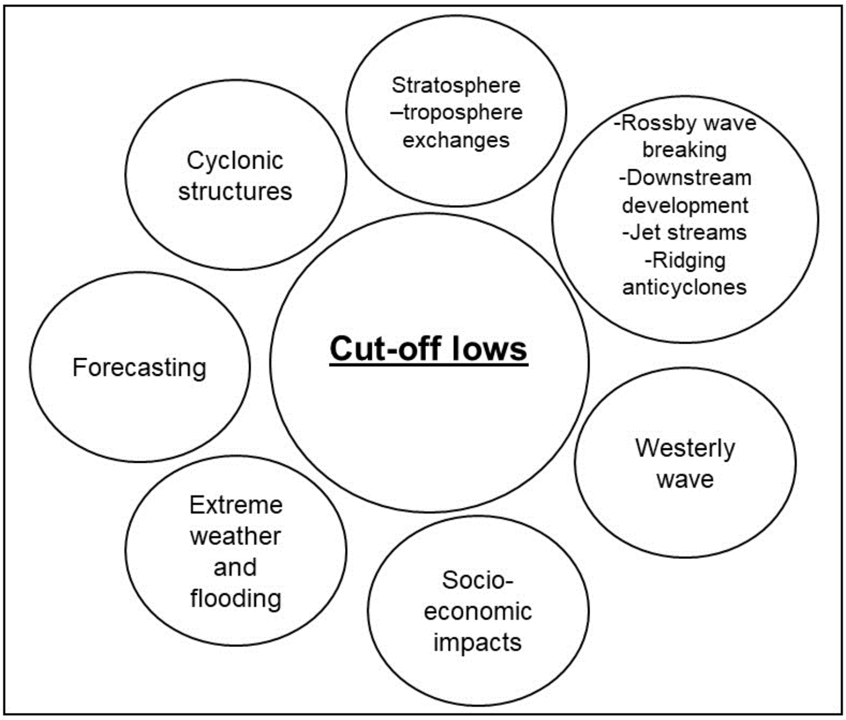

Figure 8.1: Conceptual framework demonstrating the literature focus on the study of COLs.

8.2 DEFINING CUT-OFF LOWS

The definition of COL weather systems varies throughout the literature. They have been defined as cold-cored synoptic-scale mid-tropospheric low-pressure systems which occur in the mid-latitudes but extend to the subtropics, accounting for major severe rainfall and cold events [10,11]. COLs occur when they become isolated from the westerlies and are displaced equatorward [12]. Others define COLs as quasi-stationary, short-lived weather systems [13] that form and develop within the westerly wave, equatorward of the polar jet-stream, forming closed cyclonic circulations in the middle and upper troposphere [9,14]. Due to consistent COL features, most studies define COLs as closed circulations at 500 hPa [15,16] and between 200 and 300 hPa [8,16,17,19,34]. Rainfall in the subtropical regions is influenced by COLs, one of the major synoptic-scale systems [8].

COLs form as low atmospheric pressure regions without a closed isobaric contour in the upper levels. The systems result from deep moist convection caused by cold air aloft (depression) and are detached from the westerlies visualised through an equatorward cyclonic segregation at 500 hPa [19,20]. Through this development, COLs form a closed low system detaching from the westerly wave extending towards the surface, causing unstable and severe weather conditions (i.e., thunderstorms, strong winds, heavy rain, hail or snow [21].

The life cycle of a COL is characterised by four stages as determined by Nieto et al. [17] for the Northern Hemisphere and adapted to Southern Hemispheric COLs by Robeita et al. [16]. The first stage is the development of an upper-level trough and a temperature wave found west of the geopotential wave. The second stage involves the detachment from the westerly wave also referred to as the tear-off stage. The third stage involves the cold air penetrating the centre of the trough moves equatorward independently and is also referred to as the cut-off stage. When the COL dissipates and merges with a deep trough in the westerly zonal jet, this is known as the fourth stage of the weather system [22].

While most weather systems are ‘travelling’ disturbances, a cut-off low is unique as it is slow-moving, resulting in the persistence of anomalous weather conditions for up to 3–4 days on average [8,23]. In some cases that affect southern Africa, the westerly wave develops a blocking high over the Indian Ocean, resulting in COLs developing behind it [24]. Over South Africa, mid-tropospheric COLs are often accompanied by surface ridging anticyclones. Ridging occurs when a South Atlantic anticyclone (St Helena High) extends or propagates eastwards around the southern Africa landmass. Two types of ridging anticyclones have been identified over the South African domain, being equatorward (Type N) or poleward (Type S) of the 40S latitude [25]. When COLs extend to a surface low with no presence of a ridging anticyclone, they have been found to cause more extreme weather conditions [22]. COLs that are linked to surface lows over South Africa are frequent during autumn, over high latitudes and are sprightly and long-lived [8,22].

Quasi-stationary subtropical anticyclones are characterised by minimal frontal activity and weak pressure gradients [24]. The system can be centred over southern Africa and mostly influences subsidence and settled weather over most parts. However, when located south or southwest of the subcontinent, the system can be termed ridging, causing wide-spread unsettled weather over the eastern coastal areas.

As COLs occur in westerly waves where cold frontal systems are located, they occur throughout the year over South Africa, though with an autumn (March–May) maximum and a secondary peak during the austral spring from September to November [8]. In spring (from September to October or November), COL rainfall is more intense and widespread over the region. In South Africa, the contribution of COL to annual rainfall is significantly higher during the spring and autumn months [9], with the Eastern Cape Province in the south most frequently affected by COL landfalls and heavy rainfall [26].

8.3 DESCRIPTION OF STUDY AREA

This study mainly focused on South Africa, which is located on the southern tip of southern Africa and bounded by disparate ocean currents over the Atlantic and Indian Oceans (Figure 2). In the southern Africa region, South Africa is the most affected by COLs, which often lead to severe socio-economic impacts. COLs occasionally bring extreme rain-fall to the south of Namibia, Botswana and Zimbabwe, following Singleton and Reason [8]. As shown in Figure 8.1, COLs exhibit different structures depending on whether they occur over polar, mid-latitudes or tropical latitudes [27]. Over the Southern Hemisphere, COLs also affect the continents of South America and Australia. They are responsible for 50% of April–October rainfall, and 80% of daily rainfall in south eastern Australia [28,29], increasing the frequency of heavy rainfall when compared to other weather systems [30,31]. In Australia, COLs are the second highest distinct synoptic weather system contributor of rainfall dominating the interannual variability [30–33] and are most frequent during the positive phase of the Southern Annular Mode [18]. Although southern Africa has the lowest number of COL occurrences [15,16,34], intense COLs have been responsible for extreme rainfall events over the subcontinent. It is also noted that studies on COLs over the Southern Hemisphere have increased over the years.

The complex topography of South Africa, characterised by a steep coastal escarpment and a high inland plateau (Figure 8.2), affects the atmospheric circulation, strongly influencing the occurrence and modification of COLs [10,35,36]. COLs that are located above topographic gradients due to elevated escarpments are affected by orographic forcing, which enhances lifting, resulting in deep convection. Sometimes, low-level jets impinge on the escarpment during COL events or cloud bands, resulting in extreme rainfall and flooding [26,37].

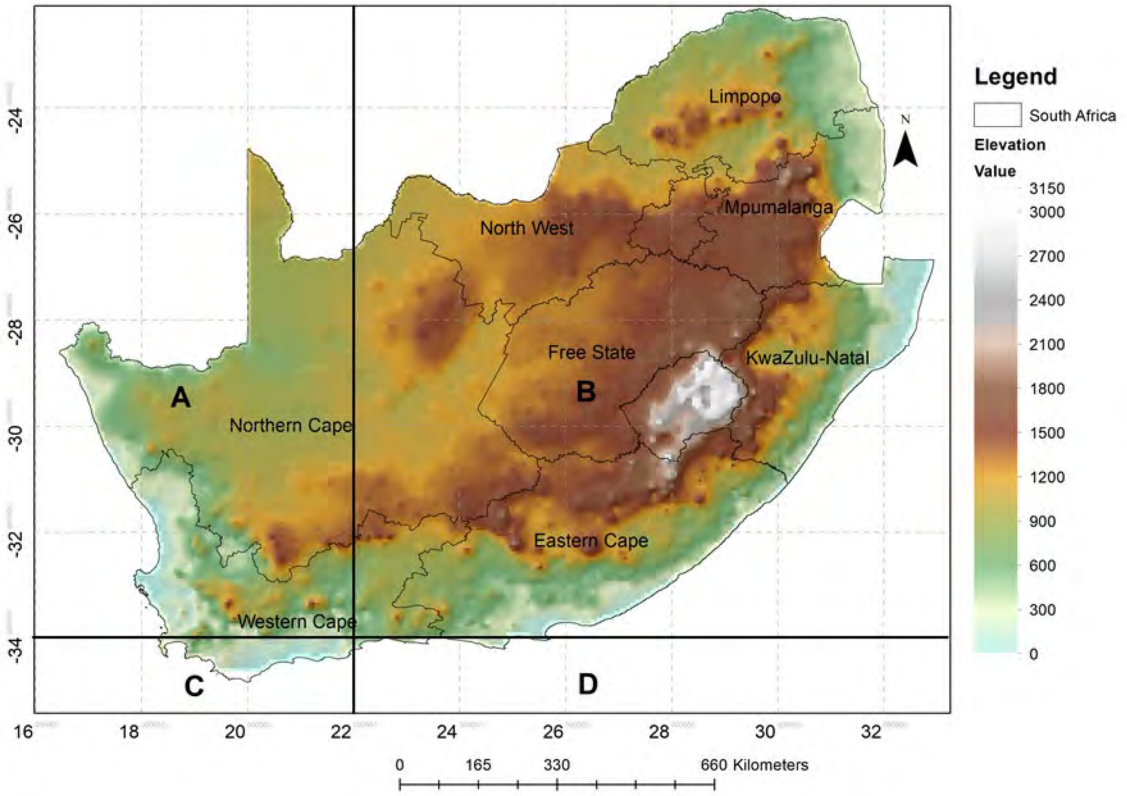

Figure 8.2: Map showing four South African COL regions and elevation (after Singleton and Reason [8]).

8.4 SEASONALITY AND CONTRIBUTION OF COLS TO ANNUAL RAINFALL OVER SOUTH AFRICA

COLs occur throughout the year, with an average of approximately 11 making land-fall over South Africa in a year [8,38]. Despite an all-year climatology, COLs are most frequent during the transition seasons: March–April–May and September–October–November [8]. Comparatively, in the southern Australian region, COLs are most frequent during the period from May to October [39]. In South America (i.e., Peru, Chile, Argentina) they occur frequently in spring and autumn over the region 68–80° W and 30–45° S, with most occurrences in the Pacific region, followed by the Atlantic and continental regions [40,41]. COLs are likely to produce heavy rainfall across parts of South Africa when they occur [9] and contribute significantly to the annual accumulation of rainfall in South Africa. The movement of COLs occurring in the tropics has been found to be more erratic as they tend to move in a westerly direction or decay with an equatorward trajectory [9].

8.5 DYNAMICAL PROCESSES AND UPPER-AIR INTERACTIONS DURING COLS

Typically, COLs occur in the upper air in the presence of a ridging anticyclone at the surface, with low-level convergence and enhanced lifting in the mid-troposphere (Figure 8.3). The development of COLs is usually due to the presence of unstable baroclinic Rossby waves (RWs) [9,41,43] that form due to the rotation of the planet. RWs (or planetary waves) are identified by their horizontal uniformity, whereby air particles move in a north–south direction with latitudinal circular propagation [24].

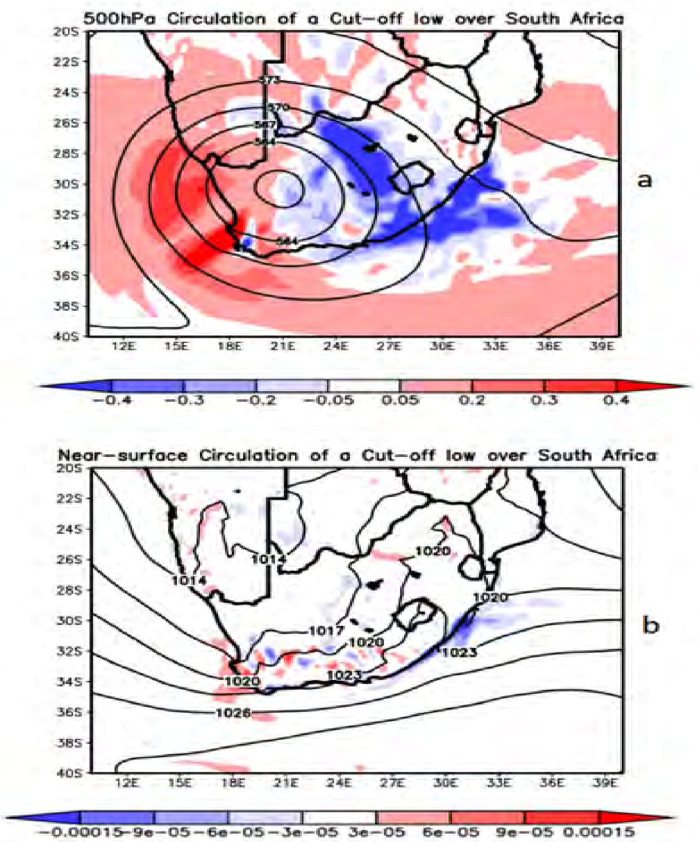

Figure 8.3: Typical 500 hPa (geopotential height and omega) and (b) near-surface (MSLP and divergence) circulation associated with a cut-off low over South Africa [24]. The variables plotted here were obtained from the ECMWF ERA5 reanalysis [42].

RWs can continue to be sufficiently unstable, forming vortices (i.e., depressions, COLs or blocking anticyclones). They are a dominant component of the Ferrel circulation. The existence of these waves explains the low-pressure cells (cyclones) and high-pressure cells (anticyclones) that are important in producing the weather of the middle and higher latitudes.

The closed cyclonic circulation results from a high potential vorticity (PV) anomaly [44] that is caused by the isentropic transport of high PV stratospheric air, which in turn is associated with upper-tropospheric Rossby wave breaking (RWB) processes [34]. COLs are characterised as closed geopotential height contours in the middle levels, associated with significant potential vorticity (PV) anomalies cut off from the stratosphere due to RWB [34,45]. The occurrence of high PV anomalies and RWB in the troposphere is associated with COLs [17,46,47]. RWB is a rapid and irreversible transformation of PV contours [48]. PV anomalies result from the invasion of high PV stratospheric air transported isoentropically and equatorially into the upper troposphere [49].

The upper layers of the troposphere are characterised by high baroclinicity during COLs [50]. The presence of cold air aloft allows for the shrinking of the tropopause. A key role played by COLs is in stratosphere–troposphere exchanges, which sometimes alters the ozone concentration at high altitudes [51–53], allowing PV to be useful when tracking COLs [54]. Deep intrusions of stratospheric ozone-rich air downward can be caused by the occurrence of COLs [55]. This stratospheric intrusion can be important at high altitudes since ozone is a pollutant in the troposphere. The significance of the occurrence of COLs is in the dissipation, exchange and mixing of the tropospheric ozone balance [56,57]. Tropopause folding also enhances the exchange of air between the stratosphere and tropo-sphere, which is rich in ozone [58,59].

Along the tropopause, there are fast-moving streams of wind known as jet streams influencing large-scale global circulations. They result from a strong horizontal temperature gradient along the top of the troposphere due to the difference in high- and low-pressure columns. They are known as subtropical and polar jets over both hemi-spheres [24]. The portion of the overall jet stream where winds along the jet core flow stronger than in other areas along the jet stream is referred to as the jet streak. The entrance (exit) region of a jet streak is where winds are accelerating into the back/upstream (decelerating out of the front/downstream) side of the streak. Within the entrance region of a jet streak, divergence (of the ageostrophic wind) usually occurs along and to the right of the jet core (i.e., the right-entrance region) [43]. Upper-level divergence causes pressure/height falls at the surface and/or lower-to-middle levels underneath the upper divergence maxi-mum. Southern African weather is largely affected by the subtropical jet, which migrates poleward in the austral summer and equatorward in the austral winter. The powerful winds of the jet stream are responsible for pushing weather patterns around the world. Typically, they move from west to east in a steady fashion. Occasionally, a low-pressure system or storm will be pinched off from the jet stream and become stalled. This is where a cut-off low derives its name from.

8.6 IMPACT OF COLS

Extreme weather events usually lead to several incidences of social, environmental and economic impacts. In many cases, the occurrence of flooding due to COLs in South Africa has been declared a national disaster. This follows the need to implement the response requirements of South Africa’s Disaster Management Act, Act No. 57 of 2002, by all three spheres of government. The South African Weather Service (SAWS) has records, archives and information on weather extremes and their impacts in South Africa dating back to the

1500s in a publication called Caelum. This is a publication that is updated monthly and uses information collected mainly from media sources such as newspapers. The Caelum publication describes notable weather and weather-related events that made it to media publication and is shared with South Africa's National Disaster Management Centre (NDMC) as well as other research institutions on request. Information stored in this document includes dates of the weather events, their socio-economic impacts and the regions affected.
Of all rainfall-producing systems occurring over South Africa, COLs have the most devastating impact, claiming many lives each year. In April 2022, at least 443 people died and 40,000 were displaced when floods from a COL ravaged the east coast of KwaZulu-Natal [60]. Approximately 4000 homes were destroyed by floods in the area, whilst schools, clinics and roads were destroyed by the same system [60]. As far back as 1981, over 100 people drowned in COL-induced floods in Laingsburg [61]. Other common im-pacts of COLs recorded in the SAWS Caelum include negative impacts on agricultural yields, water-borne diseases (e.g., cholera, diarrhoea) and damage to power stations because of heavy rainfall and strong winds associated with these weather systems. It is evident that COL occurrence over South Africa has impacts that include widespread flooding, damage to bridges and roads and displacement of vulnerable affected communities. While Caelum is a good source of information on extreme weather-related impacts, it has been criticised for lacking proper quality-control schemes and for under-reporting impacts in certain regions.

COLs can cause flooding over South Africa due to persistent heavy rainfall [8], resulting in severe infrastructure damage and halting local economic activities [10]. Flooding can have an overwhelming toll on the socio-economic exercises of any community, particularly in developing countries, where human strength and preparedness for climate extremes are exceptionally low [62,63].

The slow-moving nature of COLs contributes to their high impact, as happens when anticyclonic conditions persist. COL movements tend to be quasi-stationary, causing large rainfall accumulation over a particular region and, thus, contributing to flooding events over South Africa [26]. Some regions experience worse weather than others—with snow-fall (e.g., Andean highlands), flash floods, mudslides and disruption to transportation and electricity supply. In addition, the deep moist convection taking place within COLs can produce short bursts of extreme rainfall, leading to 20% of all flash-flooding events over South Africa [8].
Whilst COLs are more frequent over South Africa than tropical revolving systems, they may be comparable to tropical cyclones in terms of producing severe weather, heavy rainfall, floods and destruction. However, not all COLs are associated with severe weather. The occurrence of COLs over South Africa induces forest fire suppression due to flooding, snow and extreme cold conditions. Other impacts of COLs include economic losses which run into billions of South African Rand, due to the destruction of electrical power transmission lines, roads and bridges. It is important to note that although some of the re-cent COLs have led to destruction and fatalities, some of them have not been as intense. Thus, any deluge of rainfall from these systems was exacerbated by human factors that led to flash flooding, mudslides, infrastructure collapse, etc. For example, rural–urban migration has led to illegal infrastructure developments, more sewer demands or the blocking of drainage systems and riverbank farming, especially in wetlands or on unstable platforms [64].

As a result, several studies have documented case studies of severe COLs which produced extreme rainfall and devastating impacts [10,26,35,65,66]. From our review, it appears most high-impact events associated with COLs occur along the coast and cause damage to properties, infrastructure and the environment. We focus here on two such COL cases [8,10] which resulted in anomalous weather and very high impacts, including the loss of lives and livelihoods in East London (Eastern Cape) on the south coast and Durban (Kwa-Zulu Natal) on the east coast. In both cases, the role of the coastal escarpment was dominant. The study used the geopotential height, vertical velocity (omega), wind vector and total rainfall from the ECMWF ERA5 reanalysis [42] to analyse these events.

8.6.1 Case 1: 14 – 17 August 2002

On 15 August 2002, an intense COL spinning independently from the westerly wave was well developed over East London in the Eastern Cape province (Figures 8.4–8.6), where 317.2 mm rainfall was measured [67]. The event dumped devastating rainfall, which was approximately four times the monthly average in 24 h [26]. The region experienced a relatively high amount of moisture uplift induced by the presence of low pressure aloft, low temperatures at the surface and high convection rates. A low-level jet was impinged on the escarpment, enhancing lifting and convection and resulting in extreme rainfall for a short duration [26]. The conditions over East London during this period were anomalously cold and wet. The SAWS Caelum reported that this COL led to the death of 14 people, 3000 were left homeless and the estimated cost of all damage was around ZAR 2 million.

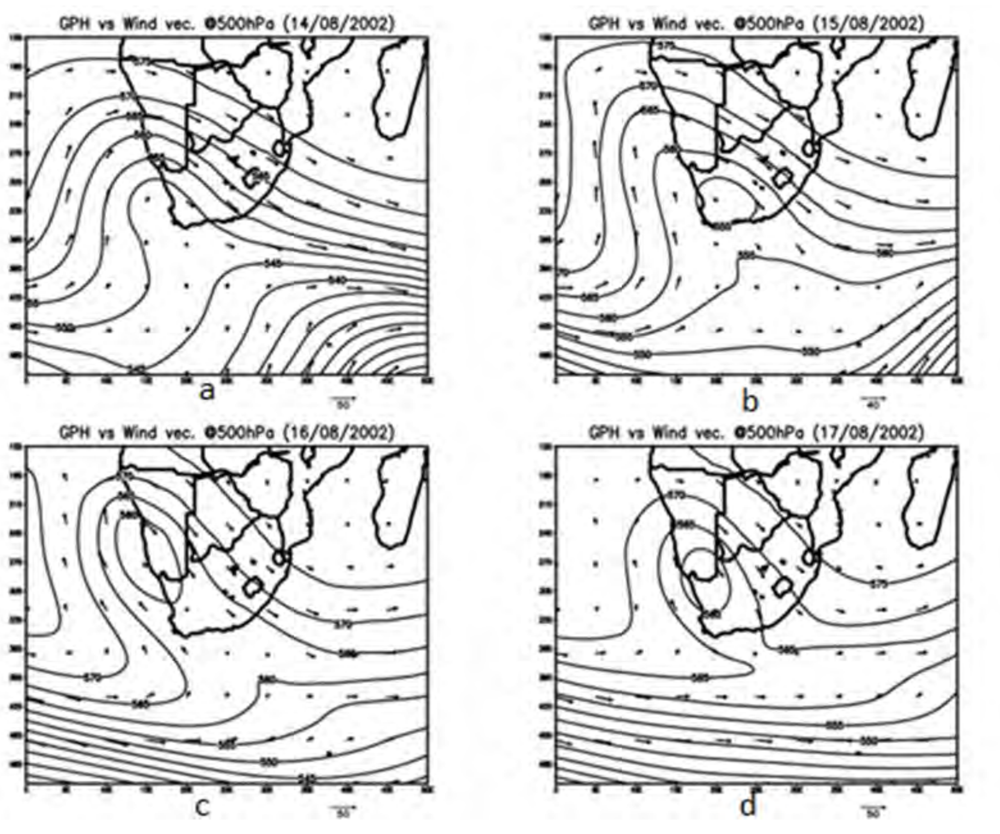

Figure 8.4: Geopotential height vs. wind vector at 500 hPa (14–17 August 2002).

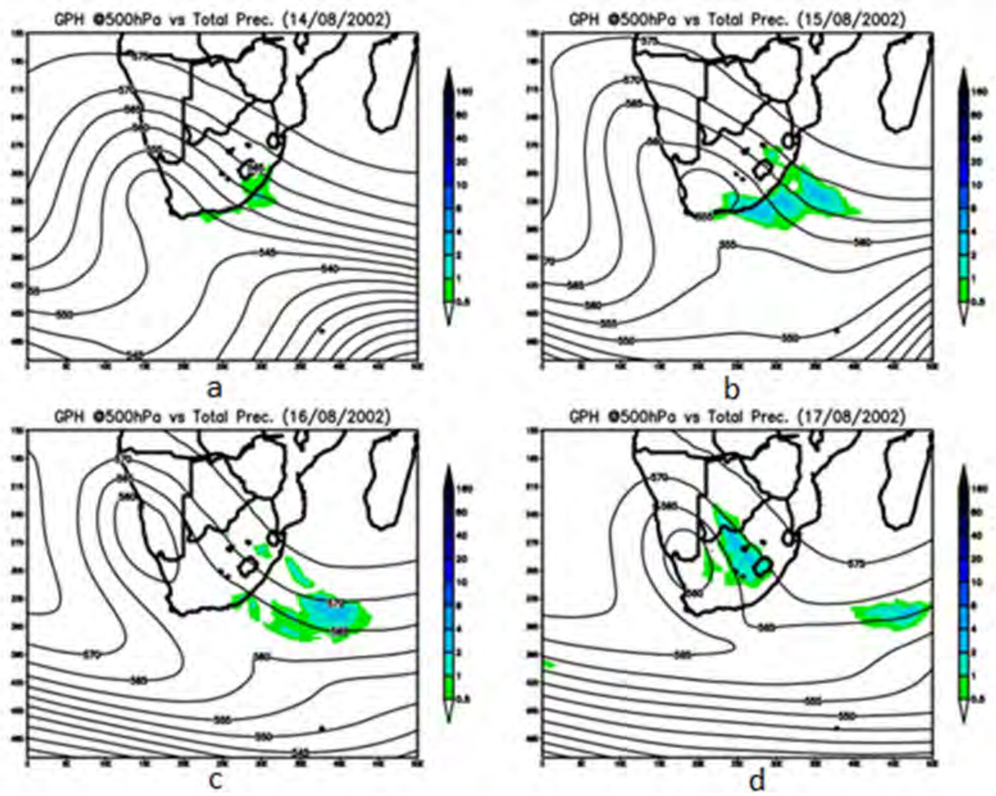

Figure 8.5: Geopotential height 500 hPa vs. total rainfall (14–17 August 2002).

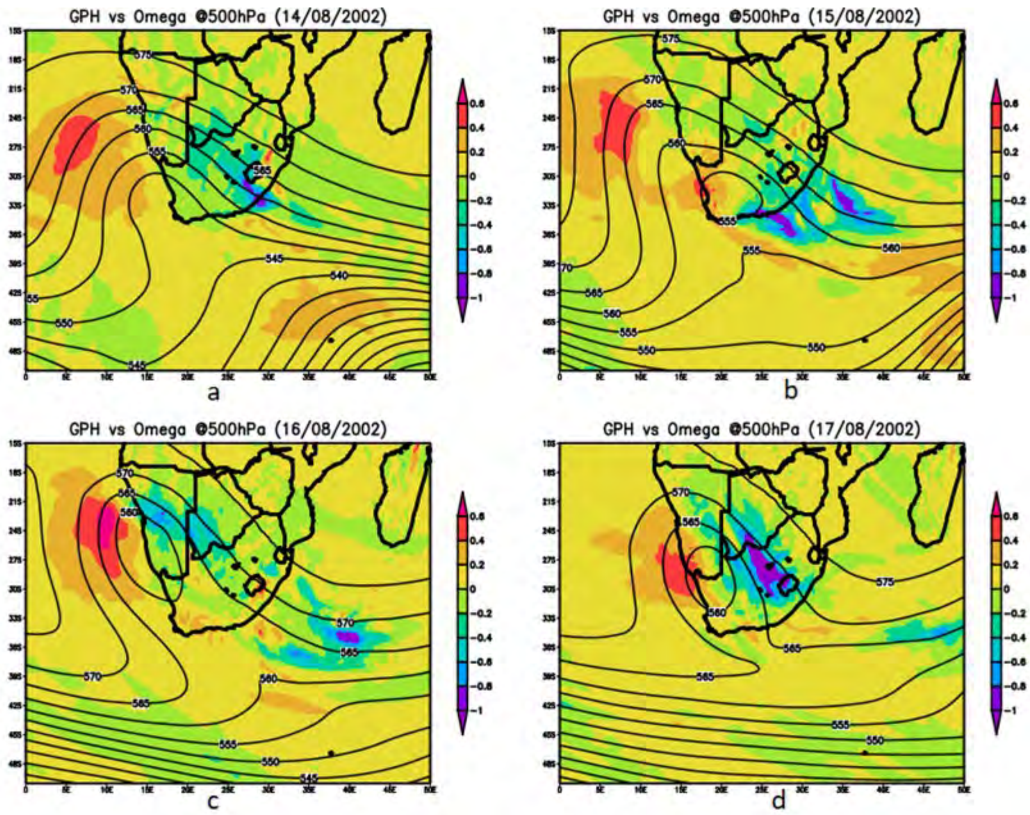

Figure 8.6: Geopotential height vs Omega at 500 hPa (14–17 August 2002).

8.6.2 Case 2: 22 – 25 April 2019

This slow-propagating COL produced intense rainfall and severe flooding over parts of South Africa [10]. There was the presence of a Type S ridging high pressure system at the surface. This occurrence took place during 22–25 April 2019 (Figures 8.7–8.9), which was an Easter weekend in South Africa. The independent spinning of the COL that detached from the westerly wave was evident. During this period, there are usually high peaks or road travel. The COL dumped prolonged rainfall of approximately 150–200 mm in 48 h [68] and resulted in 80 deaths and damage to infrastructure, settlements, roads and the water and electricity supply in KwaZulu-Natal province due to localised flooding [69]. While Caelum did not report any estimated costs associated with the damage caused by this COL, it did document that several bridges and roads were washed away, and many businesses were lost because of the severe flooding and mudslides that occurred. Town-ships, informal settlements and developed urban areas were also severely affected. The unusual flooding and destruction over developed urban areas was an indicator of possible poor planning, maintenance and decaying infrastructure.

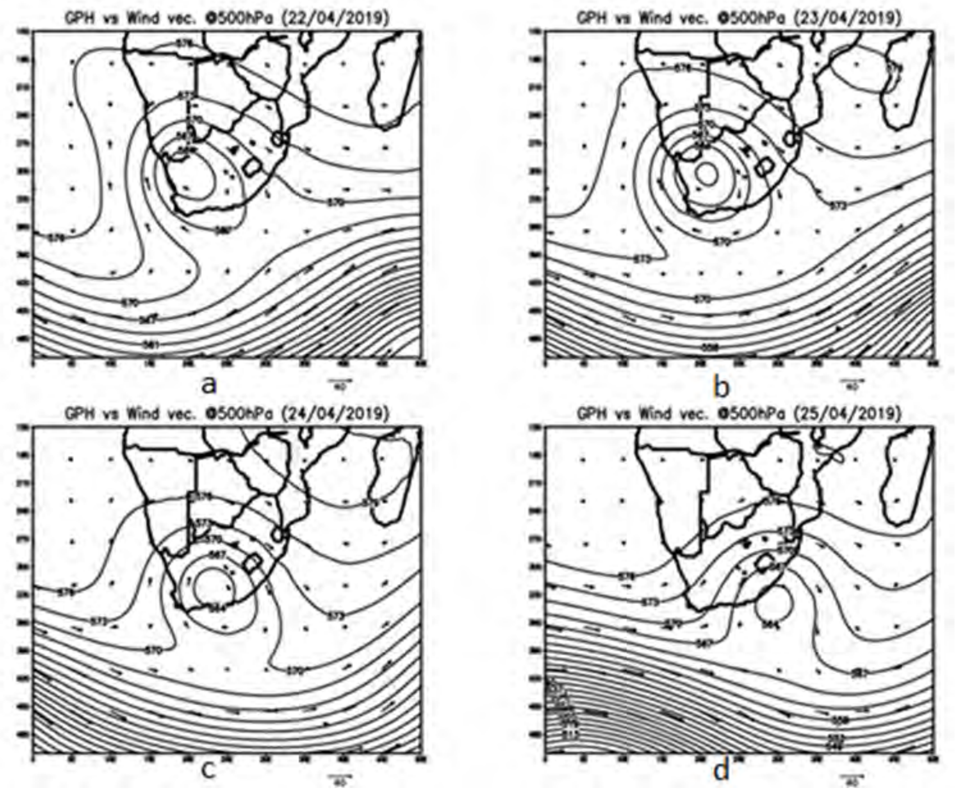

Figure 8.7: Geopotential height vs. wind vector at 500 hPa during the period 22–25 April 2002.

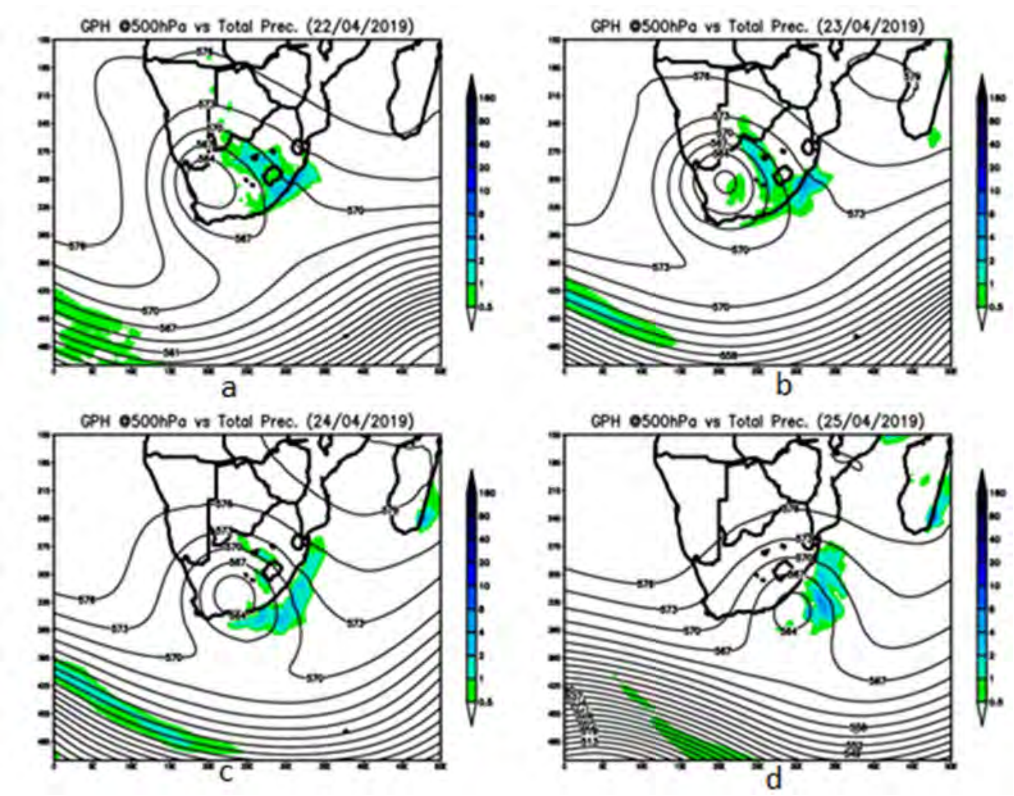

Figure 8.8: Geopotential height 500 hPa vs. total rainfall (22–25 April 2002).

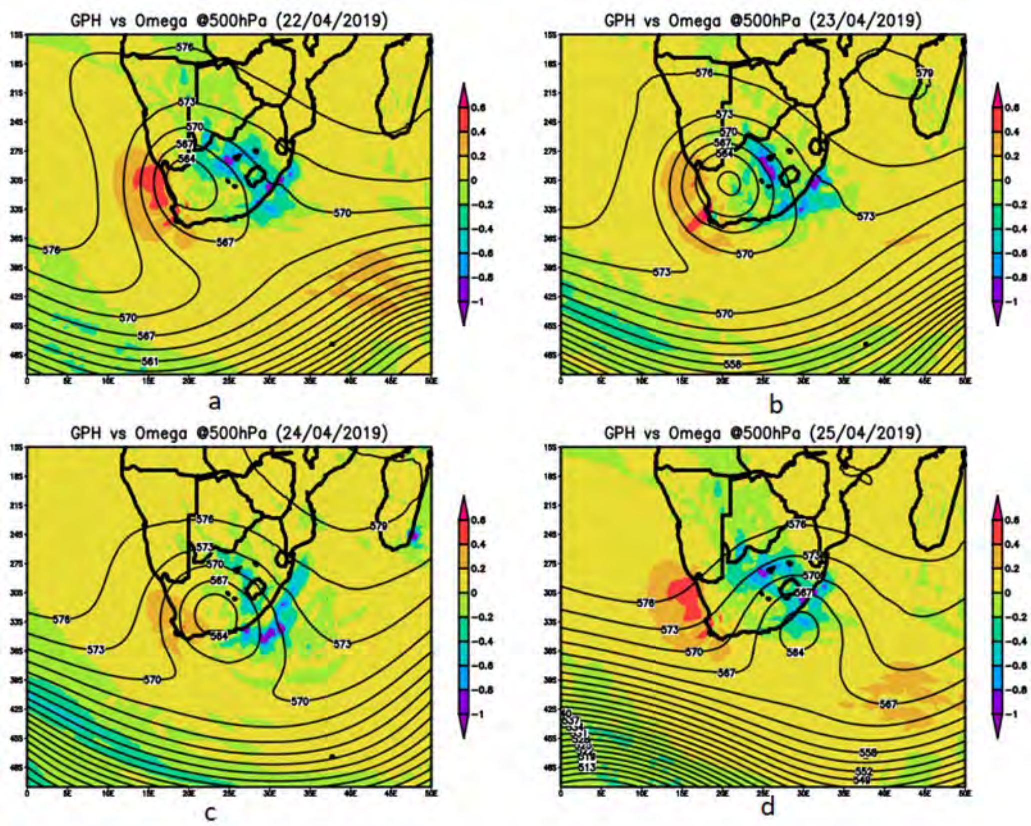

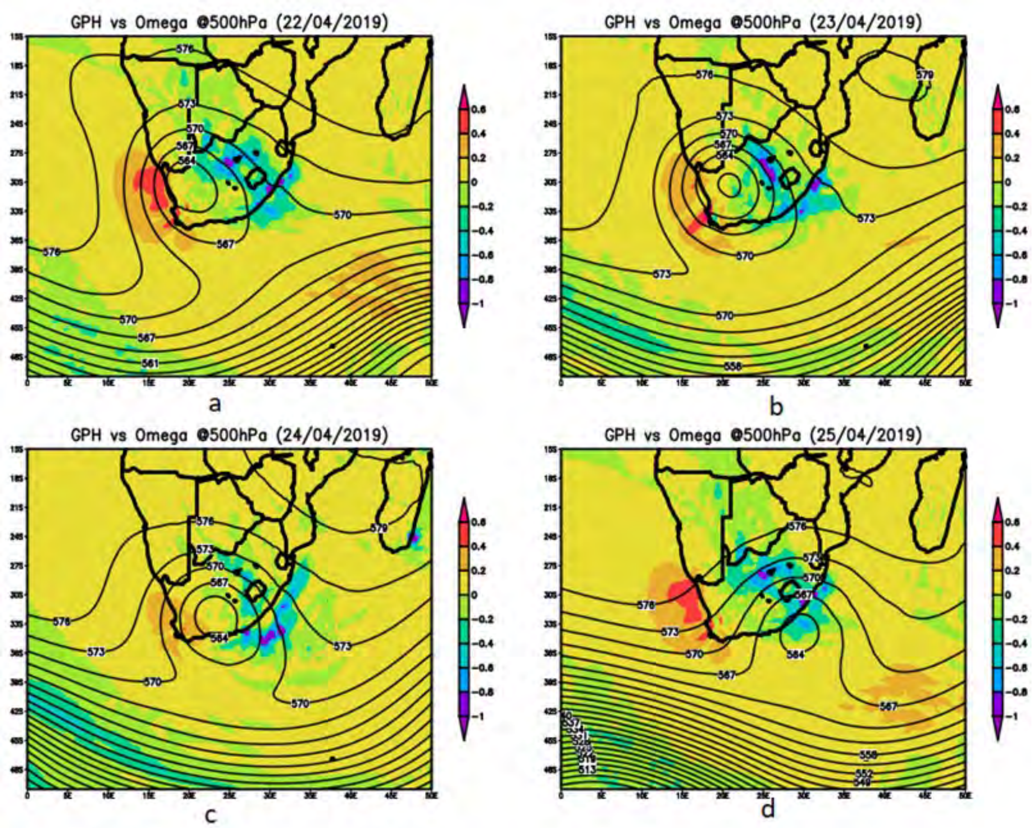

Figure 8.9: Geopotential height vs. omega at 500 hPa (22–25 April 2002).

8.7 FORECASTING CUT-OFF LOWS

The forecasting and research communities have become increasingly interested in COLs over the past several decades [36,70]. In order to make numerical weather and cli-mate predictions, understanding the characteristics of COLs and their variability is of particular importance [53]. Information about the potential impacts is made possible by im-pact-based forecasts and warnings [71]. This indicates that there will be an increase in climate- and weather-related challenges in the future. A better consideration of the physical processes that influence temperature and rainfall variability, changes and trends over South Africa, such as COL dynamics, may prove to be very useful in adapting to projected future climate changes. This may also improve the reliability of forecasting anomalous events caused by COLs, leading research institutions and weather services to become interested in COLs in the twenty-first century [21,36,43].

However, there has been a lack of efficient tools and effective warning methods [72] for societies who are usually non-scientists and the most affected by weather extreme events. Since COLs produce severe and destructive weather, it is imperative that meteor-ologists forecast them accurately and with adequate lead time. Information about the potential impacts is made possible by impact-based forecasts and warnings [71] which are important considering the weather and climate challenges in the future. Better consideration of physical processes that influence temperature and rainfall variability, changes and trends over South Africa may also improve the reliability of forecasting anomalous events caused by COLs, leading to positive implications for quality of life, economic well-being and growth in South Africa. Furthermore, investigating teleconnection patterns (e.g., EN-SO) and the predictability of COLs is crucial [70].

With advanced prediction systems, accurate rainfall and position forecasts of COLs are still a challenge due to their irregular trajectories [10]. More recently, climate models have been used to simulate COLs with more frequency and accuracy (e.g., [10,36,73–75]). The weather research forecast (WRF) regional model was used to simulate the characteristics of COL rainfall over the western cape and the influence of topography on cut-off lows over southern Africa [36]. The WRF successfully captured COLs' seasonal and annual climatology [36], as well as the influence of the western and eastern topography over South Africa, which enhances and suppresses rainfall, respectively [36]. The use of models is largely influenced by COL intensification and frequency in a changing climate, impacting regional climate variability. The use of ensemble models has been found to have improved outcomes compared to using an individual model. It has been recently documented that the spatial distribution, temporal and lifetime distributions of COLs are realistically simulated by the Coupled Model Intercomparison Project Phase 6 (CMIP6) models [70]. Ensemble prediction systems tend to produce reliable forecasts, especially if they have accurate initial conditions. However, a recent study by Muofhe et al. [10] found that the Unified Model used operationally by the South African Weather Service simulates rainfall differently, with higher skill during the formation stage of the systems of COLs over South Africa due to its low skill when placing COL centres. In addition, understating the frequency of COL occurrence may be an important factor for government and disaster management to become more proactive than reactive when forecast alerts or warnings are issued.

8.8 CONCLUSIONS

In South Africa, COLs are one of the most important rainfall-producing synoptic-scale weather systems that occur year round [10] and occur from 20°S to 50°S. It was indicated that COLs can induce heavy rainfall conditions over parts of South Africa, causing mass destruction to infrastructure, economy, lives and livelihoods. The loss of lives during the occurrences of COL over South Africa still raises a need for the future improvement of early warning systems, tools and communication of climate information. During COL occurrences, rainfall was found to be anomalously high and usually complemented by snow, very cold or flooding conditions. It has been reported that in some parts of South Africa, occurrences of extreme rainfall events (e.g., COLs) reduce the severity of dry conditions when they occur during the austral summer [76]. Furthermore, investigations about COLs forming surface lows and thereafter becoming barotropic as they weaken (strengthen) and less (more) intense [8,36] still requires attention in future assessments.

There has been a focus on studying specific and individual COL events, which have largely contributed to model development and theories [63]. However, more studies focusing on climatology and model forecasting of COLs must be conducted using the more re-cent high-resolution reanalyses and trackers. Moreover, work focusing on dynamical evolution has been minimal. Therefore, there is a need to investigate the dynamic structure of global COLs. In this paper, COL occurrences over South Africa have been widely documented and reviewed. Each COL occurrence over South Africa has unique characteristics and impacts, resulting in harsh conditions over affected parts. COL blocking is another form of quasi-stationary west–east tracking, causing unsettled weather for an extended period in the process. In Australia, cut-off low formation and intensification depend heavily on the development and maintenance of the frequent blocking high events over the Tasman Sea [39].

As COLs are the leading cause of weather-related deaths in South Africa, it is critical that timely and accurate weather warnings are issued by the national meteorological ser-vice and civil protection and disaster management authorities. The ability of developing countries to adapt to climate stresses tends to be hindered by widespread poverty, political instability and civil war. These are major issues, as several climate change models project that some regions will experience an increase in extreme weather conditions. Our review has shown that NWP models have struggled with forecasting the amounts and location of extreme rainfall. As some of the greatest impacts have occurred in poorly built informal settlements, urban planners and disaster managers are encouraged to review infrastructure in vulnerable coastal areas towards natural disaster risk reduction.

8.9 REFERENCES

1. Engelbrecht, F.A.; Monteiro, P.M. The IPCC Assessment Report Six Working Group 1 report and southern Africa: Reasons to take action. South Afr. J. Sci. 2021, 117. https://doi.org/10.17159/sajs.2021/12679.
2. Xulu, N.G.; Chikoore, H.; Bopape, M.-J.; Nethengwe, N. Climatology of the Mascarene High and Its Influence on Weather and Climate over Southern Africa. Climate 2020, 8, 86. https://doi.org/10.3390/cli8070086.
3. Hart, N.C.; Reason, C.J.; Fauchereau, N. Cloud bands over southern Africa: Seasonality, contribution to rainfall variability and modulation by the MJO. Clim. Dyn. 2013, 41, 1199–1212.
4. Blamey, R.C.; Reason, C.J.C. The role of mesoscale convective complexes in southern Africa summer rainfall. J. Clim. 2013, 26, 1654–1668.
5. Webster, E.M. A Synoptic Climatology of Continental Tropical Low Pressure Systems over Southern Africa and Their Contribution to Rainfall over South Africa. Doctoral Dissertation, University of Pretoria, Pretoria, South Africa, 2019.
6. Chikoore, H.; Vermeulen, J.H.; Jury, M.R. Tropical cyclones in the Mozambique channel: January–March 2012. Nat. Hazards 2015, 77, 2081–2095.
7. Engelbrecht, F.; Adegoke, J.; Bopape, M.-J.; Naidoo, M.; Garland, R.; Thatcher, M.; McGregor, J.; Katzfey, J.; Werner, M.; Ichoku, C.; et al. Projections of rapidly rising surface temperatures over Africa under low mitigation. Environ. Res. Lett. 2015, 10, 085004.
8. Singleton, A.T.; Reason CJ, C. A Numerical Model Study of an Intense Cutoff Low Pressure System over South Africa. Mon. Weather. Rev. 2007, 135, 1128–1150. https://doi.org/10.1175/MWR3311.1.

9. Favre, A.; Hewitson, B.; Lennard, C.; Cerezo-Mota, R.; Tadross, M. Cut-off Lows in the South Africa region and their contribution to precipitation. Clim. Dyn. 2013, 41, 2331–2351. https://doi.org/10.1007/s00382-012-1579-6.

10. Muofhe, T.P.; Chikoore, H.; Bopape, M.-J.M.; Nethengwe, N.S.; Ndarana, T.; Rambuwani, G.T. Forecasting Intense Cut-Off Lows in South Africa Using the 4.4 km Unified Model. Climate 2020, 8, 129. https://doi.org/10.3390/cli8110129.

11. Zhao, S.; Sun, J. Study on cut-off low-pressure systems with floods over Northeast Asia. Meteorology and Atmospheric Physics 2007, 96, 159–180. https://doi.org/10.1007/s00703-006-0226-3.

12. Palmen, E.; Newton, C. Atmospheric Circulation Systems; Academic Press: New York, NY, USA, 1969.

13. Pinheiro, H.R.; Hodges, K.I.; Gan, M.A. An intercomparison of subtropical cut-off lows in the Southern Hemisphere using recent reanalyses: ERA-Interim, NCEP-CFRS, MERRA-2, JRA-55, and JRA-25. Clim. Dyn. 2020, 54, 777–792.

14. Muñoz, C.; Schultz, D.; Vaughan, G. A midlatitude climatology and interannual variability of 200-and 500-hPa cut-off lows. J. Clim. 2020, 33, 2201–2222. https://doi.org/10.1175/JCLI-D-19-0497.1.

15. Fuenzalida, H.A.; Sánchez, R.; Garreaud, R.D. A climatology of cut-off lows in the Southern Hemisphere. J. Geophys. Res. Atmos. 2005, 110, 1–10. https://doi.org/10.1029/2005JD005934.

16. Reboita, M.S.; Nieto, R.; Gimeno, L.; Da Rocha, R.P.; Ambrizzi, T.; Garreaud, R.; Krüger, L.F. Climatological features of cutoff low systems in the Southern Hemisphere. J. Geophys. Res. Atmos. 2010, 115. https://doi.org/10.1029/2009JD013251.

17. Nieto, R.; Gimeno, L.; de la Torre, L.; Ribera, P.; Gallego, D.; García-Herrera, R.; García, J.A.; Nuñez, M.; Redaño, A.; Lorente, J. Climatological features of cut-off low systems in the Northern Hemisphere. J. Clim. 2005, 18, 3085–3103. https://doi.org/10.1175/JCLI3386.1.

18. Risbey, J.; Pook, M.; McIntosh, P.; Wheeler, M.; Hendon, H. On the remote drivers of rainfall variability in Australia. Mon. Weather. Rev. 2009, 137, 3233–3253. https://doi.org/10.1175/2009MWR2861.1.

19. Pinheiro, H.R.; Hodges, K.I.; Gan, M.A. Sensitivity of identifying cut-off lows in the Southern Hemisphere using multiple criteria: Implications for numbers, seasonality and intensity. Clim. Dyn. 2019, 53, 6699–6713. https://doi.org/10.1007/s00382-019-04984-x.

20. Fuenzalida, H.A.; Sánchez, R.; Garreaud, R.D. A climatology of cutoff lows in the Southern Hemisphere. J. Geophys. Res. Atmos. 2005, 110, 1–10.

21. Pinheiro, H.R.; Hodges, K.I.; Gan, M.A.; Ferreira, S.H.; Andrade, K.M. Contributions of downstream baroclinic development to strong Southern Hemisphere cut-off lows. Q. J. R. Meteorol. Soc. 2021, 148, 214–232. https://doi.org/10.1002/qj.4201.

22. Barnes, M.A.; Ndarana, T.; Landman, W.A. Cut-off lows in the southern Hemisphere and their extension to the surface. Climate Dynamics 2021, 56, 3709–3732. https://doi.org/10.1007/s00382-021-05662-7.

23. Price, J.D.; Vaughan, G. Statistical studies of cut-off low systems. Ann. Geophys. 1992, 10, 96–102.

24. Tyson, P.D.; Preston-Whyte, R.A. The Weather and Climate of Southern Africa; Oxford University Press: Cape Town, South Africa, 2000; 396p.

25. Ndarana, T.; Lekoloane, L.E.; Rammopo, T.S.; Reason, C.J.; Bopape MJ, M.; Chikoore, H.; Engelbrecht, F.A. Downstream development associated with two types of ridging South Atlantic Ocean anticyclones over South Africa. Weather. Clim. Dyn. Discuss. 2022, 1–29.

26. Singleton, A.T.; Reason, C.J.C. Variability in the characteristics of cut-off low pressure systems over subtropical southern Africa. Int. J. Climatol. 2006, 27, 295–310. https://doi.org/10.1002/joc.1399.

27. Baray, J.L.; Baldy, S.; Diab, R.D.; Cammas, J.P. Dynamical study of a tropical cut-off low over South Africa, and its impact on tropospheric ozone. Atmos. Environ. 2003, 37, 1475–1488.

28. Pook, M.J.; McIntosh, P.C.; Meyers, G.A. The synoptic decomposition of cool-season rainfall in the southeastern Australian cropping region. J. Appl. Meteorol. Clim. 2006, 45, 1156–1170. https://doi.org/10.1175/JAM2394.1.

29. Buckley, B.W.; Leslie, L.M.; Sullivan, W.; Leplastrier, M.; Qi, L. A rare East Indian Ocean autumn season tropical cut-off low: Impacts and a high-resolution modelling study. Meteorol. Atmos. Phys. 2007, 96, 61–84. https://doi.org/10.1007/s00703-006-0221-8.

30. Risbey, J.S.; Pook, M.J.; McIntosh, P.C.; Ummenhofer, C.C.; Meyers, G. Characteristics and variability of synoptic features associated with cool season rainfall in southeastern Australia. Int. J. Clim. 2009, 29, 1595–1613. https://doi.org/10.1002/joc.1775.

31. Lavender, S.L.; Abbs, D.J. Trends in Australian rainfall: Contribution of tropical cyclones and closed lows. Clim. Dyn. 2013, 40, 317–326. https://doi.org/10.1007/s00382-012-1566-y.

32. Pook, M.J.; Risbey, J.S.; McIntosh, P.C. A comparative synoptic climatology of cool-season rainfall in major grain-growing regions of southern Australia. Theor. Appl. Climatol. 2013, 117, 521–533. https://doi.org/10.1007/s00704-013-1021-y.

33. Hauser, S.; Grams, C.M.; Reeder, M.J.; McGregor, S.; Fink, A.H.; Quinting, J.F. A weather system perspective on winter–spring rainfall variability in southeastern Australia during El Niño. Q. J. R. Meteorol. Soc. 2020, 146, 2614–2633. https://doi.org/10.1002/qj.3808.

34. Ndarana, T.; Waugh, D.W. The link between cut-off lows and Rossby wave breaking in the Southern Hemisphere. Q. J. R. Meteorol. Soc. 2010, 136, 869–885. https://doi.org/10.1002/qj.627.

35. Muofhe, T.P. Characteristics of Deep Moist Convection and Rainfall in Cut-Off Lows over South Africa. Master Dissertation, University of Venda, Thohoyandou, South Africa, 2019. http://hdl.handle.net/11602/1499.

36. Abba-Omar, S.; Abiodun, B.J. Simulating the characteristics of cut-off low rainfall over the Western Cape using WRF. Clim. Dyn. 2021, 56, 1265–1283.

37. Chikoore, H.; Bopape, M.-J.M.; Ndarana, T.; Muofhe, T.P.; Gijben, M.; Munyai, R.B.; Manyanya, T.C.; Maisha, R. Synoptic structure of a sub-daily extreme precipitation and flood event in Thohoyandou, north-eastern South Africa. Weather. Clim. Ex-tremes 2021, 33, 100327.

38. Taljaard 1985.

39. Qi, L.; Wang, Y.; Leslie, L.M. Numerical simulation of a cut-off low over southern Australia. Meteorol. Atmos. Phys. 2000, 74, 103–115. https://doi.org/10.1007/s007030070028.

40. Campetella, C.M.; Possia, N.E. Upper-level cut-off lows in southern South America. Meteorology and Atmospheric Physics 2007, 96, 181–191. https://doi.org/10.1007/s00703-006-0227-2.

41. Godoy, A.A.; Possia, N.E.; Campetella, C.M.; Skabar, Y.G. A cut-off low in southern South America: Dynamic and thermodynamic processes. Rev. Bras. Meteorol. 2011, 26, 503–514. https://doi.org/10.1590/S0102-77862011000400001.

42. Hersbach, H.; Bell, B.; Berrisford, P.; Hirahara, S.; Horanyi, A.; Muñoz-Sabater, J.; Nicolas, J.; Peubey, C.; Radu, R.; Schepers, D.; et al. The ERA5 global reanalysis. Q. J. R. Meteorol. Soc. 2020, 146, 1999–2049.

43. Ndarana, T.; Rammopo, T.S.; Bopape, M.J.; Reason, C.J.; Chikoore, H. Downstream development during South African cut-off low pressure systems. Atmos. Res. 2021, 249, 105315. https://doi.org/10.1016/j.atmosres.2020.105315.

44. Hoskins, B.; McIntyre, M.E.; Robertson, A.W. On the use and significance of isentropic potential vorticity maps. Q. J. R. Meteorol. Soc. 1985, 111, 877–946. https://doi.org/10.1256/SMSQJ.47001.

45. Ndarana, T.; Rammopo, T.S.; Chikoore, H.; Barnes, M.A.; Bopape, M.-J. A quasi-geostrophic diagnosis of the zonal flow associated with cut-off lows over South Africa and surrounding oceans. Clim. Dyn. 2020, 55, 2631–2644. https://doi.org/10.1007/s00382-020-05401-4.

46. Bell, G.D.; Bosart, L.F. A case study diagnosis of the formation of an upper-level cutoff cyclonic circulation over the eastern United States. Mon. Weather. Rev. 1993, 121, 1635–1655.

47. van Delden, A.; Neggers, R. A case study of tropopause cyclogenesis. Meteorol. Appl. 2003, 10, 187–199.

48. Mcintyre, M.E.; Palmer, T.N. Breaking planetary waves in the stratosphere. Nature 1983, 305, 593–600. https://doi.org/10.1038/305593a0.

49. Hoskins, B.J.; Hodges, K.I. A new perspective on Southern Hemisphere storm tracks. J. Clim. 2005, 18, 4108–4129.

50. Hoskins, B.J. Atmospheric frontogenesis models: Some solutions. Q. J. R. Meteorol. Soc. 1971, 97, 139–153. https://doi.org/10.1002/qj.49709741202.

51. Price, J.D.; Vaughan, G. The potential for stratosphere-troposphere exchange in cut-off-low systems. Q. J. R. Meteorol. Soc. 1993, 119, 343–365. https://doi.org/10.1002/qj.49711951007.

52. Rondanelli, R.; Gallardo, L.; Garreaud, R.D. Rapid changes in ozone mixing ratios at Cerro Tololo (30°10′ S, 70°48′ W, 2200 m) in connection with cut-off lows and deep troughs. J. Geophys. Res. Atmos. 2002, 107, ACL-6. https://doi.org/10.1029/2001JD001334.

53. Pinheiro, H.; Ambrizzi, T.; Hodges, K.; Gan, M.; Andrade, K.; Garcia, J. Are Cut-off Lows simulated better in CMIP6 compared to CMIP5?. Clim. Dyn. 2022, 59, 2117–2136. https://doi.org/10.1007/s00382-022-06200-9.

54. Wernli, H.; Sprenger, M. Identification and ERA-15 climatology of potential vorticity streamers and cutoffs near the extratropical tropopause. J. Atmos. Sci. 2007, 64, 1569–1586. https://doi.org/10.1175/JAS3912.1.

55. Ancellet, G.; Beekmann, M.; Papayiannis, A. Impact of a cutoff development on downward transport of ozone in the stratosphere. J. Geophys. Res. 1994, 99, 3451–3463. https://doi.org/10.1029/93JD0255.

56. Baray, J.L.; Baldy, S.; Diab, R.D.; Cammas, J.P. Dynamical study of a tropical cut-off low over South Africa, and its impact on tropospheric ozone. Atmos. Environ. 2003, 37, 1475–1488.

57. Gimeno, L.; Trigo, R.M.; Ribera, P.; Garcia, J.A. Special issue on cut-off low systems (COL). Meteorol. Atmos. Phys. 2006, 96, 1. https://doi.org/10.1007/s00703-006-0216-5.

58. Ebel, A.; Hass, H.; Jakobs, H.; Laube, M.; Memmesheimer, M.; Oberreuter, A.; Geiss, H.; Kuo, Y.-H. Simulation of ozone intrusion caused by a tropopause fold and cut-off low. Atmos. Environ. Part A Gen. Top. 1991, 25, 2131–2144. https://doi.org/10.1016/0960-1686(91)90089-P.

59. Langford, A.; Masters, C.; Proffitt, M.; Hsie, E.; Tuck, A. Ozone measurements in a tropopause fold associated with a cut-off low system. Geophys. Res. Lett. 1996, 23, 2501–2504. https://doi.org/10.1029/96GL02227.

60. South African Government. National State of Disaster-In-Numbers—18 April 2022. 2022. Available online: https://www.gov.za/speeches/national-state-disaster-numbers-%E2%80%93-18-april-2022-18-apr-2022-0000 (accessed on 29 June 2022).

61. Mac Mahon, A.G.; Swart, J.P. The Laingsburg flood disaster. South Afr. Med J. 1983, 63, 865–866. https://pubmed.ncbi.nlm.nih.gov/6857404/.

62. Nath, P.K.; Behera, B. A critical review of impact of and adaptation to climate change in developed and developing economies. Environ. Dev. Sustain. 2010, 13, 141–162. https://doi.org/10.1007/s10668-010-9253-9.

63. Llasat, M.C.; Martín, F.; Barrera-Escoda, A. From the concept of “Kaltlufttropfen” (cold air pool) to the cut-off low. The case of September 1971 in Spain as an example of their role in heavy rainfalls. Meteorol. Atmos. Phys. 2006, 96, 43–60. https://doi.org/10.1007/s00703-006-0220-9.

64. Mashao, F.M.; Mothapo, M.C.; Munyai, R.B.; Letsoalo, J.M.; Mbokodo, I.L.; Muofhe, T.P.; Matsane, W.; Chikoore, H. Extreme Rainfall and Flood Risk Prediction over the East Coast of South Africa. Water 2022, 15, 50.

65. Pyle, D.M.; Jacobs, T.L. The Port Alfred floods of 17–23 October 2012: A case of disaster (mis) management?. Jàmbá J. Disaster Risk Stud. 2016, 8, a207. https://doi.org/10.4102/jamba.v8i1.207.

66. Barnes, M.A.; Turner, K.; Ndarana, T.; Landman, W.A. Cape storm: A dynamical study of a cut-off low and its impact on South Africa. Atmos. Res. 2021, 249, 105290. https://doi.org/10.1016/j.atmosres.2020.105290.

67. Molekwa, 2012.

68. ENCA. Travelers Warned as Wet Weather Continues in Parts of SA. 2019. Available online: https://www. enca.com/news/wet-weather-affect-many-travel-plans (accessed on 11 May 2022).

69. CNN. 70 People Killed in South Africa Floods. 2019. Available online: https://edition.cnn.com/2019/04/24/ africa/51-dead-south-africa-flood-intl/index (accessed on 11 May 2020).

70. Pinheiro, H.R.; Ambrizzi, T.; Hodges, K.I.; Gan, M.A. Understanding the El Niño Southern Oscillation Effect on Cut-Off Lows as Simulated in Forced SST and Fully Coupled Experiments. Atmosphere 2022, 13, 1167. https://doi.org/10.3390/atmos13081167.

71. WMO. Impact-Based Forecasting Informs Anticipatory Action. 2021. Available online: https://public.wmo.int/en/media/news/impact-based-forecasting-informs-anticipatory-action (accessed on).

72. Pyle and Jacobs 2016.

73. Bozkurt, D.; Rondanelli, R.; Garreaud, R.; Arriagada, A. Impact of warmer eastern tropical Pacific SST on the March 2015 Atacama floods. Mon. Weather. Rev. 2016, 144, 4441–4460. https://doi.org/10.1175/MWR-D-16-0041.1.

74. Reyers, M.; Shao, Y. Cut-off lows of the coast of the Atacama Desert under present day conditions and in the Last Glacial Maximum. Glob. Planet. Chang. 2019, 181, 102983. https://doi.org/10.1016/j.gloplacha.2019.102983.

75. Omar, S.A.; Abiodun, B.J. Simulating the characteristics of cut-off low rainfall over the Western Cape using WRF. Clim. Dyn. 2021, 56, 1265–1283.

76. Mpungose, N.; Thoithi, W.; Blamey, R.C.; Reason, C.J.C. Extreme rainfall events

CHAPTER 9: CAPACITY BUILDING INITIATIVES, STAKEHOLDER EGAGEMENTS AND INFORMATION DISSEMINATION

9.1 WORKSHOPS

9.1.1 CCAM Webinar

On 8 – 12 November 2021, the project team hosted a webinar, where the model developers were invited to present talks on the model, amongst other activities. The programme for this webinar is as follows:

CCAM Webinar

8 – 12 November 2012

South African Weather Service, Pretoria, South Africa

DAY 1: 8 November 2021

TIME	ITEM	PRESENTER
9:30 -9:35	Opening and Welcome	**Robert Maisha**
9:35 -9:45	Purpose of workshop	**Mary-Jane Bopape**
9:45 -10:35	Introduction to CCAM	**Prof. Francois Engelbrecht**
10:35 – 10:45	Break	
10:45 – 11:25	CCAM – geometry and advection aspects	John McGregor
11:25 – 11:35	Break	
11:35 – 12:30	CCAM – dynamics aspects	**John McGregor**
	END OF DAY 1	

DAY 2: 9 November 2021

TIME	***ITEM***	***PRESENTER***
9:30 – 9:40	Welcome and opening	**Lesetja**

9:40 -10:30	Overview of CCAM atmospheric physics parameterisations	**Marcus Thatcher**
10:30 -10:45	Break	
10:40 -10:40	NWP Modelling	**Hector Chikore**
10:40 – 10:45	Break	
10:45 – 11:25	Introducing the Conformal-Cubic Atmospheric Model at SAWS	**Robert Maisha**
11:25 -11:30	Break	
11:30 -12:30	Air Quality Modelling with CCAM 1 km output	**Mogesh Naidoo**
	END OF DAY 2	

DAY 3: 10 November 2021

TIME	*ITEM*	*PRESENTER*
9:30 -9:40	Opening and welcome	**Gift Rambuwani**
9:40 - 10:40	Seasonal Predictions using CCAM	**Jack Katzfey**
10:40 – 10:45	Break	
10:45 – 11:35	CCAM boundary layer physics	**Lesetja Lekoloane**
11:35 -11:45	Break	

11:45 – 12:30	Modelling Resources at the CHPC	Mthetho Sovara
	END OF DAY 3	

DAY 4: 11 November 2021

TIME	***ITEM***	***PRESENTER***
9:30 -9:40	Opening and welcome	**Robert Maisha**
9:40 - 10:40	CCAM setup and demo	**Robert Maisha**
10:40 – 10:50	break	
10:50 – 12:30	Practical Exercise	All
	END OF DAY 4	

DAY 5: 12 November 2021

TIME	***ITEM***	***PRESENTER***
9:30 -9:40	Opening and welcome	**Robert Maisha**
9:40 - 10:40	CCAM setup and demo	**Robert Maisha**
10:40 – 10:50	break	
10:50 – 12:25	Practical Exercise	**All**
12:25 -12:30	Closing remarks and vote of thanks	**Robert Maisha**
	END OF DAY 5	

End of Document

9.1.2 NWP and GIS Training Workshop

The project team, in collaboration with the NRF-SEAON and the CSIR hosted a training workshop, which included participants from several SADC countries. The programme for this workshop is as follows:

Agenda for the NWP and GIS Training Workshop

21-25 November 2022

Albert Luthuli Auditorium, National Research Foundation, Pretoria, South Africa

I. Topics to be covered	
High Performance Computing (HPC) • Linux for High Performance Computing • Simple PBS jobscript • Running the jobscript • Scaling on LENGAU	**Python** • Libraries and Syntax • Python and NetCDF files Examples
Weather and Research Forecasting Model (WRF) • WRF Libraries and Configuration • WRF Pre-Processing System (WPS) • WRF Solver (WRF) • Some thoughts on WRF in operational use and Data Assimilation	**QGIS** • Introduction • Rastor vs Vector files • Demo, Hands-on session: Import NetCDF • Questions & Bonus Task • Plugins e.g. Google Earth Engine

II. Team members for the training and email addresses

- Robert Maisha: Robert.Maisha@weathersa.co.za
- Gift Rambuwani: Gift.Rambuwani@weathersa.co.za
- Patience Mulovhedzi: Patience.Mulovhedzi@weathersa.co.za
- Claire Davis Reddy: cl.davisreddy@saeon.nrf.ac.za
- Galaletsang Keebine: gl.keebine@saeon.nrf.ac.za
- Keneilwe Hlahane: km.hlahane@saeon.nrf.ac.za
- Caroline Mfopa: cr.mfopa@saeon.nrf.ac.za
- Mthetho Sovara: MSovara@csir.co.za

III. Schedule

Time	Activities	Responsibility
DAY 1 – 21 Nov. 2022 (First Session before coffee/tea break)		
Session 1 – Opening		
09:00 – 09:30	Registration	Organizers
09:30 – 10:00 Welcoming Remarks		Mr Bishen Singh - Group Executive: Finance and Business Systems and CFO - NRF
		Dr Happy Sithole – Centre Manager: NICIS
		Mr Mmikeli Ndabambi – Executive, Infrastructure and Information Systems-SAWS
10:00 – 10:30	Introduction of participants	Participants
Session 2 – Setting the Scene		
10:30 – 10:40	Overview of CR4D	Dr Frank Rutabingwa, CR4D-ACPC
10:40 – 10:50	Overview of AICCRA	Dr Yosef Amha, Researcher, AICCRA
10:50 – 11:00	Overview of the training	Dr Mary-Jane Bopape - Managing Director, SAEON - NRF

TIME			SESSION 1 Monday 11/21/22 NRF	SESSION 2 Tuesday 11/22/22 NRF	SESSION 3 Wednesday 11/23/22 CSIR ICC	SESSION 4 Thursday 11/24/22 NRF	SESSION 5 Friday 11/25/22 NRF
09:00	-	09:30	Welcome and Registration	Welcome and Registration	Welcome and Registration	Welcome and Registration	Welcome and Registration
09:30	-	11:00	Opening and setting the scene	WRF Configuration	QGIS & Python	QGIS & Python	GrADS Visualization
11:00	-	11:15	Break	Break	Break	Break	Break
11:15	-	13:00	Linux Basics	WRF (WPS)	QGIS & Python	QGIS & Python	Feedback & Closing
13:00	-	14:00	Lunch	Lunch	Lunch	Lunch	Lunch
14:00	-	16:30	HPC Basics	WRF (WRF)	QGIS & Python	GrADS Visualization	
16:30	-	17:00	Session 1 Round-up	Session 2 Round-up	Session3 Round-up	Session 4 Round-up	

9.1.3 Modelling workshop: 28 - 29 November 2022

A modelling workshop was organised by the Project team and it was in collaboration with the NRF-SEAON and WITS. The workshop was held at the NRF, Pretoria. Various experts were invited and the program looks as follows:

<u>THE EARTH SYSTEM OBSERVATIONS AND MODELLING WORKSHOP</u>

Date:28-29 NOVEMBER 2022,

Venue: Albert Luthuli Auditorium, National Research Foundation, Pretoria, South Africa

AGENDA ITEMS	
	DAY 1
	WELCOME, OPENING REMARKS & SETTING THE SCENE – CHAIR: Francois Engelbrecht
09h00-09h10	Mary-Jane Bopape – SAEON Welcome Remarks
09h11-09h20	Francois Engelbrecht – Global Change Institute
09h21-09h30	Robert Maisha – South African Weather Service
09h31-09h40	Sue Van Rensburg- South African Environmental Observation Network (SAEON-NRF)
09h41-10h45	INTRODUCTION OF ALL PARTICIPANTS
10h46– 11h00	TEA BREAK
	OVERARCHING TOPICS - Chair: Mary-Jane Bopape
11h01-11h20	Vhalinavho Khavhagali – International Union for Conservation of Nature 2030 vision: constraints and opportunities
11h21 – 11h40	hetho Sovara – The future of weather and climate prediction in Southern Africa: HPC and Exascale Supercomputing
11h41-12h00	Gregor Feig – South African Research Infrastructure Roadmap at SAEON

12h01-12h20	Francois Engelbrecht – Latest trends in Earth System Modelling
12:21 – 12:40	Discussion
12h41-13h40	LUNCH
	FOCUS ON ARC AND THE OCEAN- CHAIR: Hector Chikoore
13h41-14h00	Ramontsheng Rapolaki – Forecasting and Climate Modelling at the Agricultural Research Council (ARC)
14h01-14h20	Johan Malherbe – Observation Research at the Agricultural Research Council (ARC)
14h21-14h40	Zakiena Hoossen – The Effects of Geostatistical Downscaling on Eddy Kinetic Energy in the Southern Ocean
14h41-15h00	Jenny Veitch - SOMISANA: a Sustainable Ocean Modelling Initiative, a Southern African Approach
15h00-15h15	Tea Break
15h15-15h35	Nicolette Chang- Modelling the Southern Ocean carbon-climate
15h35-15h55	Francois Engelbrecht - Regional climate modelling of regional tipping points in southern Africa
15h55-16h15	Tumelo Moalusi - Scalability of the CCAM code on the Lengau cluster
16h15-17h00	Discussion
CLOSURE FOR DAY 1	
DAY 2	
09h01-09h10	DAY 1 RECAP
	FOCUS ON LAND- CHAIR:
09h11-09h30	Naledzani Ndou - Spatial analysis research at Fort Hare

09h31-10h10	Sue van Rensburg, Paul Gordijn and Michele Toucher- Grasslands node research at SAEON
10h11-10h30	Robert Maisha – Urban heart island modelling
10h31-10h50	Mary-Jane Bopape – Modelling the planetary boundary layer
10h51 – 11h00	Discussion
11h01 – 11h15	TEA BREAK
	FOCUS ON THE PHYSICS - CHAIR: Thando Ndarana
11h15 -11h35	Mogesh Naidoo – Emissions and Modelling
11h36- 11h55	Gift Rambuwani – cloud microphysics / Nkosinathi G. Xulu - cut-off low simulations
11h56 – 12h15	Jessica Steinkopf - Convection parameterization tests with CCAM towards CMIP6.
12h16 -12h35	Patience Mulovhedzi – Cumulus schemes
12h35 – 12h45	Discussion
12h45 – 13h45	LUNCH
	FOCUS ON THE ATMOSPHERE- CHAIR:
13h46 -14h05	Nohlahla Dlamini – Southern Ocean Storm tracks during wet and dry years in the southwestern Cape
14h06 – 14h25	Percy Muofhe - Recent trends of the SH westerlies in response to the ozone recovery
14h26 – 14h45	Hadisu Abubakar - Statistical Analysis of Trends in Monthly Precipitation of the Enkangala Escarpment, Drakensberg, South Africa
14h46 -15h05	DISCUSSION & WAY FORWARD
15h05 – 15h10	
15h10 – 16h00	

END OF WORKSHOP

9.1.4 CCAM Data Assimilation workshop: 22- 23 November 2023

The CCAM-DA workshop was held online during the period Wednesday 22 November to Thursday 23 November 2023, with the aim of getting expert advice on how data assimilation could be implemented on the CCAM system. Various experts were invited and the program were as follows:

WRF-DA AGENDA		
Wednesday 22 November 2023		
09h00-09h10	**Welcome**	**SAWS Executive**
09h10-09h30	**Introduction to DA in SA**	**Mr. Robert Maisha**
09h30-10h30	**Challenges/CCAM -DA**	**Prof. Marcus Thatcher**
10h30-11h30	**SARCHAIR and DA**	**Prof. Ndarana**
11h30-12h30	**Discussions?**	**Dr. Bopape**

Thursday 23 November 2023		
09h00-09h30	**DA Science talk (Video recording)**	**Dr/Prof. Craig Schwartz**
09h30-10h30	**WRF DA simulations over Africa**	**Dr/Prof. Agostino Meroni**
10h30-11h00	**Vote of Thanks by WRC**	**Dr/Prof. Brilliant Petja**
11h00-11h10	**Conclusions and Vote of thanks**	**Dr. Katlego Ncongwane**

From this workshop further engagements with the CCAM developer, Dr/Prof. Marcus Thatcher will be required in order to determine which form of data assimilation could be easier to implement on the CCAM.

9.1.5 Python training workshop: 17 – 21 July 2023

Python Training was organised by the University of Pretoria. Ms Lebogang Makgati and Mr Robert Maisha attended for the whole week.

9.2 CONFERENCES

9.2.1 SASAS Conference (2022)

Project team members presented their work supported by the WRC at the SASAS Conference hosted by GCI at the University of Witwatersrand. They presented a peer reviewed paper on: ”Parameterization of cumulus convection within the Conformal Cubic Atmospheric Model”a paper on “data Assimilation at SAWS '', whereby the SAWS operational forecasts were compared against WRF and CCAM predictions.

9.2.2 CHPC International Conference (2022)

A project team member gave a presentation on “Simulation of mesoscale convective systems with the Conformal Cubic Atmospheric Model on the CHPC” at the CHPC conference held in the CSIR convention centre, Pretoria.

9.2.3 SASAS Conference (2023)

Project team members presented their work at the SASAS Conference hosted by the University of Western Cape. Both papers were peer-reviewed and support their PHD studies. The papers were titled: ”Assessing the scale awareness of the Conformal Cubic Atmospheric Model convection scheme for a heavy rainfall event” and:” WRF simulations of squall line features over the South African Highveld”

9.2.4 Open Science Conference of the World Climate Research Programme (WCRP) conference (2023).

A project team member gave a presentation on “Advances in model development at the South African Weather Service”. The conference was held in Kigali, Rwanda.

9.2.5 CHPC International Conference (2023)

Project team members presented their work supporting the WRC at the CHPC Conference hosted by CSIR. They presented:” Variable resolution numerical weather modelling on the CHPC”. and “Modelling of eThekwini heat island, which has been published in the American Meteorological Society, Journal of Applied Meteorology and Climatology.

9.3 INTELLECTUAL PROPERTY

9.2.1 The CCAM numerical prediction system

This system will run be at SAWS on the CSIR-CHPC supercomputer for research and later for operational forecasting to support SAWS operational forecasting.

9.2.2. The CCAM seasonal prediction system

The system will run be at SAWS on the CSIR-CHPC supercomputer for research and later for operational forecasting to support SAWS operational forecasting and projects.

9.2.3. Securing of laptops

Through the project, at least five laptops are planned to be purchased by SAWS for the five PhD students

9.4 INSTALLATION OF CCAM SEASONAL FORECASTING SYSTEM

The CCAM project is meant to develop a “Locally developed model for both numerical weather prediction, seasonal forecasting, and climate projection. However, the project has focused on most important components, including cloud microphysics, cumulus parametrization and boundary layer schemes. These components of the physics are applicable at NWP, seasonal forecasting, and climate projection. However, both NWP and climate components have been developed, and the seasonal forecasting component of the model needed to be implemented. As a result of this requirement, the Research team undertook a trip to meet the model developers.

During the week from 01 - 08 July 2023, the team of SAWS Researchers underwent a trip to the CSIRO in Australia to receive training on CCAM. This includes the microphysics and cumulus parameterization. Through collaboration, Prof. Jack Katzfey provided advice, scripts and training on the CCAM seasonal forecasting system. When the research team returned to South Africa, we started to work on the scripts used for seasonal forecasting. Currently due to persistence, the scripts have been adapted to the CHPC system and the forecast trial has been achieved. More tests still need to be conducted on this seasonal forecast system (this will include testing the system with more ensemble members, and also including different initialization data sets). .

An image below shows the initial seasonal forecasts from the CCAM. This system will be used by the SAWS seasonal forecasting in producing forecasting for up to a lead time of six (6) to 12 months depending on the computing and the resolution demand. The forecasts will also be used by the Hydrology group (stream flow, river run off products) and also to support the energy group (for solar radiation forecasts).

```
-rw-rw-r-- 1 grambuwani grambuwani         0 Dec 11 13:52 err.2023
-rw-rw-r-- 1 grambuwani grambuwani 318091038 Dec 11 13:59 ccam_210.0km.2023121012.0.nc.000001
-rw-rw-r-- 1 grambuwani grambuwani 322493241 Dec 11 13:59 ccam_210.0km.2023121012.0.nc.000000
-rw-rw-r-- 1 grambuwani grambuwani  36543156 Dec 11 13:59 Restccam_210.0km.2023121012.0.nc.000001
-rw-rw-r-- 1 grambuwani grambuwani  35048849 Dec 11 13:59 Restccam_210.0km.2023121012.0.nc.000000
-rw-rw-r-- 1 grambuwani grambuwani 481023690 Dec 11 14:08 ccam_210.0km.2023121012.1.nc.000001
-rw-rw-r-- 1 grambuwani grambuwani 489712098 Dec 11 14:08 ccam_210.0km.2023121012.1.nc.000000
-rw-rw-r-- 1 grambuwani grambuwani  36423300 Dec 11 14:08 Restccam_210.0km.2023121012.1.nc.000001
-rw-rw-r-- 1 grambuwani grambuwani  34966488 Dec 11 14:08 Restccam_210.0km.2023121012.1.nc.000000
-rw-rw-r-- 1 grambuwani grambuwani 456278618 Dec 11 14:17 ccam_210.0km.2023121012.2.nc.000001
-rw-rw-r-- 1 grambuwani grambuwani 456969527 Dec 11 14:17 ccam_210.0km.2023121012.2.nc.000000
-rw-rw-r-- 1 grambuwani grambuwani  34798517 Dec 11 14:17 Restccam_210.0km.2023121012.2.nc.000000
-rw-rw-r-- 1 grambuwani grambuwani  36443567 Dec 11 14:17 Restccam_210.0km.2023121012.2.nc.000001
-rw-rw-r-- 1 grambuwani grambuwani 496086384 Dec 11 14:27 ccam_210.0km.2023121012.3.nc.000001
-rw-rw-r-- 1 grambuwani grambuwani 493753976 Dec 11 14:27 ccam_210.0km.2023121012.3.nc.000000
-rw-rw-r-- 1 grambuwani grambuwani  36296429 Dec 11 14:27 Restccam_210.0km.2023121012.3.nc.000001
-rw-rw-r-- 1 grambuwani grambuwani  34910063 Dec 11 14:27 Restccam_210.0km.2023121012.3.nc.000000
-rw-rw-r-- 1 grambuwani grambuwani 476621838 Dec 11 14:36 ccam_210.0km.2023121012.4.nc.000000
-rw-rw-r-- 1 grambuwani grambuwani 487993532 Dec 11 14:36 ccam_210.0km.2023121012.4.nc.000001
-rw-rw-r-- 1 grambuwani grambuwani  35996840 Dec 11 14:36 Restccam_210.0km.2023121012.4.nc.000001
-rw-rw-r-- 1 grambuwani grambuwani  35071365 Dec 11 14:36 Restccam_210.0km.2023121012.4.nc.000000
-rw-rw-r-- 1 grambuwani grambuwani      1728 Dec 11 14:36 aeroemiss.nml
-rw-rw-r-- 1 grambuwani grambuwani      4584 Dec 11 14:36 input
-rw-rw-r-- 1 grambuwani grambuwani         0 Dec 11 14:36 err.2024
-rw-rw-r-- 1 grambuwani grambuwani        74 Dec 11 14:36 eigenv.out
-rw-rw-r-- 1 grambuwani grambuwani   1078634 Dec 11 14:36 aero.nc
-rw-rw-r-- 1 grambuwani grambuwani      2384 Dec 11 14:36 aero.log
-rw-rw-r-- 1 grambuwani grambuwani     56061 Dec 11 14:36 nrun.dat
-rw-rw-r-- 1 grambuwani grambuwani 495424426 Dec 11 14:45 ccam_210.0km.2023121012.5.nc.000000
-rw-rw-r-- 1 grambuwani grambuwani 506033302 Dec 11 14:45 ccam_210.0km.2023121012.5.nc.000001
-rw-rw-r-- 1 grambuwani grambuwani  34958966 Dec 11 14:45 Restccam_210.0km.2023121012.5.nc.000000
-rw-rw-r-- 1 grambuwani grambuwani         8 Dec 11 14:46 year.qm
-rw-r--r-- 1 grambuwani grambuwani     27825 Dec 11 14:46 run_ccam_seasfcst.out
-rw-r--r-- 1 grambuwani grambuwani      1737 Dec 11 14:46 run_ccam_seasfcst.err
-rw-rw-r-- 1 grambuwani grambuwani  35626109 Dec 11 14:46 Restccam_210.0km.2023121012.5.nc.000001
-rw-rw-r-- 1 grambuwani grambuwani    278547 Dec 11 14:46 prnew.ccam_210.0km.2023121012
-rw-rw-r-- 1 grambuwani grambuwani       971 Dec 11 14:46 cc.nml
[grambuwani@login2 scripts2]$
```

Figure 9.1: The CCAM seasonal forecasting system trial runs at a global horizontal scale of 210 km produced at the CHPC.

CHAPTER 10: CONCLUSIONS & RECOMMENDATIONS

10.1 CONCLUSIONS

The application of the CCAM's in various applications, including NWP, downscaling projections and seasonal predictions provides opportunities to the modelling community to study its components to enhance their understanding of this model. The CCAM has been studied at its highest resolution, less than 10 km horizontal resolution. The importance of high-resolution information in contemporary modelling is emphasised, with a consideration of CCAM's ability to resolve convective storms and boundary layer processes. From an analysis of the boundary layer parameterization schemes, it was found that coupling the EDMF with TKE improves the simulations of the boundary layer evolution, structure, and properties.

An analysis of the cloud microphysics was undertaken using two datasets, GFS and ERA5. In this analysis of the cloud microphysics case, the model underestimated the rainfall when compared to observations. However, there was an improvement in the simulation with the ERA5 dataset.

When comparing the three cumulus parameterization scheme versions (2015a, 2015b, 2017, and 2015aM), all versions exhibited a lack of skill in simulating precipitation over the South African domain, but the 2015aM cumulus scheme consistently yielded lower precipitation than other versions. When analysing the cumulus schemes for scale awareness, the study found that as the model resolution increases, the model increases its accuracy in locating intense rainfall events.

In simulating extreme weather events such as tropical cyclones, cut-off lows and heat waves, results show that the CCAM is able to reproduce the spatial distributions and temporal distribution. The model also depicts shortcomings (i.e., underpredicts some extreme weather events), and therefore further research is still required.

10.2 RECOMMENDATIONS

- The recommended dynamical core tests for CCAM involve thorough investigation into the grid setup, including vertex placement, and testing the accuracy and efficiency of different conformal-cubic (C-C) grid orientations. These tests aim to identify potential topographically induced errors and optimise the semi-Lagrangian advection scheme, particularly in regions with complex terrain. Additionally, it is recommended that tests for the nonhydrostatic equation set developed by Engelbrecht (2006) in comparison with the current non-hydrostatic CCAM dynamical core, especially at ultra-high resolutions be conducted.

- Analysis of the two boundary layer schemes led to the following recommendations for the SA domain: (i) conduct further sensitivity analysis of the CCAM ABL schemes, which includes the coupling with the oceanic turbulence scheme. (ii) implement and test the EDMF-TKE scheme for the dry and moist boundary layers.

- An analysis of the cloud microphysics scheme shows that the model underestimates rainfall with a slight displacement of rainfall, therefore it is important to do further tests with different global initialisation datasets. In addition, It is recommended that the double moment microphysics scheme be introduced to the CCAM and test its performance as compared to the current single moment cloud scheme

- In the analysis of the model cumulus scheme, there were not much difference in the scheme versions used, but when analysing the results for scale awareness, it was found that the model increases as resolution increase. Therefore recommendations include a more processed-based analysis, extending scale-awareness tests to sub-kilometre scales, adjusting formulation for scale-awareness, studying dynamical processes at various grid scales, and implementing model developer recommendations for further model development.

- it is also recommended that CCAM hindcasts (e.g., for multiple seasons) be made in order to evaluate the model systematically.

REFERENCES

ABEL, SJ and BOUTLE, IA (2012) An Improved Representation of the Raindrop Size Distribution for Single-Moment Microphysics Schemes: Improved Representation of the Raindrop Size Distribution. Quarterly Journal of the Royal Meteorological Society **138 (669)** 2151–2162.

ARAKAWA, A, KATAYAMA, A and MINTZ, Y (1969) Numerical simulation of the general circulation of the atmosphere. In: proceedings of the WMO/ITJGa Symposium on Numerical Weather Prediction, in Japan, Tokyo, 26 November– 4 December 1968, WMO/IUGG, Japanese Meteorological Agency, Japan, Tokyo.

ARAKAWA, A (1972) Design of the UCIA, general circulation model. Numerical Simulation of Weather and Climate. Technical Report No. 7., Department of Meteorology, University of California, Los Angeles.

ARAKAWA A and SCHUBERT WH (1974) Interaction of a Cumulus Cloud Ensemble with the Large-Scale Environment, Part I. Journal of Atmospheric Sciences **31(3)** 674-701.

ARAKAWA, A and WU, C-M (2013) A Unified Representation of Deep Moist Convection in Numerical Modeling of the Atmosphere. Part I. Journal of the Atmospheric Sciences, **70** 1977-1992.

BABA Y (2020) Shallow convective closure in a spectral cumulus parameterization. Atmospheric Research **233**(104707).

BAE, SY, HONG, S-Y and. TAO, W-K (2018) Development of a single-moment cloud microphysics scheme with prognostic hail for the Weather Research and Forecasting (WRF) model. Asia-Pacific Journal of Atmospheric Science **55** 233–245.

BARNSTON AG and TIPPETT MK (2017) Do statistical pattern corrections improve seasonal climate predictions in the North American Multimodel Ensemble models? Journal of Climate **30(20)** 8335–8355.

BECKER, EH (2014) Application of a Quantitative Precipitation Estimation Algorithm for the S-Band Radar at Irene, South Africa. University of KwaZulu-Natal, Durban, South Africa.

BÈLAIR S, MAILHOT J, STRAPP JW and MACPHERSON JI (1999) An examination of local versus nonlocal aspects of a TKE-based boundary layer scheme in clear convective conditions. American Meteorological Society **38** 1499-1518.

BONAVENTURA L (2004) The ICON project: development of a unified model using triangular geodesic grids. Recent developments in numerical methods for atmosphere and ocean modelling. Max Planck Institut fur¨ Meteorologie, Hamburg, Germany.

BOPAPE, M-JM, ENGELBRECHT, FA, MAISHA, R, CHIKOORE, H, NDARANA, T, LEKOLOANE, L, THATCHER, M, MULOVHEDZI, PT, RAMBUWANI, GT, BARNES, MA, MKHWANAZI M and MPHEPYA J (2022) Rainfall Simulations of High-Impact Weather in South Africa with the Conformal Cubic Atmospheric Model (CCAM). Atmosphere **13**, 1987.

BRAHAM, RJR and SQUIRES, P (1974) Cloud physics 1974. Bulletin of Atmospheric Meteorological Society **55** 543–586.

BUSH M, ALLEN T, BAIN C, BOUTLE I, EDWARDS J, FINNENKOETTER A, FRANKLIN C, HANLEY K, LEAN H, LOCK A, MANNERS J, MITTERMAIER M, MORCRETTE C, NORTH R, PETCH J, SHORT C, VOSPER S, WALTERS D, WEBSTER S, WEEKS M, WILKINSON J, WOOD N, and ZERROUKAT M

(2020) The first Met Office Unified Model–JULES Regional Atmosphere and Land configuration, RAL1. Geoscientific Model Development **13(4)** 1999–2029.

CHOW, FK SCHÄR, C, BAN, N, LUNDQUIST, KA, SCHLEMMER, L and SHI, X (2019) Crossing Multiple Gray Zones in the Transition from Mesoscale to Microscale Simulation over Complex Terrain. Atmosphere **10** 274.

COLLINS SN, JAMES RS, RAY P, CHEN K, LASSMAN A, and BROWNLEE J (2013) Grids in Numerical Weather and Climate Models. In: Climate Change and Regional/Local Responses. RAY, P, InTech, London, United Kingdom.

DAWSON, DT II, MANSELL, ER, JUNG, Y, WICKER, LJ, KUMJIAN, MR and XUE, M (2014) Low-level ZDR signatures in supercell forward flanks: The role of size sorting and melting of hail. Journal of the Atmospheric Sciences **71(1)** 276–299.

DUC L, SAITO K, SEKO H (2013) Spatial-temporal fractions verification for high-resolution ensemble forecasts. Tellus A **65** 18171–18193.

ECMWF. 2020. IFS Documentation CY47R1 - Part III: Dynamics and Numerical Procedures. IFS Documentation CY47R1, (June): 1–31. ECMWF, Reading, United Kingdom.

ENGELBRECHT F (2019) Green Book – Detailed Projections of Future Climate Change Over South Africa. CSIR, Pretoria, South Africa.

ENGELBRECHT FA (2006) Theory and application of quasi-elastic equations in terrain-following coordinates based on the full pressure field. University of Pretoria, Pretoria, South Africa.

ENGEBRECHT FA, MCGREGOR, JL AND RAUTENBACH, CJD (2007) On the development of a new nonhydrostatic atmospheric model in South Africa. S. Afr. J. Sci., 103, 127–134.

ENGELBRECHT FA, LANDMAN WA, ENGELBRECHT CJ, LANDMAN S, BOPAPE MM, ROUX B, MCGREGOR JL, THATCHER M (2011) Multi-scale climate modelling over Southern Africa using a variable-resolution global model. Water SA **37(5)** 647–658.

FAGGIAN N, ROUX B, STEINLE P and EBERT E (2015). Fast calculation of the Fractions Skill Score. Mausam 66 457-466.

FLOODLIST (2019). South Africa – Deadly Floods and Landslides Hit KZN and Eastern Cape. https://floodlist.com/africa/south-africa-floods-kzn-eastern-cape-april-2019 (accessed 15th October 2023).

FREIDENREICH S and RAMASWAMY V (1999) A new multiple-band solar radiative parameterization for general circulation models. Journal of Geophysical Research **104(D24)** 31389–31409.

FREITAS S, GRELL G and HAIQIN LI (2020) The GF Convection Parameterization: recent developments, extensions, and applications. Geoscientific Model Development.

GERARD L, PIRIOU J-M, BROŽKOVÁ R, GELEYN J-F and BANCIU D (2009) Cloud and precipitation parameterization in a meso-gamma scale operational weather prediction model. Monthly Weather Review **137** 3960–3977.

GORDON HB, ROTSTAYN LD, MCGREGOR JL, DIX MR, KOWALCZYK EA, O'FARRELL OA, WATERMAN LJ, HIRST AC, WILSON SG, COLLIER MA, WATTERSON IG, and ELLIOTT TI. (2002). The CSIRO

Mk3 Climate System Model. Technical Paper No. 60, CSIRO Atmospheric Research: CSIRO Atmospheric Research, Victoria, Australia.

GROSS M, WAN H, RASCH P, CALDWELL P, WILLIAMSON D, KLOCKE D, JABLONOWSKI C, THATCHER D, WOOD, CULLEN M, BEARE B, WILLETT M, LEMARIÉ F, BLAYO E, MALARDEL S, TERMONIA P, GASSMANN A, LAURITZEN P, JOHANSEN H and LEUNG R (2018) Physics–Dynamics Coupling in Weather, Climate, and Earth System Models: Challenges and Recent Progress. Monthly Weather Review. **146**.

HARRIS L, ZHOU L, CHEN X, CHEN J-H (2020) The GFDL Finite-Volume Cubed-Sphere Dynamical Core: Release 201912. Technical Memorandum GFDL2020001. Geophysical Fluid Dynamics Laboratory, NOAA, Princeton, New Jersey.

HEIKES RP, RANDALL DA, and KONOR CS (2013) Optimized icosahedral grids: Performance of finite-difference operators and multigrid solver. Monthly Weather Review **141(12)** 4450–4469.

HÉREIL P and LAPRISE R (1996) Sensitivity of internal gravity waves solutions to the time step of a semi-implicit semi-Lagrangian nonhydrostatic model. Monthly Weather Review **124(5)** 972–999.

HERSBACH, H., BELL, B., BERRISFORD, P., HIRAHARA, S., HORÁNYI, A., MUÑOZ-SABATER, J., NICOLAS, J., PEUBEY, C., RADU, R., SCHEPERS, D., SIMMONS, A., SOCI, C., ABDALLA, S., ABELLAN, X., BALSAMO, G., BECHTOLD, P., BIAVATI, G., BIDLOT, J., BONAVITA, M., CHIARA, G., DAHLGREN, P., DEE, D., DIAMANTAKIS, M., DRAGANI, R., FLEMMING, J., FORBES, R., FUENTES, M., GEER, A., HAIMBERGER, L., HEALY, S., HOGAN, R.J., HÓLM, E., JANISKOVÁ, M., KEELEY, S., LALOYAUX, P., LOPEZ, P., LUPU, C., RADNOTI, G., ROSNAY, P., ROZUM, I., VAMBORG, F., VILLAUME, S. AND THÉPAUT, J.N. (2020) The ERA5 global reanalysis. *Quarterly Journal of the Royal Meteorological Society*, **146**(730), 1999–2049. https://doi.org/10.1002/qj.3803.

HOLT T and RAMAN S (1988) A review and comparative evaluation of multilevel boundary layer parameterizations for first-order and turbulent kinetic energy closure schemes. Review of Geophysics **26(4)** 761-780.

S and PAN H (1998) Convective Trigger Function for a Mass-Flux Cumulus Parameterization Scheme, Monthly Weather Review **126(10**) 2599-2620.

HONG S-Y, DUDHIA J and CHEN S-H (2004) A Revised Approach to Ice Microphysical Processes for the Bulk Parameterization of Clouds and Precipitation. Monthly Weather Review **132** 103-120.

HOU AY, KAKAR RK, NEECK S, AZARBARZIN AA, KUMMERO CD, KOJIMA M, OKI R, NAKAMURA K and IGUCHI T (2014) The Global Precipitation Measurement Mission. Bulletin of American Meteorological Society **95 (5)** 701–722.

HOUZE Jr RA (1993) Cloud Dynamics, DMOWSKA R. Academic Press, Cambridge, US.

HOUZE Jr RA (2014) Cloud Dynamics, Second Edition. Academic Press, Cambridge, US.

HUANG D and GAO S (2017) Impact of different cumulus convective parameterization schemes on the simulation of precipitation over China. Tellus A: Dynamic Meteorology and Oceanography. **69**,1.

HUANG W, BAO J-W and CHEN B (2014). Parameterization of Subgrid Deep Convective Cloud at Gray-Zone Resolutions: Preliminary Results. Tropical Cyclone Research and Review **3(4)** 218-228.

HURLEY P (2007) Modelling mean and turbulence fields in the dry convective boundary layer with the eddy-diffusivity/massflux approach. Boundary-Layer Meteorology **125** 525–36.

IGUCHI T, NAKAJIMA T, KHAIN AP, SAITO K, TAKEMURA T and SUZUKI K (2008) Modeling the influence of aerosols on cloud microphysical properties in the east Asia region using a mesoscale model coupled with a bin-based cloud microphysics scheme. Journal of Geophysical Research **113**.

JONES B (2014) How does the skill of global model precipitation forecasts over Europe depend on spatial scale? University of Reading, England, United Kingdom.

KAGEYAMA A and SATO T (2004) “Yin-Yang grid”: An overset grid in spherical geometry. Geochemistry, Geophysics, Geosystems, **5(9)**.

KAIN JS (2004) The Kain–Fritsch Convective Parameterization: An Update. Journal of applied meteorology **43** 170-181.

KATZFEY J, SCHLÜNZEN KH, HOFFMANN P, and THATCHER M (2020) How an urban parameterization affects a high-resolution global climate simulation. Quarterly Journal of Royal Meteorological Society **146** 3808–3829.

KESSLER E (1969) On the distribution and continuity of water substance in atmospheric circulation. Meteorological Monograph **32**. American Meteorological Society.

KHAIN AP, BEHENG KD, HEYMSFIELD AJ, KOROLEV A, KRICHAK SO, LEVIN Z, PINSKY M, PHILLIPS V, TELLER A, VAN DEN HEEVER SC and YANO J-I (2015) Representation of microphysical processes in cloud-resolving models: Spectral (bin) microphysics versus bulk parameterization. Reviews of Geophysics **53** 247–322.

KLEIN R (2014) Asymptotic Models for Atmospheric Flows. In: Handbook of Geomathematics, FREEDEN W, NASHED M AND SONAR T (eds), Springer, Berlin, Heidelberg.

KOWALCZYK E, WANG Y, LAW R, DAVIES H, MCGREGOR J, and ABRAMOWITZ G (2006) The CSIRO Atmosphere Biosphere Land Exchange (CABLE) model for use in climate models and as an offline model. CSIRO Marine and Atmospheric Research Paper **13** 42.

KRUGER AC and SHONGWE S (2004) Temperature Trends in South Africa: 1960-2003. International Journal of Climatology **24** 1929-1945.

KUHNLEIN C, DECONINCK W, KLEIN R, MALARDEL S, PIOTROWSKI ZP, SMOLARKIEWICZ PK, SZMELTER J, WEDI NP (2019) FVM 1.0: A nonhydrostatic finite-volume dynamical core for the IFS. Geoscientific Model Development **12(2)** 651–676.

LANDMAN WA, ENGELBRECHT FA, BERAKI A, ENGELBRECHT C, MBEDZ M, GILL T and NTSANGWANE L (2009) Model Output Statistics Applied to Multi-Model Ensemble Long[1]Range Forecasts over South Africa. WRC Report No. 1492/1/08. Water Research Commission, Pretoria, South Africa. 56 pp.

LANDMAN WA, ENGELBRECHT F, PARK R, BOPAPE M and LOTTER D (2010) Atmospheric modelling and prediction at time-scales from days to seasons. Proc. CSIR Biannual Conference, August/September 2010, Pretoria, South Africa. Reference NE05-P0-F

LE ROUX N (2009) Seasonal Maize Yield Simulations for South Africa Using a Multi-Model Ensemble System. M.Sc. thesis. University of Pretoria, Pretoria, South Africa. 152 pp.

LANDMAN S (2012) A multi-model ensemble system for short-range weather prediction in South Africa. M.Sc. thesis, University of Pretoria, Pretoria.

LANDMAN WA, BERAKI A, DEWITT D and LÖTTER D (2014) SST prediction methodologies and verification considerations for dynamical mid-summer rainfall forecasts for South Africa. Water SA **40(4)** 615–622.

LANDMAN WA, ENGELBRECHT F, PARK R, VAN DER MERWE J, DEDEKIND Z, BERAKI A, MALHERBE J and MPHESHEA L (2015) Unifying weather and climate variability predictions – an operational seamless forecasting system for southern Africa at time scales from days to seasons. Water Research Commission Report No. 2050/1/14. Water Research Commission, Pretoria, South Africa.

LAPRISE R (1998) Semi-implicit semi-Lagrangian fully elastic nonhydrostatic model formulation. In: Seminar on Recent Developments in Numerical Methods for Atmospheric Modelling, Reading, London, 7-11 September 1998, p266 -280. ECMWF, Reading, United Kingdom.

LEE H and BAIK J-J (2018) A Comparative Study of Bin and Bulk Cloud Microphysics Schemes in Simulating a Heavy Precipitation Case. Atmosphere **9(12)** 475.

LI X, TAO W-K, KHAIN AP, SIMPSON J, JOHNSON DE (2009) Sensitivity of a cloud-resolving model to bulk and explicit bin microphysical schemes. Part I: Comparisons. Journal of Atmospheric Science **66** 3–21.

LI X, TAO W-K, MATSUI T, LIU C and MASUNAGA H (2010) Improving a Spectral Bin Microphysical Scheme Using TRMM Satellite Observations: Improving Spectral Bin Microphysics Using Trmm. Quartely Journal of Royal Meteorological Society **136 (647)** 382–399.

LIM KS and HONG S (2010) Development of an Effective Double-Moment Cloud Microphysics Scheme with Prognostic Cloud Condensation Nuclei (CCN) for Weather and Climate Models. Monthly Weather Review **138** 1587–1612.

LIN Y-L, FARLEY RD and ORVILLE HD (1983) Bulk Parameterization of the Snow Field in a Cloud Model. Journal of Climate and Applied Meteorology **22(6)** 1065–1092.

LOCK AP, BROWN AR, BUSH MR, MARTIN GM and SMITH RNB (2000) A new boundary layer mixing scheme. Part 1: Scheme description and single-column model tests. Monthly Weather Review **128** 3187- 3199.

LOFTUS AM, COTTON WR and CARRIÓ GG (2014) A triple-moment hail bulk microphysics scheme. Part I: Description and initial evaluation. Atmospheric Research **149** 35–57.

MALARDEL S, WEDI N, DECONINCK W, DIAMANTAKIS M, KÜHNLEIN C, MOZDZYNSKI G, HAMRUD M, SMOLARKIEWICZ P (2015) A new grid for the IFS METEOROLOGY A new grid for the IFS. from Newsletter Number, **14616(146)** 23–28.

MAILHOT J AND BENOIT R (1982) A finite-element model of the atmospheric boundary layer suitable for use with numerical weather prediction models. American Meteorological Society **39** 2249-2266.

MAISHA RT, NDARANA T, ENGELBRECHT FA and THATCHER M (2023) Simulation of the eThekwini Heat Island in South Africa. https://doi.org/10.1175/JAMC-D-2.

MCGREGOR, JL, GORDON, HB, WATTERSON, IG, DIX, R and ROTSTAYN, LD (1993) The CSIRO 9-level atmospheric general circulation model. Technical Report 26, CSIRO Atmospheric Research, 89 pp.

MCGREGOR JL. 1996. Semi-Lagrangian advection on conformal- cubic grids. Mon. Weather Rev. 124 1311-1322.

MCGREGOR JL. 2003. A new convection scheme using a simple closure. In: Current Issues in the Parameterization of Convection. BMRC Research Report 93. 33-36.

MCGREGOR JL (2005) C-CAM: Geometric aspects and dynamical formulation. CSIRO Atmospheric Research Tech. Paper No. 70. CSIRO, Australia.

MCGREGOR J and DIX M (2008) An Updated Description of the Conformal-Cubic Atmospheric Model. In: High Resolution Numerical Modelling of the Atmosphere and Ocean, HAMILTON K and OHFUCHI W. Springer, New York.

MCGREGOR JL, NGUYEN KC, KIRONO DGC and KATZFEY JJ (2016) High-resolution climate projections for the islands of Lombok and Sumbawa, Nusa Tenggara Barat Province, Indonesia: Challenges and implications. Climate Risk Management. Elsevier B.V. **12** 32–44.

MESINGER F and ARAKAWA A (1976) Numerical Methods used in Climate Models. GARP Publication Series **1(17)** 1–64.

MESINGER F, CHOU SC, GOMES JL, JOVIC D, BASTOS P, BUSTAMANTE JF, LAZIC L, LYRA AA, MORELLI S, RISTIC I and VELJOVIC K (2012) An upgraded version of the Eta model. Meteorology and Atmospheric Physics **116(3–4)** 63–79.

MILBRANDT JA and YAU MK (2005) A multimoment bulk microphysics parameterization. Part II: A proposed three-moment closure and scheme description. Journal of the Atmospheric Sciences **62(9)** 3065–3081.

MILLER MJ and WHITE AA. 1984. On the non-hydrostatic equations in pressure and sigma coordinates. Quarterly Journal of the Royal Meteorological Society **110(464)** 515–533.

MILLER MJ (1985) A new convective adjustment scheme and its impact ECMWF model. European Centre for Medium-Range Weather Forecasts; Reading, United Kingdom.

MILTENBERGER AK, FIELD PR, HILL AA, ROSENBERG P, SHIPWAY BJ, WILKINSON JM, SCOVELL R and BLYTH (2018) AM Aerosol–Cloud Interactions in Mixed-Phase Convective Clouds – Part 1: Aerosol Perturbations. Atmospheric Chemistry and Physics **(5)** 3119–3145.

MOLTHAN AL and COLLE BA (2012) Comparisons of Single- and Double-Moment Microphysics Schemes in the Simulation of a Synoptic-Scale Snowfall Event. Monthly Weather Review **140 (9)** 2982–3002.

MONIN AS.and OBUKHOV AM (1954) Basic laws of turbulent mixing in the surface layer of the atmosphere, Tr. Geofiz. inst. Akad. Nauk SSSR 151 163–187.

MORRISON H, VAN LIER-WALQUI M, FRIDLIND AM, GRABOWSKI WW, HARRINGTON JY, HOOSE C, et al.(2020). Confronting the challenge of modeling cloud and precipitation microphysics. Journal of Advances in Modeling Earth Systems**12,e2019MS001689.**

MITTERMAIER MP (2021) A “Meta” Analysis of the Fractions Skill Score: The Limiting Case and Implications for Aggregation. Monthly Weather Review **149(10)** 3491-3504.

MURPHY AH (1973) A new vector partition of the probability score. Journal of Applied Meteorology **12,** 595–600.

NAUMANN AK and SEIFERT A (2016) Evolution of the Shape of the Raindrop Size Distribution in Simulated Shallow Cumulus. Journal of Atmospheric Science **73** 2279–2297.

MUTHIGE, MS, MALHERBE, J, ENGELBRECT, FA, GRAB, S, BERAKI, A, MAISHA, TR, and VAN DER MERWE, J (2018) Projected changes in tropical cyclones over the South West Indian Ocean under different extents of global warming. *Environ. Res. Lett.*, **13**, https://doi.org/10.1088/1748-9326/aabc60.

NGUYEN KC, KATZFEY JJ and MCGREGOR JL (2012) Global 60 km simulations with CCAM: Evaluation over the tropics. Climate Dynamics **39(3)** 637–654.

OCHA (UNITED NATIONS OFFICE FOR THE COORDINATION OF HUMANITARIAN AFFAIRS) (2022) ReliefWeb: SOUTHERN AFRICA: Cyclone Season Flash Update No. 1. https://reliefweb.int/sites/reliefweb.int/files/resources/ROSEA_20220201_Southern%20Africa%20Cyclone%20Season_Flash%20Update_for%20circulation.pdf (Accessed 06th April 2022).

OGURA Y and TAKAHASHI T (1973) The development of warm rain in a cumulus model. Journal of Atmospheric Science **30** 262–277.

ONISHI R and TAKAHASHI K (2011) A Warm-Bin–Cold-Bulk Hybrid Cloud Microphysical Model. Journal Of The Atmospheric Sciences **69** 1474- 1497.

OOYAMA K (1971) Convection and convection adjustment: A theory on parameterization of cumulus convection. Journal of Meteorological Society of Japan **49** 744-756.

PHILLIPS NA (1957) A Coordinate System Having Some Special Advantages For Numerical Forecasting. Journal of Meteorology **14(2)** 184–185.

PICKERING KE (2015) Convective Cloud Modelling. NASA Goddard Space Flight Center Adjunct Professor, UMD/AOSC. AOSC 620.

PLANT RS and CRAIG GC (2008) A Stochastic Parameterization for Deep Convection Based on Equilibrium Statistics. Journal of the Atmospheric Sciences **65** 87-105.

PU Z and KALNAY E (2018) Numerical Weather Prediction Basics: Models, Numerical Methods, and Data Assimilation. In: Handbook of Hydrometeorological Ensemble Forecasting, DUAN Q., PAPPENBERGER F., THIELEN J., WOOD A., CLOKE H AND SCHAAKE J. (eds). Springer, Berlin, Heidelberg.

RANČIĆ M, PURSER RJ, MESINGER F (1996) A global shallow-water model using an expanded spherical cube: Gnomonic versus conformal coordinates. Quarterly Journal of the Royal Meteorological Society **122(532)** 959–982.

RANDALL DA (1994) Geostrophic Adjustment and the Finite-Difference Shallow-Water Equations. Monthly Weather Review **122(6)** 1371–1377.

RANDALL DA, RINGLER TD, HEIKES RP, JONES P and BAUMGARDNER J (2002) Climate modeling with spherical geodesic grids. Computing in Science and Engineering **4(5)** 32.

ROBERTS N (2008) Assessing the spatial and temporal variation in the skill of precipitation forecasts from an NWP model. Meteorological Applications **15** 163-169.

ROTSTAYN LD (1997) A physically based scheme for the treatment of stratiform clouds and precipitation in large-scale models. I: Description and evaluation of the microphysical processes. Quarterly Journal of Royal Meteorological Society **123** 1227–1282.

ROTSTAYN LD, RYAN BF and. KATZFEY JJ (2000) A scheme for calculation of the liquid fraction in mixed-phase stratiform clouds in large-scale models. Monthly Weather Review **128** 1070- 1088.

SADOURNY R (1972) Conservative Finite-Difference Approximations of the Primitive Equations on Quasi-Uniform Spherical Grids. Monthly Weather Review **100(2)** 136–144.

SADOURNY R, ARAKAWA A and MINTZ Y (1968) Integration Of The Nondivergent Barotropic Vorticity Equation With An Icosahedral-Hexagonal Grid For The Sphere. Monthly Weather Review **(443)** 2–7.

SATYAWARDHANA HG (2019) Comparison of seasonal prediction outputs based on dynamic atmosphere model and observations (case study: Seasonal prediction in 2016 - 2017). IOP Conference Series: Earth and Environmental Science, **303(1)** 0–8.

SAWS (SOUTH AFRICAN WEATHER SERVICE; 2017) Historical synoptic maps. https://www.weathersa.co.za/Documents/Publications/20171230.pdf (Accessed July 2022)

SAWS (SOUTH AFRICAN WEATHER SERVICE; 2019). WEATHERSMART NEWS: Scientific meteorological and climatological news from the South African Weather Service. (August 2019). https://www.weathersa.co.za/Documents/Corporate/WeatherSmart%20Newsletter%20August%202019%20v4%20web.pdf

SAWS (SOUTH AFRICAN WEATHER SERVICE; 2019b). Caelum: Notable weather and weather-related events in 2019. South African Weather Service: Pretoria, South Africa.

SAWS (SOUTH AFRICAN WEATHER SERVICE; 2019c) Historical synoptic maps. https://www.weathersa.co.za/Documents/Publications/20191112.pdf (Accessed July 2022)

SAWS (SOUTH AFRICAN WEATHER SERVICE; 2021) Historical synoptic maps. https://www.weathersa.co.za/Documents/Publications/20210201.pdf (Accessed March 2023)

SAWS (SOUTH AFRICAN WEATHER SERVICE; 2022). South African Weather Service Annual Report 2021/2022. https://www.weathersa.co.za/Documents/AnnualReports/SAWS_ANNUAL_REPORT_-_Reduced_File_Size-1_27092022093113.pdf

SAWS (SOUTH AFRICAN WEATHER SERVICE; 2022b) South African Weather Service Annual Report 2021/2022. South African Weather Service, Pretoria, South Africa.

SCHMIDT F (1977) Variable fine mesh in spectral global model. Beiträge zur Physik der Atmosphäre **50** 211–217.

SCHULZ J-P (2011) Introducing a sea ice scheme in the COSMO model. COSMO Newsletter **11,** 32–40.

SEIFERT A and BEHENG KD (2001) A double-moment parameterization for simulating autoconversion, accretion and self-collection, Atmospheric Research **59–60** 265–281.

SHIPWAY BJ and HILL AA (2012) Diagnosis of systematic differences between multiple parametrizations of warm rain microphysics using a kinematic framework. Quarterly Journal of the Royal Meteorological Society **138(669)** 2196–2211.

SIMPSON J and WIGGERT V (1969) Models of precipitating cumulus towers. Monthly Weather Review **97** 471–489.

SKOK G and ROBERTS N (2016) Analysis of Fractions Skill Score properties for random precipitation fields and ECMWF forecasts. Quarterly Journal of the Royal Meteorological Society **145(700)** 2599-2610.

SMILJANIC I, KERKMANN J and PRIETO J (2022). EUMETSAT. Retrieved from Tropical Cyclone Eloise: https://www.eumetsat.int/tropical-cyclone-eloise (Accessed September 2011).

SMITH CJ (2000) The Semi-Lagrangian Method in Atmospheric Modelling. University of Reading, London, UK.

SOARES P, MIRANDA P, SIEBESMA A and TEIXEIRA J (2004) An eddy- diffusivity/mass-flux parametrization for dry and shallow cumulus convection. Q. J. R. Meteorol. Soc. 130 3365–3384.

STENSRUD D (2007). Microphysics parameterizations. In Parameterization Schemes: Keys to Understanding Numerical Weather Prediction Models, Cambridge University Press, Cambridge, US.

STRAKA JM (2009) Cloud and Precipitation Microphysics: Principles and Parameterizations, Cambridge University Press, Cambridge, UK.

STULL RB (1988) An introduction to boundary layer meteorology, Kluwer Academic Publishers, Dordrecht, Netherlands.

THATCHER, M and HURLEY, P (2012) Simulating Australian Urban Climate in a Mesoscale Atmospheric Numerical Model. *Boundary-Layer Meteorol.*, **142**, 149–175, https://doi.org/10.1007/s10546-011-9663-8.

THATCHER M (2021) Overview of CCAM atmospheric physics parameterisations. In: CCAM Webinar. Pretoria, South Africa. 8-12 November 2021. South African Weather Service, Pretoria, South Africa.

THATCHER M AND MCGREGOR J (2008) Dynamically downscaled Mk3.0 climate projection for the Marine and Tropical Sciences Research Facility (MTSRF) from 2060-2090. Journal of Climate Studies **42(8)** 1234-1256.

TOMITA H (2008) A stretched icosahedral grid by a new grid transformation. Journal of the Meteorological Society of Japan **86A** 107–119.

TIEDTKE M (1989) A comprehensive mass flux scheme for cumulus parameterization in large-scale models. Monthly Weather Review **117** 1779-1800.

Troen, I.B., &, Mahrt, L., 1986: A simple model of the atmospheric boundary layer; sensitivity to surface evaporation, Boundary-Layer Meteorology, 37, 129-148.

UNITED NATIONS (2022) Mozambique: UN responds as thousands are caught in the wake of devastating Cyclone Eloise. https://news.un.org/en/story/2021/01/1082972 (Accessed 5 September 2022)

WILKINSON J (2020). The Large-Scale Precipitation Parametrization Scheme, Unified Model Documentation Paper 026, Met Office, United Kingdom.

WANG N and LEE J-L (2011) Geometric Properties of the Icosahedral-Hexagonal Grid on the Two-Sphere. SIAM Journal on Scientific Computing **33(5**) 2536–2559.

WILLIAMSON DL (2007) The evolution of dynamical cores for global atmospheric models. Journal of the Meteorological Society of Japan **85 B(February)** 241–269.

WILLIAMSON DL and LAPRISE R (2000) Numerical Modeling of the Global Atmosphere in the Climate System. Numerical Modeling of the Global Atmosphere in the Climate System.

Yoshimura, H., Mizuta, R., & Murakami, H. (2015). A Spectral Cumulus Parameterization Scheme Interpolating between Two Convective Updrafts with Semi-Lagrangian Calculation of Transport by Compensatory Subsidence, Monthly Weather Review, 143(2), 597-621. Retrieved Sep 6, 2021, from

WITEK ML, TEIXEIRA J and MATHEOU G (2010) An Integrated TKE-Based Eddy Diffusivity/Mass Flux Boundary Layer Closure for the Dry Convective Boundary Layer. Journal of the Atmospheric Sciences **68** 1526-1540.

XIE B, FUNG JC-H, CHAN A and LAU AK-H (2012) Evaluation of nonlocal and local planetary boundary layer schemes in the WRF Model. J. Geophys. Res, **117**, D12103.

XULU, NG (2017) Impact of spatio-temporal variability of the Mascarene High on weather and climate over Southern Africa, Msc Dissertation, University of Venda

ZHANG G and MCFARLANE N (1995) Sensitivity of climate simulations to the parameterization of cumulus convection in the Canadian Climate Centre general circulation model. Atmosphere-Ocean Dynamics **33** 407–407,

Zhao Y, Wen Z, li X, Chen R and Chen G (2021) Structure and maintenance mechanisms of the Mascarene High in austral winter, Int. Journal. Climatol..42,9, 4700-4715, https://doi.org/10.1002/joc.7498

APPENDIX A: CLOUD MICROPHYSICS CODE CHANGES

- Cloud microphysics scheme switches (before update a and b) and (after update c and d)

a

```
cloudset=0
if [[ $ncld -eq 0 ]]; then
  cloudset=1
  ncloud=0
fi
if [[ $ncld -eq 1 ]]; then
  cloudset=1
  ncloud=3
fi
if [[ $cloudset -eq 0 ]]; then
  echo "ERROR: Invalid cloud option $ncld"
  exit
fi
```

c

```
cloudset=0
if [[ $ncld -eq 0 ]]; then
  cloudset=1
  ncloud=0
  rcrit_l=0.75
 rcrit_s=0.85
fi
if [[ $ncld -eq 1 ]]; then
  cloudset=1
  ncloud=2   # ncloud=3 was a typo
  rcrit_l=0.75
 rcrit_s=0.85
fi
if [[ $ncld -eq 2 ]]; then
  cloudset=1
  ncloud=3
  rcrit_l=0.8
 rcrit_s=0.8
fi
if [[ $cloudset -eq 0 ]]; then
  echo "ERROR: Invalid cloud option $ncld"
  exit
fi
```

b

```
nradiation=0    ;# Radiation (0=Older/faster, 1=Newer/slower)
ncld=1          ;# Cloud microphysics (0=Liq/Ice, 1=Liq/Ice/Snow/Graupel)
npbl=0          ;# Boundary layer (0=Local Ri, 1=k-e)
nconv=0         ;# Convection (0=2015a, 1=2015b+GWD, 2=2017)
nstrongnudge=0  ;# Strong nudging (0=standard, 1=strong)
nlev=35         ;# Number of levels (27, 35, 54, 72, 108)
```

d

```
nradiation=0    ;# Radiation (0=Older/faster, 1=Newer/slower)
ncld=0          ;# cloud microphysics (0=liq+ice, 1=liq+ice+rain, 2=liq+ice+rain+snow+graupel)
npbl=0          ;# Boundary layer (0=Local Ri, 1=k-e)
nconv=3        ;# convection (0=2014, 1=2015a, 2=2015b, 3=2017, 4=Mod2015a)
nstrongnudge=0 ;# Strong nudging (0=standard, 1=strong)
nlev=35         ;# Number of levels (27, 35, 54, 72, 108)
```

- A namelist file adopted to pre-process ERA5 reanalysis data (to be used as input to CCAM).

```
cat << EOF1 > g2n.nml
&splice
outputunit  = "pres", "hPa"
levinvert   = .TRUE.
splicename  = "Z", "T", "U", "V", "R", "LSM", "MSL", "Z", "SP", "SKT", "SD", "SF","SKT","STL1","STL2","STL3","STL4","STL4","SWVL1","SWVL1","SWVL2","SWVL3","SWVL4","S
WVL4"
spliceunit  = "ISBL", "ISBL", "ISBL", "ISBL", "ISBL", "SFC", "SFC", "SFC", "SFC", "SFC", "SFC", "SFC","SFC","0-  0-DBLL","0.1-0.3-DBLL","0.3-1.0-DBLL","1.0-2.5-DBLL"
,"1.0-2.5-DBLL","0-  0-DBLL","0-  0-DBLL","0.1-0.3-DBLL","0.3-1.0-DBLL","1.0-2.5-DBLL","1.0-2.5-DBLL"
newname     = "hgt", "temp", "u", "v", "rh", "land", "pmsl",  "zs", "ps", "tss", "siced", "fracice","tgg1","tgg2","tgg3","tgg4","tgg5","tgg6","wetfrac1","wetfrac2","
wetfrac3","wetfrac4","wetfrac5","wetfrac6"
/
EOF1
```